THE REACTIVE TRANSPORT OF SUSPENDED PARTICLES:

MECHANISMS AND MODELING

by

RICHARD STEVEN MERCIER

B.A.Sc., University of Waterloo
(1978)

S.M., Massachusetts Institute of Technology
(1982)

SUBMITTED IN PARTIAL FULFILLMENT
OF THE REQUIREMENTS FOR THE
DEGREE OF

DOCTOR OF PHILOSOPHY

at the

MASSACHUSETTS INSTITUTE OF TECHNOLOGY

and the

WOODS HOLE OCEANOGRAPHIC INSTITUTION

October, 1984

Signature of Author _____
Joint Program in Oceanographic Engineering
Massachusetts Institute of Technology
Woods Hole Oceanographic Institution
October 16, 1984

Certified by _____
Keith D. Stolzenbach
Thesis Supervisor

Accepted by _____
William D. Grant
Chairman, Joint Committee on Oceanographic Engineering

THE REACTIVE TRANSPORT OF SUSPENDED PARTICLES: MECHANISMS AND MODELING

by

RICHARD S. MERCIER

Submitted to the Massachusetts Institute of Technology-Woods Hole Oceanographic Institutio Joint Program in Oceanographic Engineering in partial fulfillment of the requirer for the Degree of Doc ilosophy

ABSTRACT

The computational modeling of the reactive transport of suspended particles is particularly challenging because particles settle differentially and they are involved in physicochemical reactions that are often nonlinear and sometimes fast with respect to the fluid turbulence. Examples of such reactions are particle coagulation, precipitation/dissolution, adsorption, and secondary nucleation. The kinetics of coagulation are examined and it is concluded that in the aquatic environment particle number concentration correlations are significant and that particles of size greater than about 0.1 micron tend to collide most often with particles that are much smaller in size, contrary to the theory of Hunt (1982). An improved model for the collision frequency function for turbulent shear is proposed that takes into account the intermittency in the microscale shear rate. Extending the work of Daly (1984), a kinetic model of frazil ice growth is formulated and verified against experimental data. To incorporate fast, nonlinear reaction kinetics into a general transport model, the transport equation for the one-point, joint scalar probability density function (pdf) is employed. Pope's (1981) Monte Carlo technique for solving the pdf transport equation is extended to allow simulation over nonuniform grids. In addition, stochastic algorithms for simulating differential sedimentation and radial diffusion are developed. Finally, the capabilities of the model are demonstrated by simulations of frazil ice formation in a river, transport and deposition of sludge particles discharged from a coastal outfall, and desorption of trace elements from resuspended, contaminated sediments.

Thesis Supervisor: Keith D. Stolzenbach
Title: Associate Professor of Civil Engineering

To my wife, Alex,
for her encouragement when I was in doubt,
her patience when I was frustrated,
and her faith when I was unavailable.

ACKNOWLEDGEMENTS

This research was funded by grants from the Woods Hole Oceanographic Institution, the National Oceanic and Atmospheric Administration, and the Environmental Protection Agency.

The interest and assistance of my friends and colleagues at the Parsons Lab have contributed significantly to the completion of this thesis. I am especially indebted to Edmund Lo for consultation on numerical techniques, Kevin Farley and Steve Daly for sharing their expertise in the modeling of coagulation and frazil ice kinetics, respectively, Bob Hudson and Dave Dzombak for instruction in the essentials of aquatic chemistry, and Tom Army and John Trowbridge for numerous stimulating philosophical discussions. The helpful comments of the thesis committee are gratefully acknowledged. I would also like to thank Ms. Diane Westerink for expertly typing the thesis.

I reserve special thanks for Prof. Keith Stolzenbach, teacher par excellence, for his patient encouragement and unselfish support of the thesis. I am most grateful for the knowledge and insight that I have gained through countless discussions with him over the past six years.

TABLE OF CONTENTS

LIST OF FIGURES

Page

Page

Page

Page

Page

LIST OF TABLES

I. BACKGROUND AND REVIEW

The ultimate goal of environmental research is the understanding of the dynamics of individual natural processes in a local sense, and how they interact in a global sense. The ability to predict the dynamic behavior of the environment is requisite to the assessment of the impact of artificial perturbations and the development of effective management strategies.

Experimental research over the past two or three decades has greatly increased our understanding of individual physical, biological and chemical processes that contribute to variations in the environment. There is still much to be done. However, as part of the research effort, it is useful to attempt to synthesize the available knowledge of individual processes by formulating global analytical models. These global models may then be used to study interactions among various processes and further enhance our insight. With sufficient testing and refinement, global models may eventually be used in a predictive mode.

The formulation and implementation of a global model is particularly challenging because of the potentially large number of component processes involved, the nonlinear interactions that must be preserved, and the resulting wide range of space and time scales that must be simulated. To be of any practical value, however, the global model must maintain flexibility in problem specification, accuracy of results, and efficiency in computation.

The goal of this thesis is to develop the capability to model simultaneously the transport and reaction of dissolved and solid constituents in rivers, lakes and coastal waterbodies. A major part of the effort is devoted to developing a general framework within which accurate and efficient algorithms for computing transport and reaction may be incorporated. In the hope of being able to gain insight into the dynamic interactions amongst processes, a minimum of empiricism is used. Before going into details about the modeling approach some general aspects of aquatic transport modeling will be reviewed.

1.1 Formulation of the General Problem

In general terms, the equation that governs the mean reactive transport of both solid and dissolved constituents in the environment is the familiar advective-diffusion equation,

$$\frac{\partial \langle \phi_j \rangle}{\partial t} = - \left(\langle U_i \rangle + w_s^{(j)} \delta_{i3} \right) \frac{\partial \langle \phi_j \rangle}{\partial x_i} + \frac{\partial}{\partial x_i} \left((\Gamma^{(i)} + D^{(j)}) \frac{\partial \langle \phi_j \rangle}{\partial x_i} \right) + \langle S^{(j)}(\underset{\sim}{\phi}) \rangle \qquad (1\text{-}1)$$

where $\langle \phi_j \rangle$ is the local mean concentration of constituent j, $\langle U_i \rangle$ is the mean advection velocity, $w_s^{(j)}$ is the settling velocity of j-particles (if constituent j is dissolved then $w_s^{(j)} = 0$), $\Gamma^{(i)}$ is the turbulent eddy diffusivity corresponding to the i-direction, $D^{(j)}$ is the molecular diffusivity, δ_{ij} is the Kroenecher delta function, i = 1,2 correspond to horizontal directions, i = 3 corresponds to the vertical direction and $S^{(j)}(\underset{\sim}{\phi})$ is a source term which is in general a function of the total ensemble of constituent concentrations, $\underset{\sim}{\phi}$.

Accordingly, the terms on the right hand side represent the contributions of advection, particle buoyancy, turbulent dispersion, molecular diffusion, and reaction processes to the net temporal change in the local concentration.

The possible types of interactions amongst the various processes may conveniently be classified according to the ordering of the component time scales. For example, consider a steady flow remote from physical boundaries. Defining the scales

$$\phi_{o,j} = \frac{\phi_j}{\phi_j^*} \qquad U_o = \frac{U_i}{U_i^*} \qquad w_{s,o}^{(j)} = \frac{w_s^{(j)}}{w_s^{*(j)}}$$

$$S_o^{(j)} = \frac{S^{(j)}}{S^{*(j)}} \qquad L = \frac{x_i}{x_i^*} \qquad \Gamma_o = \frac{\Gamma^{(i)} + D^{(j)}}{\Gamma^{*(i)} + D^{*(j)}} \qquad (1\text{-}2)$$

Eq. 1-1 may be rewritten as

$$\frac{\partial \langle \phi_j^* \rangle}{\partial t} = -\left(\frac{1}{t_a}\right) \langle U_i^* \rangle \frac{\partial \langle \phi_j^* \rangle}{\partial x_i^*} - \left(\frac{1}{t_s^{(j)}}\right) w_s^{*(j)} \delta_{i3} \frac{\partial \langle \phi_j^* \rangle}{\partial x_i^*}$$

$$+ \left(\frac{1}{t_d}\right) \frac{\partial}{\partial x_i^*} \left(\left(\Gamma^{*(i)} + D^{*(i)}\right) \frac{\partial \langle \phi_j^* \rangle}{\partial x_i^*} \right) + \left(\frac{1}{t_r^{(j)}}\right) \langle S^{*(j)} \rangle \qquad (1\text{-}3)$$

where

$$t_a = \frac{L}{U_o} \qquad t_d = \frac{L^2}{\Gamma_o} \qquad t_s^{(j)} = \frac{L}{w_{s,o}^{(j)}} \qquad t_r^{(j)} = \frac{\phi_j}{S_o^{(j)}} \qquad (1\text{-}4)$$

are the time scales characterizing each process. If there are σ constituents under consideration, then there are $(2\sigma + 2)$ time scales.

Nonlinear interactions occur between processes that add or remove mass from a material volume of fluid as it is being advected at the local mean velocity $\langle U_i \rangle$. These processes are settling, diffusion and reaction. Consider the time scale ordering $t_r^{(j)} \ll t_d \ll t_s^{(j)}$ for all $j = 1,2,\ldots,\sigma$, for example. For this case settling may be neglected as a transport process, but diffusion will be extremely important in controlling the rate at which the reaction proceeds. The interaction between diffusion and reaction will be nonlinear insofar as the reaction is nonlinear. The time scale ordering $t_d \ll t_r^{(j)} \ll t_s^{(j)}$, on the other hand, will not result in any nonlinear interactions since in this case the system will be well mixed and reaction will proceed independently of the diffusion or settling processes. In the general case the separation of time scales will not be so distinct and the time scales for the settling or reaction of different species will vary greatly. Also, for unsteady flows or flows near non-homogeneous boundaries additional time and length scales will be introduced to describe the associated temporal or spatial variability. Nevertheless, in formulating a general procedure for solving Eq. 1-1, it is necessary to include the capability to handle any ordering of the time scales, either directly or indirectly.

The influence of fluid turbulence on reactive transport is accounted for in the general conservation equation, Eq. 1-1, through the terms representing turbulent diffusion and reaction. By writing the turbulent diffusion term as we have in Eq. 1-1 we have already adopted the "eddy diffusivity" approach for modeling the correlation between turbulent fluctuating velocity and concentration, namely,

$$- \langle u_i' \phi' \rangle = \Gamma_{ij} \frac{\partial \langle \phi \rangle}{\partial x_j} \tag{1-5}$$

where Γ_{ij} is the eddy diffusivity tensor which is assumed diagonal ($\Gamma_{ij} = 0$ for $i \neq j$, $\Gamma_{ij} = \Gamma^{(j)}$ for $i = j$). The scalar flux $-\langle u_i' \phi' \rangle$ is also responsible for the generation of concentration variance, $\langle \phi'^2 \rangle$.

The eddy diffusivity $\Gamma^{(j)}$ is related to the (assumed stationary and homogeneous) turbulence through the relation (Tennekes and Lumley, 1972)

$$\Gamma^{(j)} = \langle u_j'^2 \rangle \int_0^t R_j(\tau)\, d\tau \tag{1-6}$$

where $R_j(\tau)$ is the Lagrangian velocity autocorrelation function for the j-direction. If $R_j(\tau)$ is a monotonically decreasing function of the time shift, τ, then for short times, t, we see that the eddy diffusivity increases with diffusion time (i.e., with the diffusion length scale). For long times the autocorrelation approaches zero and the integral approaches the Lagrangian time scale. Thus for diffusion times longer than the Lagrangian time scale (or diffusion scales larger than the integral length scale of the turbulence) the eddy diffusivity is constant. In isotropic turbulence the Lagrangian time scale is of order k/ε, where $k = \langle u_i' u_i' \rangle/2$ is the turbulent kinetic energy and ε is the energy dissipation rate. This means that the eddy diffusivity for long diffusion times must be of order k^2/ε. Although the use of an eddy diffusivity formulation to model turbulent dispersion is not without problems (Tennekes and Lumley, 1972) given our ignorance of turbulent dispersion mechanisms, it is not clear that a more complex approach would yield any better results.

The influence of turbulence on reaction can be uncovered by expanding the source term about the mean concentrations,

$$\langle S(\underset{\sim}{\phi})\rangle = S(\langle \underset{\sim}{\phi}\rangle) + \sum_{i=2}^{\infty} \frac{1}{i!} \langle d^{(i)}\, S(\underset{\sim}{\phi})\Big|_{\langle \underset{\sim}{\phi}\rangle}\rangle \tag{1-7}$$

where the differentials are given by (Williamson, Crowell and Trotter, 1972)

$$\begin{aligned}\langle d^{(i)} S(\underset{\sim}{\phi})\Big|_{\langle \underset{\sim}{\phi}\rangle}\rangle &= \langle \Big(\sum_{j=1}^{\sigma} \phi_j \frac{\partial}{\partial \phi_j}\Big)^i S(\underset{\sim}{\phi})\Big|_{\langle \underset{\sim}{\phi}\rangle}\rangle \\ &= \sum_{a_1+a_2+\ldots a_\sigma=i} \frac{i!}{a_1!a_2!\ldots a_\sigma!} \langle \phi_1^{a_1}\, \phi_2^{a_2} \ldots \phi_\sigma^{a_\sigma}\rangle \\ &\quad \times \frac{\partial^i}{\partial \phi_1^{a_1}\, \partial \phi_2^{a_2} \ldots \partial \phi_\sigma^{a_\sigma}} S(\underset{\sim}{\phi})\Big|_{\langle \underset{\sim}{\phi}\rangle}\end{aligned} \tag{1-8}$$

Thus we see that, if the reaction is nonlinear, the turbulence correlations $\langle \phi_1^{a_1}, \phi_2^{a_2} \ldots \phi_\sigma^{a_\sigma}\rangle$, where σ is the total number of constituents and a_i are the multinomial coefficients, will affect the mean reaction rate. Of course we cannot neglect the role of molecular diffusion. While turbulence is the source of such correlations as $\langle \phi_1^{a_1}, \phi_2^{a_2} \ldots \phi_\sigma^{a_\sigma}\rangle$, molecular diffusion acts to remove the correlations. The actual levels of correlation at any point in space and time are determined by the dynamic balance between local turbulent generation and redistribution, and molecular dissipation processes.

For example, under homogeneous and isotropic conditions, the equation governing the decay of concentration variance is

$$\frac{\partial \langle \phi'^2 \rangle}{\partial t} = -12\, D \left\langle \left(\frac{\partial \phi'}{\partial x}\right)^2 \right\rangle = -\frac{\langle \phi'^2 \rangle}{t_m} \tag{1-9}$$

where

$$t_m = \frac{\langle \phi'^2 \rangle}{12D \left\langle \left(\frac{\partial \phi'}{\partial x}\right)^2 \right\rangle} = \frac{\int_0^\infty E_\phi(n)\, dn}{12D \int_0^\infty n^2 E_\phi(n)\, dn} \tag{1-10}$$

is the characteristic mixing time scale and $E_\phi(n)$ is the concentration variance spectrum as a function of wave number n. Corrsin (1964) approximated the integrals in Eq. 1-10 using universal forms for $E_\phi(n)$ to obtain estimates of the mixing time scale. His results may be expressed in terms of the integral time scale k/ε and the Kolmogorov time scale $(\nu/\varepsilon)^{1/2}$ as

$$t_m \simeq 2.7\, (3 - Sc)^{-2}\, k/\varepsilon \qquad S_c \leq O(1) \tag{1-11}$$

$$t_m \simeq 2.0\, k/\varepsilon + 0.5(\nu/\varepsilon)^{1/2} \ln Sc \qquad S_c \gg 1 \tag{1-12}$$

where Sc is the Schmidt number for mass transfer or the Prandtl number for heat transfer. These relations may be used to estimate the rate at which concentration variance is dissipated by turbulent mixing and molecular diffusion.

Just as viscosity determines the smallest scale of fluid motion, molecular diffusion controls the smallest scale of concentration fluctuations. The smallest scale of fluid motion is the Kolmogorov microscale $(\nu^3/\varepsilon)^{1/4}$. If the Schmidt number is less than one, the concentration variance will be destroyed faster than the turbulent kinetic energy so that the smallest scale of concentration fluctuation

will be larger than the Kolmogorov scale, by a factor $Sc^{-3/4}$ (Batchelor, Howells and Townsend, 1959). Conversely, if the Schmidt number is greater than one the smallest scale of concentration fluctuation will be smaller than the Kolmogorov scale, by a factor $Sc^{-1/2}$ (Batchelor, 1959).

Thus, to model the turbulent transport of dissolved and solid constituents we need to have information on the distributions of k, ε and $\Gamma^{(j)}$. Methods for estimating these parameters will be discussed in the following section.

1.2 Methods of Estimating Turbulence Parameters

There are three strategies, in general, that one may use to estimate the distributions of k, ε and $\Gamma^{(j)}$ for use in the general mass conservation equation. If the flow is sufficiently simple these parameters may be computed from established semi-empirical relationships and scaling laws, provided one already has a good estimate of the sources and sinks of turbulent energy (e.g., mean current shear, density stratification, etc.). If no mean flow information is available, one may rely on observational data to obtain typical magnitudes. If the flow is not sufficiently simple or more detailed information is required, one may use a turbulence model to obtain the necessary parameters. Rodi (1980) and Lumley (1980) have provided general reviews of current techniques in turbulence modeling. Models for the eddy diffusivity in environmental flows may be found in Okubo (1971) and Fischer et al. (1979). In this section observations of k and ε in natural waters will be summarized and some simple relationships for estimating the distributions of these parameters in channels and boundary layers will be presented.

Table 1-1 summarizes measurements of the energy dissipation rate and the turbulence intensity that have been made in natural waters. It is emphasized that the measurements are presented here only to indicate order of magnitude variations, since the accuracy of some of the data sets is suspect. The turbulence intensity can only be identified in flows that are bounded and have reasonably well defined integral scales, such as channels and boundary layers. Knowing the mean velocity, one can estimate the turbulent kinetic energy from the turbulence intensity.

The majority of turbulence measurements have been made in the oceanic environment. The energy dissipation rate in the ocean mixed layer is highly variable and seems to respond quite quickly to atmospheric forcing (Dillon and Caldwell, 1980). Levels of ε around 10^{-3} to 10^{-1} cm^2/sec^3 are characteristic of near surface waters under high wind conditions. Levels of ε around 10^{-5} to 10^{-4} cm^2/sec^3 are typical of calm surface waters and deeper waters including and below the thermocline. The same can be said for the energy dissipation rate in lakes, although the average levels seem to be slightly higher than in the ocean. The energy dissipation rates in the ocean bottom boundary layer are dependent both on the mean current velocity and on the distance from the bed. These factors account for the large range of values presented in Table 1-1.

Taking all the observations into consideration, the overall range of ε appears to be from 10^{-6} to 10^{0} cm^2/sec^3. This corresponds to ranges of the Kolmogorov length and time scales of 0.03 cm to 1 cm and 0.1 sec to 100 sec, respectively. For mean current speeds ranging from 1 cm/sec to 100 cm/sec (Okubo, 1971) the values of the turbulence intensity in Table 1-1 indicate turbulent kinetic energy varying from

Table 1-1. Observations of Turbulence Parameters in Natural Waters

Flow	Location	Energy Dissipation Rate, ε (cm^2/sec^3)	Turbulent Intensity $\langle u'^2 \rangle^{1/2}/\langle U \rangle$	Source
ocean surface mixed layer	Atlantic Ocean			
	36 to 140 m depth	8×10^{-3} to 4×10^{-1}		Belyaev et al. (1975)
	0 to 10 m depth	5×10^{-5} to 5×10^{-4}		Webster (1969)
	10 to 100 m depth	5×10^{-5} to 1×10^{-4}		Webster (1969)
	Pacific Ocean			
	10 to 40 m depth	5×10^{-6} to 5×10^{-3}		Dillon and Caldwell (1980)
	off Nova Scotia coast			
	0 to 20 m depth	1×10^{-5} to 6×10^{-2}		Oakey and Elliott (1980)
	off Vancouver Island			
	15 to 90 m depth	4×10^{-4} to 3×10^{-2}		Grant et al. (1968)
	off Oregon coast			
	0 to 10 m depth	6×10^{-2}		Marmorino and Caldwell (1978)
	off California coast			
	20 to 120 m depth	3×10^{-2} to 4×10^{-1}		Gibson et al. (1974)

Table 1-1 (cont'd)

Flow	Location	Energy Dissipation Rate, ε (cm^2/sec^3)	Turbulent Intensity $\langle u'^2 \rangle^{1/2}/\langle U \rangle$	Source
ocean currents	Atlantic equitorial undercurrent	4×10^{-5} to 3×10^{-3}		Osborn (1980)
	Pacific equatorial undercurrent	8×10^{-2}		Williams and Gibson (1974)
ocean thermocline		3×10^{-4}		Woods (1968)
deep ocean waters	Atlantic Ocean			
	500 m depth	3×10^{-5}		Webster (1969)
	1000 m depth	1×10^{-5}		
	2000 m depth	1×10^{-5}		

Table 1-1 (cont'd)

Flow	Location	Energy Dissipation Rate, ε (cm^2/sec^3)	Turbulent Intensity $\langle u'^2 \rangle^{1/2}/\langle U \rangle$	Source
ocean bottom boundary layer	off Connecticut coast			
	25 to 100 cm height	2×10^{-2} to 3×10^{-1}		Cook et al. (1977)
	off Oregon coast			
	19 cm height	10^{-2}		Caldwell and Chriss (1981)
	0 to 10 m height	1×10^{-5} to 3×10^{-4}	0.02 to 0.05	Newburger and Caldwell (1981)
	Irish Sea			
	2 m height	10^{0}	0.07 to 0.15	Heathershaw (1976)
	off North Wales coast			
	50 to 175 cm height		0.06 to 0.13	Bowden (1962)
lake surface mixed layers	Lake Ontario			
	6 m depth	9×10^{-2} to 1×10^{-1}		Palmer (1973)
	Lake Huron			
	2 m depth		0.02 to 0.05	Jones and Kenney (1971)

Table 1-1 (cont'd)

Flow	Location	Energy Dissipation Rate, ε (cm^2/sec^3)	Turbulent Intensity $\langle u'^2 \rangle^{1/2}/\langle U \rangle$	Source
lake surface mixed layers	Lake Tahoe			
	0 to 18 m depth	4×10^{-4} to 5×10^{-3}		Dillon and Powell (1976)
	Green Peter Reservoir, Oregon			
	0 to 7 m depth	10^{-3} to 10^{-2}		Dillon et al. (1981)
tidal channels and estuaries	Discovery Passage, B.C.			
	5 to 25 m depth	2×10^{-3} to 1×10^{0}		Grant et al. (1962;1968)
	Georgia and Juan de Fuca Straits, B.C.			
	1 to 2 m depth	5×10^{-3} to 5×10^{-2}		Stewart and Grant (1962)
	12 to 15 m depth	3×10^{-4} to 1×10^{-3}		
	Patuxent River Estuary, Maryland			
	1 m depth		0.14 to 0.20	Wiseman (1969)
	2 to 10 m depth		0.01 to 0.18	

about 5×10^{-4} cm^2/sec^2 to 300 cm^2/sec^2. This corresponds to ranges of the integral length ($k^{3/2}/\varepsilon$) and time (k/ε) scales of 0.1 m to 50 m and, say, 30 sec to 3,000 sec. Figure 1-1 is a convenient plot of the variation of the Kolmogorov length and time scales as a function of ε.

Table 1-2 presents some empirical relationships for estimating the distribution of k, ε and Γ in open channel flows and constant shear mixing layers. These relationships were determined by assuming that the flow is in local equilibrium with production of turbulent kinetic energy balancing the energy dissipation rate and by modeling the turbulent eddy viscosity ν_t as (Rodi, 1980)

$$\nu_t = 0.09\ k^2/\varepsilon \tag{1-13}$$

The eddy diffusivity was obtained through use of Reynold's analogy with the turbulent Schmidt number set equal to one. The values of the turbulence parameters obtained with these relationships compare quite well with the available data (Nagakawa et al. 1975; El Telbany and Reynolds, 1981).

1.3 Modeling of Environmental Reactions

The types of reactions that occur in the aquatic environment may be classified into two broad categories according to whether they are fast or slow with respect to the rate of turbulent mixing. Slow reactions proceed independently of turbulent transport because by the time the reaction has progressed to any extent molecular mixing has virtually eliminated any local variance in concentration. Since the time scale

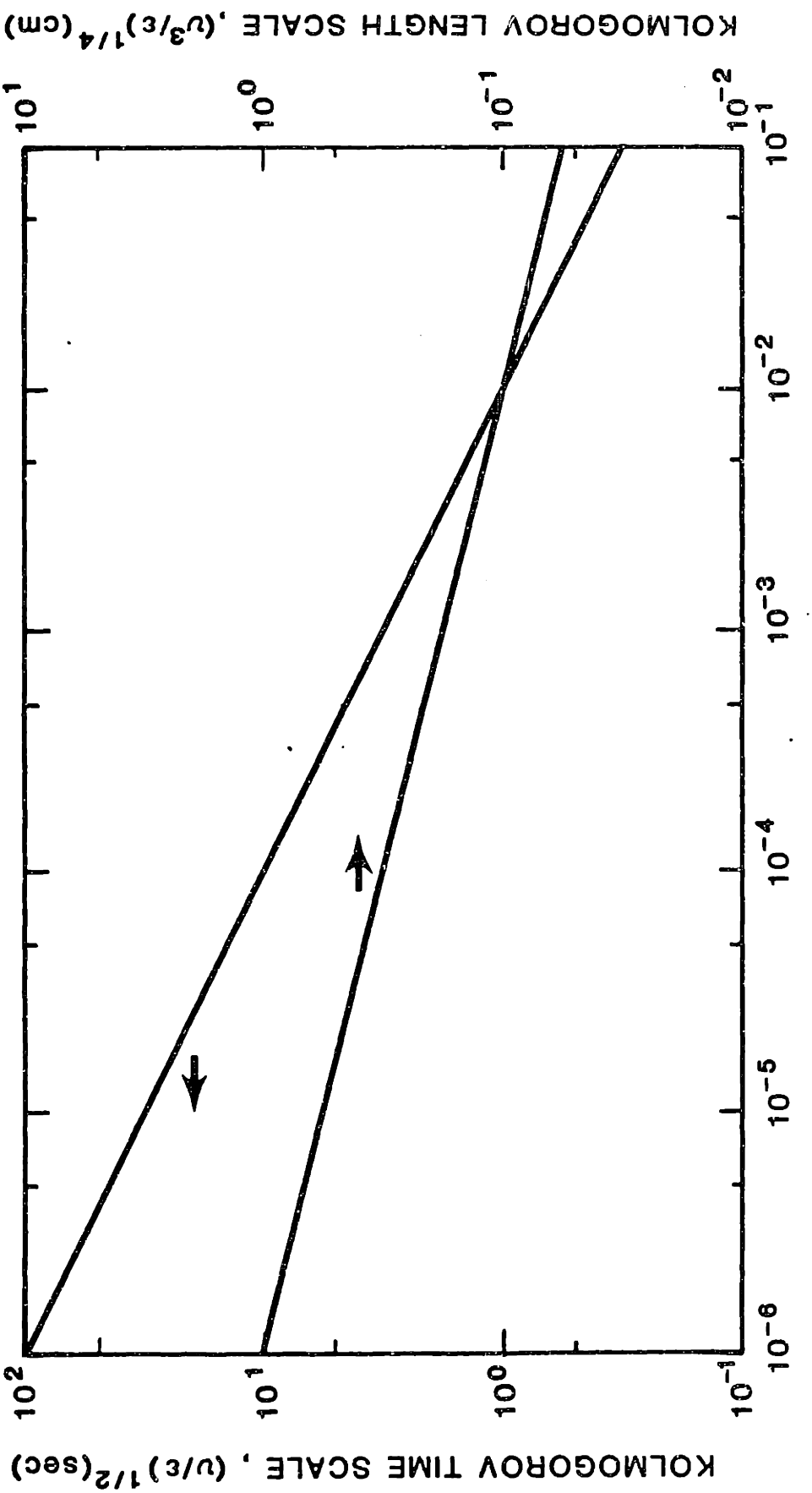

Figure 1-1 Kolmogorov length and time scales versus energy dissipation rate ($\nu = 10^{-2}$ cm^2/sec)

Table 1-2. Distributions of Turbulence Parameters in Channels and Constant Stress Layers

Flow	Turbulent Kinetic Energy, k	Energy Dissipation Rate, ε	Isotropic Eddy Diffusivity, Γ
open channel	$\frac{u_*^2}{0.3}(1 - y/H)$	$\frac{u_*^3}{\kappa y}(1 - y/H)$	$\kappa u_* y(1 - y/H)$
constant stress layer	$\frac{u_*^2}{0.3}$	$\frac{u_*^3}{\kappa y}$	$\kappa u_* y$

u_* = friction velocity

y = distance from boundary

H = depth of channel

κ = von Karman's constant

for turbulent mixing, as measured by the ratio k/ε, varies from a minute to an hour, slow reactions have a characteristic time scale of several hours or longer. Included in this category are some oxidation/reduction reactions, such as the oxidation of Mn^{II} to Mn^{IV}, and the coagulation of particles under conditions of low particle number concentrations or low ionic strength.

Fast reactions may be further subdivided into linear and nonlinear reactions. For zero or first order single-species reactions the computation of the mean source term is straightforward. If the reaction is nonlinear, however, the local reaction rate will be limited by the local rate of turbulent mixing. As indicated in Section 1.1, the mean source term for nonlinear reactions may be expressed in terms of a series of correlations $\langle \phi_1^{a_1}, \phi_2^{a_2} \ldots \phi_\sigma^{a_\sigma} \rangle$ where the level of correlation is determined by the balance between turbulent generation and diffusion, and molecular destruction processes. Examples of such reactions include transport-limited growth reactions such as frazil ice formation and the formation of certain chemical precipitates.

Irrespective of whether the reaction is linear or nonlinear, if the reaction is chemically reversible then it may be possible to assume that the reaction is always in local chemical equilibrium. If the processes that disrupt the local chemical equilibrium, such as differential sedimentation, diffusion across a chemical gradient or interfering irreversible reactions, occur much more slowly than local mixing, then departures from equilibrium will be small and re-equilibration will be very fast. Indeed, we can then assume that local chemical equilibrium will always prevail.

There have been few attempts to model the reactive transport of both dissolved and solid constituents. When solid species have been included in the model, either the effect of the distribution of particle size on sedimentation and coagulation was neglected (Sayre, 1969; Nihoul and Adam, 1975; Ariathurai and Krone, 1976; Smith and O'Connor, 1977; Chapman, 1982) or the modeling of these processes was over-simplified (Somlyody, 1978; Hahn, Kaser and Klute, 1980). When nonlinear reactions such as precipitation/dissolution and sorption were considered the resulting nonlinear interactions between the reaction, diffusion, and sedimentation processes were neglected either by assuming that settling and reaction obey first-order kinetics (Chen and Orlob, 1975; Yousef and Gloyna, 1977) or that reaction proceeds independently of transport (Grove and Wood, 1979; Chapman, 1982). Most reactive transport models that have been successfully applied have involved only dissolved constituents and reactions amongst them that are relatively slow with respect to the rate of transport. These include models for the reactive transport of dissolved nutrients discharged from local sources (Orlob, 1972).

All nonlinear reactions are sensitive to turbulence to some extent. It may be argued, though, that the majority of environmental reactions amongst dissolved constituents are either so slow that chemical kinetics control the reaction rate or are reversible and so fast that local chemical equilibrium always prevails. However, there is an important class of environmental reactions that, be they slow or fast with respect to the turbulence, are directly controlled by the microscale turbulent shear rate. These reactions involve interactions with or amongst suspended particles.

By controlling the relative velocity with which particles approach each other, the microscale shear rate $(\varepsilon/\nu)^{1/2}$ determines the rate of shear-induced coagulation (Krone, 1976; Hunt, 1980) and the rate of secondary nucleation of frazil ice crystals (Garabedian and Strickland-Constable, 1974; Evans et al., 1974). For diffusion-controlled growth of a particle the transport of dissolved substance to or from the concentration boundary layer surrounding the particle is modulated by the microscale shear rate (Batchelor, 1979, 1980). Diffusion-control of particle growth is known to be important for frazil ice growth (Kallungal and Barduhn, 1977) and may be important for the nucleation and dissolution of some precipitates and the initial adsorption of trace elements onto particles (Morel, 1983).

The inability of existing models to properly incorporate the reactive transport of particles may be partially attributed to the inefficiency of conventional finite difference and finite element schemes for computing differential sedimentation within the framework of a set of coupled partial differential equations of the form of Eq. 1-1. Since sedimentation is modeled with an advection operator, to maintain sufficient accuracy with these techniques one either has to use a higher order advection operator or an unreasonably small grid spacing in the vertical direction. These alternatives are both computationally expensive. In addition the modeling of nonlinear reactions presents special difficulties because of the appearance of concentration correlations in the average reaction rate, Eq. 1-6. To close the system of equations one must somehow model these correlations. The current practice in the modeling of environmental reactions is to ignore the correlations. It is clear that if these limitations are to be overcome

a new outlook will have to be adopted in the formulation of the reactive transport model.

1.4 Scope and Objectives of Present Study

The review presented in the previous sections indicates that there are a number of environmental processes that involve or are controlled by the reactive differential transport of suspended particles. In addition some of these processes are modulated by the local rate of turbulent mixing. Because of the computational limitations of the numerical scheme existing reactive transport models either do not include these processes or treat them in such an oversimplified manner as to neglect many of the important interactions. Accordingly this thesis has the following major objectives:

1. To incorporate particle reaction kinetics into a general 3-D transport model.
2. To demonstrate the capabilities of the model by applying it to several case studies.

Chapter II deals with the modeling of coagulation in natural waters. An improved model for the collision frequency function for turbulent shear-induced coagulation is proposed which takes into account the intermittency in the microscale shear rate. The stochastic nature of the coagulation process is examined, and it is concluded that correlations of particle number concentrations may have a significant effect on the evolution of the particle size distribution, particularly for the larger particles. Other than by direct Monte Carlo simulation we have no means at present of modeling these correlations. By considering the influence of individual particle interactions it is

shown, contrary to the theory of Hunt (1980, 1982), that coagulation of particles is mainly a result of collisions with the very smallest particles. Numerical simulations are used to demonstrate that the generally observed shape of the particle size distributions in coastal waters is a result of particle interactions that may be related to the inclusion of collision efficiency functions in the numerical scheme rather than the local (in particle size space) equilibrium of volume flux, as proposed by Hunt.

The details of the general reactive transport model are presented in Chapter III. The basis for the model is the solution of the general transport equation for the one-point, joint scalar probability density function, rather than the conventional moment equations. Pope (1981) has devised a simple Monte Carlo technique for solving this transport equation. His technique is extended to allow simulation over a variable mesh grid. An improved advection algorithm is proposed which permits accurate modeling of the differential sedimentation process. Advantage is taken of the gain in computational efficiency to incorporate realistic reaction kinetics for such processes as coagulation and precipitation/dissolution that have been beyond the capacity of previous models.

Applications of the modeling techniques presented in Chapters II and III are demonstrated in Chapter IV. Extending the work of Daly (1984), a kinetic model for frazil ice growth is proposed. The model is calibrated and verified against experimental data. To demonstrate its flexibility and capabilities, the Monte Carlo model is applied to such problems of current interest as the formation of frazil ice in rivers, the disposal of sewage sludge from coastal outfalls, and the desorption

of copper from resuspended sediments. Finally, the work is summarized and conclusions are given in Chapter V.

II. THE KINETICS OF COAGULATION

The representation of the kinetics of particle coagulation in mathematical equations is a very difficult task. On the one hand, one does not want to approach the problem by accounting for the motion of individual particles; on the other hand, one does not want to misrepresent the physics by oversimplification. As a result of this difficulty there has been much confusion in the literature regarding a number of subtleties involved in the modeling of coagulation. The purpose of this chapter is to clarify some existing problems in the literature in order to make the theoretical basis for coagulation modeling more coherent. Before proceeding to this task the foundation upon which the modeling of suspended particle transport is based will be laid out.

2.1 Some Aspects of Modeling the Transport of Particles

Suspended particles are ubiquitous in natural waters. It is not surprising that they play an important role in the biogeochemical cycle of nearly all chemicals. For example, through adsorption-desorption reactions coupled with coagulation and sedimentation processes, particles are thought to control the geochemistry of most trace elements (Morel, 1983; Karickhoff, 1984). Particles also affect water quality by limiting the penetration of sunlight (Ariathurai and Krone, 1976). Suspended particulate matter consists mainly of clays, metal oxides, microorganisms, organic polymers (Hahn et al., 1980; Karickhoff, 1984) and, in colder waters, frazil ice. The smallest particles that may be detected by present electronic or optical measurement techniques are about 1 μm in "diameter". The largest suspended particles observed are of order 100 μm in size.

Table 2-1 summarizes some observations of suspended particle distributions in natural waters. The concentration range of filterable suspended particles spans six or seven orders of magnitude from 0.01 mg/ℓ in the deep ocean to 50,000 mg/ℓ near the outlet of sludge outfalls. In rivers and estuaries the suspended sediment load is very sensitive to the flow conditions, ranging from a few mg/ℓ to as high as 10,000 mg/ℓ under flood flows. In estuaries the particle concentrations decrease with depth and downstream distance. In productive lake and reservoir surface waters the solids concentrations are of the order 1 to 10 mg/ℓ under normal conditions, but may reach up to a few hundred mg/ℓ if the waters become eutrophic. In the open ocean suspended solids concentrations rarely exceed 1 mg/ℓ and decrease rapidly with depth in the surface 200 m until a concentration of the order of 0.01 mg/ℓ is reached, after which the decrease in concentration is very small. Bottom nepheloid layers and coastal submarine canyons represent local regions of elevated solids concentrations, as do waste outfalls.

Particle size distributions are often described by an equation of the form

$$g(\ell) = \frac{d\phi(\ell)}{d\ell} = A\,\ell^{-b} \qquad (2\text{-}1)$$

where $g(\ell)$ is the number density distribution (number of particles per unit fluid volume per unit particle length), $d\phi(\ell)$ is the number concentration (number of particles per unit fluid volume) of particles of length scale $\ell - d\ell/2$ to $\ell + d\ell/2$, and A and b are constants. For regions far from sources of particles, such as the mid-depths of the ocean, the slope deviates little from an average value of $b = 4.0$.

Table 2-1. Observations of Particle Distributions in Natural Waters

Water Body	Location	Observed Suspended Solids Concentration (mg/ℓ)	Coefficient b	Source
1) river	Susquehana River, Maryland			
	- moderate to low flow	10 - 100		Schubel (1974)
	- high flow	100 - 300		
	- flood flow	up to 10,000		
	American R., San Joaquin R. and Sacramento R., California		3.4 - 4.2	Kavanaugh et al. (1980)
2) lake	Lake Zurich, Switzerland	~13	1.7 - 2.4	
	Lake Murten, Switzerland		1.6 - 2.2	Kavanaugh et al. (1980)
	Dear Creek Reservoir, Utah	~500	3.3	
3) estuary	Chesapeake Bay			
	- moderate to low flow	3 - 20		Schubel (1974)
	- high flow	20 - 100		
	- flood flow	50 - 1400		

Table 2-1 (cont'd)

Water Body	Location	Observed Suspended Solids Concentration (mg/ℓ)	Coefficient b	Source
3) estuary	Delaware Bay			
	- surface waters	10 - 80		Oostdam (1977)
	- bottom waters	20 - 500		
	- flood flows	1300		
	various, around the world			
	- surface waters	5 - 5000		Drake (1976)
	- bottom waters	5 - 5000		
4) ocean	North Atlantic			
	- upper 200 m	0.04 - 0.3	4.0	Lerman et al. (1977)
	- at 5 km depth	0.01		
	- at surface	0.5 - 1.0	~4.0	Sheldon et al. (1972)
	- at mid-depths	0.005 - 0.05		Brewer et al. (1976)
	East Pacific - Panama Basin			
	- at 1 km depth		4.07 - 4.43	Carder et al. (1971)
	- at 2 km depth		4.36	

Table 2-1 (cont'd)

Water Body	Location	Observed Suspended Solids Concentration (mg/ℓ)	Coefficient b	Source
4) ocean	Mediterranean Sea			
	- 600 m to 1500 m depth		3.5 - 4.16	Brun-Cottan (1971)
	bottom nepheloid layers	0.01 - 0.5	~4.0	McCave (1983)
	Southern California			
	- submarine canyons	0.4 - 6.0		Drake (1974)
	- primary and secondary effluent discharges	60 - 220		Herring (1980)
	- digested sludge discharges	20,000 - 50,000	4.2	Faisst (1980)

McCave (1983) notes that for bottom nepheloid layers and in shallow coastal waters the size distribution is characterized by two segments of slope $b < 4$ for sizes finer and $b > 4$ for sizes coarser than about 4 to 8 μm. The data of Faisst (1980) indicates that the size distribution of sewage sludge is well described by a slope of $b \approx 4$. In the surface waters of lakes and oceans, and in rivers (and presumably in estuaries as well, although I could not find any data on size distributions in such waters) the coefficient b ranges from about 1.5 to 4.0. This large variation in b probably reflects the input of suspended particles due to resuspension of bottom sediments and algal productivity.

For particles smaller than about 1 μm in size that are beyond the detection limit there is reason to believe that the mass and number densities decrease with decreasing size because coagulation has incorporated them into larger aggregates (O'Melia, 1980). The numerical simulations to be presented in section 2.5.2 support this reasoning. Hence it will be assumed that particles less than 1 μm in size contribute negligibly to the total suspended particle mass, and that the number flux of particles through 1 μm size due to coagulation may either be specified or neglected, depending on the situation.

To model suspended particle transport and coagulation with an equation of the form of Eq. 1-1, several assumptions and approximations have to be made. The most basic assumption that is implicit in Eq. 1-1 is that the fluid-solid suspension behaves as a continuum. To be considered as a continuum, however, the local particle concentration must be a well defined quantity. That is, the local volume over which the concentration is defined must be large enough to contain a statistically significant number of particles, yet it must be small

enough that it does not include real variations in the suspension. Lumley (1976) presented, without proof, an expression for estimating the accuracy of applying the continuum assumption as a function of the local number concentration of particles. Because Lumley's result is so important for assessing the validity of the continuum assumption, it is derived here from first principles for the purpose of identifying the assumptions and approximations on which it is based.

First, the error committed in defining the particle concentration over a volume, V, too small to contain a significant number of particles will be estimated. To do this the volume V is subdivided into smaller volumes each of equal size ΔV and sufficiently small that the following assumptions are satisfied:

1) the probability that the volume ΔV contains a single particle is approximately $p = \langle N \rangle \Delta V/V$ where $\langle N \rangle$ is the average number of particles in the volume V;
2) the probability that the volume ΔV contains two or more particles is negligible compared to p;
3) the number of particles in any volume ΔV is independent of the number of particles in any other non-overlapping volume ΔV.

Under these conditions the statistics of the total number of particles in V is described by the binomial distribution (Benjamin and Cornell, 1970),

$$p_N(n) = \binom{V/\Delta V}{n} p^n (1 - p)^{V/\Delta V - n} \qquad n = 0,1,2,\ldots,V/\Delta V \qquad (2\text{-}2)$$

The mean number of particles in V is

$$\langle N \rangle = pV/\Delta V \qquad (2\text{-}3)$$

If $V/\Delta V$ is very large then the binomial distribution may be approximated by the Poisson distribution

$$p_N(n) = \frac{\langle N\rangle^n \exp(-\langle N\rangle)}{n!} \qquad n = 0,1,2,\ldots,\infty \qquad (2\text{-}4)$$

for which the root-mean-square (rms) number of particles in V is $\langle N\rangle^{1/2}$. As the averaging volume increases the rms error in the resulting number concentration decreases.

To improve the accuracy of the concentration estimate, the averaging volume may be increased until the smallest dynamically significant scale of fluid motion, η, is reached. Any further increase in the size of the averaging volume will result in real variations in the particle number concentration being averaged into the estimate. Let us assume that the x-axis is oriented in the direction of the local gradient in the number concentration ϕ. The local variation in ϕ may be written as

$$\phi = \phi_o + a_1 x + a_2 x^2 + \ldots \qquad (2\text{-}5)$$

where ϕ_o is the number concentration defined over a volume of scale much less than η. If η is the scale of variation in ϕ then

$$a_1 \sim O(\phi_o/\eta) \qquad a_2 \sim O(\phi_o/\eta^2) \qquad (2\text{-}6)$$

The total number of particles in a volume V' of length scale L is

obtained by integration,

$$N(V') = \iiint_{V'} \phi \, dV \sim O\left(\phi_o L^3 + \frac{\phi_o L^5}{3\eta^2}\right) \tag{2-7}$$

Note that the linear variation in ϕ does not contribute to the volume integral. Hence the error committed in averaging over a volume that is too large increases as the square of the ratio of L to η. The total error E in the estimate of the number concentration is the sum of the component errors

$$E = \langle N \rangle^{-1/2} + \frac{1}{3}\left(\frac{L}{\eta}\right)^2 = (L^3 \phi_o)^{-1/2} + \frac{1}{3}\left(\frac{L}{\eta}\right)^2 \tag{2-8}$$

The total error is minimized at the point where $\partial E/\partial L = 0$, that is,

$$L = \left(\frac{81}{16} \frac{\eta^4}{\phi_o}\right)^{1/7} \tag{2-9}$$

The total error in the concentration estimate at this point is

$$E \approx (\phi_o \eta^3)^{-2/7} \tag{2-10}$$

As stated by Lumley (1976), the error in applying the continuum assumption is proportional to the -2/7 power of the number of particles in the volume corresponding to the smallest dynamically significant scale of fluid motion, η.

In turbulent natural waters the smallest dynamically significant scale is the Kolmogorov length scale, $\eta = (\nu^3/\varepsilon)^{1/4}$, which varies from about 0.03 cm to 1 cm. The volume η^3 thus ranges from about

3×10^{-3} cm^3 to 10^0 cm^3. Within such a volume the suspension may be considered to be well mixed so that the volume may be taken as the characteristic volume over which the local concentration is defined. For an error of 1%, Eq. 2-10 indicates that the volume η^3 should contain 10^7 particles, for 10% error it should contain 3×10^3 particles and for 20% error it should contain 10^2 particles. Assuming that in natural waters particles range from 1 to 100 μm in diameter d and are distributed in number as d^{-4}, then at a concentration of 10^x mg/ℓ there will be approximately 10^{x+5} particles/cm^3. For a minimum averaging volume of $\eta^3 = 10^{-3}$ cm^3 we need a mass concentration of 10 mg/ℓ or greater to be able to apply the continuum assumption with an error of less than 10%. Thus we see from Table 2-1 that the application of the assumption will be valid in all cases except for mid-ocean waters. Further, when we discretize the particle size range into size classes we must ensure that each size class contains a sufficiently high number concentration. To partially compensate for the fact that particle number densities decrease logarithmically with size it is often expedient to choose particle size classes whose size band increases logarithmically with size.

To model the settling behavior of suspended particles Stokes' law is frequently employed. The Stokes approximation may safely be applied for a particle Reynolds number $U_t\, d/\nu$ less than 1/2, where U_t is the terminal settling velocity and d is the diameter of the (assumed spherical) particle (Lumley, 1976). The maximum particle size for which Stokes law may be applied is thus

$$d_{max} = \left[\frac{\nu^2}{g(s-1)}\right]^{1/2} \qquad (2\text{-}11)$$

where s is the specific gravity of the particle. The bulk specific gravity of relatively large suspended particles is typically 1.01 to 1.20 (Dillon, 1964; Riley, 1970; Krone, 1972; Chase, 1979) for which d_{max} ranges from about 170 μm to 450 μm. From the point of view of the Reynolds number criterion, then, the application of Stokes law will always be valid.

There are some complications, however. The presence of a double layer on colloidal (< 1 μm) particles is well known and leads to a different force balance on the particle than that assumed by Stokes law. For particles larger than about 5 μm in size the effect of the double layer is largely unknown. From detailed observations of the settling behavior of individual natural aggregates in a settling chamber, Chase (1979) has concluded that surface coatings, solution electrolytes, and dissolved organic substances all contribute to a nonlinear drag reduction on natural particles relative to the Stokes drag assumption. Chase noted that the effect of the reduced skin friction was particularly apparent for the smaller aggregate sizes. Another factor that must be taken into account is the reduction in the density of aggregates with increasing size (McCave, 1984). Because of the diversity in types of particles, there is a large range in observed densities for aggregates of the same size. These complicating factors are normally circumvented by using an empirical function that describes the variation of apparent density with size in conjunction with Stokes law (Tambo and Watanabe, 1979; McCave, 1984).

Another assumption implicit in Eq. 1-1 is that the particles have negligible inertia and, apart from settling, they are advected with the

fluid. We note that for Kolmogorov length scales in natural waters ranging from 0.03 cm to 1 cm, suspended particles are always small relative to the smallest length scale of the turbulence. In addition, for Kolmogorov time scales spanning 0.1 sec to 100 sec the particle time constant

$$a = \frac{(s-1)d^2}{18\nu} \tag{2-12}$$

is short compared to the shortest time scale of the turbulence for $s_{max} = 1.2$ and $d_{max} = 200$ μm. Under these conditions, Lumley (1976) showed that the particle inertia may be neglected if

$$d/\eta \leq 5\, Re_{\ell}^{-1/4} \tag{2-13}$$

where η is the Kolmogorov length scale and Re_{ℓ} is the Reynolds number of the turbulence based on the integral scale. For turbulence time scales k/ε, where k is the turbulent kinetic energy, ranging from 30 sec to 3000 sec the largest turbulence Reynolds number will be about 10^6 for which the critical diameter will be about 160 μm. Hence the neglect of particle inertia will always be a valid approximation.

Finally we note that the particles will have a negligible effect on the fluid motion. Batchelor and Green (1972b) computed that for a suspension of identical spherical particles in pure strain a volume concentration of 0.003 is required to modify the dilute fluid viscosity by 1%. The volume concentration in natural waters, on the other hand, rarely exceeds 0.001 so that the energy dissipated by the particles will normally be negligible.

It is clear that to model the transport of suspended particles one must be willing to make a number of approximations. One hopes, however, that with the level of detail adopted here the essential physics will be captured and the model will describe at least the average behavior of particle transport in natural waters.

2.2 The Mechanics of Particle Collisions

The mechanisms that cause suspended particles to collide include Brownian motion, fluid shear, and differential sedimentation. In addition, turbulent shear can cause particles to break up. However, the experimental evidence indicates that particle breakup is limited to large (> 1 μm), weakly bonded aggregates under high shear (> 10^2 cm^2/sec^3) (Tambo and Hozumi, 1979). Since such shear rates are very rarely observed in natural waters, particle breakup will not be considered as a mechanism affecting the distribution of particles.

To compute the frequency with which a test particle collides with other particles we first assume that the test particle does not interfere in any way with other particles (i.e., we assume that the test particle occupies no space) and compute the frequency with which other particles come into contact with the imaginary test particle. The modification to the collision rate due to short range hydrodynamic deflection, van der Waals' forces, and electrostatic effects is then accounted for with a collision efficiency function.

2.2.1 Collision Frequency Functions

For non-interfering particles a test particle of radius r_i is said to have collided with a second particle of radius r_j when the

second particle has come to within a distance $(r_i + r_j)$ of the test particle (i.e., the particles are just touching). The collision frequency function $\beta(r_i,r_j)$ is a measure of the rate at which non-interfering i- and j-particles collide, and depends on the mechanism of collision.

Table 2-2 summarizes the collision frequency functions for the various mechanisms. The functions are expressed in terms of particle volume v_i. Since volume is conserved during the coagulation process, it is a more useful indicator of particle size. Presented in Table 2-2 is an improved model for the collision frequency function due to turbulent shear. The modification to Saffman and Turner's (1956) model is to account for the intermittent behavior of the fluctuating energy dissipation rate field. The derivation of the improved collision frequency function is the main subject of this section.

When turbulent shear motions exist in the fluid, particles may collide by differential advection. The instantaneous flux of j-particles to a test i-particle may be written as

$$4\pi (r_i + r_j)^2 \omega_r\big|_{r_i+r_j} \phi_j \tag{2-14}$$

where ϕ_j is the number concentration of j-sized particles and ω_r is the inward radial velocity relative to the test particle. If the turbulence is assumed to be locally isotropic, then the shear will be randomly oriented and

$$\omega_r\big|_{r_i+r_j} = \frac{1}{2} (r_i + r_j) \left| \frac{\partial u}{\partial x} \right|_{r_i+r_j} \tag{2-15}$$

Table 2-2. Collision Frequency Functions

Mechanism	$\beta(v_i, v_j)$	Source
Brownian motion	$\frac{2kT}{3\mu} \frac{(v_i^{1/3} + v_j^{1/3})^2}{(v_i v_j)^{1/3}}$	Smoluchowski (1916)
Turbulent shear	a) $0.31 \frac{\langle\varepsilon\rangle^{1/2}}{\nu^{1/2}} (v_i^{1/3} + v_j^{1/3})^3$	Saffman and Turner (1956)
	b) $0.39 \frac{\langle\varepsilon\rangle^{1/2}}{K_u^{1/4} \nu^{1/2}} (v_i^{1/3} + v_j^{1/3})^3$	present work
Differential Sedimentation	$0.1 \frac{g}{\nu} \frac{\lvert\rho_s - \rho_f\rvert}{\rho_f} \lvert v_j^{2/3} - v_i^{2/3}\rvert (v_j^{1/3} + v_i^{1/3})^2$	Findheisen (1939)

notation:
- k = Maxwell-Boltzman constant
- T = absolute temperature
- μ = dynamic viscosity
- ν = kinematic viscosity
- g = gravitational acceleration
- ρ_s = density of particles
- ρ_f = density of fluid
- K_u = kurtosis of fluctuating shear
- $\langle\varepsilon\rangle$ = mean energy dissipation rate

where $\partial u/\partial x$ is the linear shear rate and the factor of 1/2 is included to account for the fact that, on average, the shear will be such that half the time the particles will diverge rather than converge. Since the particles are much smaller than the Kolmogorov length scale, $(r_i + r_j) \ll (\nu^3/\varepsilon)^{1/4}$, and local isotropy has already been assumed, then

$$\left(\frac{\partial u}{\partial x}\right)^2 = \frac{\varepsilon}{15\nu} \tag{2-16}$$

At this point in their derivation, Saffman and Turner (1956) assumed that $G = \partial u/\partial x$ is normally distributed. If such is the case then the probability density function for $|G|$ is

$$p(|G|) = \frac{2}{(2\pi)^{1/2}\,\sigma_G^2} \exp\left[-\frac{1}{2}\frac{G^2}{\sigma_G^2}\right] \tag{2-17}$$

where σ_G^2 is the variance of G, and the mean value of $|G|$ may be easily computed to be

$$\langle |G| \rangle = (2/\pi)^{1/2}\,\sigma_G \tag{2-18}$$

Hence, as obtained by Saffman and Turner (1956), the mean flux of j-particles to the test particle is

$$\begin{aligned} 4\pi(r_i + r_j)^2 \langle \omega_r |_{r_i + r_j} \rangle \phi_j &= 2\pi(r_i + r_j)^3 \left(\frac{2}{\pi}\right)^{1/2} \left(\frac{\langle\varepsilon\rangle}{15\nu}\right)^{1/2} \phi_j \\ &= 1.29(r_i + r_j)^3 \frac{\langle\varepsilon\rangle^{1/2}}{\nu^{1/2}} \phi_j \end{aligned} \tag{2-19}$$

and the collision frequency function is

$$\beta(r_i,r_j) = 1.29(r_i + r_j)^3 \langle\varepsilon\rangle^{1/2}/\nu^{1/2} \qquad (2\text{-}20)$$

Given what was known about turbulence at the time, Saffman and Turner's assumption that the local shear rate is normally distributed was reasonable. However, it is now well known that the small-scale structure of turbulence is highly intermittent. Observations by a number of researchers (Batchelor and Townsend, 1949; Van Atta and Chen, 1970; Van Atta and Park, 1972; Kuo and Corrsin, 1971) suggest that the distributions of small-scale turbulence parameters are highly nonuniform in space and time and have an intermittent nature which becomes more clearly defined with increasing Reynolds number. That is, as the Reynolds number increases, the degree of intermittency increases, and simultaneously the scale range (or wave number range) for which there is appreciable intermittency continues to expand. Grant, Stewart and Moilliet (1962) noted measured values of ε that varied by a factor of four or more even when there was no appreciable evidence of any change in the overall nature of the turbulence.

The strong intermittency of the small-scale fluctuations ensures that the probability distributions for the small-scale turbulence components are highly non-Gaussian. In the papers by Obukhov (1962) and Kolmogorov (1962) it was suggested that the dissipation rate $\varepsilon(\underset{\sim}{x},t)$ has a log-normal probability distribution. This hypothesis prompted a great amount of experimental research aimed at determining the probability distribution of velocity derivatives (Van Atta and Chen, 1970; Kholmyanskii, 1970; Stewart, Wilson and Burling, 1970; Gibson, Stegen

and Williams, 1970). The data are presented and discussed in Monin and Yaglom (1975). The measurements show noticeable departure of the measured distributions from the log-normal distribution at extreme values of the measured variables. Hence, the log-normal distribution does not accurately describe the extreme tail of the true velocity derivative distribution so that moments of relatively high order may not be accurately evaluated if this distribution is assumed. However, the use of an assumed log-normal distribution is a great improvement over the assumption of normally-distributed velocity derivatives used by Saffman and Turner (1956) and will be adopted here.

Assuming that $z = G^2 = (\partial u/\partial x)^2$ is log-normally distributed, the probability density function for z may be written as

$$p(z) = \frac{2}{(2\pi)^{1/2}\, z\, \sigma_{\ln z}} \exp\left[-\frac{1}{2}\left(\frac{\ln z - \langle \ln z \rangle}{\sigma_{\ln z}}\right)^2\right]$$

$$= \frac{2}{(2\pi)^{1/2}\, z\, \sigma_{\ln z}} \exp\left[-\left(\frac{1}{(2)^{1/2}\, \sigma_{\ln z}} \ln\left(\frac{z}{\tilde{m}_z}\right)\right)^2\right] \qquad (2\text{-}21)$$

where $\tilde{m}_z$ is the median of z and $\sigma^2_{\ln z}$ is the variance of ln z (Benjamin and Cornell, 1970). For the log-normal distribution it can easily be shown that if b is any real number, then

$$\langle z^b \rangle = \int_0^\infty z^b\, p(z)\, dz = \tilde{m}_z^{\,b} \exp\left(\frac{1}{2}\, b^2\, \sigma^2_{\ln z}\right) \qquad (2\text{-}22)$$

Hence any moment of z can be related to $\langle z \rangle$ by the relationship

$$\frac{\langle z^b \rangle}{\langle z \rangle^b} = \exp\left[\frac{1}{2}\, \sigma^2_{\ln z}\, (b^2 - b)\right] \qquad (2\text{-}23)$$

To determine $\sigma^2_{\ln z}$ in terms of known parameters we first observe that

$$\frac{\langle z^2 \rangle}{\langle z \rangle^2} = \exp[\sigma^2_{\ln z}] \tag{2-24}$$

so that

$$\sigma^2_{\ln z} = \ln\left(\frac{\langle z^2 \rangle}{\langle z \rangle^2}\right) = \ln\left(\frac{\langle (\partial u/\partial x)^4 \rangle}{\langle (\partial u/\partial x)^2 \rangle^2}\right) = \ln K_u \tag{2-25}$$

where K_u is the kurtosis of the velocity derivative.

The kurtosis of the velocity derivative is known to be Reynolds number dependent. Summaries of the available data by Kuo and Corsin (1971) and by Van Atta and Antonia (1980) indicate that for $R_\lambda < 200$, $K_u \sim R_\lambda^{0.2}$ while for $R_\lambda > 200$, $K_u \sim R_\lambda^{0.41}$, where R_λ is the Reynolds number based on the Taylor microscale. Figure 2-1, taken from Van Atta and Antonia (1980), illustrates these trends. Hence $\sigma^2_{\ln z}$ can be determined from the kurtosis using the empirical information represented by Fig. 2-1, if the Reynolds number is known.

The use of a Reynolds number based on the Taylor microscale is impractical and a functional dependence on more basic variables is desirable. If we again invoke local isotropy, then $\langle u^2 \rangle = 2k/3$, where k is the turbulent kinetic energy, and using Eq. 2-16 the Taylor microscale may be approximated as

$$\lambda = \frac{\langle u^2 \rangle^{1/2}}{\langle (\partial u/\partial x)^2 \rangle^{1/2}} = \left(\frac{10k\nu}{\langle \varepsilon \rangle}\right)^{1/2} \tag{2-26}$$

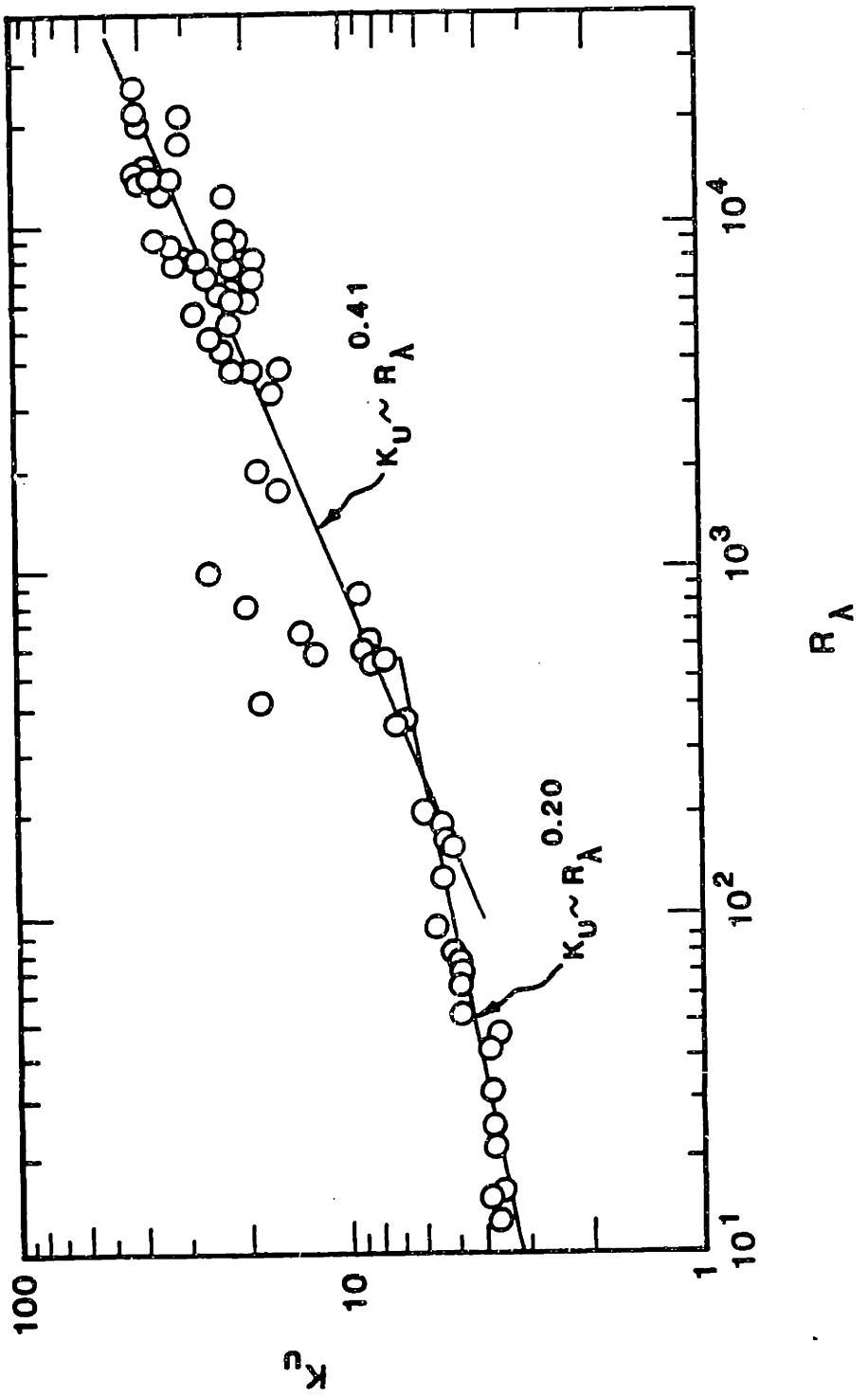

Figure 2-1 Experimental variation of Ku with R_λ (from Van Atta and Antonia, 1980)

and the Reynolds number as

$$R_\lambda = \frac{\langle u^2 \rangle^{1/2} \lambda}{\nu} = \frac{2(15)^{1/2}}{3} \frac{k}{(\langle \varepsilon \rangle \nu)^{1/2}} \tag{2-27}$$

Knowing $\sigma^2_{\ln z}$ in terms of $K_u(k, \langle \varepsilon \rangle)$ we then use Eq. 2-23 again to determine

$$\langle z^{1/2} \rangle = \langle z \rangle^{1/2} \exp \left[-\frac{1}{4} \ln K_u \right] = \frac{\langle z \rangle^{1/2}}{K_u^{1/4}} \tag{2-28}$$

Since $\langle z^{1/2} \rangle = \langle \left| \partial u / \partial x \right| \rangle$ we can finally obtain the collision frequency function for turbulent shear as

$$\begin{aligned} \beta(r_i, r_j) &= 2\pi (r_i + r_j)^3 \langle \left| \partial u / \partial x \right| \rangle \\ &= \frac{2\pi}{(15)^{1/2}} (r_i + r_j)^3 \frac{\langle \varepsilon \rangle^{1/2}}{K_u^{1/4} \nu^{1/2}} \\ &= 1.62 (r_i + r_j)^3 \frac{\langle \varepsilon \rangle^{1/2}}{K_u^{1/4} \nu^{1/2}} \end{aligned} \tag{2-29}$$

This result differs from that of Saffman and Turner, Eq. 2-20, by the numerical constant and the factor $K_u^{-1/4}$.

Support for this improved model of the collision frequency function may be derived from the experimental measurements of Delichatsios and Probstein (1975). These researchers investigated the coagulation of latex particles in a fully developed turbulent pipe flow. During the course of their experiments the observed particle sizes ranged from 0.2 μm to 0.8 μm in radius. To remove any electrostatic effects the

particle suspension was initially completely destabilized with the addition of chemical coagulants. As a result the collision efficiencies will be very close to one for the range of particle sizes observed. Delichatsios and Probstein assumed a model for the collision frequency function due to turbulent shear of the form $\beta(r_i,r_j) = b(r_i^3+r_j^3)\ (\varepsilon/\nu)^{1/2}$ and determined the constant b from their measurements. For coagulation in a flow of 10 gallons per minute through a smooth-walled 1-inch diameter pipe, they report a value of b = 0.86. If d is the pipe diameter, $\bar{U}$ is the average velocity, and f is the friction factor then the friction velocity may be estimated as $u_* = \bar{U}(f/8)^{1/2}$, the energy dissipation rate is approximately $\langle\varepsilon\rangle = f\bar{U}^3/2d$, and the turbulent kinetic energy $k = 3u_*^2/2$. For a smooth-walled pipe the friction factor is computed to be f = 0.024 and using Eq. 2-27 the turbulence Reynolds number is $R_\lambda = 30$. From Figure 2-1 the corresponding magnitude of the kurtosis is $K_u \approx 5$. Substituting into Eq. 2-29 indicates a value of b = 1.08, which is closer to the experimentally determined value than that of 1.29 in Saffman and Turner's model.

Of course, given the possible experimental measurement errors and the errors involved in estimating the turbulence parameters, it is difficult to attach much significance to the small differences in the above values of the parameter b; it can be argued that the experimental measurements do not invalidate either model. Note also from Figure 2-1 that the value of K_u varies only over a factor of 10 for four orders of magnitude change in R_λ so that K_u can vary at most by a factor of 1.8. It is thus doubtful that any experiment will demonstrate the superiority of either model, especially given the limitations in current techniques for generating homogeneous turbulence and for measuring

particle size distributions. However the improved model is recommended for use since it is physically more rigorous.

2.2.2 Collision Efficiency Functions

The collision frequency functions derived in the previous section assume that particles travel in rectilinear paths without interference from each other. In reality the motion of a particle generates a velocity gradient in its vicinity that affects the paths of oncoming particles. Also, when the particles get close enough attractive London van der Waals' forces and repulsive electrostatic double-layer forces come into play and modify the particle paths. These real effects are accounted for with collision efficiency functions which when multiplied by the collision frequency function provide a complete measure of the frequency of collision between particles.

The strategy for computing collision efficiency functions is to integrate from a given starting point the equations of motion for a j-particle approaching a test i-particle. The van der Waals' and electrostatic forces are included in the equations of motion. The possible starting points are those that would result in collision if the particles did not interfere with each other. The fraction of the starting points that result in collision when particle interference is accounted for is the collision efficiency, $E(v_i, v_j)$.

The derivation of collision efficiency functions for the various collision mechanisms is obviously complex and beyond the scope of this discussion. Only the results will be presented here. For collisions due to Brownian motion, Valioulis et al. (1984) have computed efficiency functions for particles in water that behave as shown in Figure 2-2,

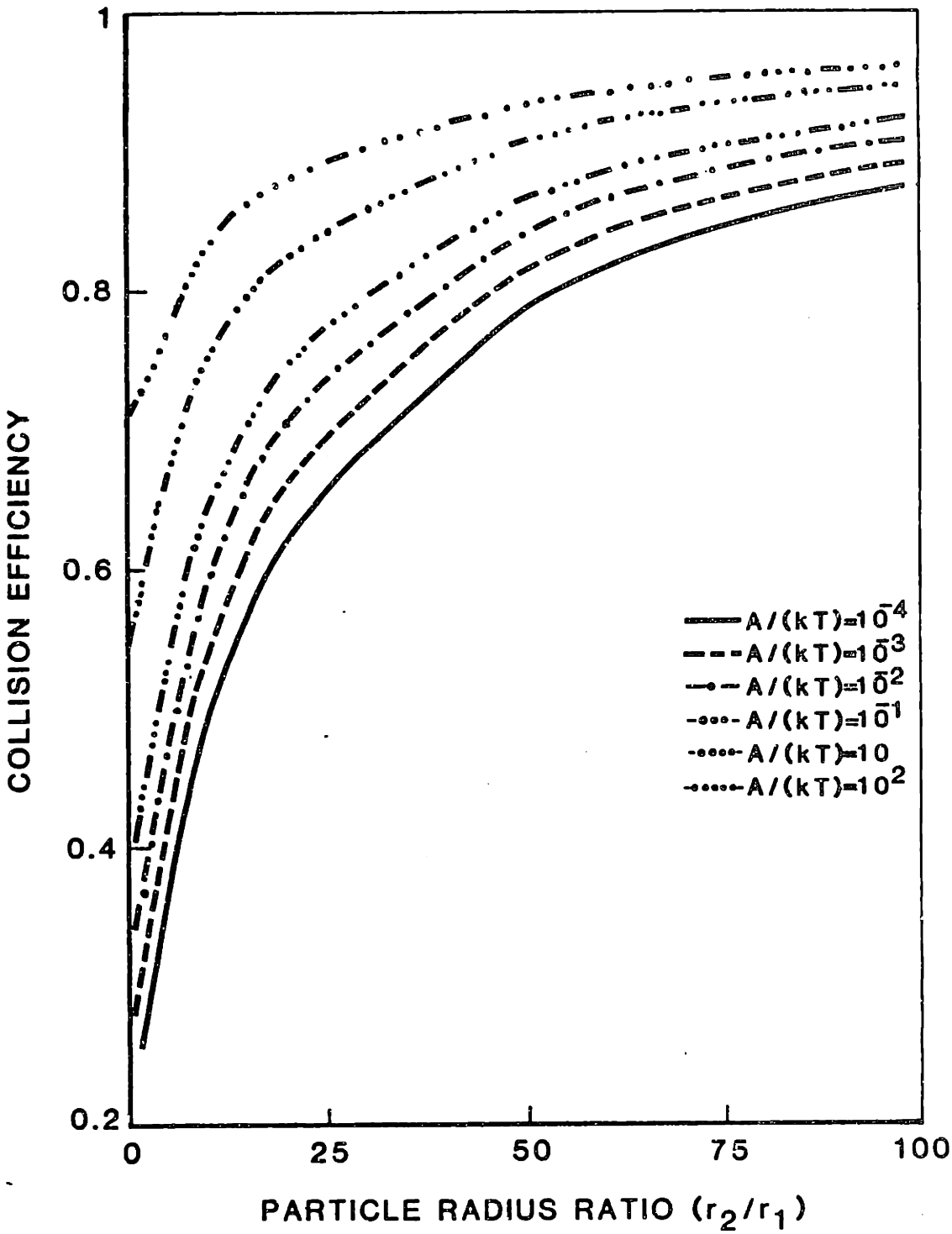

Figure 2-2 Collision efficiency function for collisions due to Brownian motion (from Valioulis et al., 1984).

that is, the efficiency increases as the ratio of particle radii. The sole effect of the double layer forces, as indicated by the ionic strength I appears to be to determine the critical value of A/kT beyond which coagulation may occur. The dimensionless parameter A/kT is the Hammaker group and is a measure of the relative strength of the van der Waals' forces and the Brownian diffusion (A is the Hammaker constant, k is the Maxwell-Boltzman constant and T the absolute temperature).

Adler (1981) used the theory of Batchelor and Green (1972a) for the hydrodynamic interaction of two spheres in a shear flow to compute collision efficiency functions for shear-induced collisions. His results, as interpreted by Valioulis et al. (1984), are shown in Figure 2-3. Here the efficiency of collisions decreases with the ratio of particle radii. The parameter that governs the overall level of efficiency is

$$H = \frac{A}{144\pi\mu\, r_2^3\, G} \qquad (2\text{-}30)$$

where μ is the dynamic viscosity, G is the strain rate and r_2 is the radius of the larger particle. The parameter H represents the relative strength of the van der Waals' force and the fluid shear.

For differential sedimentation, Neiburger et al. (1974) have obtained a collision efficiency function which takes into account only hydrodynamic effects. The efficiency is a function of the radius of the smaller particle, r_1, and the relative particle size, r_2/r_1, as shown in Figure 2-4. For a fixed relative particle size the collision efficiency increases with increasing particle size since the deflecting hydrodynamic forces become less important as particle inertia

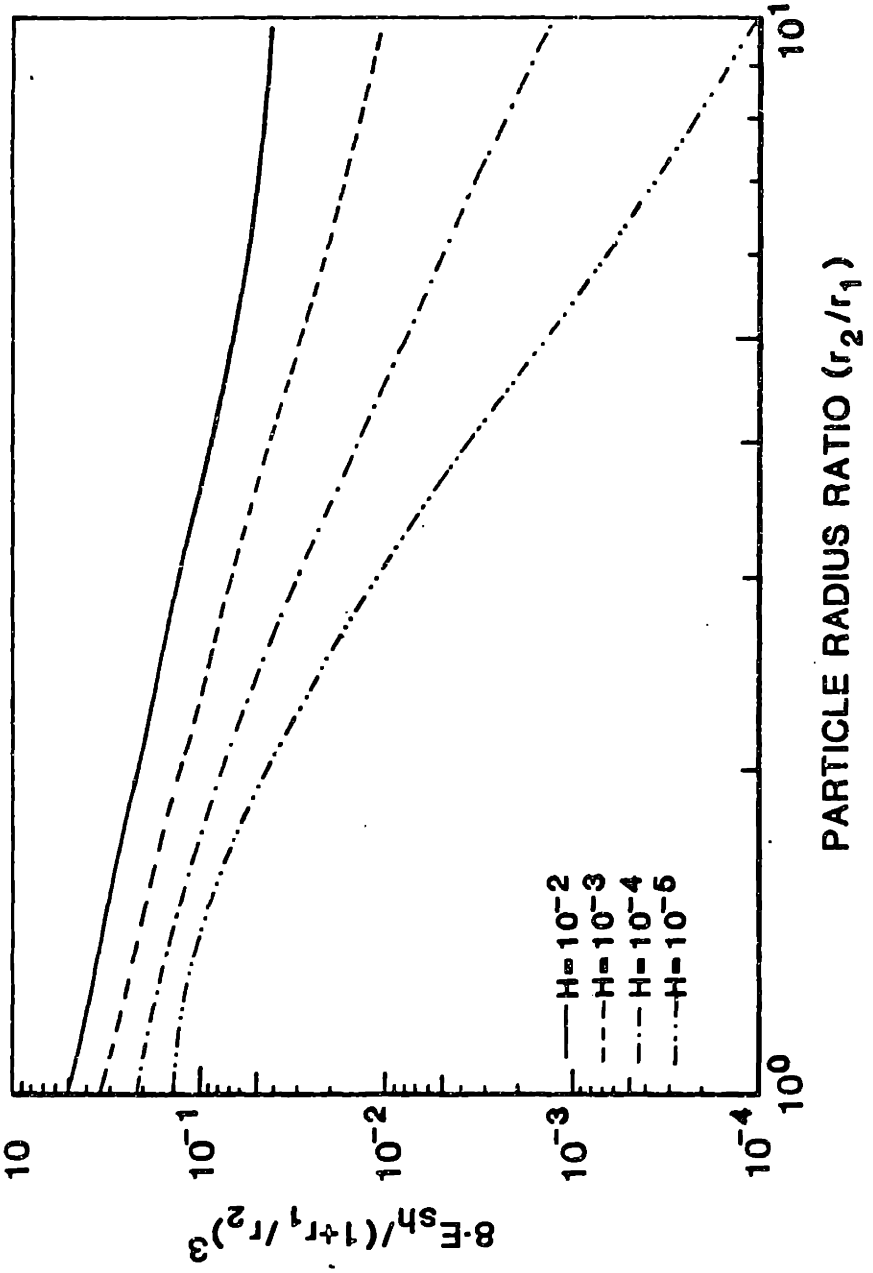

Figure 2-3 Collision efficiency function for collisions due to shear (from Valioulis et al., 1984, as derived by Adler, 1981)

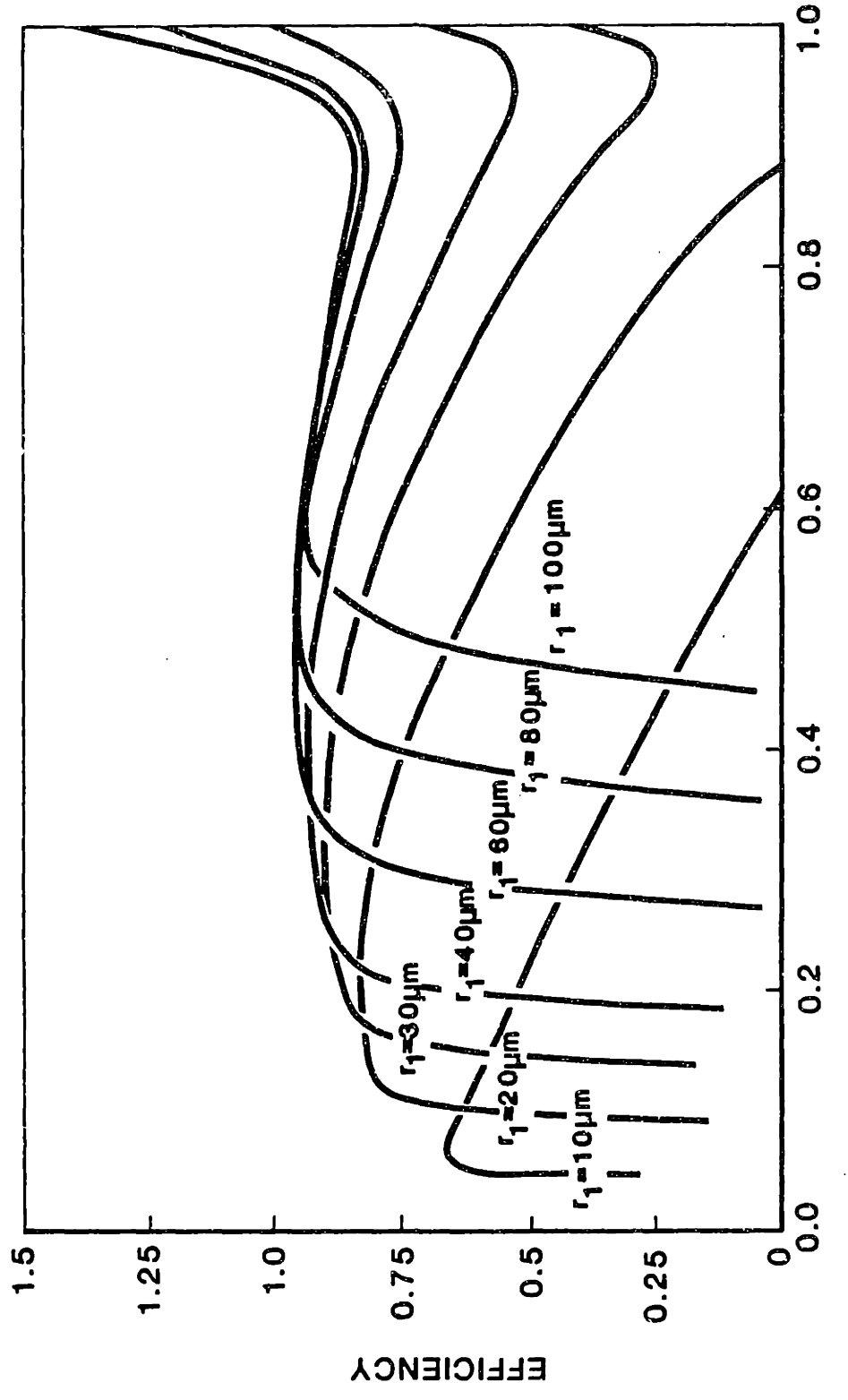

Figure 2-4 Collision efficiency function for collisions due to differential sedimentation (from Valioulis et al., 1984, as derived by Neiburger et al., 1974)

increases. For the same reason the collision efficiency decreases with the relative particle size for fixed r_1. For r_1/r_2 near one wake capture occurs when the two particles are large enough for inertial effects to become appreciable.

Note that the effect of Brownian motion has not been included in the collision efficiency for shear or differential sedimentation. Preliminary work by Feke and Schowalter (1983) has shown that Brownian motion can have a significant influence in either increasing or decreasing the collision rate. However, incorporating this effect into collision efficiency functions is very difficult and remains to be done in any general way.

2.3 The Stochastic Coagulation Equation

It was shown in Section 2.2 that the instantaneous expected number of collisions of j-particles with an arbitrary i-particle per unit volume per unit time is $\beta(v_i,v_j)\ E(v_i,v_j)\ \phi_j$. It follows that the instantaneous expected number of collisions between all i- and j-particles per unit volume per unit time is $\beta(v_i,v_j)\ E(v_i,v_j)\ \phi_i\phi_j$. Each collision per unit volume results in the local number concentration of i- and j-particles each being reduced by one and that of particles of volume $(v_i + v_j)$ being increased by one. As particles in a local region of space coagulate there is a local decrease in the number of particles available for further coagulation. It is to be expected that all particles of any given size will not experience the same history of collisions. As a result it is possible that some particles in the local region will become very large in a relatively short time by coagulating with a few other large particles. There will

be a limit on the size that these few fortunate particles may attain because of the finite amount of mass in their immediate vicinity. Other particles will take a relatively long time to achieve the same increase in size because they will have coagulated with smaller particles. It is apparent that the coagulation process itself will cause local fluctuations in the number concentration of particles. Thus, for example, the average number of collisions between i- and j-particles over a long period of time is

$$\beta(v_i,v_j)\ E(v_i,v_j)\ \langle\phi_i\phi_j\rangle = \beta(v_i,v_j)\ E(v_i,v_j)\ [\langle\phi_i\rangle\ \langle\phi_j\rangle + \mathrm{cov}(\phi_i,\phi_j)] \qquad (2\text{-}31)$$

where $\mathrm{cov}(\phi_i,\phi_j)$ is the covariance between ϕ_i and ϕ_j. Irrespective of any fluid turbulence, coagulation is evidently a stochastic process.

It is important to stress at this point that coagulation causes local fluctuations in concentration at a scale that is much smaller than the smallest scale of the turbulence. Concentration correlations due to the coagulation process occur over length scales comparable to the particle length scale where the flow is essentially a laminar shear of fluctuating magnitude and direction. This non-interference of length scales ensures that turbulence and coagulation will be stochastically independent. Whereas the generation mechanisms for particle concentration correlations may be different, both turbulent and coagulation-induced fluctuations are damped by the same mechanism, that is, molecular or Brownian diffusion. As discussed in Section 1.2, the interaction of turbulence with molecular processes results in damping of

the turbulent fluctuations at the length scale $(D^2\nu/\varepsilon)^{1/4}$ for a Schmidt number greater than one, where D is the molecular diffusivity. The scale at which coagulation-induced fluctuations will be damped will similarly be determined by the balance between the rates of generation and dissipation of concentration correlations. In this section we will be concerned with coagulation-induced fluctuations only, implying length scales much smaller than the Kolmogorov scale.

The equation that describes the time evolution of the mean number concentration of i-particles, $\langle\phi_i\rangle$, is called the stochastic coagulation equation. This equation, which has been derived by Bayewitz et al. (1974), has the form

$$\frac{d\langle\phi_i\rangle}{dt} = \frac{1}{2}\sum_{j=1}^{i-1}\left[\langle\phi_j\rangle\langle\phi_{i-j}\rangle + \mathrm{cov}(\phi_j, \phi_{i-j})\right]\beta(v_j, v_{i-j})\,E(v_j, v_{i-j}) - \sum_{j=1}^{\infty}\left[\langle\phi_j\rangle\langle\phi_i\rangle + \mathrm{cov}(\phi_j, \phi_i)\right]\beta(v_i, v_j)\,E(v_i, v_j) \tag{2-32}$$

The equation presupposes that the smallest particles in the system have volume v_1 but places no limit on the largest particle size. In addition, Eq. 2-32 does not account for any sources or sinks of particles. The first term on the right-hand size represents the creation of i-particles by coagulation between smaller j- and (i-j)-particles. The second term represents the loss of i-particles by coagulation with any other particle.

Not surprisingly, the stochastic coagulation equation is not closed since it includes higher order statistics in the form of covariances of concentrations. The alternatives for closing the equation are (a)

ignore the covariances, (b) model the covariances in terms of known variables such as the mean concentrations, or (c) include the evolution equations for the covariances and either ignore the higher-order statistics in those equations or model them in terms of known variables. Scott (1967) adopted the third approach and modeled the triple correlations appearing in the evolution equation for $\langle \phi_i \phi_j \rangle$ in terms of mean concentrations. He was then able to demonstrate that correlation effects in a coagulating cloud of particles decrease with time. This result, however, seems to be strongly influenced by the form of his model for $\langle \phi_i \phi_j \rangle$ which unfortunately lacks a firm physical basis. The first approach for closing the coagulation equation seems to be the most popular (Warshaw, 1967; Marcus, 1968; Gillespie, 1972). Gillespie (1972) showed that if the covariances are ignored then as time progresses the probability distribution of particle concentration approaches a Poisson form. Indeed, if the concentration fluctuations are initially Poisson distributed then they will remain so for all time. This result is not surprising since by removing particle covariances we have introduced a basic requirement for the spatial distribution of particles to be Poisson, namely, the presence or absence of a particle in any volume of space sufficiently small to contain at most one particle is independent of the presence or absence of a particle in any other similar but non-overlapping small volume of space (Benjamin and Cornell, 1970). The random appearance and disappearance of i-sized particles at random points in space by coagulation has no effect on the overall statistical distribution of i-particles, or of any other size particle. Hence, as discussed in section 2.1, the probability distribution for the number of particles in any given volume is the Poisson distribution.

Bayewitz et al. (1974) were able to solve the full stochastic coagulation equations including the covariances for the particular case where the collision frequency and collision efficiency functions are both constant and independent of particles size, say $\beta(v_i,v_j)$ $E(v_i,v_j) = c$. Their solution is for the time evolution of an initial population of unit-sized particles of number concentration $\phi_1(0)$. Their results show that the particle concentrations become Poisson distributed with time, as predicted by Gillespie (1972). They were also able to show that for $\phi_1(0)ct \ll 1$, that is, for small initial particle number concentrations or short times after initiation of coagulation, the covariances in the stochastic coagulation equation could be ignored with negligible error. However, for $\phi_1(0)ct \geq O(1)$ the effect of neglecting the covariances is to under-predict the rate of growth of the large-particle tail of the size distribution. Bayewitz et al. further note that with a size-dependent coagulation kernel, $\beta(v_i,v_j)$ $E(v_i,v_j)$, the discrepancy between the solution to the full stochastic equation and that with the covariances neglected would be even greater.

There are a number of Monte Carlo algorithms that have been developed to simulate the stochastic coalescence of rain drops in a cloud. The early efforts by Lapidus and Shafrir (1972), Chin and Neiburger (1972), and Robertson (1974) unfortunately suffered from lack of statistical rigor. Chin and Neiburger (1972) and Robertson (1974) simulated the growth of a single drop falling through a cloud of smaller drops. Chin and Neiburger assumed a size distribution for the smaller drops while Robertson assigned all the smaller drops the same size. Both techniques fail to account for all possible particle collisions,

since only collisions with the initial drop are accounted for, and thus do not properly simulate the effect of particle correlations (Gillespie, 1975). The technique of Lapidus and Shafrir (1972) is more general but still does not properly treat particle correlations because more than one collision is permitted during a given time step (Gillespie, 1975). Gillespie (1975) developed an algorithm which is quite general and fully statistically rigorous. Unfortunately he did not apply his algorithm to any test problem.

None of the analytical or Monte Carlo models presented above have considered the mechanism which limits the extent of correlation between particles, namely, microscale mixing by Brownian diffusion. Pearson, Valioulis, and List (1984) developed a Monte Carlo technique for simulating coagulation directly in physical space. The algorithm tracks the positions and sizes of a variable population of spherical particles in a fixed cubical control volume. Periodic boundary conditions are applied in that particles leaving the control volume are replaced with image particles entering from the opposite boundary. The procedure may be run in two basic modes: (a) to check the analytical collision frequency functions (assuming the collision efficiency is unity for all particle interactions), when two particles collide the collision is counted and one of the particles is randomly repositioned, (b) to simulate coagulation, when two particles collide a new particle is created that conserves the total volume of the two initial particles. Between collisions particles move in straight paths at constant speeds determined by the collision mechanism (or combination of mechanisms) being applied. Although short-range interactions described by the collision frequency function are not simulated, if the Brownian

diffusion of particles is simulated along with any of the collision mechanisms, then particle correlations will be properly accounted for.

Pearson et al. (1984) developed their Monte Carlo technique primarily for the purpose of verifying Hunt's (1980, 1982) theory on particle size distributions resulting from stationary coagulation. This topic will be addressed in Section 2.5. For the moment some of their results may be used to examine the effect of neglecting particle correlations when the collision frequency function is size dependent.

Pearson et al. (1984) considered a spatially homogeneous population of coagulating particles of volume $v_i = iv_1$ defined over the finite range $i = 1,2,\ldots,M$. Particles of volume v_i are continuously introduced into the population at the constant rate I (number per unit fluid volume per unit time) and are removed from the population when they have reached a size greater than v_M. When stationarity is achieved the rate of volumetric addition of particles, Iv_1, is equal to the volumetric rate of removal of particles. Hence, at steady state the general equation governing the flux of particles through any given particle size v_i is

$$\frac{1}{2}\sum_{j=1}^{i-1}\left[\langle\phi_j\rangle\langle\phi_{i-j}\rangle + \mathrm{cov}(\phi_j, \phi_{i-j})\right]\beta(v_j, v_{i-j}) + I\delta(i-1)$$

$$= \sum_{j=1}^{M}\left[\langle\phi_i\rangle\langle\phi_j\rangle + \mathrm{cov}(\phi_i,\phi_j)\right]\beta(v_i,v_j) \qquad i = 1,2,\ldots,M \tag{2-33}$$

where the collision efficiency function is assumed to be unity.

Figures 2-5 and 2-6 are the steady state particle size distributions obtained by Pearson et al. (1984) for coagulation due to Brownian motion and turbulent shear, respectively. Their results are expressed in terms of a number density distribution g(v) non-dimensionalized with the system parameters, I, v_1, and kT/μ or $(\varepsilon/\nu)^{1/2}$. To assess the relative contribution of concentration correlations, Eq. 2-33 without the covariance terms was solved numerically and the numerical solution was compared with the Monte Carlo results. As with the Monte Carlo algorithm, in the numerical scheme unit-sized particles are introduced into the distribution at every time step at the rate I and particles are removed when they have reached a size greater than v_M. All possible integral particle sizes between v_1 and v_M are included. The numerical algorithm thus corresponds exactly to the Monte Carlo algorithm except for the fact that since the motion of individual particles is not accounted for, particle correlations are not modeled.

For the case of coagulation due to Brownian motion only, Figure 2-5 shows that neglecting the concentration correlations causes the large particle tail of the distribution to be over-estimated. This conclusion also applies to the numerical results of Bayewitz et al. (1974) for the case where the collision frequency function is constant and independent of particle size. However, for the case of Brownian motion, Pearson et al. simulated coagulation by tracking the motion of individual particles; that is, they simulated Brownian diffusion as well. It is demonstrated in Section 2.5 that for steady state coagulation due to either Brownian motion or turbulent shear, the major contribution to the volume flux through any size class v_i is due to collisions of

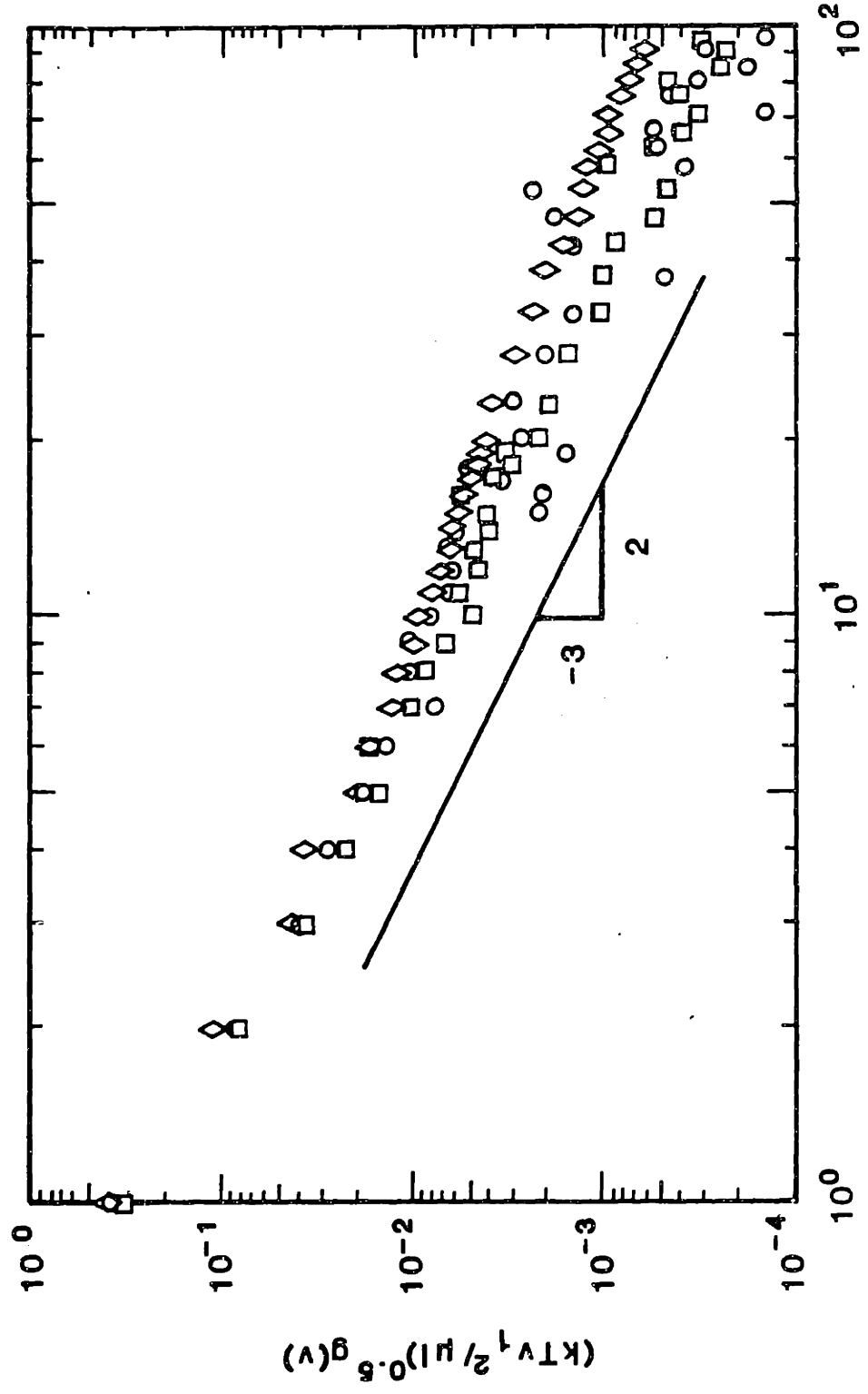

Figure 2-5 Comparison of Pearson et al.'s (1984) Monte Carlo results for stationary coagulation due to Brownian motion with the numerical solution with covariances neglected ($v_1 = 1.8 \times 10^{-3}$, M = 125; circles, Monte Carlo, volume fraction = 0.0155; squares, Monte Carlo, volume fraction = 0.0212; diamonds, numerical integration)

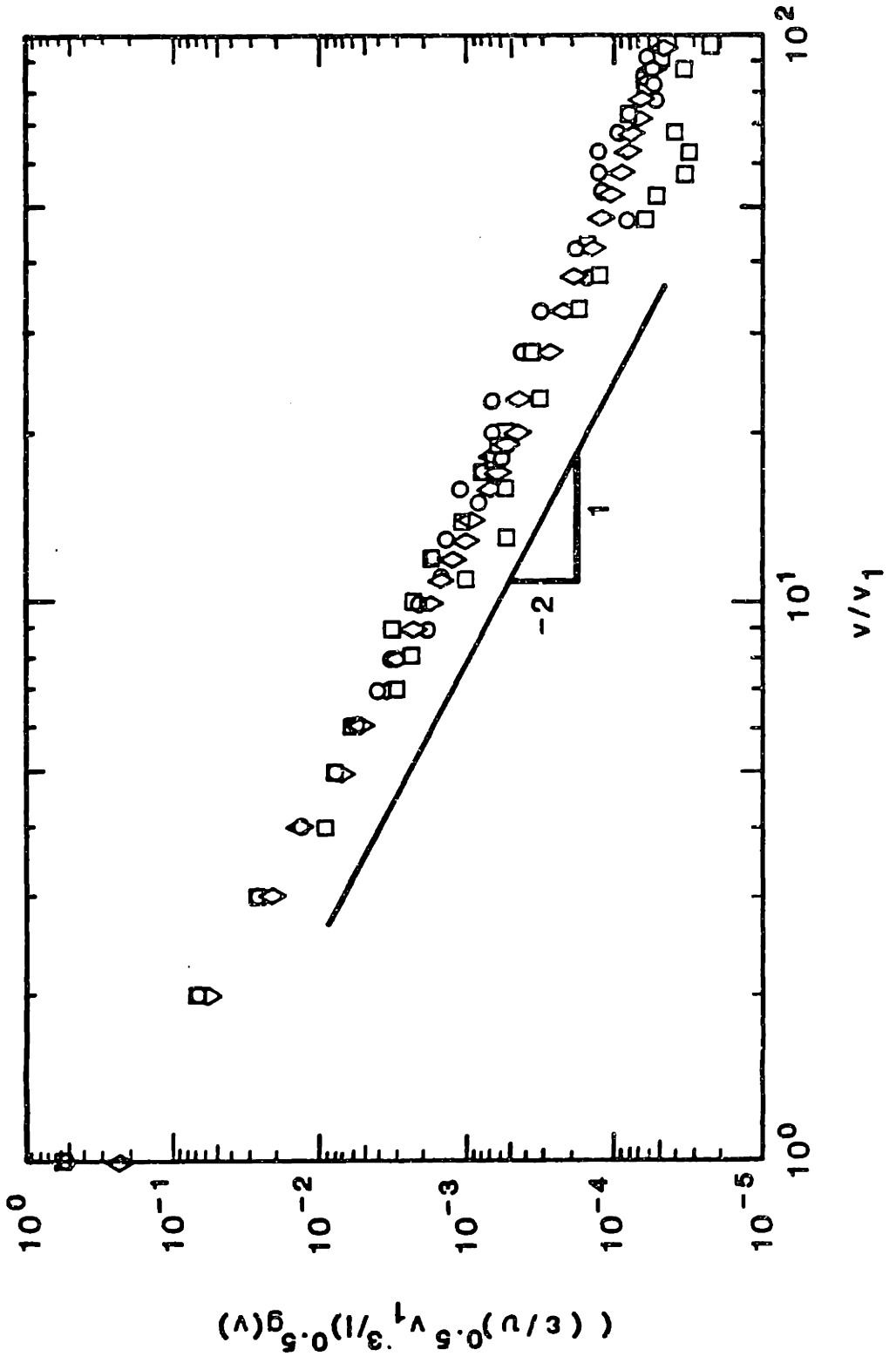

Figure 2-6 Comparison of Pearson et al.'s (1984) Monte Carlo results for stationary coagulation due to turbulent shear with the numerical solution with the covariances neglected ($v_1 = 1.1 \times 10^{-4}$, M = 125; circles, Monte Carlo, volume fraction = 0.0529; squares, Monte Carlo, volume fraction = 0.0103; diamonds, numerical integration).

particles of size v_1 and v_{i-1}. Hence, for any $i \neq 1$ both sides of Eq. 2-33 may be approximated by $\langle\phi_1\rangle\langle\phi_{i-1}\rangle + \text{cov}(\phi_1,\phi_{i-1})$.

A criteria for the neglect of $\text{cov}(\phi_1,\phi_{i-1})$ as compared to $\langle\phi_1\rangle\langle\phi_{i-1}\rangle$ may be derived through the following line of reasoning. A particle of volume v_{i-1} in its path through a cloud of unit-sized particles sweeps out a tube within the cloud of radius approximately equal to r_{i-1}. This "wake" behind the (i-1)-particle is the cause of particle correlation. The mechanism by which the correlation is erased is mixing by Brownian diffusion. If the time scale for the unit-sized particles to completely mix behind the (i-1)-particle is much less than the time scale for creation of the wake by coagulation, then the particle correlation will be negligible. The time scale t_d for radial diffusion of unit-sized particles by Brownian motion over a tube of radius r_{i-1} is

$$t_d = 6\pi \mu r_1 r_{i-1}^2/kT \tag{2-34}$$

The time scale t_r for removal of unit-sized particles by an (i-1) particle is

$$t_r = \left[\beta(v_1, v_{i-1})\, g(v_1)\, v_1\right]^{-1} = \frac{3\mu}{2kT} \frac{1}{v_1^{2/3}\, v_{i-1}^{1/3}\, g(v_1)} \tag{2-35}$$

A criteria for the correlation effect to be small is $t_d \ll t_r$ or

$$v_{i-1} \ll \left[3v_1\, g(v_1)\right]^{-1} \tag{2-36}$$

Substituting the system parameters corresponding to Figure 2-5 yields the results $v_{i-1} \ll 890\, v_1$ for the circles and $v_{i-1} \ll 320\, v_1$ for

the squares. If by "much less than" we mean "an order of magnitude less than" then, indeed, we see from Figure 2-5 that the numerical results without the concentration correlations begin to diverge from the Monte Carlo results at approximately $v_{i-1} = 20\ v_1$.

For the case of coagulation due to turbulent shear only, Figure 2-6, there does not seem to be any significant difference between the numerical solution and the Monte Carlo results. This might seem surprising since Pearson et al. did not simulate Brownian diffusion for this case. Without any mechanism to limit the extent of correlation other than the removal of v_M-particles and the addition of v_1-particles from random points in space it would seem that there should be some noticeable effect of particle correlations, especially given the results in Figure 2-5. However, further consideration will reveal that the lack of correlation is an artifact of the technique used to model shear-induced coagulation.

Without Brownian diffusion the distribution of particles within the control volume, once steady state conditions have been established, must be such that each particle is separated from its neighbors by a distance of order $(\nu^3/\varepsilon)^{1/4}$. Indeed the role of molecular mixing processes is to reduce the scale of segregation beyond the minimum scale of the turbulence. If molecular mixing is absent, then turbulence cannot reduce the segregation any further than the Kolmogorov microscale (Brodkey, 1975). If the addition of unit-sized particles into the population was discontinued, then we would expect coagulation to cease as well. The only reason that coagulation is observed is that unit-sized particles are continuously introduced into the control volume at random points. Once introduced, a unit particle will soon coagulate

with the particle already occupying the local volume of space. The growth of each particle will thus be limited by the average rate at which unit-sized particles are introduced into their local volume. When a collision with a v_1-particle results in a particle exceeding the maximum size, v_M, it is removed. Hence, the growth history of every particle involves correlation only with unit-sized particles. Since the unit-sized particles are placed at random within the control volume, there is effectively no particle correlation whatsoever. Hence, the results of Figure 2-6 cannot be used to conclude anything about the extent of particle correlations caused by shear-induced coagulation (although the comparison with the Monte Carlo results further confirms the accuracy of the numerical integration procedure employed).

If Brownian motion and turbulent shear are superimposed, then a criterion for neglecting particle correlations may be derived as above. In this case the time scale for coagulation is

$$t_r = \left[b(\varepsilon/\nu)^{1/2} v_{i-1} v_1 g(v_1)\right]^{-1} \tag{2-37}$$

where b is an appropriate constant depending on the choice of collision frequency function for turbulent shear (see Section 2.2.1). Hence, if

$$v_{i-1} \ll \left[\frac{2kT}{9 (\varepsilon/\nu)^{1/2} \mu b v_1^{4/3} g(v_1)}\right]^{3/5} \tag{2-38}$$

then the correlation effect will be small (for steady state coagulation with a constant input of unit-sized particles). Similarly, for Brownian

motion and differential settling the time scale for coagulation is

$$t_r = \left[0.1 \frac{g}{\nu} \left| \frac{\rho_p - \rho_f}{\rho_f} \right| v_{i-1}^{4/3} v_i \, g(v_i) \right]^{-1} \qquad (2\text{-}39)$$

and the criterion for neglecting correlations is

$$v_{i-1} \ll \left[\frac{2kT}{0.9 \, g \left| \rho_p - \rho_f \right| v_1^{4/3} \, g(v_1)} \right]^{3/5} \qquad (2\text{-}40)$$

These criteria indicate that high particle concentrations increase the extent of correlation between particles, in agreement with the results of Bayewitz et al. (1974).

From the observations of particle size distributions presented in Table 2-1, it is evident that particles tend to be distributed as v^{-2} over the size range 0.5 μm < r < 50 μm. Letting r_1 = 0.5 μm and assuming a minimum mass concentration of 0.01 mg/l, to be able to neglect particle correlations, eq. (2-36) indicates that the maximum particle size should be much less than 390 μm; for a typical shear rate of 1 sec^{-1}, eq. (2-38) indicates a maximum particle size much less than 38 μm; for a specific gravity of 0.05, eq. (2-40) indicates a maximum particle size much less than 25 μm. Since particle mass concentrations much greater than 0.01 mg/l are usually of interest, we can anticipate that particle correlations will always be significant, particularly for the larger particles.

Summarizing, it has been shown that coagulation is a stochastic process so that modeling the evolution of the mean number concentration of any size particle, in a strict sense, requires having to deal with particle concentration correlations. Small-scale mixing by Brownian

diffusion or low particle concentrations can reduce the extent of these correlations. For typical particle concentrations observed in the aquatic environment, it appears that particle correlations will always be significant. Since there is no means of modeling these correlations at present, other than by the approach of Pearson et al. (1984) involving direct Monte Carlo simulation of individual particle collisions, we must be aware that numerical simulations will tend to under-estimate the extent of coagulation.

2.4 Numerical Integration of the Coagulation Equations

The numerical solutions presented in Section 2.3 involved particle size ranges of only two orders of magnitude in volume (or less than one order of magnitude in radius). To model coagulation in the aquatic environment, one needs to consider particle volumes ranging over eight or nine orders of magnitude. This requirement precludes including all possible integral particle sizes in the numerical scheme. It is thus necessary to subdivide the particle size range into a smaller number of sections, or size classes. Within each size class the distribution function of any property of interest may be taken as constant or assigned some higher order functional form with additional continuity constraints at the boundaries of the size classes.

Numerical difficulties are introduced when the discretization results in non-integral size classes, that is, when collisions of particles from the i^{th} and j^{th} size classes do not produce particles belonging to the $(i + j)^{th}$ size class. For the case when the distribution function is taken as constant within each size class two techniques have been developed for overcoming this difficulty. Gelbard,

Tambour and Seinfeld (1980) have developed a method that essentially involves modifying the coagulation kernel, $\beta(v_i,v_j)\ E(v_i,v_j)$ for each possible interaction that results in a change in the total volume of particles in size class k, in such a manner that volume is conserved overall and coagulation proceeds at the proper rate. The general coagulation kernel now becomes a function of v_k as well as v_i and v_j. These modified coagulation kernels are specific to the discretization scheme and the coagulation kernel employed. For each new coagulation kernel or discretization of particle size classes a whole new set of modified coagulation kernels must be computed, in general, by numerical integration of double integrals. Once the modified coagulation kernels have been computed they are substituted into the coagulation equations and time integration may proceed as usual with any conventional scheme. Although the method is completely general it does suffer from the inflexibility and large computational cost of having to pre-compute the modified coagulation kernels.

A much simpler technique has been developed by Lawler, O'Melia and Tobiason (1980). The method is equivalent to that of Gelbard et al. in that volume is conserved overall and the technique is applicable only to the case where the distribution function is assumed constant within each size class. When particles of nominal size v_i and v_j coagulate they form a particle of size $(v_i + v_j)$. In general the volume $(v_i + v_j)$ will not correspond to a nominal size class volume but will be within the range v_k to v_{k+1}, where v_k is the nominal value of the k^{th} size class and similarly for v_{k+1}. To conserve volume the number flux $F_n = \beta(v_i,v_j)\ E(v_i,v_j)\ \phi(v_i)\ \phi(v_j)$ is divided into two fractions. The fraction

$$f_{ijk} = \left[\frac{v_{k+1} - (v_i + v_j)}{v_{k+1} - v_k}\right] < 1 \qquad (2\text{-}49)$$

of F_n is assigned to the k^{th} size class and the fraction $(1 - f_{ijk})$ of F_n is assigned to the $(k+1)^{th}$ size class. If $(v_i + v_j) > v_M$, where M is the last size class, then the fraction

$$f_{ijM} = \frac{v_i \cdot v_j}{v_M} > 1 \qquad (2\text{-}42)$$

of F_n is assigned to the M^{th} size class. Since the volume flux is $F_v = F_n(v_i + v_j)$, we see that this technique conserves volume, although the total number of particles is not properly reduced. Note that without additional constraints or equations it is not possible to both conserve volume and properly reduce numbers when non-integral size classes are used. The fractions f_{ijk}, one for each possible i-j interaction, are pre-computed before time integration proceeds. However, as compared to Gelbard et al.'s method, the coefficients are obviously much simpler to compute and are a function of the particle size range discretization only, not of the coagulation kernel. Because of its simplicity and cost effectiveness Lawler et al.'s method is preferred to that of Gelbard et al., especially since both methods have the same level of computational accuracy.

Note that in the aquatic environment particle volume may not be strictly conserved during coagulation. As mentioned in Section 1.3 the density of suspended particles is observed to decrease with increasing size (McCave, 1984). This implies that when two particles coagulate to form a larger particle water must be entrapped in the aggregate

resulting in a larger effective particle size (and a smaller effective particle density) than that given by the sum of the two initial particle volumes. To take this effect into account in the numerical scheme would require empirical input specifying the actual volume that each pair of particles would adopt upon coagulation. Since this type of information is not presently available, we must keep in mind this possible source of error in our numerical simulations.

The discretization of the particle size range into size classes, like any discretization procedure, should provide sufficient resolution where the curvature in the distribution function is the greatest. Because most of the particle numbers are normally concentrated in the smallest-sized particles it is usually necessary to have the finest resolution at the small end of the size range and the coarsest resolution at the large end. The discretization of the size range into logarithmically increasing size intervals is often employed to achieve the proper resolution and reduce the number of size classes in the numerical scheme (Berry, 1967). In addition, as previously mentioned, logarithmic size classes compensate for the logarithmic reduction in particle numbers with size, thus permitting the application of the continuum assumption in defining local particle concentrations.

The integration of the coagulation equations may be performed with a simple explicit time stepping procedure provided the time step is chosen appropriately. The coagulation time scale for any size class i is

$$t_r^{(i)} = \left| \frac{1}{\phi_i} \left(\frac{\Delta\phi}{\Delta t}\right)_i \right| \qquad (2\text{-}43)$$

and the integration time step should be smaller than this time scale. There are various ways of accomplishing this goal, two of which will be described here. To evaluate their relative merits, results obtained using each technique will be compared against an exact solution.

Exact unsteady solutions to the coagulation equations (without concentration correlations) have been obtained by Golovin (1963), Scott (1968), Drake and Wright (1972) and Bayewitz et al. (1974) for various analytical coagulation kernels and initial conditions. A solution that is convenient for our purposes is that for a constant coagulation kernel independent of particle size and an initial exponential particle number density distribution of the form

$$g(v,0) = g(v_1)\exp(-v/v_1) \tag{2-44}$$

The solution, due to Scott(1968), is

$$g(v,T) = \frac{4\, g(v_1)\, \exp\left(\frac{-2v}{v_1(T+2)}\right)}{(T+2)^2} \tag{2-45}$$

where the non-dimensional time $T = c\, v_1\, g(v_1)\, t$ and c is the magnitude of the constant coagulation kernel.

The first method of integrating the coagulation equations involves using a single time step for all particle size classes. The time step chosen should be smaller than the smallest value of $\Delta t_r^{(i)}$, i = 1,2,...,M. Thus at each time step a complete sweep of all possible collisions between i- and j-particles (j > i) is performed by looping through j = i, i+1,...,M while i ranges from 1 to M. For each i,j pair the number flux out of size class i and j and into size class k and k+1,

where $v_k \leq v_i + v_j \leq v_{k+1}$, is accumulated. With the net fluxes $(\Delta\phi/\Delta t)_i$ the time scales for each size class i are updated from

$$\Delta t_r^{(i)} = b \left| \frac{1}{\phi_i} \left(\frac{\Delta\phi}{\Delta t}\right)_i \right| \tag{2-46}$$

where b is a fixed constant of magnitude less than one (usually set at b = 0.1) and the minimum value $\Delta t = \min(\Delta t_r^{(1)}, \Delta t_r^{(2)}, \ldots, \Delta t_r^{(M)})$ is chosen as the time step for the next time interval. After the time step has been computed the particle concentrations are updated with the net fluxes $\Delta\phi_i$. Because a single time step is used in the integration procedure this algorithm will be called the single time step algorithm.

Figure 2-7 is a comparison of the numerical solution using the single time step algorithm with Scott's exact solution, with the coagulation kernel set at $c = 3.5 \times 10^{-18}$ cm^3/sec and the initial particle number density distribution specified as $g(v_1,0) = 6.5 \times 10^{-3}$ cm^{-3} μm^{-3}. Integer size classes were employed with $v_1 = 0.5$ μm^3. The size range was truncated at $v_M/v_1 = 125$. Hence there is some truncation error at the large end of the size range that is not shown in Figure 2-7 since only the results for the first 65 size classes are plotted. The agreement is excellent and confirms the accuracy of the numerical scheme.

To demonstrate the validity of using logarithmic size classes Figure 2-8 is a comparison of the numerical and exact solutions corresponding to Figure 2-7 except that the size classes are spread apart by a factor of $v_i/v_{i-1} = 10^{0.77}$. The size range $v_M/v_1 = 125$ is represented by 8 size classes, instead of 125. Although there

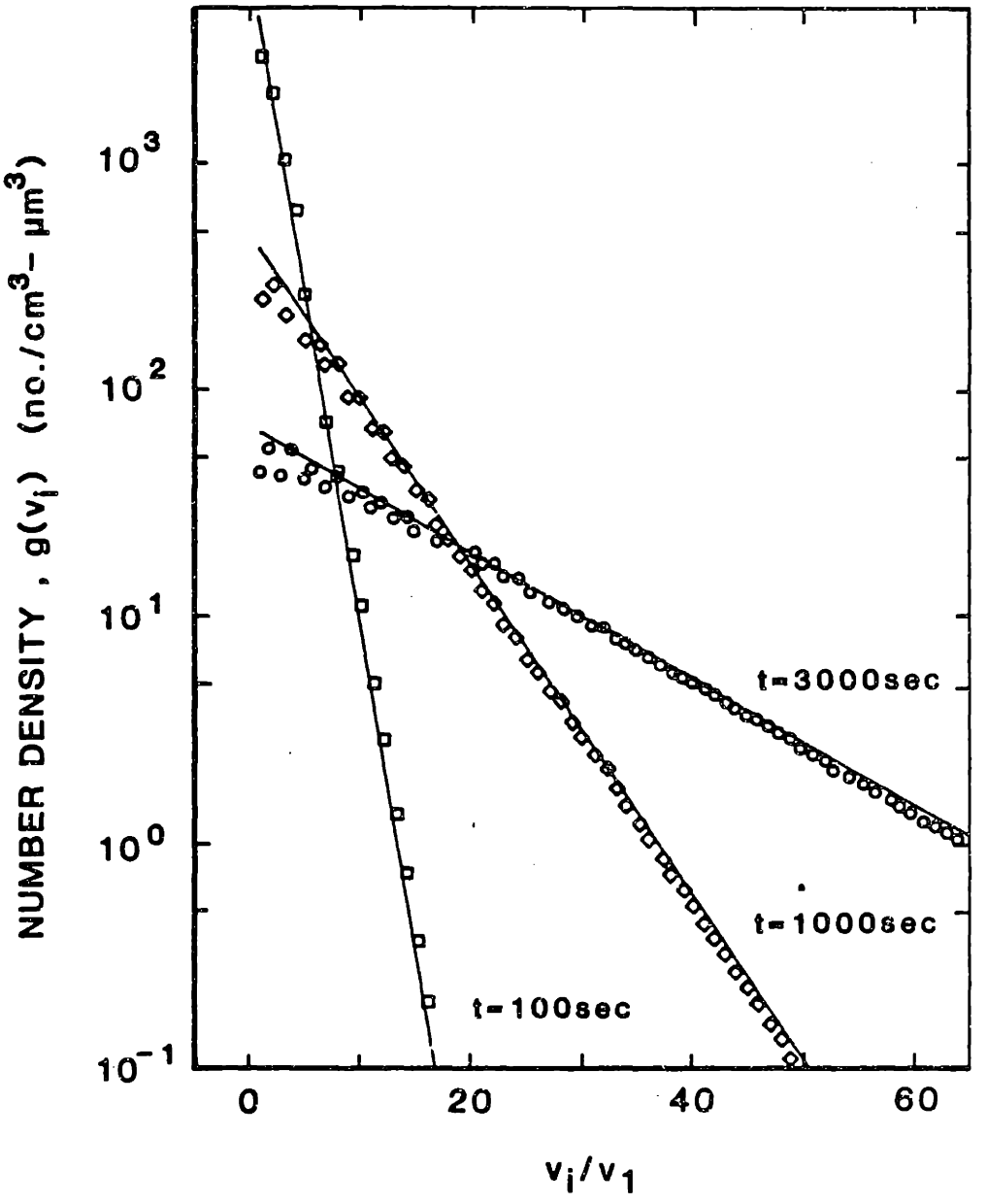

Figure 2-7 Comparison of numerical solution using the single time step algorithm with Scott's (1968) exact solution ($g(v_1,,0)$ = 6.5×10^{-3} cm^{-3} μm^{-3}, $c = 3.5 \times 10^{-18}$ cm^3/sec, $v_1 = 0.5$ μm^3, M = 125 integer size classes).

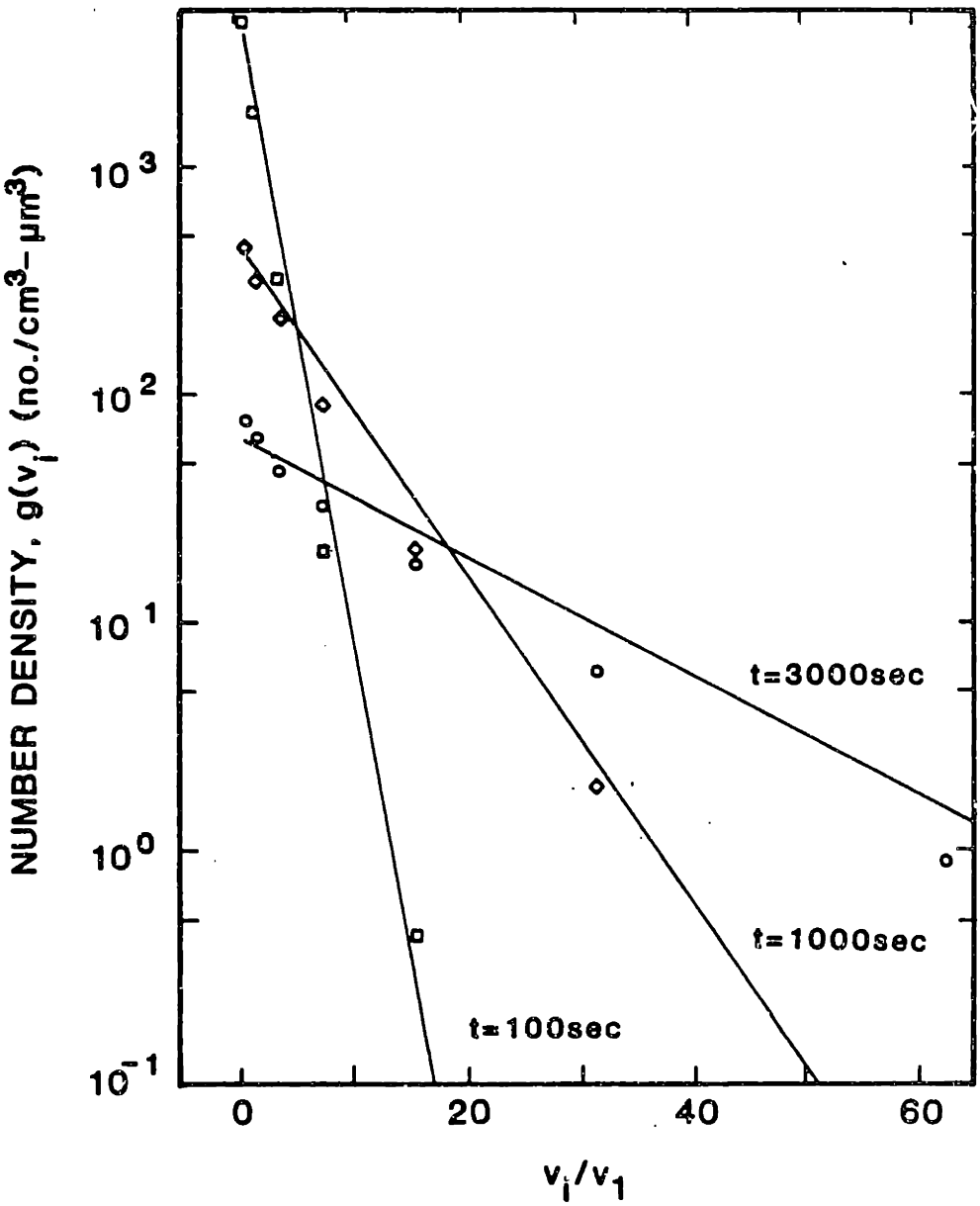

Figure 2-8 Comparison of numerical solution using the single time step algorithm with Scott's (1968) exact solution (same conditions as Figure 2-7 except 8 logarithmic size classes, $v_i/v_{i-1} = 10^{0.77}$).

has been some degradation of accuracy the numerical solution compares quite well with the exact solution. The discrepancy between the solutions may be partially due to the truncation error which must be accommodated over a larger apparent particle size range since the size classes are spread so far apart.

An alternative technique for integrating the coagulation equations is based on the premise that if there is a wide range in the time scales $\Delta t_r^{(i)}$ determined from Eq. 2-46, then it may be computationally more efficient to use a separate integration time step for each particle size class. This procedure will be called the multiple time step algorithm. Since the coagulation equations are coupled, that is, each $v_k < v_i + v_j < v_{k+1}$ interaction appears as a number flux F_n in three separate equations if integer size classes are used or four equations with non-integer classes, then additional book-keeping is required to conserve particle volume. In particular, each interaction must be assigned to a single equation and all three, or four, number fluxes (i.e., the flux out of size classes i and j and into size classes k and k+1) are accumulated simultaneously. Of the three possible choices each interaction is assigned to the equation that has the smallest time scale. Thus, considering all the equations, the one that has the minimum time scale, say the equation for size class ℓ, will have all the interactions that include particles of size v_ℓ assigned to it. The equation that has the next smallest time scale will have somewhat fewer terms and so on until the equation with the longest time scale is reached, which will be assigned no interactions if integer size classes are used, or at most one term if logarithmic size classes are employed. In other words, instead of performing all interactions each time step,

as with the single time step algorithm, each interaction is assigned its own time step chosen from the finite set of time scales $\Delta t_r^{(i)}$, i = 1,...,M. Given an interaction $v_i + v_j = v_k$, the time step assigned to it is the smallest of $\Delta t_r^{(i)}$, $\Delta t_r^{(j)}$, or $\Delta t_r^{(k)}$.

To prevent numerical instability, if at any given time an interaction results in a number flux that will cause the concentration of a size class to become negative, then the flux is not accumulated and the interaction is reassigned to the equation with the next smallest time scale of the three possible choices. During the course of the numerical integration if the relative ordering of the equations should change as a result of a change in the relative time scales, then the interactions that are assigned to equations whose time scales become relatively longer must be reassigned to equations that may now have smaller time scales.

This algorithm is as difficult to program as it is to describe. However, it does work quite well, in fact, it is as accurate as the single time step algorithm. Figure 2-9 corresponds to Figure 2-8 except that the multiple time step algorithm was used to compute the numerical solution. The numerical solutions in Figure 2-8 and 2-9 are essentially indistinguishable. Unfortunately the multiple time step algorithm is not as computationally efficient as the single time step method. A number of different simulations were performed each designed to favor the multiple time stepping capability of this second algorithm. In every case the multiple time step algorithm required more CPU time, by a factor of 1.5 or more. Even when the distribution of time scales was such that the shortest time scale was more than 10 times as small as its nearest competitor, the single time step algorithm was found to be more

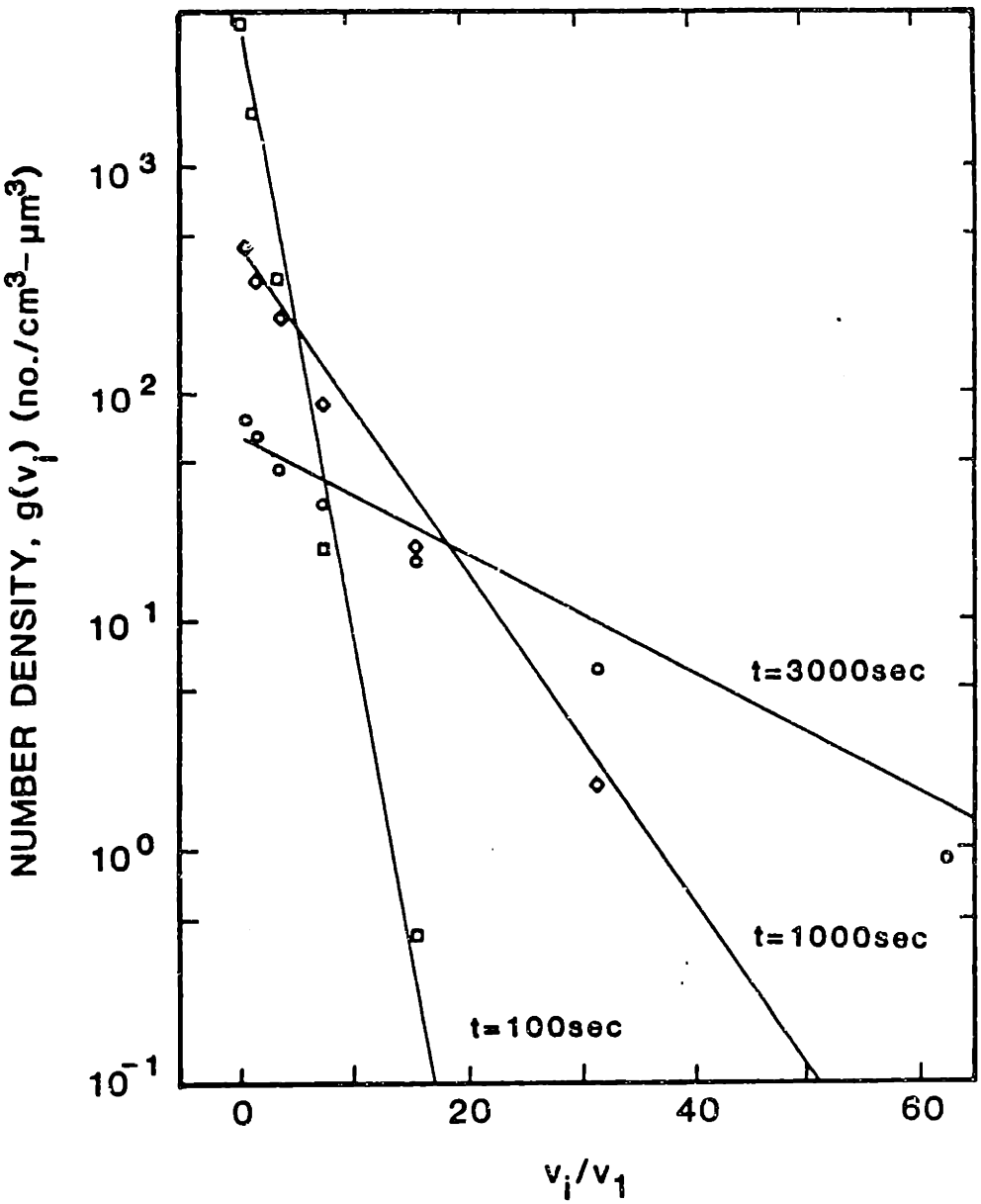

Figure 2-9 Comparison of numerical solution using the multiple time step algorithm with Scott's (1968) exact solution (same conditions as Figure 2-7 except 8 logarithmic size classes, $v_i/v_{i-1} = 10^{0.77}$).

efficient. Apparently the cost of book-keeping interactions and guarding against numerical instability is sufficient to more than compensate for the savings incurred by having a few less interactions to compute at every time step. In particular, the re-ordering of equations and the consequent reassignment of interactions required by the evolution of the size distribution was found to be very expensive.

The number of interactions that must be computed every time step with the single time step algorithm is of order $M^2/2$, where M is the total number of size classes. In principle, if the time scales are sufficiently spread out, the number of interactions that must be computed with the multiple time step algorithm is of order M. It would thus seem that the multiple time step procedure should become relatively more efficient as the number of size classes is increased. However, numerical simulations have shown exactly the opposite trend. Apparently with more size classes we have more opportunities for equations to change their relative ordering and the cost of reassigning interactions increases tremendously with increasing numbers of equations.

Hence, based on this comparison of the two algorithms along with a few other unsuccessful algorithms that have not been reported here, the simplest way of integrating the coagulation equations also happens to be the most computationally efficient. In all subsequent cases the explicit single time step algorithm has been employed to integrate the coagulation equations.

2.5 Particle Interactions During Stationary Coagulation

2.5.1 Coagulation Due to a Single Collision Mechanism

There has been recent interest in applying Friedlander's (1960a,b) local equilibrium hypothesis for explaining observed particle size distributions in the oceans and atmosphere (Hunt, 1980, 1982; Jeffrey, 1981; Pearson et al, 1984). In analogy with its famous counterpart in turbulence theory, the concept implies such notions as stationarity, equilibrium subranges, and universal constants. The theory is supported by the favorable agreement between the predicted size distributions and those observed experimentally (Hunt, 1980) and simulated by Monte Carlo techniques (Pearson et al., 1984).

Hunt's (1980, 1982) local equilibrium theory is based on five assumptions: (a) the coagulation process must be in a dynamic steady state with a constant volume flux through the size distribution, (b) the collision efficiency must be independent of particle size, (c) collisions must be dominated by particles comparable in size, (d) only one coagulation mechanism is dominating the volume flux through a particle size subrange, and (e) the coagulating power of each collision mechanism may be characterized by a single parameter (kT/μ, $(\varepsilon/\nu)^{1/2}$, $g(\rho_s-\rho_f)/\mu$ for Brownian motion, turbulent shear and differential sedimentation, respectively). Hunt (1982) lumps assumptions (c) and (d) into one assumption, but clearly they are independent. It is possible for one mechanism to be dominating the volume flux without that flux being mostly due to collisions between equal-size particles. Alternatively, it is also possible for collisions of equal-sized

particles to be dominating the volume flux with each mechanism causing about the same number of collisions per unit time.

With these assumptions, dimensional analysis may be applied to obtain the form of the size distribution in each size subrange over which a single mechanism is controlling the rate of coagulation between particles comparable in size. The size distributions based on particle volume are (Hunt, 1982)

a) for Brownian motion

$$g(v) = A_b \left[\frac{F_v}{(kT/\mu)}\right]^{1/2} v^{-3/2} \qquad (2\text{-}47)$$

b) for shear

$$g(v) = A_{sh} \left[\frac{F_v}{G}\right]^{1/2} v^{-2} \qquad (2\text{-}48)$$

c) for differential sedimentation

$$g(v) = A_{ds} \left[\frac{F_v}{g(\rho_s - \rho_f)/\mu}\right]^{1/2} v^{-13/6} \qquad (2\text{-}49)$$

where F_v is the volume flux, $G = (\varepsilon/\nu)^{1/2}$ is the turbulent shear rate, and A_b, A_{sh}, A_{ds} are "universal" dimensionless constants.

The physical justification for Hunt's (and Friedlander's, 1960a,b) first assumption has been questioned by Junge (1969) for atmospheric aerosols and by McCave (1984) for oceanic particles on the grounds that typical coagulation rates are too slow compared to the rate of change of the oceanic or atmospheric conditions for stationarity to be achieved. In addition, McCave(1984) points out that in the ocean the sources for particles are distributed throughout the particle size range and not limited to nucleation of the smallest-sized particles so that the volume

flux through any subrange, even if it is constant, is not due to coagulation alone. With respect to the second assumption Valioulis et al. (1984), based on a comprehensive review of the literature, have shown that in general collision efficiencies are strongly dependent on particle size. They conclude that only for those mechanisms for which the collision efficiency functions favor collisions between equal-sized particles may local equilibrium be invoked. From Figures 2-2, 2-3 and 2-4 we see that for Brownian motion and, if the radius of the small particle is less than about 30 μm, for differential sedimentation, collisions between equal-sized particles are, in fact, not favored.

Jeffrey (1981) gave an alternate derivation of Hunt's theoretical results. If collisions between equal-sized particles dominate the volume flux, then local equilibrium is established over particle size ranges of order v_j. Hence Jeffrey approximated the expression representing the volume flux out of size class v_j by

$$(v_j)(\Delta v_j)\sum_{i=1}^{\infty}\beta(v_i,v_j)g(v_i)g(v_j)\Delta v_i \approx \beta(v_j,v_j)g^2(v_j)v_j^3 = F_v \qquad (2\text{-}50)$$

where F_v is the volume flux and $\Delta v_j \sim O(v_j)$. Substituting into Eq. 2-50 the expressions for $\beta(v_j,v_j)$ for the various collision mechanisms yields the results corresponding to Hunt's theory, namely, Eqs. 2-47, 2-48, and 2-49.

From Jeffrey's derivation it is evident that for local equilibrium to be in effect the terms representing collisions between equal-sized particles must dominate the summation in Eq. 2-45. However, using Hunt's forms for $g(v_i)$ it is easy to show that for each collision mechanism $\beta(v_i,v_j)\ g(v_i)\ g(v_j) \gg \beta(v_j,v_j)\ g^2(v_j)$ for $i \ll j$. That is, it appears that the summation in Eq. 2-61 is dominated by terms representing collisions with the smallest sized particles of order v_1,

not collisions with equal-sized particles of order v_j. This internal inconsistency leads us to doubt the validity of Hunt's local equilibrium hypothesis.

In the remainder of this section the general validity of Hunt's third assumption will be examined. The question of which particle interactions dominate the flux of particles through any size class is not just of academic interest. Indeed, McCave (1984) has shown that, for the low particle concentrations observed in the ocean, the time required for a particle to travel through the size distribution would be several hundred years if collisions between particles comparable in size dominate. If small particles have to coagulate with particles much larger in size, however, this "travel" time could be shortened considerably.

Analytically, a stationary particle size distribution may be generated by considering a spatially homogeneous population of coagulating particles of size $v_i = iv_1$, $i = 1,2,\ldots,M$ into which particles of volume v_1 are continuously introduced at a rate I (number/volume/time) and from which particles are removed when they have reached a size greater than v_M. If the resulting stationary size distribution is in local equilibrium the finite domain errors introduced by the double truncation will be restricted to regions near the boundaries of the size distribution. Varying the range of particle size should not affect the shape of the size distribution. If local equilibrium is not the rule, then the effect of the truncation should be evident throughout the size distribution, and changing the particle size range should affect the shape of the distribution. This is the kind of reasoning that has been applied by Pearson, Valioulis and List (1984) in

their attempt to verify Hunt's theory. Their Monte Carlo technique and some of their results have already been discussed in Section 2.2.

Pearson et al. obtained steady-state particle size distributions for the Brownian motion and turbulent shear mechanisms each acting alone (so that Hunt's assumption (d) is automatically satisfied) and with the collision efficiency set equal to one. Since collisions between equal-sized particles do not occur by differential sedimentation, with the technique of constantly introducing unit-sized (v_1-sized) particles it is impossible to verify Hunt's predicted form of the size distribution for this mechanism acting alone, the solution being $g(v) = c(t)\ \delta(v_1)$ with $c(t) \to \infty$ as $t \to \infty$. That is, to verify Hunt's form for the differential sedimentation subrange it is necessary to have a mechanism that will allow particles of size v_1 to collide with each other. Because their results seemed to be insensitive to the particle size range employed and since the slopes of the particle number distributions they obtained generally agreed with those predicted by Hunt's theory, Pearson et al. conclude that their results give further support for the validity of the theory.

The agreement between the Monte Carlo simulations of Pearson et al. and Hunt's theoretical results may be explained with reference to a class of exact solutions derived by Klett (1975). Klett (1975) derived the general solution for coagulation frequency functions that have the functional form $\beta(v_i,v_j) = \beta_o(v_i v_j / v_1^2)^b$, where β_o and b are constants. Writing each collision frequency function as the product of a magnitude, which in general depends on the volume of the larger particle, and a non-dimensional function of the ratio of the particle volumes results in

a) for Brownian motion

$$\beta(v_i,v_j) = \frac{8kT}{3\mu}\left\{\frac{\left[(v_i/v_j)^{1/3}+1\right]^2}{4\,(v_i/v_j)^{1/3}}\right\} = \frac{8kT}{3\mu}\,f_1\,(v_i/v_j) \qquad (2\text{-}51)$$

b) for shear

$$\beta(v_i,v_j) = 2.5G\,v_j\left\{\frac{\left[(v_i/v_j)^{1/3}+1\right]^3}{8}\right\} = 2.5G\,v_j\,f_2(v_i/v_j) \qquad (2\text{-}52)$$

c) for differential sedimentation

$$\beta(v_i,v_j) = 0.1\,\frac{g}{\nu}\,\frac{|\rho_s-\rho_f|}{\rho_f}\,v_j^{4/3}\left\{\left[1-(v_i/v_j)^{1/3}\right]\left[1+(v_1/v_j)\right]\right\}$$

$$= 0.1\,\frac{g}{\nu}\,\frac{|\rho_s-\rho_f|}{\rho_f}\,v_j^{4/3}\,f_3\,(v_i/v_j) \qquad (2\text{-}53)$$

For the case b = 0 Klett pointed out the excellent agreement between his solution and Friedlander's (1960) steady state size distribution for coagulation due to Brownian motion only (which is the same as Hunt's, i.e., Eq. 2-47). The reason for the agreement is immediately apparent from Eq. 2-51 and the plot of the function $f_1(v_i/v_j)$ in Figure 2-10. For $v_1/v_j > 0.01$, $f_1(v_i/v_j) \approx 1$. Unless $v_1/v_H \ll 0.01$ the exact solution for stationary coagulation due to Brownian motion only will be very similar to that for $\beta = \beta_o = 8kT/3\mu$. For the case b = 0 Klett's exact solution is

$$g(v_i) = \left(\frac{2I}{v_1^2\,\beta_o}\right)^{1/2}\begin{cases} 1 & i = 1 \\ \dfrac{(2i-3)!}{2^{2(i-1)}(i-2)!\;i!} & i \geq 2 \end{cases} \qquad (2\text{-}54)$$

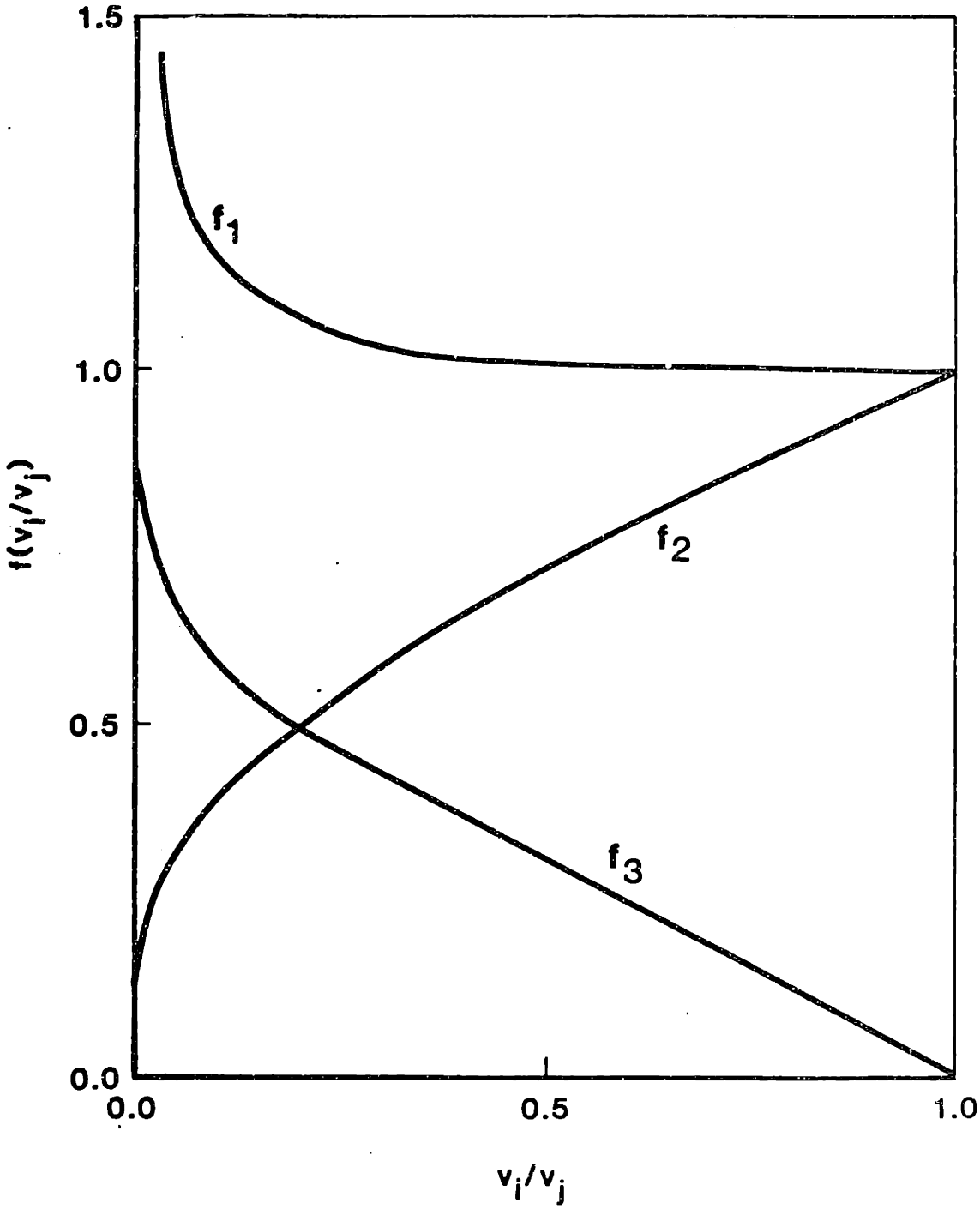

Figure 2-10 The functions f_1, f_2 and f_3.

For $i \gg 1$ the solution may be approximated by (Klett, 1975)

$$g(v_i) \approx \frac{1}{(2\pi)^{1/2}} \left(\frac{Iv_1}{\beta_o}\right)^{1/2} v_i^{-3/2} \qquad (2\text{-}55)$$

In general the solution for this case must depend only on the parameters I, β_o and v_i, $i = 1,\ldots,M$. Dimensional analysis reduces the number of independent variables to $(I/\beta_o)^{1/2}$ and v_i, $i = 1,\ldots,M$. By invoking local equilibrium the number of independent variables is further reduced to $(Iv_1/\beta_o)^{1/2}$ and the local particle volume v_i. Dimensional analysis then yields the functional form

$$g(v_i) = A \left(\frac{F_v}{\beta_o}\right)^{1/2} v_i^{-3/2} \qquad (2\text{-}56)$$

where A is a dimensionless constant. The kind of reasoning that has been applied by Hunt (1980, 1982) and Pearson et al. (1984) is that since Eq. 2-56 is consistent with the asymptotic solution, Eq. 2-55, then the particle size distribution must be in local equilibrium. However, as will soon become evident, this consistency, though necessary, is not sufficient to guarantee local equilibrium.

A direct method of verifying the local equilibrium assumption is to examine the magnitude of the terms in the summations in the governing equation,

$$\frac{1}{2} \sum_{j=1}^{i-1} \beta(v_j, v_{i-j})\, g(v_j)\, g(v_{i-j}) + \frac{I}{v_1^2}\, \delta(i-1)$$

$$= \sum_{j=1}^{M} \beta(v_i, v_j)\, g(v_i)\, g(v_j) \qquad ;\ i = 1,2,\ldots M \qquad (2\text{-}57)$$

To do this we solve Eq. 2-57 numerically as described in Section 2.4. No sectional representation of the particle size distribution is employed; all integral particles sizes from v_1 to v_M are retained in the numerical scheme. The computed solution is thus exact to within machine round-off error and the finite-domain error resulting from truncation of the size distribution at v_M. Klett (1975) has shown that the truncation error for this case is

$$\frac{g_T(v_i)}{g(v_i)} \approx \left(1 + \frac{1}{\pi M}\right)^{i-1} \tag{2-58}$$

where $g_T(v_i)$ is the truncated size distribution. For a fixed M the relative error increases with relative particle size $i = v_i/v_1$. Figure 2-11 shows the comparison between the analytical solution, Eq. 2-54, and the numerical solutions for $\beta = \beta_o$ and $\beta = 8kTf_1/3\mu$ with M = 50 and serves as a check on the numerical scheme. The numerical solutions are indistinguishable from each other.

Figure 2-12 illustrates the variation of $\beta(v_i,v_j)g(v_i)g(v_j)$ with v_j for various v_i. The absolute magnitudes of the values on the ordinate scale have no significance; the scale indicates relative values only. The results were obtained from the numerical solution rather than the exact solution (only because it was more convenient). Contrary to the local equilibrium hypothesis it is evident that the dominant collisions are with particles of size comparable to v_1. Alternatively, as shown in Figure 2-13, the major volume flux through the size distribution is due to the interaction $v_1 + v_j = v_{j+1}$ for all j. Hence, though the solution is self-similar with the similarity parameter $(F_v/\beta_o)^{i/2}$, the physical justification for the volume

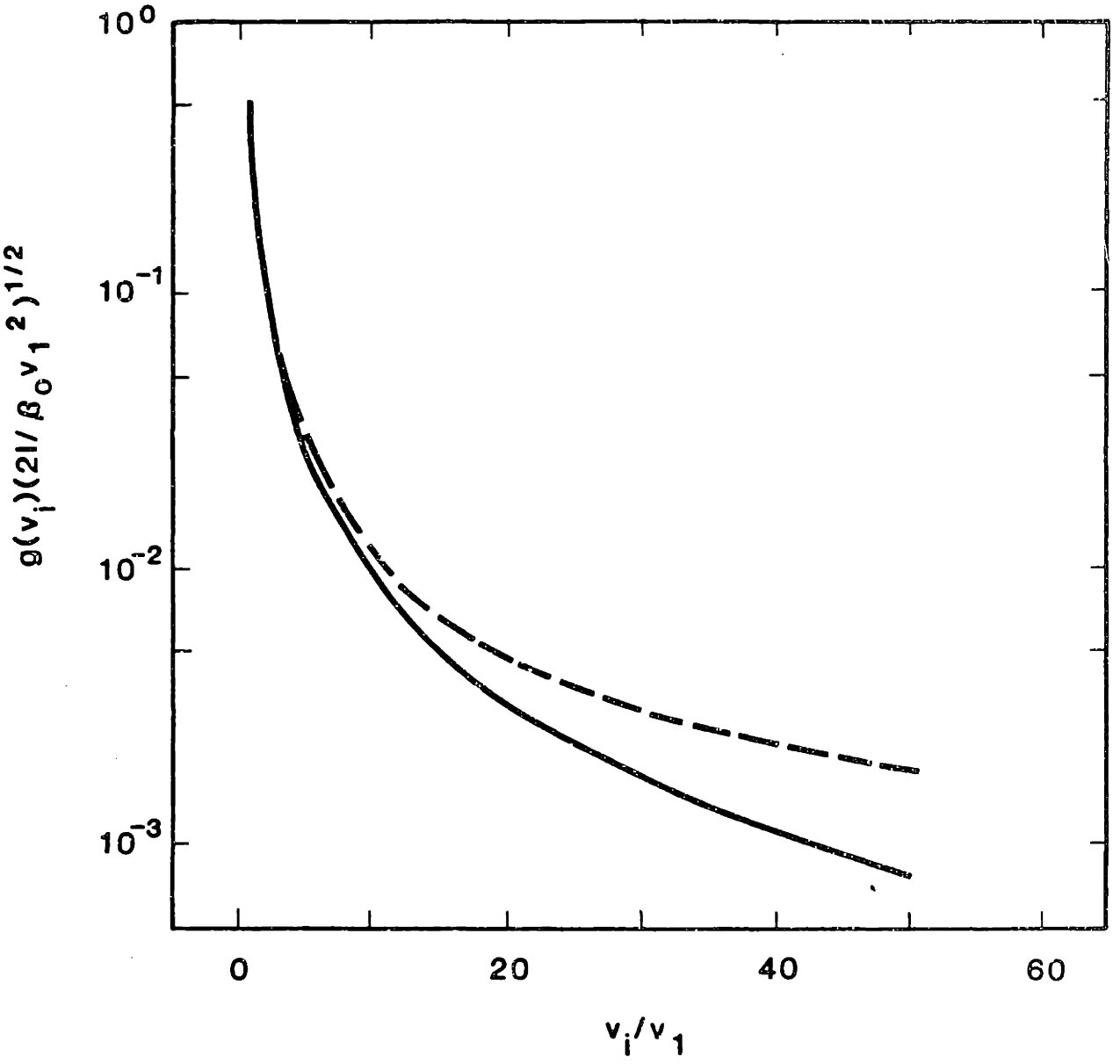

Figure 2-11 Comparison of the numerical solution for $\beta = \beta_o$ and $\beta = 8kTf_1/3\mu$ with the exact solution for $\beta = \beta_o$ ($\beta_o = 8kT/3\mu = 10^{-21}$ cm^3/sec, $v_1 = 56$ μm^3, M = 50, I = 1.7 $\times 10^{17}$/cm^3-sec; solid line, exact solution; dashed line, numerical solution).

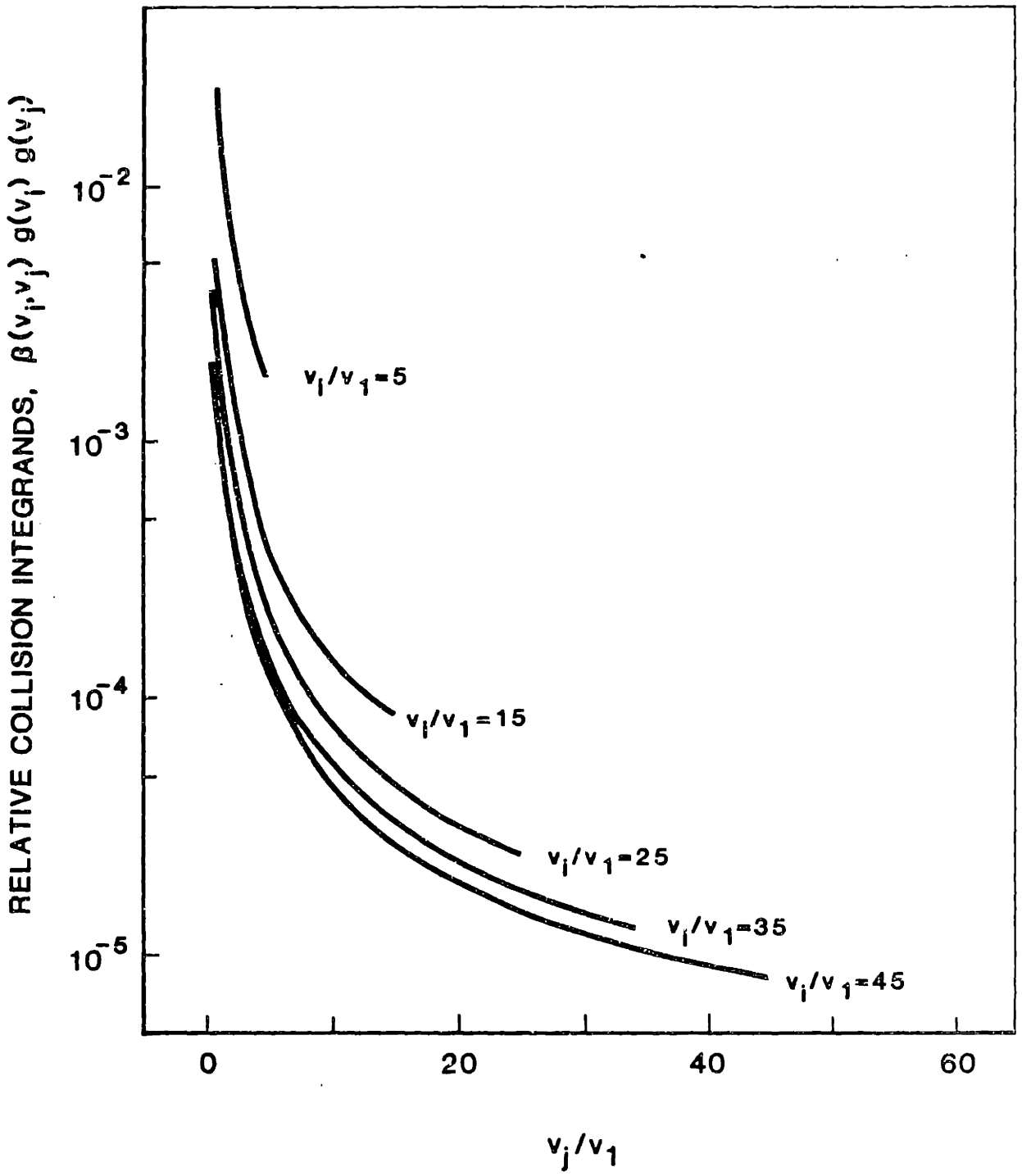

Figure 2-12 Relative contributions of individual collisions to the total number of collisions. Values correspond to the numerical solution in Figure 2-11

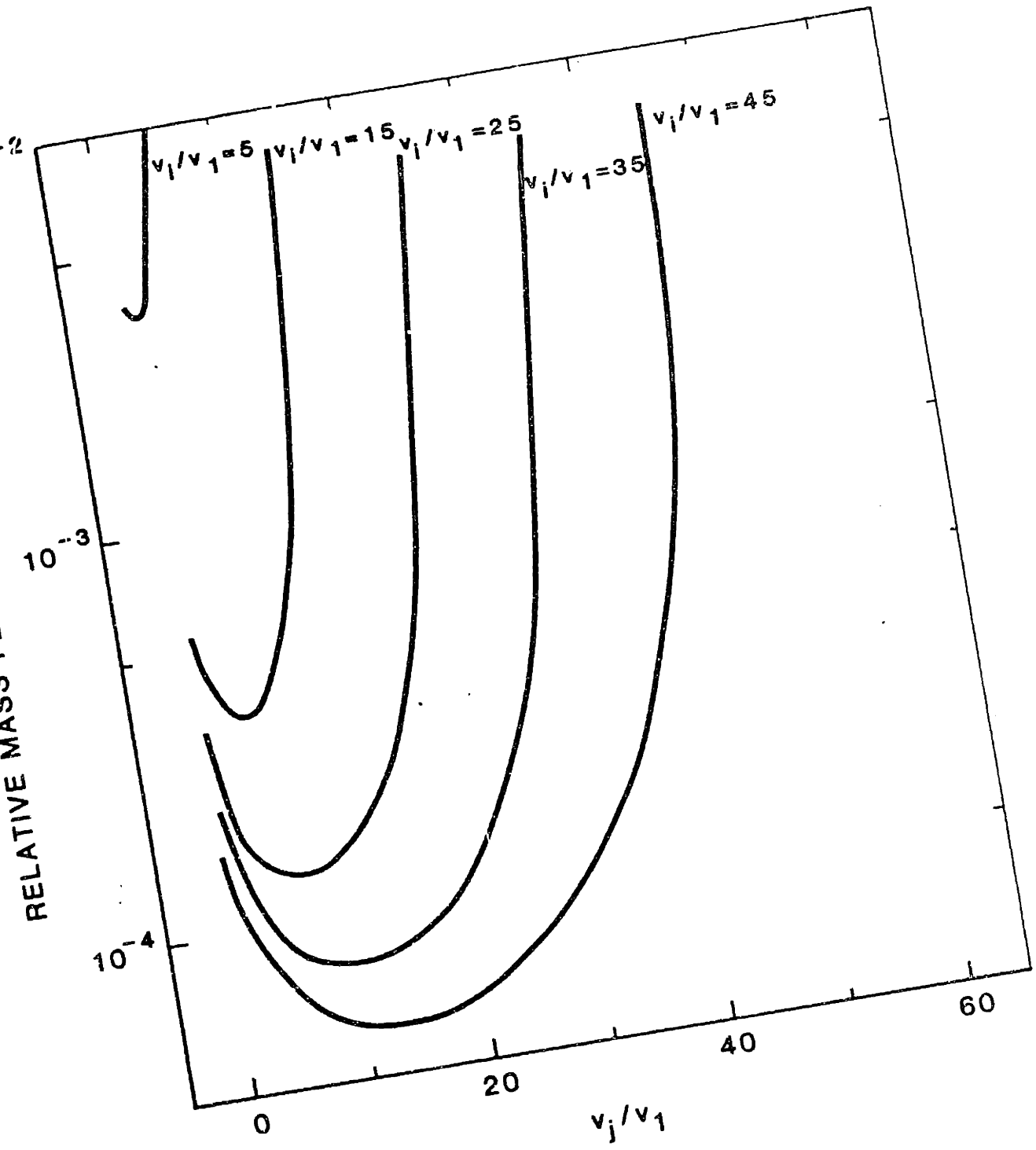

Figure 2-13 Relative contributions to the mass flow from individual collisions. Values correspond to the numerical solution in Figure 2-11

flux F_v appearing in the solution is not local equilibrium. The consistency between Eq. 2-55 and 2-56 is simply a dimensional accident.

From Figure 2-14 it is evident that the function $f_2(v_i/v_j)$ is well approximated by the function $(v_i/v_j)^{1/2}$. This is fortunate because the stationary size distribution for coagulation due to shear alone can then be approximated by Klett's solution for b = 1/2 if we let $\beta_o = 2.5\ G\ v_1$. Figure 2-15 is a comparison of the two solutions. For this case as well, though the solution scales with the volume flux, the size distribution is not in local equilibrium, as illustrated in Figure 2-16.

The equivalence between the stationary solutions for coagulation due to Brownian motion and shear with Klett's solutions for b = 0 and b = 1/2, respectively, helps to explain the results obtained by Hunt (1980, 1982) and Pearson et al. (1984). As previously explained, for differential settling acting alone, however, no stationary solution is possible if only unit-sized particles are introduced into the distribution. Even if we ignore this difficulty and accept the result $g(v) \sim v^{-13/6}$ derived by Hunt, using the simple test of comparing $\beta(v_i,v_j)g(v_i)g(v_j)$ with $\beta(v_j,v_j)g^2(v_j)$ for $i \ll j$ we can conclude that local equilibrium is not in effect for this mechanism acting alone either.

Summarizing, what we have shown in this section is that when steady state coagulation is established by introducing unit-sized particles at a constant rate into a homogeneous population and removing them when they have exceeded a preset size, if there is one and only one mechanism causing collisions, then the coagulation process will not be dominated

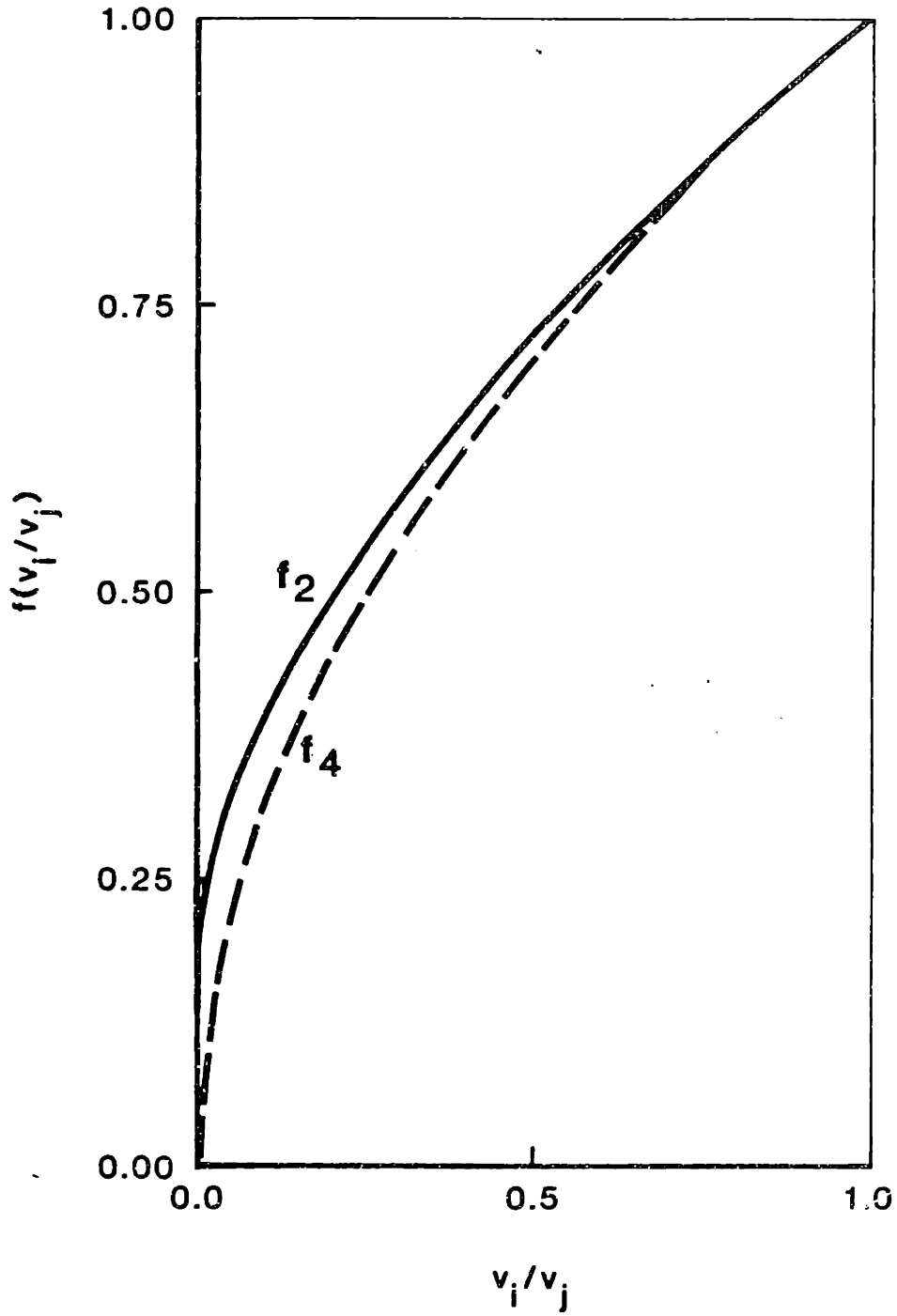

Figure 2-14 Comparison of the function $f_2(v_i/v_j)$ with the function $f_4(v_i/v_j) = (v_i/v_j)^{1/2}$.

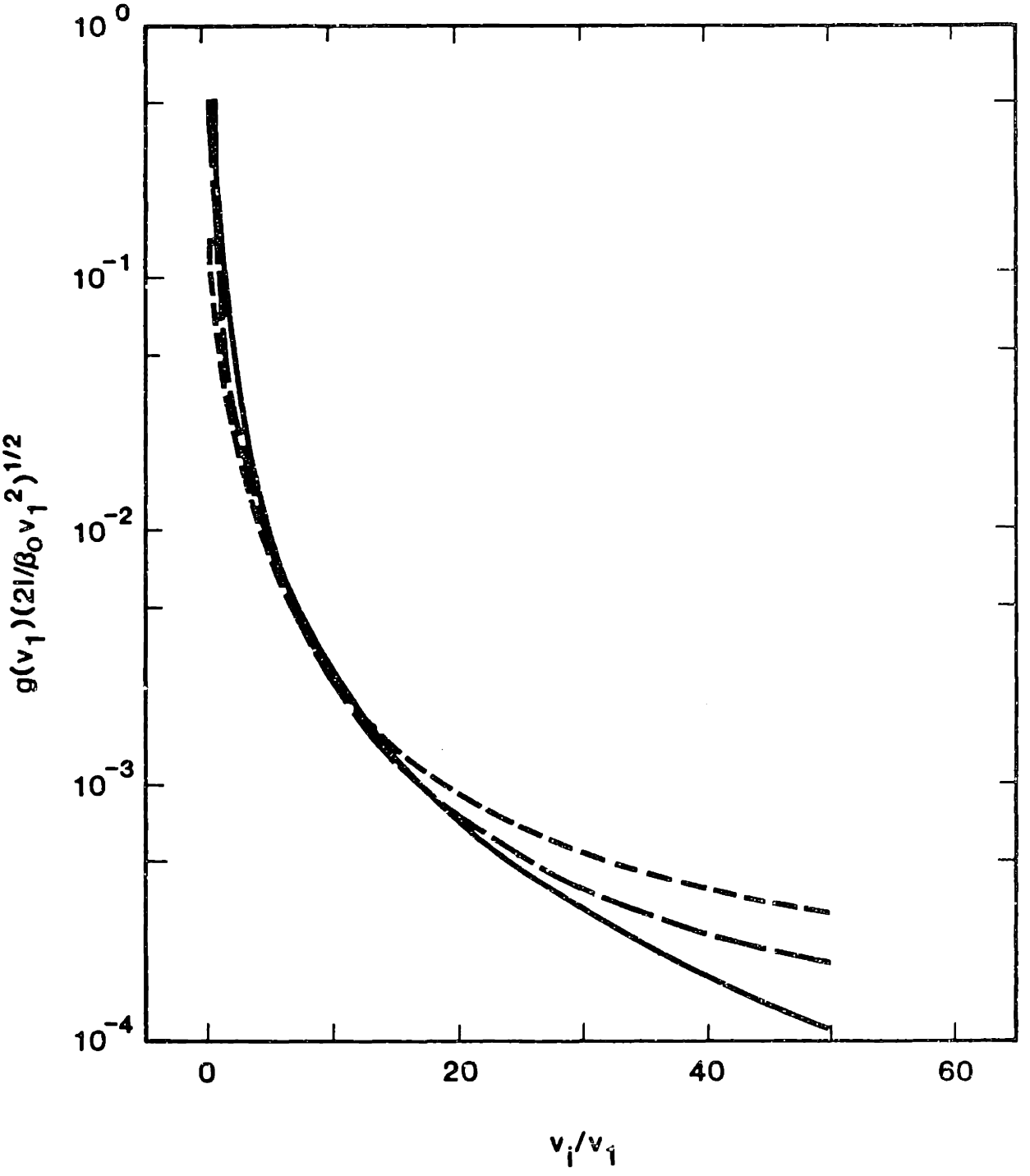

Figure 2-15 Comparison of solutions; solid line, exact solution for $\beta = \beta_o f_4(v_i/v_j)$; long-dashed line, numerical solution for $\beta = \beta_o f_2(v_i/v_j)$; short-dashed line,numerical solution for $\beta = \beta_o f_4(v_i/v_j)$ (β_o = 2.5 Gv_1 = 140 cm_3/sec, v_1 = 56 μm_3, M = 50, I = 0.24/cm^3-sec).

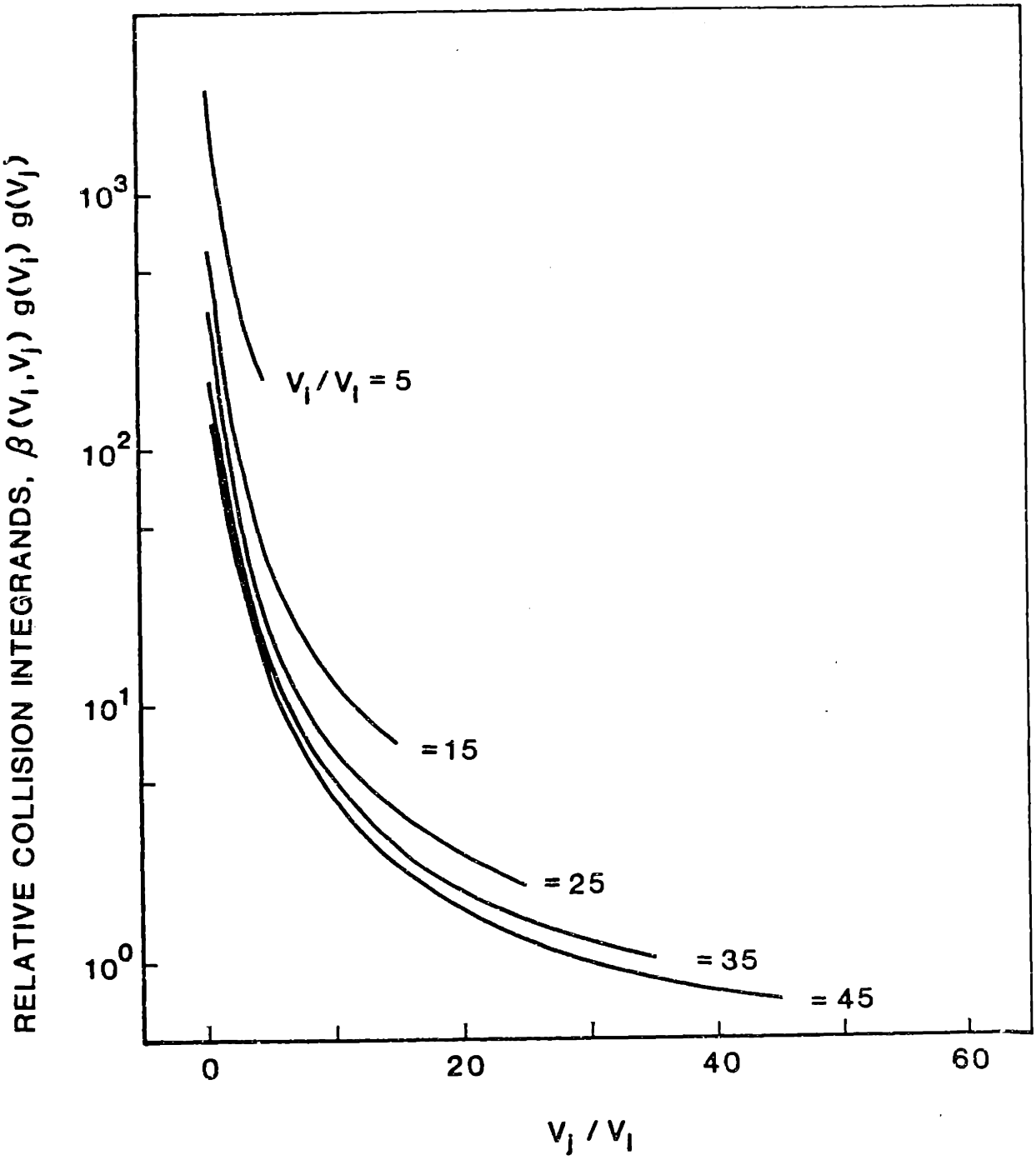

Figure 2-16 Relative contributions of individual collisions to the total number of collisions. Values correspond to the numerical solution for $\beta = \beta_o f_2(v_i/v_j)$ in Figure 2-14.

by coagulation of particles comparable in size. The particle interactions that will dominate the volume flux are those of any size particle with the smallest, unit-sized particles. The obvious question now is what happens when there is more than one collision mechanism acting simultaneously? This topic will be addressed in the following section.

2.5.2 Coagulation Due to Combined Mechanisms

It was noted in the previous section that under steady state conditions when there is a single mechanism inducing coagulation, particles of any given size tend to coagulate most often with the smallest particles in the system. It would be interesting to determine whether this still holds for the case where all three mechanisms act simultaneously. In simulating coagulation due to combined mechanisms it is normally assumed that, since each of the mechanisms acts independently, the net coagulation kernel is given by the sum of the component kernels for each mechanism, each component representing the product of a collision frequency function and a collision efficiency function for that mechanism. In all the simulations presented so far the collision efficiency has been arbitrarily set equal to one. It would also be interesting to determine what effect the collision efficiency functions presented in Section 2.2.2 have on the resulting size distributions.

In the simulations to be presented subsequently the particle size range is 0.1 μm to 100 μm in radius. The particles are assigned a specific gravity of 1.1. The Brownian diffusivity parameter $2kT/3\mu$ is set at 2.5×10^{-12} cm^3/sec, corresponding to a water temperature of

T = 15°C. For the simulations performed in previous sections integral size classes were used since the particle size range spanned only two orders of magnitude in volume. To accommodate the nine orders of magnitude in particle volume to be considered here we must resort to logarithmic size classes. Accordingly, the size range is subdivided into 28 size classes, each class representing a nominal volume larger than the previous one by a factor of $v_i/v_{i-1} = 10^{1/3}$. The total mass of particles in the system will be maintained at approximately 100 mg/l in all cases. The simulations will be presented in pairs, with one result corresponding to a case where the collision efficiency functions are all equal to one and the other result corresponding to a case where the size-dependent collision efficiency functions presented in Section 2.2.2 have been employed.

In the first pair of simulations the mean energy dissipation rate has been set at 10^{-2} cm^2/sec^3. For simplicity Saffman and Turner's (1956) model for the collision frequency function due to turbulent shear has been employed. The parameter $\rho_f \varepsilon^{1/2}/|\rho_p - \rho_f|$ is thus equal to 1 $cm/sec^{3/2}$, so we should expect to have a turbulent shear subrange. For graphical convenience Figure 2-17 is a plot of the mass density distribution, h(log v) rather than the number density distribution. In terms of the mass density distribution, the slopes predicted by Hunt's theory are 1/2 for Brownian motion, 0 for turbulent shear, and -1/6 for differential sedimentation. We see from Figure 2-17 that there is quite a large difference between the two solutions. Both solutions have an identifiable Brownian motion subrange. It is difficult to identify a turbulent shear subrange in either solution, although it seems to be apparent in the one in which size-dependent

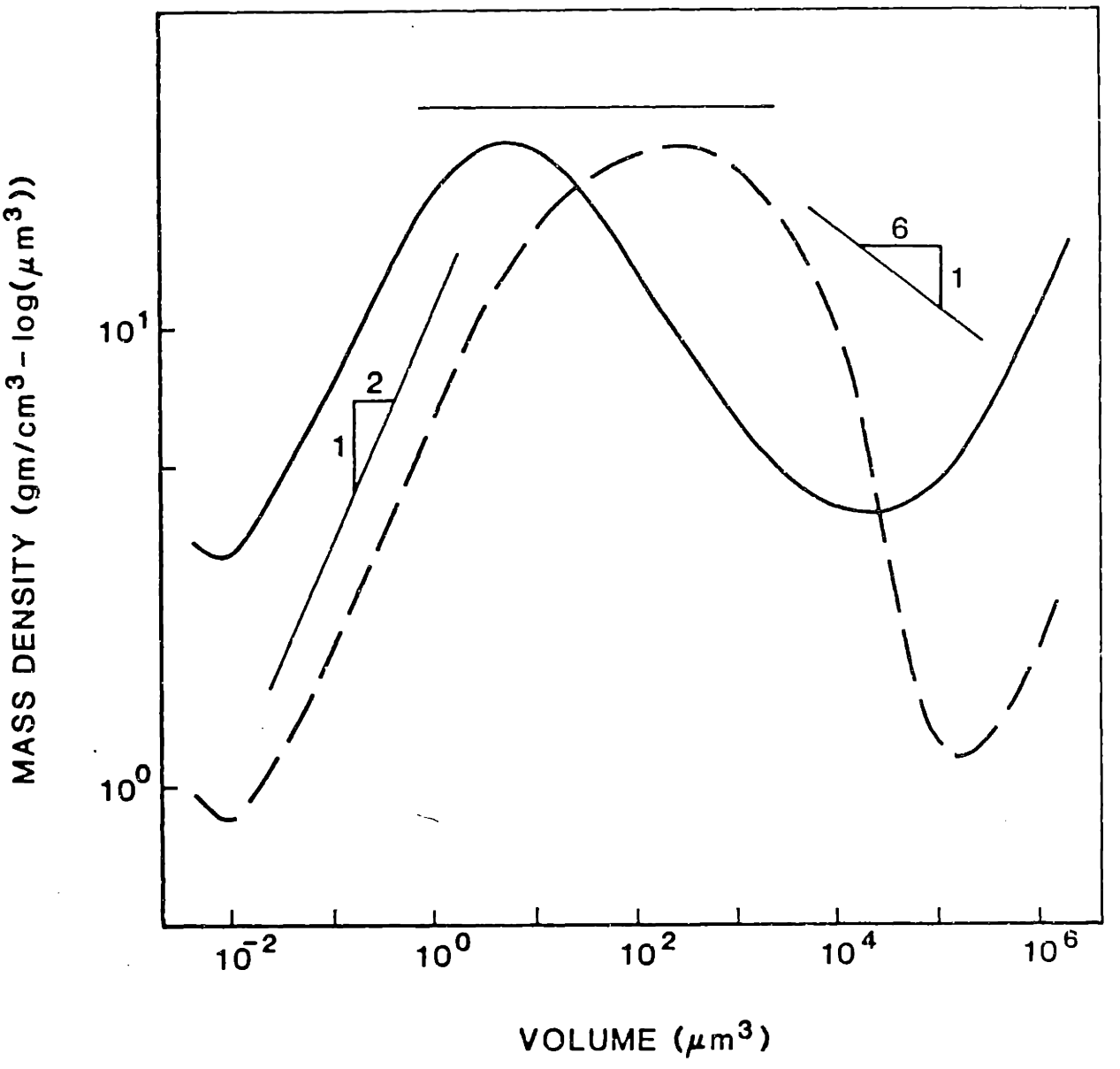

Figure 2-17 Steady state coagulation due to combined mechanisms (r_1 = 0.1 μm, r_M = 100 μm, 28 logarithmic size classes with $v_i/v_{i-1} = 10^{1/3}$, $(\rho_p-\rho_f)/\rho_f$ = 0.1, $2\kappa T/3\mu$ = 2.5×10^{-12} cm ^{3}/sec, $\varepsilon = 10^{-2}$ cm^2/sec^3; solid line, solution with collision efficiency set equal to one; dashed line, solution with collision efficiencies from Section 2.2.2, A/kT = 1, H = 10^{-2}).

collision efficiencies were included. Neither solution comes close to having a -1/6 slope differential sedimentation subrange. The trend of increasing mass density with particle size at the largest particle sizes is real insofar as the conditions simulated here are artificial. Presumably if we included the process of sedimentation through physical space in the simulation the mass density would continue to decrease with increasing particle size since this mass removal mechanism is most efficient at large particle sizes.

To see if a turbulent shear subrange could be generated a second pair of simulations was performed in which the energy dissipation rate was increased by two orders of magnitude to 1 cm^2/sec^3. The results are presented in Figure 2-18. We see that we now have an identifiable shear subrange in the solution in which collision efficiencies were included, but no such subrange is apparent in the other solution. If we are willing to say that the large particle region of the distribution is the differential sedimentation subrange, a comparison of the solutions in Figures 2-17 and 2-18 indicates that it does not have a unique slope.

Hunt (1982) presented data that indicated that the slopes of the mass density distributions should be about 0.5 for the Brownian motion subrange, -0.4 to 0.3 for the turbulent shear subrange, and -0.65 to -1.6 for the differential sedimentation subrange. Adopting an average value of -1.1 for the differential sedimentation subrange it is apparent that the solution with size-dependent collision efficiencies does a much better job of reproducing the data. This is viewed as an indication that collision efficiencies contribute strongly not only to the overall rate of coagulation but also to the form of the size distribution and

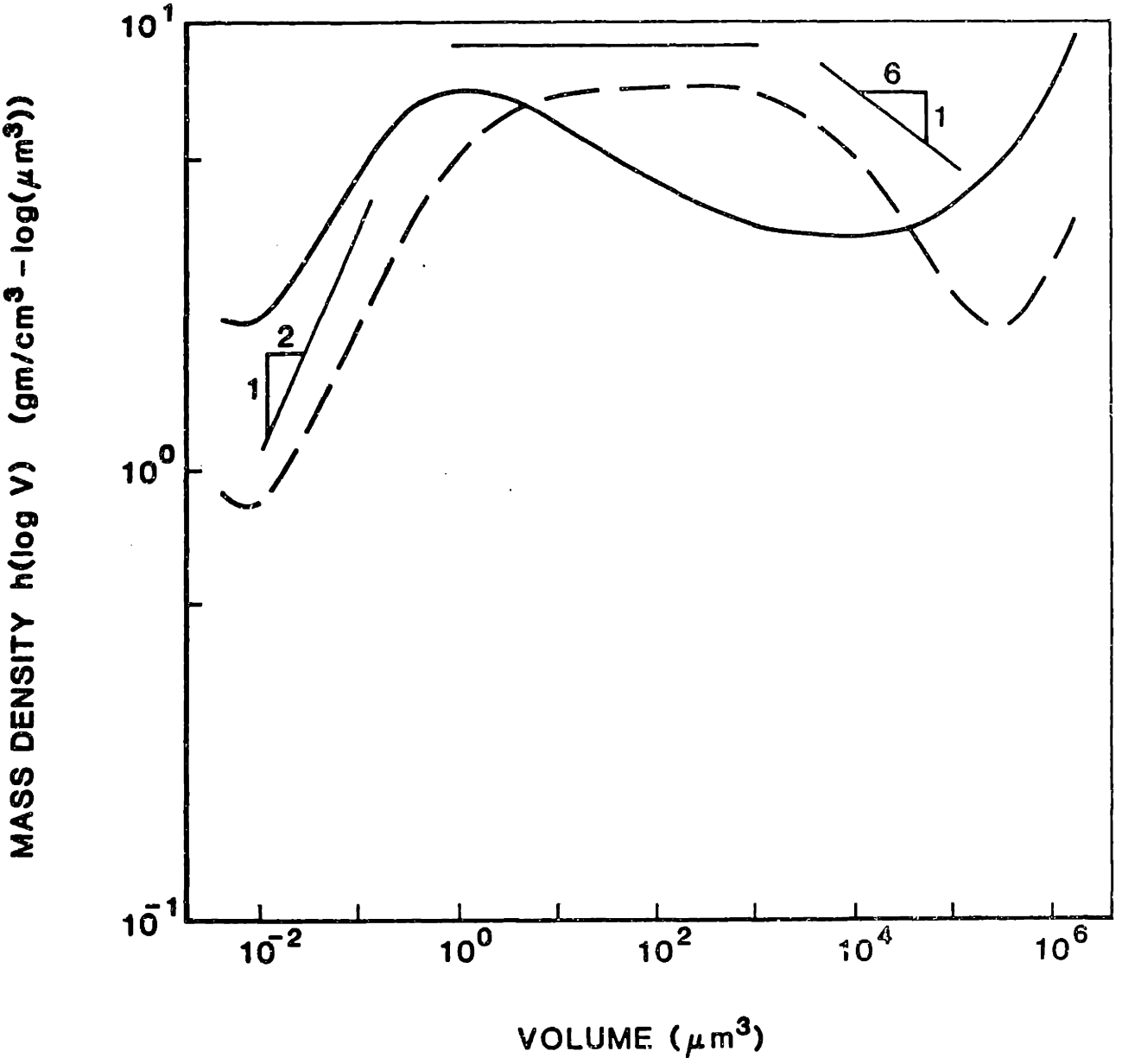

Figure 2-18 Steady state coagulation due to combined mechanisms (same conditions as in Figure 2-17 except ε = 1 cm^2/sec^3).

thus should always be employed in simulations of the coagulation process.

To determine which interactions contribute most to the number flux through the size distribution, Figures 2-19 and 2-20 are plots of the relative magnitudes of the integrands $\beta(v_i,v_j)\ E(v_i,v_j)\ \phi(v_i)\ \phi(v_j)$ for the solutions presented in Figure 2-18. Although the inclusion of size-dependent collision efficiency functions affects the overall distribution of the integrands in (v_i,v_j) space, for both cases, it appears that the dominant collisions contributing to the number flux into or out of any given size class are due to collisions with the smallest particles in the system. Figures 2-21 and 2-22 indicate that the dominant contribution to the mass flux through any size class v_i is due to collisions of particles of size comparable to v_i with the smallest particles in the system. Thus in no way is local equilibrium of particle collisions ever the rule. Farley (1984) has found that the same holds true for particle collisions in unsteady coagulation as well. The similarity of the observational data with the solutions in which size-dependent collision efficiencies were included appears to be due to the complicated distribution of the coagulation integrands in (v_i,v_j) space.

As a final note we wish to present typical coagulation time scales, as indicated by the numerical simulations. For the simulations presented in Figure 2-18 the time scales, defined by Eq. 2-54 ranged from 2×10^5 sec to 7×10^3 sec, with the smallest time scales corresponding to the equations for the largest particles. Thus, at a mass concentration of 100 mg/l the coagulation process for some size classes may be fast enough to interact nonlinearly with the turbulence.

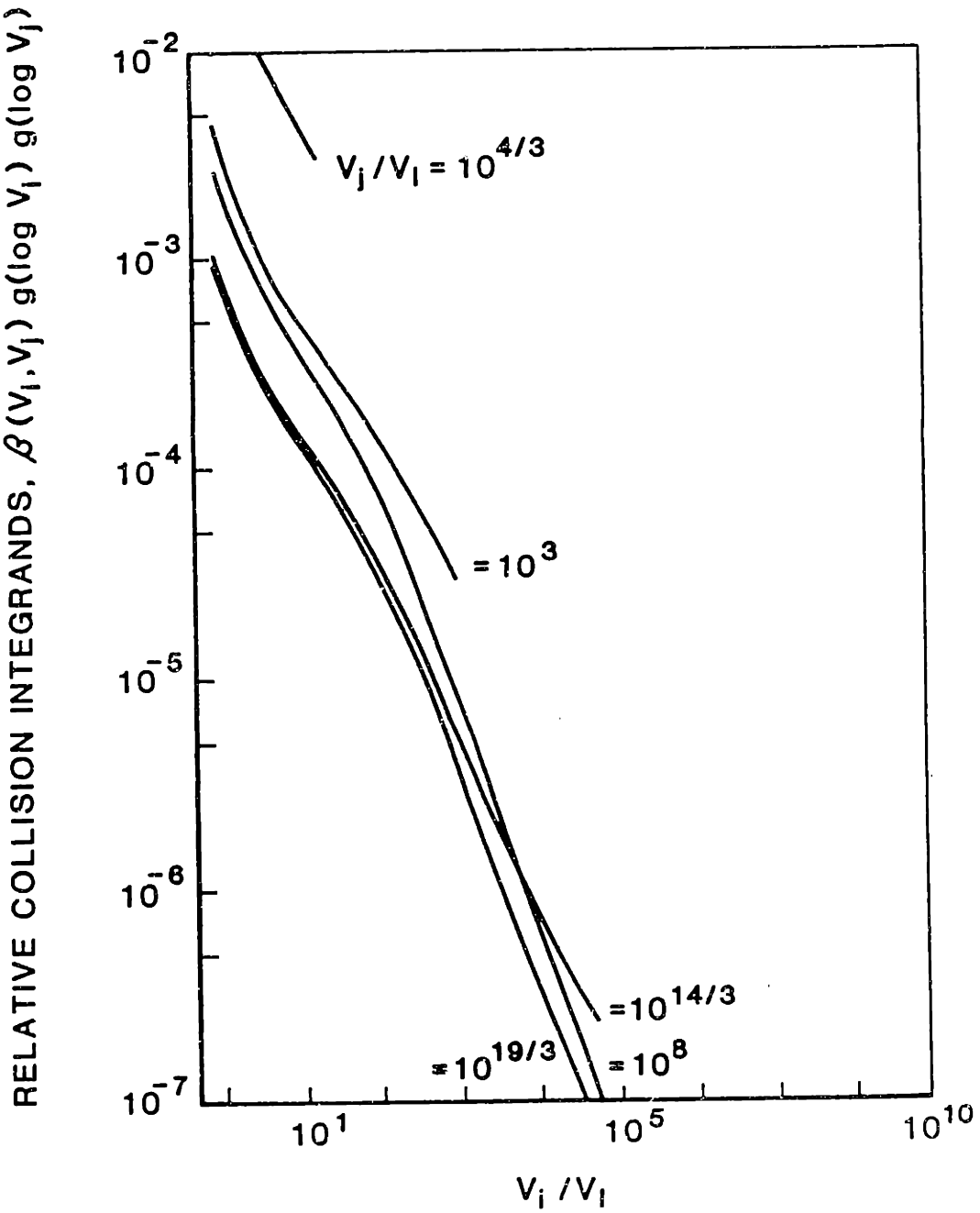

Figure 2-19 Relative contributions of individual collisions to the total number of collisions. Values correspond to the solution with collision efficiencies set equal to one in Figure 2-17.

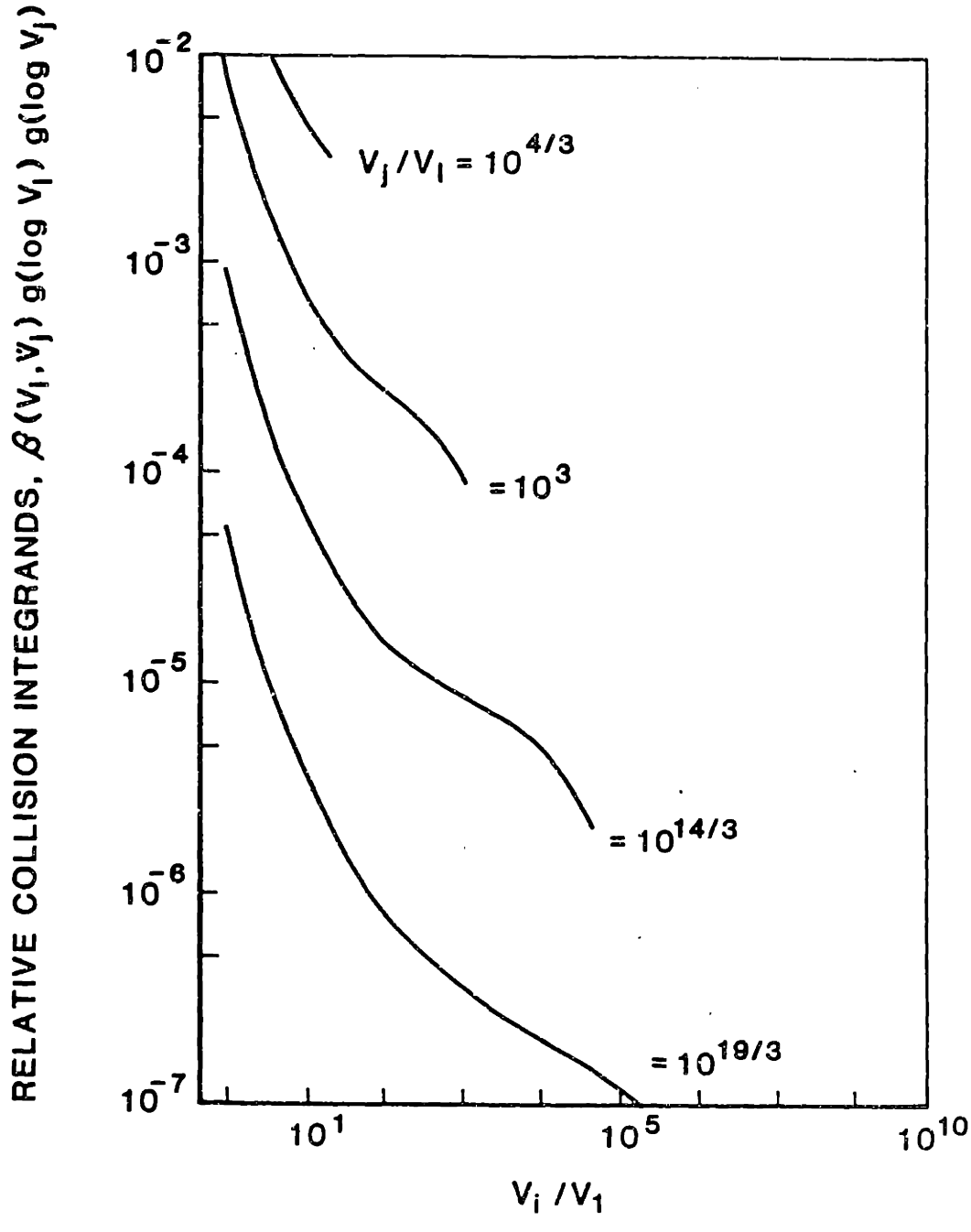

Figure 2-20 Relative contributions of individual collisions to the total number of collisions. Values correspond to the solution with collision efficiencies from Section 2.2.2 in Figure 2-17.

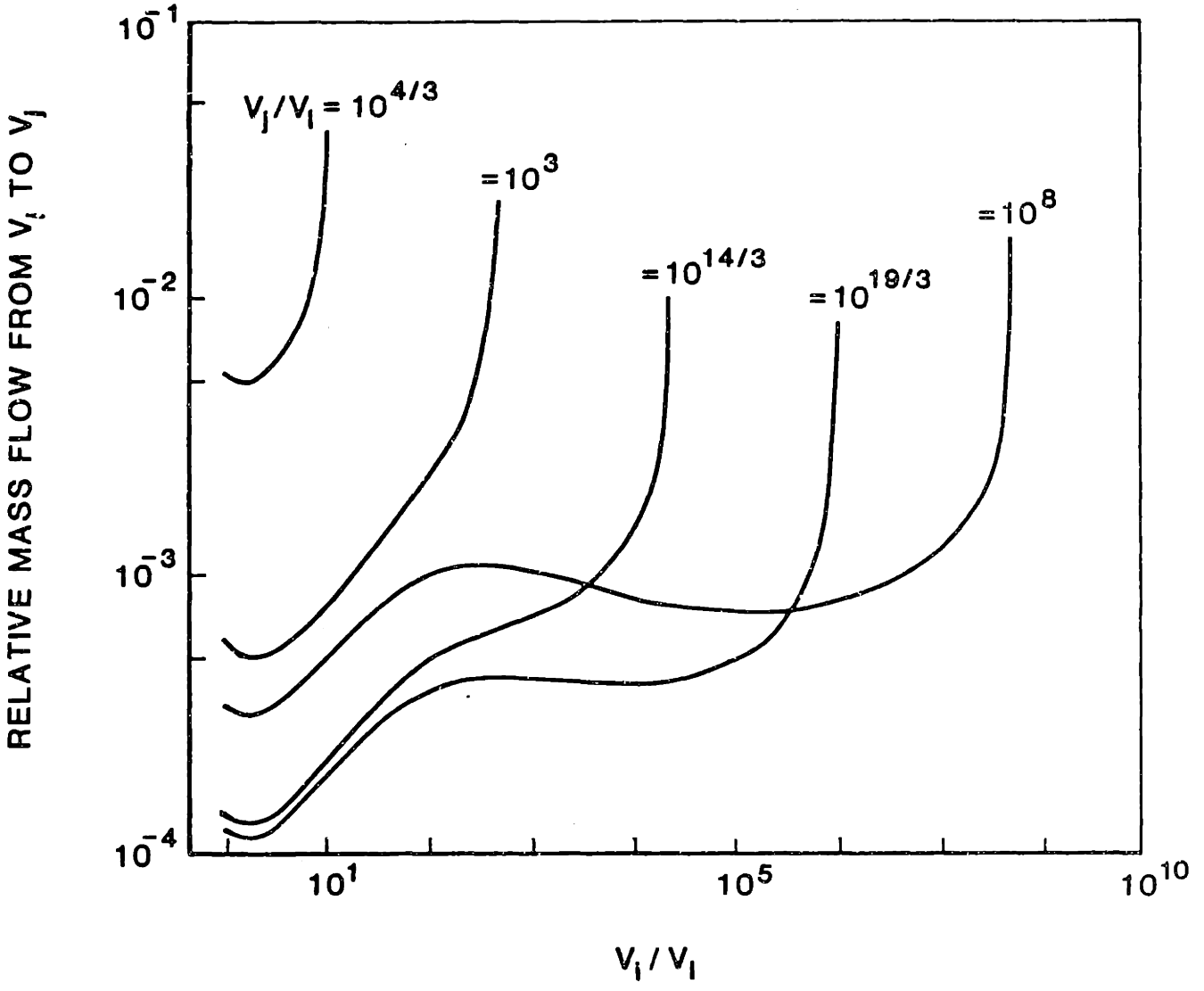

Figure 2-21 Relative contributions to the total mass flow from individual collisions. Values correspond to the solution with collision efficiencies set equal to one in Figure 2-18.

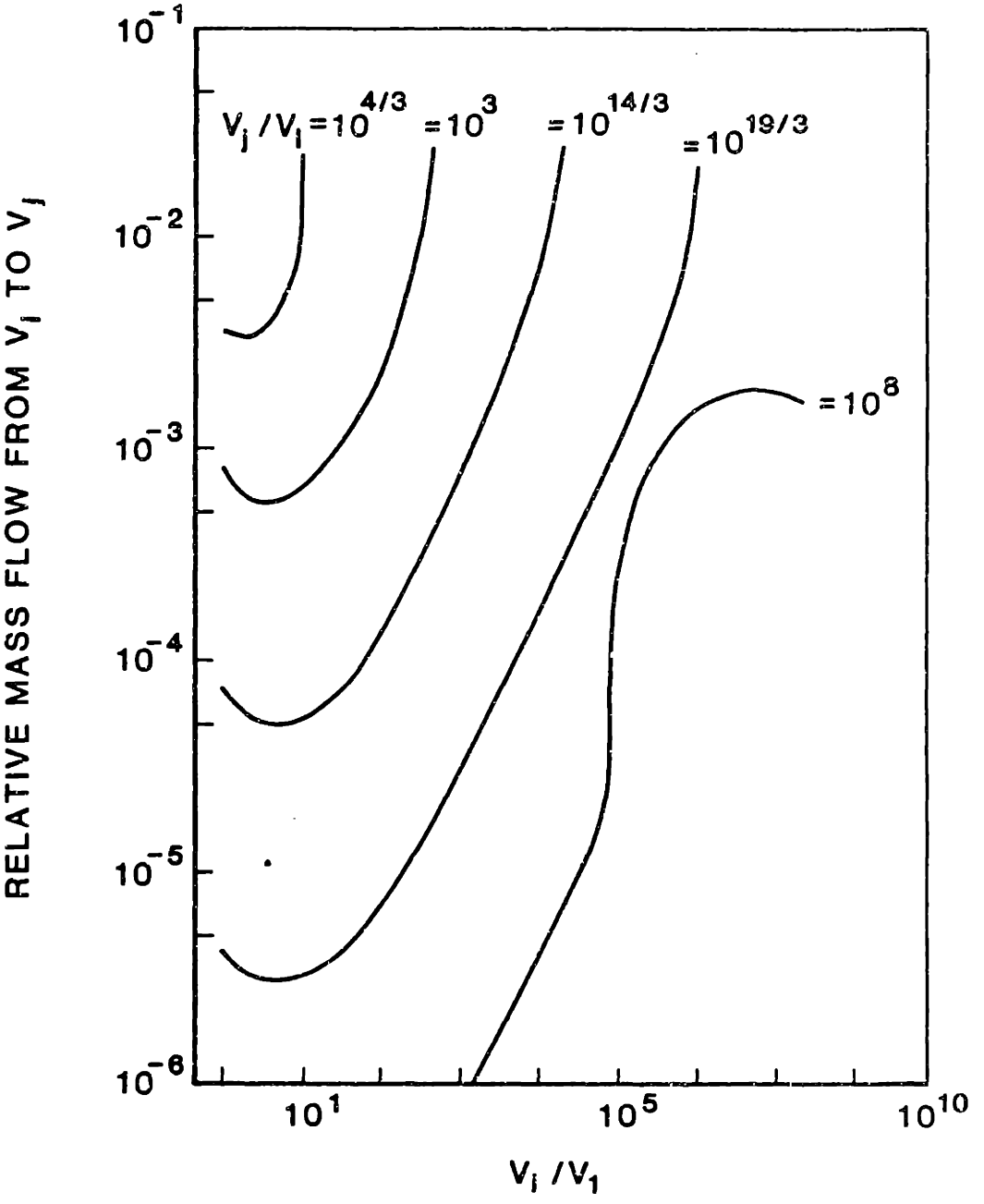

Figure 2-22 Relative contributions to the total mass flow from individual collisions. Values correspond to the solution with collision efficiencies from Section 2.2.2 in Figure 2-18.

For every order of magnitude increase in the number concentration, the time scales are reduced by one order of magnitude. As indicated in Section 1.3, typical particle mass concentrations range from 0.1 mg/l to 50,000 mg/l in the aquatic environment. For concentrations of order 10 mg/l or less the influence of turbulence on the coagulation process may be neglected. For concentrations as high as 50,000 mg/l the coagulation time scales will be of order 1 sec, so that nonlinear coupling with turbulent mixing may be anticipated.

III. MONTE CARLO TECHNIQUE FOR MODELING REACTIVE TRANSPORT IN THE AQUATIC ENVIRONMENT

In developing a numerical model for computing the transport and reaction of solid and dissolved constituents in the aquatic environment, one must be concerned with a number of issues that will limit the generality of any approach that is employed. In particular, the modeling of interactions between solid and dissolved constituents requires, at the very least, having to deal with a large number of constituents and a large number of physical and chemical processes. Associated with the various physicochemical processes will be a wide range of space and time scales that must be considered. Finally, the relative time scales between physical transport processes and reaction processes may be such that nonlinear coupling exists and must be properly accounted for.

In this chapter a novel technique for computing reactive transport will be introduced that at least partially overcomes all the limitations addressed above. The conceptual basis for the modeling approach will be presented first, followed by demonstrations of the accuracy and flexibility of the model algorithms in simulating various physical and chemical processes. Finally, the computational efficiency of the model will be assessed.

3.1 Conceptual Basis

The general problem that we wish to solve has already been outlined in Chapter I, where it was indicated that modeling the reactive

transport of solid species poses special problems, both from a theoretical and a computational point of view. If the aquatic system that we wish to model contains no particles, so that no differential settling occurs, and all the reactions are either slow with respect to the turbulent mixing or sufficiently fast and reversible, so that local chemical equilibrium may be invoked, then we can uncouple the reaction process from the physical transport processes. Since all dissolved constituents will be transported at the same rate everywhere then only one transport equation needs to be solved. The solution procedure in this case is one of iteration between the solution of the single differential transport equation and the solution of the coupled mass action or kinetic equations.

When we introduce particles into the system, however, the situation becomes considerably more complicated. Since particles settle differentially, we need to solve a separate transport equation for each particle size class considered. If we are studying the coagulation process, for example, then the transport equations will be coupled through the reaction term and, for the sake of accuracy and resolution, it will be desirable to include something on the order of 10 particle size classes. The use of an implicit finite difference formulation for such a problem would be prohibitive since the computational cost would increase exponentially as the number of equations to be solved. Indeed, we would probably be forced to use an explicit time-stepping scheme with a first-order upwind difference operator for the advection term thus limiting the scheme to first-order accuracy in both space and time. In addition, to efficiently compute the contribution of reaction to the local time rate of change, a fractional time-step or operator-splitting technique (Yanenko, 1971) would have to be employed.

The situation becomes further complicated when we attempt to allow for fast, irreversible reactions which are typically nonlinear. As indicated in Section 1.2, if we want to model the term $\langle S^{(\alpha)}(\underset{\sim}{\phi})\rangle$ then we have to somehow model the correlations $\langle \phi_1^{a_1} \phi_2^{a_2} \ldots \phi_\sigma^{a_\sigma} \rangle$.

It has been recognized by researchers who model combustion processes, where the reactions are highly nonlinear, very fast and irreversible (Dopazo, 1975; Janicka, Kolbe and Kollmann, 1979; Pope, 1976) that the most general solution to this dilemma is to attempt to model the transport equation for the one-point, joint scalar probability density function (pdf). Given a set of scalar properties that specify the reacting field, the joint pdf $p(\underset{\sim}{\psi}; \underset{\sim}{x}, t)$ provides a complete statistical description of the scalar fluctuations at any point in space $\underset{\sim}{x}$ and time t.

Following O'Brien (1980) the joint pdf transport equation may be derived as follows. Each joint realization of the random scalar field is represented mathematically as

$$p'(\underset{\sim}{\psi}; \underset{\sim}{x}, t) = \prod_{\alpha=1}^{\sigma} \delta(\phi_\alpha(\underset{\sim}{x}, t) - \psi_\alpha) \tag{3-1}$$

where $\delta(x)$ is the Dirac delta function. Hence, for each possible set of scalar values ψ_α at the point $\underset{\sim}{x}$ and time t, p' takes on the value one if each actual scalar value $\phi_\alpha(\underset{\sim}{x}, t)$ equals the corresponding ψ_α and zero if one or more of the $\phi_\alpha(\underset{\sim}{x}, t)$ do not equal ψ_α. In this manner the joint pdf is identical to the ensemble average of p',

$$p(\underset{\sim}{\psi}; \underset{\sim}{x}, t) = \langle p'(\underset{\sim}{\psi}; \underset{\sim}{x}, t)\rangle \tag{3-2}$$

Now,

$$\frac{\partial p'}{\partial t} = \sum_{\alpha=1}^{\sigma} \frac{\partial \delta}{\partial \phi_\alpha} \frac{\partial \phi_\alpha}{\partial t} \left[\prod_{\substack{\gamma=1 \\ \gamma \neq \alpha}}^{\sigma} \delta(\phi_\gamma(\underset{\sim}{x}, t) - \psi_\gamma) \right] \tag{3-3}$$

Setting $\tau_\alpha = \phi_\alpha(\underset{\sim}{x}, t) - \psi_\alpha$ we have

$$\frac{\partial \delta}{\partial \phi_\alpha} = \frac{\partial \delta}{\partial \tau_\alpha} \frac{\partial \tau_\alpha}{\partial \phi_\alpha} = \frac{\partial \delta}{\partial \tau_\alpha} = - \frac{\partial \delta}{\partial \tau_\alpha} \frac{\partial \tau_\alpha}{\partial \psi_\alpha} = - \frac{\partial \delta}{\partial \psi_\alpha} \tag{3-4}$$

so that

$$\frac{\partial p'}{\partial t} = - \sum_{\alpha=1}^{\sigma} \frac{\partial \delta}{\partial \psi_\alpha} \frac{\partial \phi_\alpha}{\partial t} \left[\prod_{\substack{\gamma=1 \\ \gamma \neq \alpha}}^{\sigma} \delta(\phi_\gamma(\underset{\sim}{x}, t) - \psi_\gamma) \right] = - \frac{\partial \phi_\alpha}{\partial t} \frac{\partial p'}{\partial \psi_\alpha} \tag{3-5}$$

where we now use the convention of summation over repeated indices. Similarly, it can be shown that

$$\frac{\partial p'}{\partial x_i} = - \frac{\partial \phi_\alpha}{\partial x_i} \frac{\partial p'}{\partial \psi_\alpha} \tag{3-6}$$

Substituting

$$\frac{\partial \phi_\alpha}{\partial t} = - U_i \frac{\partial \phi_\alpha}{\partial x_i} - w_s^{(\alpha)} \frac{\partial \phi_\alpha}{\partial x_i} \delta_{i3} + D \frac{\partial^2 \phi_\alpha}{\partial x_i \partial x_i} + S^{(\alpha)}(\underset{\sim}{\phi}) \tag{3-7}$$

into Eq. 3-5, adding Eqs. 3-5 and 3-6 multiplied by U_i together, and ensemble averaging the result, we obtain the transport equation for the

one-point, joint scalar pdf,

$$\frac{\partial p}{\partial t} = -\frac{\partial}{\partial x_i}\left(\langle U_i\rangle p + \langle u_i' p'\rangle\right) + \langle\frac{\partial p'}{\partial \psi_\alpha} w_s^{(\alpha)} \frac{\partial \phi_\alpha}{\partial x_i} \delta_{i3}\rangle$$

$$+ \langle\frac{\partial p'}{\partial \psi_\alpha} D \frac{\partial^2 \phi_\alpha}{\partial x_i \partial x_i}\rangle - \frac{\partial}{\partial \psi_\alpha}(S^{(\alpha)} p) \qquad (3\text{-}8)$$

The first term on the right-hand side represents the change in $p(\underset{\sim}{\psi}; \underset{\sim}{x}, t)$ due to the physical transport processes of advection and turbulent diffusion. The second term accounts for differential settling. The third term represents the effect of molecular mixing and the final term is the source term, representing transport through scalar space by reaction processes. The attraction of working with this equation rather than the moment equation, Eq. 1-1 is that the source term appears in closed form, that is, it does not have to be modeled. However, the turbulent diffusion, differential sedimentation and molecular mixing terms do have to be modeled since they are represented as correlations with p'. If, as before, we model the turbulent transport of the pdf as a simple gradient diffusion process then

$$-\langle u_i' p'\rangle = \Gamma^{(i)} \frac{\partial p}{\partial x_i} \qquad (3\text{-}9)$$

where $\Gamma^{(i)}$ is the turbulent eddy diffusion coefficient. A model for the differential settling term is formulated in Section 3.3.4. Various models have been proposed for the molecular mixing term. These models will be reviewed in Section 3.4.

Pope (1981) has devised a very efficient Monte Carlo technique for solving the pdf transport equation, the computational expense of which

is generally determined by the cost of integrating the reaction term. For the solution of the coagulation equation, for example, the cost increases as the square of the number of particle size classes considered. As a result it is possible to compute the simultaneous reactive transport of a much larger number of constituents, as compared to a finite difference solution of the pdf equation.

The remainder of this chapter is devoted to presenting and assessing various numerical algorithms for solving the joint pdf transport equation.

3.2 Monte Carlo Formulation for Solution of the Joint PDF Equation

The Monte Carlo technique for solving the one-point joint scalar pdf transport equation was devised and proven to be a valid simulation technique by Pope (1981). For the sake of simplicity a rather heuristic approach will be adopted here in outlining the essentials of the technique.

As with all numerical techniques the spatial domain is first discretized into finite control volumes surrounding each nodal point of an orthogonal grid. The joint pdf (i.e. the independent variable) is represented at each node by an ensemble of N elements, each of which "contains" separate representative concentrations for each constituent α. Denoting the ensemble at any node and at any time by $E(\underset{\sim}{\phi}; \underset{\sim}{x}, t)$, any of the elements of the ensemble by $\underset{\sim}{\phi}^{(k)}$, and any of the representative concentrations of the ensemble by $\phi_\alpha^{(k)}$, we see that the joint pdf is represented at any node by an ensemble of N elements, or $N\sigma$ representative concentrations,

$$E(\underset{\sim}{\phi};\ \underset{\sim}{x}, t) = \begin{bmatrix} \underset{\sim}{\phi}^{(1)} \\ \underset{\sim}{\phi}^{(2)} \\ \vdots \\ \underset{\sim}{\phi}^{(N)} \end{bmatrix} \begin{bmatrix} \phi_1^{(1)} & \phi_2^{(1)} & \cdots & \phi_\sigma^{(1)} \\ \phi_1^{(2)} & \phi_2^{(2)} & \cdots & \phi_\sigma^{(2)} \\ \vdots & \vdots & & \vdots \\ \phi_1^{(N)} & \phi_2^{(N)} & \cdots & \phi_\sigma^{(N)} \end{bmatrix} \qquad (3\text{-}10)$$

If all the statistics of the ensemble $E(\underset{\sim}{\phi};\ \underset{\sim}{x}, t)$ equal the corresponding statistics of the joint pdf $p(\underset{\sim}{\phi};\ \underset{\sim}{x}, t)$ then the ensemble is equivalent to the joint pdf. The essence of the Monte Carlo technique is the manipulation in time of these elements in such a way as to simulate the corresponding evolution of the joint pdf.

An equivalent interpretation for the elements $\underset{\sim}{\phi}^{(k)}$ is that they represent approximately equal-sized, completely mixed lumps of fluid containing representative concentrations of each of the constituents α. As illustrated schematically in Figure 3-1 each finite control volume in the discretized spatial domain may then be considered as an incompletely mixed tank reactor. Advection causes each element to remain within the reactor an average length of time equal to the residence time V_i/Q_i, where V_i is the volume of the i^{th} control volume and Q_i is the flow rate through the control volume. The exchange of elements between adjacent reactors is representative of the turbulent diffusion process. The vertical migration of representative solid concentrations from elements in a given control volume to elements in the control volume below simulates the sedimentation process. The effect of mixing may be modeled by letting random pairs of elements coalesce at a given rate,

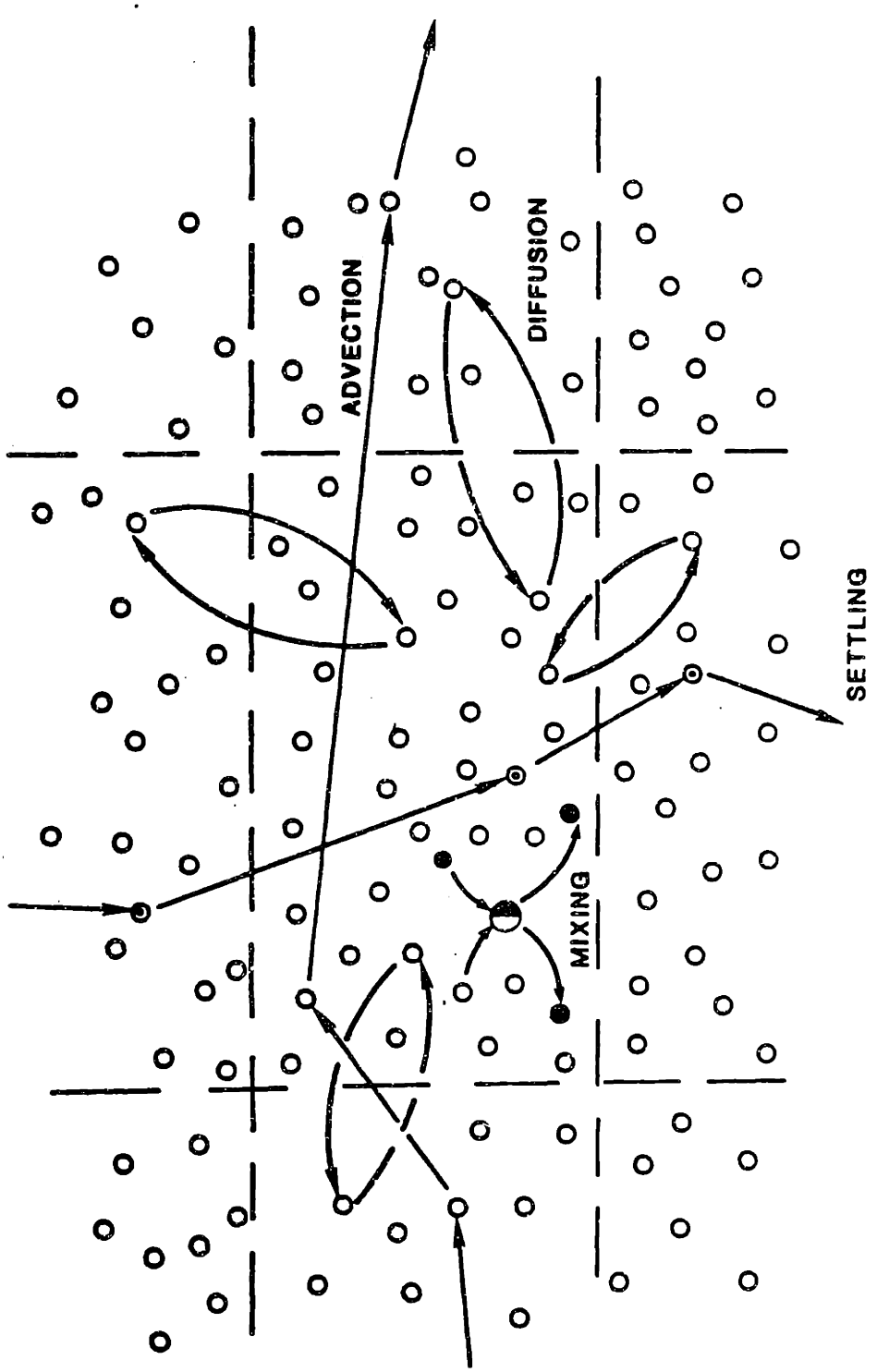

Figure 3-1 Simulation of the effect of various physical processes on the local ensemble of Monte Carlo elements.

average their representative concentrations and then redisperse instantaneously to form two elements. In the time between element coalescences, reaction may proceed independently within each element. Each of these processes is independent of the other and proceeds at a rate governed by its own time scale. To the extent that each element is completely mixed on a molecular scale the size of the elements may be assumed comparable to the Kolmogorov length scale, that is, of characteristic length scale 1 mm to 1 cm.

It is emphasized that within a control volume elements have no relative position. Since each control volume is assumed to be spatially uniform or, more properly, statistically homogeneous, the element set represents typical concentrations that one would obtain if one hypothetically took samples of volume $4\pi\eta^3/3$, where η is the Kolmogorov length scale, from random points throughout the assumed homogeneous control volume. In principle, the statistics of the representative concentrations are identical whether one samples from the entire control volume V_i or whether one confines oneself to sampling from some smaller volume ΔV where $4\pi\ell_I^3/3 < \Delta V < V_i$ and ℓ_I is the integral length scale of the turbulence. For this reason we should not concern ourselves with the misconception that we seem to be permitting elements to mix that are separated by a distance comparable to the width of the control volume. The representative concentrations that occupy the entire control volume are also the representative concentrations that occupy a volume of length scale ℓ_I surrounding any given element.

In short, we are not directly simulating the physical transport of fluid lumps through space. Rather we are simulating the effect that

each process has on the local scalar pdf by manipulating certain attributes of the statistical samples, or elements. The use of such notions as "lumps of fluid" that "move" through space and "contain" representative concentrations is an artificial device that aids in the conceptualization of the stochastic manipulations being applied.

This so-called element model has its origins in the coalescence-dispersal model of Curl (1963). Spielman and Levenspiel (1965) used the approach in a Monte Carlo simulation of coalescence and reaction of two-phase systems in backmix reactors. These authors pointed out that their dispersed phase model could be used to study mixing and reaction in homogeneous systems as well. Accordingly, Kattan and Adler (1967) and Flagan and Appleton (1974) used the stochastic mixing model to study combustion in homogeneous turbulence. Pope (1979) showed that the evolution of a reacting system described by the one-point joint scalar pdf transport equation is equivalent to that given by the element model formulation. The motivation for using the element model approach is that it is conceptually simpler and computationally less expensive than a finite difference or finite element formulation of the pdf transport equation, although the fundamental basis for the element model is not as well defined (Pope, 1979). We are thus forced to invoke the notion of "equivalence" to prove the validity of the element model formulation. We have already indicated that the ensemble of elements is equivalent to the joint pdf if all statistics of the ensemble are equal to the corresponding statistics of the pdf in the limit as the number of elements becomes infinite. Similarly, if a given operation on an ensemble of elements results in the same modification to its statistics as another operation applied to the equivalent joint pdf then the two operations will be said to be equivalent (Pope, 1981).

The evolution equation for the joint pdf may be written symbolically as a series of operators acting on $p(\underset{\sim}{\psi};\ \underset{\sim}{x},t)$,

$$\frac{\partial p}{\partial t} = \left[-\sum_{i=1}^{3} A^{(i)} + \sum_{j=1}^{3} D^{(j)} + W + M - S\right] p \qquad (3\text{-}11)$$

where $A^{(i)}$, $D^{(j)}$, W, M, S represent, respectively, advection, turbulent diffusion, differential settling, molecular mixing and reaction operators. If we approximate the time derivative with a forward-difference representation, then

$$p(\underset{\sim}{\psi};\ \underset{\sim}{x},t+\Delta t) = \left[1 + \Delta t \left(-\sum_{i=1}^{3} A^{(i)} + \sum_{j=1}^{3} D^{(j)} + W + M - S\right)\right] p(\psi;\ x,t) \qquad (3\text{-}12)$$

where Δt is the time increment. The joint pdf transport equation is a linear equation with variable coefficients. We may thus use the method of approximate factorization of operators (Yanenko, 1971) to rewrite Eq. 3-12 as

$$p(\underset{\sim}{\psi};\ \underset{\sim}{x},t+\Delta t) = \left[\prod_{i=1}^{3} (1-\Delta t\ A^{(i)}) \prod_{j=1}^{3} (1+\Delta t\ D^{(j)})(1+\Delta t W)\right.$$
$$\left.(1+\Delta t M)(1-\Delta t S)\right] p(\underset{\sim}{\psi};\ \underset{\sim}{x},t) + O(\Delta t)^2 \qquad (3\text{-}13)$$

which is equivalent to the sequence of operations

$$p(\underset{\sim}{\psi};\ \underset{\sim}{x}, t_i) = (1-\Delta t\ A^{(i)})\ p(\underset{\sim}{\psi};\ \underset{\sim}{x}, t_{i-1}) \qquad i = 1,2,3$$

$$p(\underset{\sim}{\psi};\ \underset{\sim}{x}, t_i) = (1+\Delta t\ D^{(j)})\ p(\underset{\sim}{\psi};\ \underset{\sim}{x}, t_{i-1}) \qquad \begin{matrix} i = 4,5,6 \\ j = i-3 \end{matrix}$$

$$p(\underset{\sim}{\psi};\ \underset{\sim}{x}, t_7) = (1+\Delta t\ W)\ p(\underset{\sim}{\psi};\ \underset{\sim}{x}, t_6)$$

$$p(\underset{\sim}{\psi};\ \underset{\sim}{x}, t_8) = (1+\Delta t\ M)\ p(\underset{\sim}{\psi};\ \underset{\sim}{x}, t_7)$$

$$p(\underset{\sim}{\psi};\ \underset{\sim}{x}, t_9 = t+\Delta t) = (1-\Delta t S)\ p(\underset{\sim}{\psi};\ \underset{\sim}{x}, t_8) \qquad (3\text{-}14)$$

The intermediate times $t_1, t_2, \ldots, t_8$ are notional rather than particular. They merely indicate the order in which the operations are performed since all operations represent an integration over a full time step Δt. The ordering of the operations in (3-14) is arbitrary. Further processes in the sequence may result from decomposing any of the operators in (3-14) into a series of operators. For example, there is no reason why the source term cannot be represented as a series of processes over each of the σ dimensions in scalar space just as advection is represented as a series of processes over each of the three dimensions in physical space.

To meet stability criteria any process in the sequence (3-14) may be represented as a further sequence of operations each corresponding to an integration over a shorter time step. For example, advection in the

i-direction may be represented as

$$p(\underset{\sim}{\psi};\ \underset{\sim}{x},\ t+\Delta t) = p(\underset{\sim}{\psi};\ \underset{\sim}{x},\ t + m_a \Delta t_a^{(i)})$$

$$= (1 - \Delta t_a^{(i)}\ A^{(i)})^{m_a}\ p(\underset{\sim}{\psi};\ \underset{\sim}{x}, t) \qquad (3\text{-}15)$$

The final result represents the sequence of operations

$$\begin{aligned}
p(\underset{\sim}{\psi};\ \underset{\sim}{x},\ t+\Delta t_a^{(i)}) &= (1 - \Delta t_a^{(i)}\ A^{(i)})\ p(\underset{\sim}{\psi};\ \underset{\sim}{x}, t) \\
p(\underset{\sim}{\psi};\ \underset{\sim}{x},\ t+2\Delta t_a^{(i)}) &= (1 - \Delta t_a^{(i)}\ A^{(i)})\ p(\underset{\sim}{\psi};\ \underset{\sim}{x}, t+\Delta t_a^{(i)}) \\
&\ \ \vdots \qquad\qquad\qquad\qquad \vdots \\
p(\underset{\sim}{\psi};\ \underset{\sim}{x},\ t+m_a\Delta t_a^{(i)}) &= (1 - \Delta t_a^{(i)}\ A^{(i)})\ p(\underset{\sim}{\psi};\ \underset{\sim}{x}, t+(m_a-1)\Delta t_a^{(i)})
\end{aligned} \qquad (3\text{-}16)$$

However, for these operations the intermediate times are real times since the same operation is being performed at every time step $\Delta t_a^{(i)}$. The best estimate of $p(\underset{\sim}{\psi};\ \underset{\sim}{x}, t+k\Delta t_a^{(i)})$ is obtained by updating the pdf as each process $A^{(i)}$, $D^{(j)}$, W, M or S appears in chronological order. In other words, each process is assigned a time scale ($\Delta t_a^{(i)}$, i=1,2,3, for advection, $\Delta t_d^{(j)}$, j=1,2,3 for turbulent diffusion, $\Delta t_s^{(\alpha)}$, α=1,2,...,σ for differential settling, Δt_m for mixing, Δt_r for reaction) and an absolute time. After each process is performed the absolute time of the process is updated by its time scale. The choice of which process to perform next is determined by the process with the smallest absolute time. In this manner the simulated pdf at any time between operations is a good approximation to

the "exact" pdf at that time, although a better approximation of the pdf is obtained when all processes have reached the same absolute time.

The basis of Pope's Monte Carlo method is the use of stochastic algorithms to simulate each operation in the sequences (3-14) and (3-16). The advection, diffusion and settling operations result in the shifting of elements from node to node while retaining their representative concentrations (i.e., transport in physical space). The mixing and reaction operations result in changing the representative concentrations within elements while retaining their location in physical space (i.e., transport in scalar space). We will deal with the former set of operations first.

3.3 Stochastic Modeling of Transport in Physical Space

In formulating stochastic algorithms for computing the evolution of the joint scalar pdf in space and time it will be convenient to consider each element as having a number of attributes. The obvious attributes which have already been eluded to are location in physical space and time. Other attributes will be introduced in later sections. In this section algorithms that determine how an element changes its spatial location as a result of advection, settling and turbulent diffusion will be presented. Note that the implementation of these algorithms requires that the mean velocity field $\langle U_i(x_j)\rangle$ and the distribution of the eddy diffusivity $\Gamma^{(i)}(x_j)$ be specified as input.

3.3.1 Pope's Algorithms for Advection and Diffusion

Pope (1981) developed stochastic algorithms for simulating advection and diffusion that are in direct correspondence to the

first-order upwind difference operator and second-order central difference operator, respectively, commonly used in finite-difference formulations. His algorithms, though, require a uniformly spaced grid and a constant number N of elements at each node.

For constant grid spacing $\Delta\ell$ the upwind difference operator for simulating advection in the i-direction is

$$A^{(i)}\, p(x_j) = \left|\langle U_i(x_j)\rangle\right| \left[\frac{p(x_j) - p(x_j - \Delta\ell)}{\Delta\ell}\right] + O(\Delta\ell) \qquad (3\text{-}17)$$

where the local mean velocity $\langle U_i(x_j)\rangle$ is assumed to be in the direction of increasing x. The corresponding stochastic algorithm is to choose at random $n_a^{(i)} = \text{int}[\left|\langle U_i\rangle\right| \Delta t_a^{(i)}\, N/\Delta\ell]$ elements at node x_j and node $x_j - \Delta\ell$ and replacing the $n_a^{(i)}$ elements at x_j with the $n_a^{(i)}$ elements chosen from the upstream node. The symbol int[y] means "the closest integer to the real number y". Since the grid spacing and number of elements per node are constant each node loses exactly as many elements as it receives during each advection operation.

For simulating linear diffusion in the i-direction on a uniform grid the central difference operator is

$$D^{(i)}p(x_j) = \Gamma^{(i)}(x_j + \Delta\ell/2)\,\frac{[p(x_j + \Delta\ell) - p(x_j)]}{(\Delta\ell)^2} - \Gamma^{(i)}(x_j - \Delta\ell/2)\,\frac{[p(x_j) - p(x_j - \Delta\ell)]}{(\Delta\ell)^2} + O(\Delta\ell)^2 \qquad (3\text{-}18)$$

where $\Gamma^{(i)}(x_j)$ is the local turbulent diffusion coefficient for the i-direction. The corresponding stochastic algorithm is to choose at random two groups of elements at each node without replacement. The

first group of $n_{d+}^{(i)} = \text{int}[\Gamma^{(i)}(x_j + \Delta\ell/2)\Delta t_d^{(i)} N/(\Delta\ell)^2]$ elements chosen at x_j is commuted with the $n_{d-}^{(i)} = \text{int}[\Gamma^{(i)}(x_{j+1} - \Delta\ell/2)\Delta t_d^{(i)} N/(\Delta\ell)^2]$ elements chosen at $x_{j+1} = x_j + \Delta\ell$. The second group of $n_{d-}^{(i)} = \text{int}[\Gamma^{(i)}(x_j - \Delta\ell/2)\ \Delta t_d^{(i)}\ N/(\Delta\ell)^2]$ elements chosen at x_j is commuted with the $n_{d+}^{(i)} = \text{int}[\Gamma^{(i)}(x_{j-1} + \Delta\ell/2)\ \Delta t_d^{(i)} N/(\Delta\ell)^2]$ elements chosen at $x_{j-1} = x_j - \Delta\ell$. Again, since N and $\Delta\ell$ are constant, the number of elements $n_{d\pm}^{(i)}$ chosen at any node will always equal the number of elements $n_{d\mp}^{(i)}$ to be commuted with the adjacent node.

Being equivalent to the finite difference operations, the stochastic algorithms are governed by the same stability criteria that limit the choice of the grid spacing $\Delta\ell$ and time steps, $\Delta t_a{}^{(i)}$ and $\Delta t_d{}^{(i)}$, namely,

$$\left|\langle U_i(x_j)\rangle\right| \frac{\Delta t_a^{(i)}}{\Delta\ell} < 1 \qquad \Gamma^{(i)}(x_j)\ \frac{\Delta t_d^{(i)}}{(\Delta\ell)^2} < \frac{1}{2} \tag{3-19}$$

For the stochastic operations these criteria take on the obvious significance that the number of elements chosen at any node for transport to an adjacent node cannot exceed the total number of elements available, N.

To evaluate the accuracy of Pope's stochastic algorithms the following test cases were analyzed. To test the advection algorithm we consider a one-dimensional constant velocity flow of magnitude $\langle U\rangle = 4$ transporting a tracer from a source at x = 0 towards increasing x. The x-dimension is discretized into a series of nodes spaced $\Delta\ell = 0.04$ apart and each node is assigned a constant number N = 400 of elements. The advective time step is chosen to be $\Delta t_a = 0.001$ so that N/10 = 40

elements will be transported from each node during each time step. The initial concentration of all elements at all nodes is zero. The boundary condition at $x = 0$ is that of a constant concentration of one. In other words elements transported downstream from the node $x_1 = 0$ are replaced by elements with a concentration of one. Figure 3-2 compares the simulated concentration profiles with the exact square wave solution for various times. The simulated results show that the front is advancing at the proper rate but is experiencing some undesirable numerical dispersion. This drawback is characteristic of the first-order upwind difference operator and it is evident that performing the operation in a stochastic mode does not alleviate the problem. The numerical dispersion is known to increase with the grid spacing so that for highly convective flows an unreasonably small grid spacing $\Delta\ell$ may be required to avoid large numerical errors. To circumvent this difficulty a new, more accurate advection algorithm was developed and is introduced in Section 3.3.3.

The diffusion algorithm was tested by considering a one-dimensional domain of length one, the end-points of which are maintained at a constant concentration of one. The node spacing is $\Delta\ell = 0.04$ and the total number of elements at each node is $N = 400$. Initially all the nodes are assigned a zero concentration. At time $t = 0$ tracer begins to diffuse from the boundaries at a rate $\Gamma = 0.01$. The diffusive time step is chosen to be $\Delta t_d = 0.01$ so that $N/16 = 25$ elements are commuted in each direction from each node at each time step. The exact solution describing the diffusion of the tracer in time is (Carslaw and Jaeger, 1959)

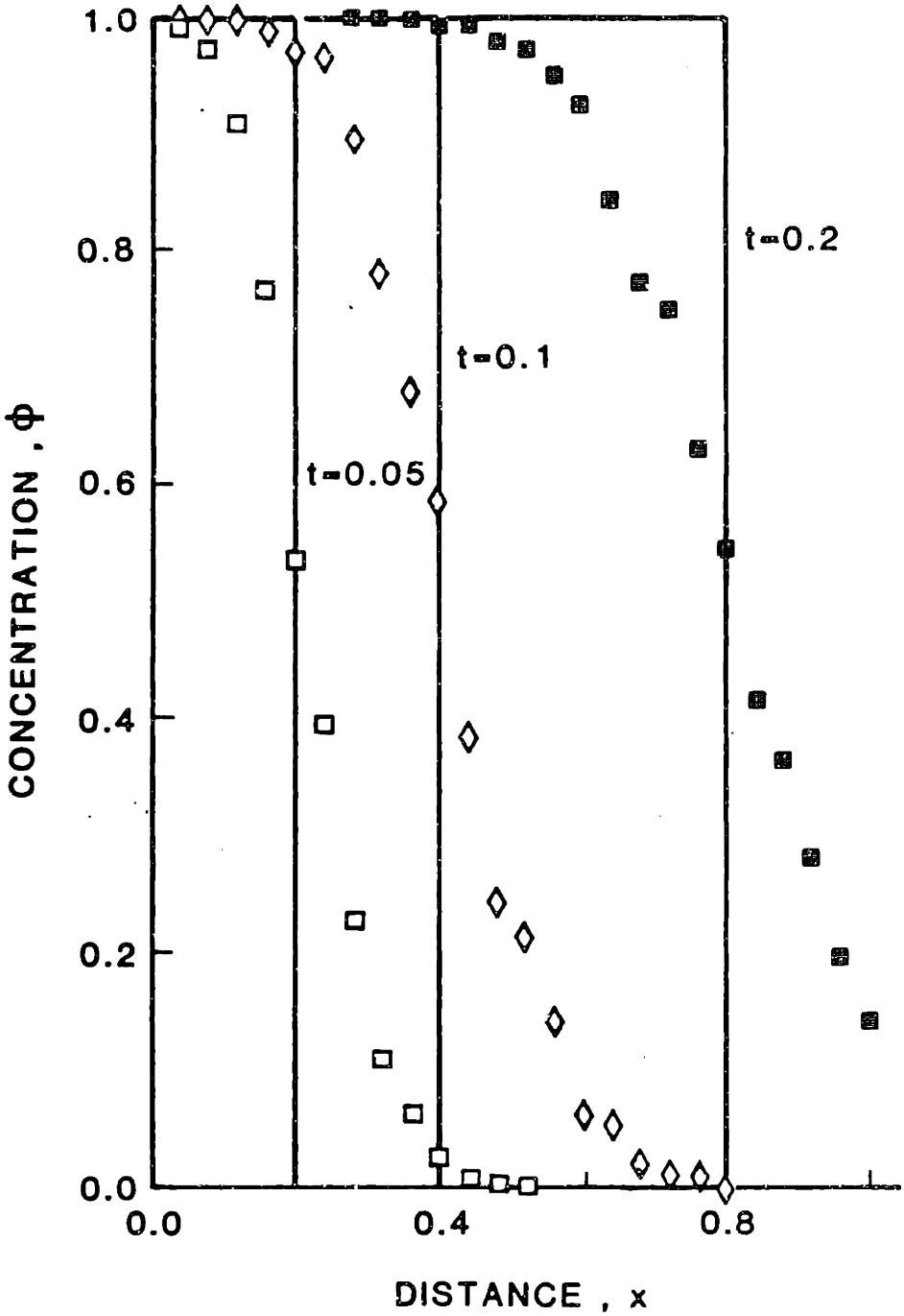

Figure 3-2 Simulation of advection with Pope's algorithm. The tracer is advected at a speed <U>=4 from a boundary at x = 0 maintained at a constant concentration of one. The solid line is the exact solution and the symbols are the simulated results (N = 400, $\Delta x = 0.004$, $\Delta t_a = 0.01$).

$$\phi(x,t) = 1 - \frac{4}{\pi} \sum_{k=0}^{\infty} \frac{(-1)^k}{2k+1} \exp\left[\frac{-\Gamma(2k+1)^2 \pi^2 t}{\ell^2}\right] \cos\left[\frac{(2k+1)\pi (x-\ell/2)}{\ell}\right] \quad (3\text{-}20)$$

where ℓ is the distance between the boundaries. Figure 3-3 compares the simulated concentration profiles with the exact solution. The simulated results are in very good agreement with the exact solution. There is some numerical inaccuracy in the region near x = 1/2 at later times. This is due to the large curvature in the concentration profile which has not been accurately resolved by the coarse grid spacing in that region. Ideally, one would like to optimize the grid to have variable spatial resolution. To overcome this limitation a new algorithm has been developed and is presented in the following section.

3.3.2 Extension to Variable Grid Spacing and Element Density

For Pope's (1981) algorithms it can be said that the element density, or the number of elements per unit spatial volume, is constant throughout the domain. For any Monte Carlo technique, increasing the element density (the number of representative values per estimate or the number of statistical trials, to use the statistician's terminology) decreases the standard error of the estimate. In fact, the standard error decreases as the inverse square root of the element density (Handscomb and Hammersley, 1965). An immediate consequence of varying the grid spacing or the total number of elements at each node is that the element density will vary throughout the spatial domain. Hence the standard error of the mean concentrations computed at each node will vary as well.

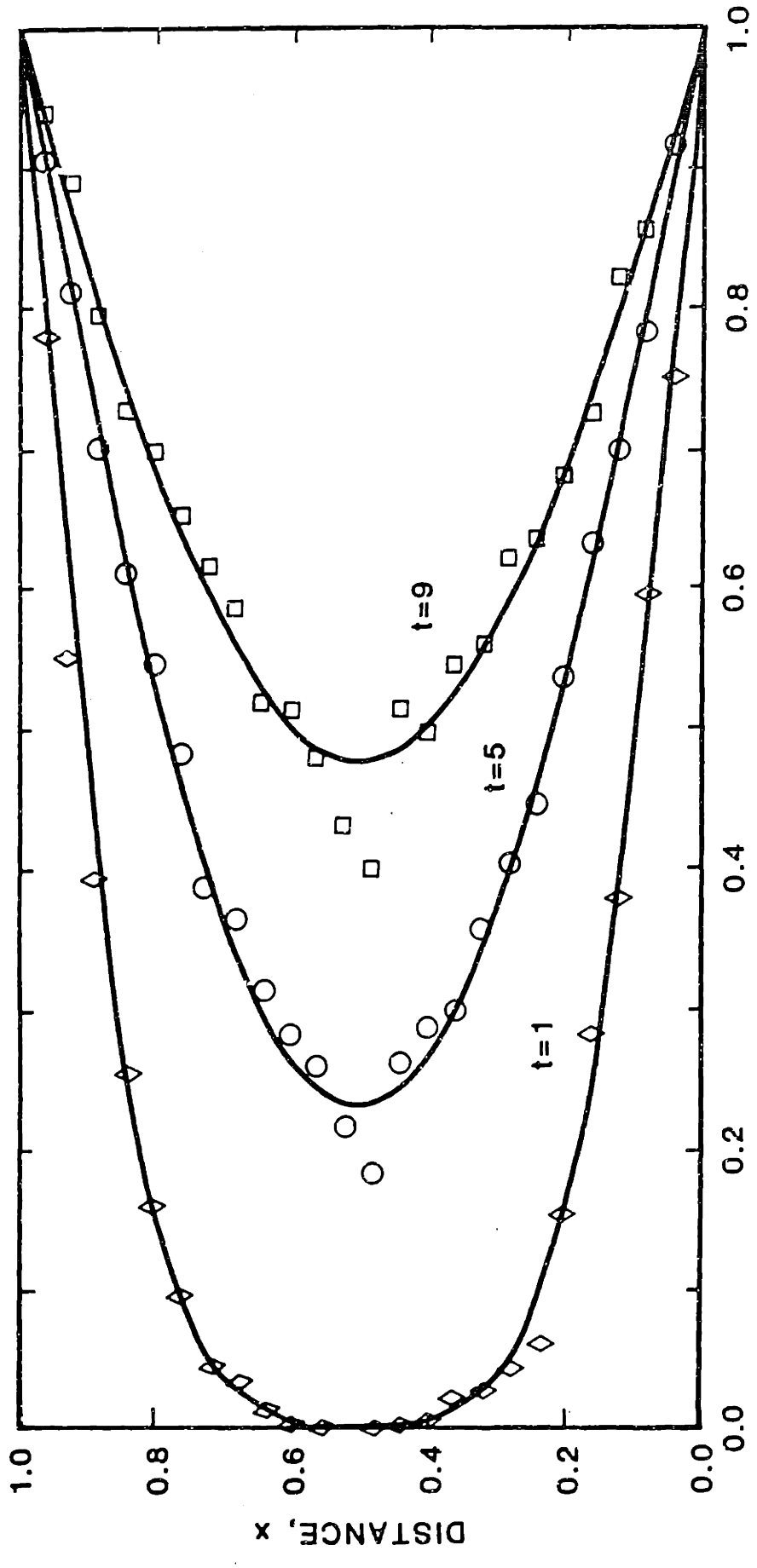

Figure 3-3 Simulation of linear diffusion with Pope's algorithm. The tracer diffuses at a rate $\Gamma = 0.01$ from two boundaries at $x = 0$ and $x = 1$ each maintained at a constant concentration of one. The solid line is the exact solution and the symbols are the simulated results ($N = 400$, $\Delta x = 0.04$, $\Delta t_a = 0.01$).

The constraint of constant spacing between nodal points and constant number of elements per node for Pope's advection and diffusion algorithms ensures that the total number of elements at each node will remain constant in time as the simulation progresses. By varying the element density the number of elements that a given node loses during any operation will generally not equal the number of elements that it receives. To overcome this difficulty we allow for elements to be duplicated or averaged as they are shifted from one node to the next. To illustrate how this procedure is carried out consider first the central difference operator for simulating diffusion in the i-direction over a non-uniform grid,

$$D^{(i)}p(x_j) = \frac{1}{\Delta\ell_j}\left[\Gamma^{(i)}\left((x_j + x_{j+1}/2)\left(\frac{p(x_{j+1}) - p(x_j)}{x_{j+1} - x_j}\right)\right)\right.$$

$$\left. - \Gamma^{(i)}\left((x_j + x_{j-1}/2)\left(\frac{p(x_j) - p(x_{j-1})}{x_j - x_{j-1}}\right)\right)\right] + O(\Delta\ell_j)^2 \qquad (3\text{-}21)$$

where $\Delta\ell_j$ is the width in the i-direction of the control volume surrounding the node x_j, and x_{j+1} and x_{j-1} are the i-coordinates of the nodes adjacent to x_j. We wish to simulate a diffusion operation over a single time step, that is, from t to t+Δt. In finite difference form this may be represented as

$$p(x_j, t+\Delta t) = \left[1 + (\Delta t)\, D^{(i)}\right] p(x_j, t)$$

$$= (1 - \omega_{d-}^{(i)} - \omega_{d+}^{(i)})\, p(x_j, t) + \omega_{d+}^{(i)}\, p(x_{j+1}, t) + \omega_{d-}^{(i)}\, p(x_{j-1}, t) \qquad (3\text{-}22)$$

where

$$\omega_{d+}^{(i)} = \frac{\Gamma^{(i)}((x_j + x_{j+1})/2)\,\Delta t}{\Delta \ell_j (x_{j+1} - x_j)}$$

$$\omega_{d-}^{(i)} = \frac{\Gamma^{(i)}((x_j + x_{j-1})/2)\,\Delta t}{\Delta \ell_j (x_j - x_{j-1})} \qquad (3\text{-}23)$$

In stochastic form the operation represented by Eq. 3-22 involves choosing at random two groups of elements without replacement from the set of N_j elements at each node x_j. The first group of $\omega_{d+}^{(i)} N_j$ elements chosen at x_j is commuted with the $\omega_{d+}^{(i)} N_{j+1}$ elements chosen at x_{j+1}. The second group of $\omega_{d-}^{(i)} N_j$ elements chosen at x_j is commuted with the $\omega_{d-}^{(i)} N_{j-1}$ elements chosen at x_{j-1}. The net gain or loss of elements at x_j is $\omega_{d+}^{(i)} (N_{j+1} - N_j) + \omega_{d-}^{(i)} (N_{j-1} - N_j)$. Hence, irrespective of the grid spacing if the number of elements differs from one node to the next then as diffusion proceeds in time we have the computationally disastrous situation of having the total number of elements at x_j either continually increase or continually decrease.

A simple way of maintaining N_j constant is, for example, to replace the $\omega_{d+}^{(i)} N_j$ elements shifted to x_{j+1} with $\omega_{d+}^{(i)} N_{j+1}(N_j/N_{j+1})$ elements. The multiplication factor N_j/N_{j+1} implies either duplicating or averaging the $\omega_{d+}^{(i)} N_{j+1}$ elements chosen at x_{j+1}. For example, if N_j/N_{j+1} equals three then for each element chosen from the ensemble at x_{j+1} to be shifted to x_j two additional identical elements should be added to the element set at x_j. On the other hand, if N_j/N_{j+1} equals one-half then each pair of elements chosen from x_{j+1} should be averaged into a single element before being added to the element set at x_j.

To prove that this multiplication/averaging operation is valid we adopt the same procedure used by Pope (1981). Let $\hat{p}(\underset{\sim}{\psi};\ \underset{\sim}{x},t)$ represent the pdf of the elements at node x_j before the diffusion operation. The function $\hat{p}(\underset{\sim}{\psi};\ x_j\ ,t)$ is related to the elements at x_j by

$$\hat{p}(\underset{\sim}{\psi};\ x_j,t) = \frac{1}{N_j} \sum_{k=1}^{N_j} \left(\prod_{\alpha=1}^{\sigma} \delta(\phi_\alpha^{(k)}\ (x_j,t) - \psi_\alpha) \right)$$

$$= \frac{1}{N_j} \sum_{k=1}^{N_j} p'(\underset{\sim}{\psi},\ \underset{\sim}{\phi}^{(k)}(x_j,t)) \qquad (3\text{-}24)$$

as shown in Section 3.1.2. As $N_j \to \infty$ the function $\hat{p}(\underset{\sim}{\psi};\ x_j,t)$ converges to the true pdf $p(\underset{\sim}{\psi},\ x_j,t)$. To prove that the stochastic diffusion algorithm is equivalent to the finite difference procedure represented by Eq. 3-22 we need to show that after a diffusion operation from t to $(t+\Delta t)$ the function $\hat{p}(\underset{\sim}{\psi};\ x_j,\ t+\Delta t)$ converges to $p(\underset{\sim}{\psi};\ x_j,\ t+\Delta t)$ in Eq. 3-22 as $N_j \to \infty$. To cover both cases let $N_j/N_{j+1} < 1$ and $N_j/N_{j-1} > 1$, that is, the elements chosen from x_{j+1} must be averaged before being added to the element set at x_j and the elements chosen from x_{j-1} must be multiplied. If the elements chosen to be shifted from one node to the next are denoted by $\underset{\sim}{\phi}^{*(k)}$ then after the diffusion operation

$$\hat{p}(\underset{\sim}{\psi};\ x_j,\ t+\Delta t) = \frac{1}{N_j} \Bigg[\sum_{k=1}^{(1-\omega_{d+}^{(i)} - \omega_{d-}^{(i)})N_j} p'\ (\underset{\sim}{\psi},\ \underset{\sim}{\phi}^{*(k)}(x_j,t))$$

$$+ \sum_{\ell=1}^{\omega_{d+}^{(i)} N_j} \left(\frac{N_j}{N_{j+1}} \sum_{k=(\ell-1)(N_{j+1}/N_j)+1}^{\ell(N_{j+1}/N_j)} p'(\underset{\sim}{\psi},\ \underset{\sim}{\phi}^{*(k)}(x_{j+1},t)) \right)$$

$$+ \frac{N_j}{N_{j-1}} \sum_{k=1}^{\omega_{d-}^{(i)} N_{j-1}} p'(\underset{\sim}{\psi}, \underset{\sim}{\phi}^{*(k)}(x_{j-1}, t))]$$

$$= (1 - \omega_{d+}^{(i)} - \omega_{d-}^{(i)})N_j \left[\frac{1}{(1-\omega_{d+}^{(i)} - \omega_{d-}^{(i)})N_j} \sum_{k=1}^{(1-\omega_{d+}^{(i)}-\omega_{d-}^{(i)})N_j} \right.$$

$$\left. p'(\underset{\sim}{\psi}, \underset{\sim}{\phi}^{*(k)}(x_j, t)) \right] + \omega_{d+}^{(i)} \left[\frac{1}{\omega_{d+}^{(i)} N_j} \sum_{\ell=1}^{\omega_{d+}^{(i)} N_j} \right.$$

$$\left. \left(\frac{N_j}{N_{j+1}} \sum_{k=(\ell-1)(N_{j+1}/N_j)+1}^{\ell(N_{j+1}/N_j)} p'(\underset{\sim}{\psi}, \underset{\sim}{\phi}^{*(k)}(x_{j+1}, t)) \right) \right]$$

$$+ \omega_{d-}^{(i)} \left[\frac{1}{\omega_{d-}^{(i)} N_{j-1}} \sum_{k=1}^{\omega_{d-}^{(i)} N_{j-1}} p'(\underset{\sim}{\psi}, \underset{\sim}{\phi}^{*(k)}(x_{j-1}, t)) \right]$$

$$= (1 - \omega_{d+}^{(i)} - \omega_{d-}^{(i)}) \hat{p}(\underset{\sim}{\psi}; x_j, t) + \omega_{d+}^{(i)} \hat{p}(\underset{\sim}{\psi}; x_{j+1}, t)$$

$$+ \omega_{d-}^{(i)} \hat{p}(\underset{\sim}{\psi}; x_{j-1}, t) \qquad (3\text{-}25)$$

and as N_{j-1}, N_j, $N_{j+1} \to \infty$ this result converges to Eq. 3-22. This confirms that the procedure of multiplying or averaging elements to be shifted in the diffusion operation is valid.

Consider now the upwind difference operator for simulating advection in the i-direction over a non-uniform grid,

$$A^{(i)} p(x_j) = \left| \langle U_i(x_j) \rangle \right| \left[\frac{p(x_j) - p(x_{j-1})}{x_j - x_{j-1}} \right] + O(x_j - x_{j-1}) \qquad (3\text{-}26)$$

In finite difference form the advection operation over a single time

step may be represented as

$$p(x_j,\ t+\Delta t) = (1 - \Delta t\, A^{(i)})\ p(x_j,t)$$

$$= (1 - \omega_a^{(i)}(x_j))\ p(x_j,t) + \omega_a^{(i)}(x_j)\ p(x_{j-1},t) \qquad (3\text{-}27)$$

where

$$\omega_a^{(i)}(x_j) = \frac{\left|\langle U_i(x_j)\rangle\right|\ \Delta t}{x_j - x_{j-1}} \qquad (3\text{-}28)$$

The corresponding stochastic algorithm is to choose at random $\omega_a^{(i)}(x_j)N_j$ elements at node x_j and replace them with $\omega_a^{(i)}(x_j)N_{j-1}$ elements chosen at x_{j-1}. However, at node x_{j-1} the number of elements that will be chosen to be shifted to node x_j is $\omega_a^{(i)}(x_{j-1})\ N_{j-1}$. If either $N_j \neq N_{j-1}$ or $\omega_a^{(i)}(x_j) \neq \omega_a^{(i)}(x_{j-1})$, or both, then in general the number of elements that x_j loses to the downstream node will not equal the number of elements that it receives from the upstream node. As before, we can remedy this situation by multiplying the number of elements received from node x_{j-1} by $\gamma = (\omega_a^{(i)}(x_j)N_j)/(\omega_a^{(i)}(x_{j-1})N_{j-1})$.

For the proof of the validity of this procedure let us first assume that $\gamma > 1$. Denoting as before the elements chosen to be shifted by $\underset{\sim}{\phi}^{*(k)}$ then after a single advection operation

$$\hat{p}(\underset{\sim}{\psi};\ x_j,\ t+\Delta t) = \frac{1}{N_j}\Big[\sum_{k=1}^{(1-\omega_a^{(i)}(x_j))N_j} p'(\underset{\sim}{\psi},\ \underset{\sim}{\phi}^{*(k)}(x_j,t))$$

$$+ \gamma \sum_{k=1}^{\omega_a^{(i)}(x_j)N_{j-1}} p'(\underset{\sim}{\psi},\ \underset{\sim}{\phi}^{*(k)}(x_{j-1},t)$$

$$= (1 - \omega_a^{(i)}(x_j))\left[\frac{1}{(1-\omega_a^{(i)}(x_j))N_j} \sum_{k=1}^{(1-\omega_a^{(i)}(x_j))N_j} p'(\underset{\sim}{\psi}, \underset{\sim}{\phi}^{*(k)}(x_j,t))\right]$$

$$+ \frac{\gamma\omega_a^{(i)}(x_j)N_{j-1}}{N_j}\left[\frac{1}{\omega_a^{(i)}(x_j)N_{j-1}} \sum_{k=1}^{\omega_a^{(i)}(x_j)N_{j-1}} p'(\underset{\sim}{\psi}, \underset{\sim}{\phi}^{*(k)}(x_{j-1},t))\right]$$

$$= (1 - \omega_a^{(i)}(x_j))\,\hat{p}(\underset{\sim}{\psi}; x_j, t) + \omega_a^{(i)}(x_j)\hat{p}(\underset{\sim}{\psi}, x_{j-1}, t) \qquad (3\text{-}29)$$

which converges to Eq. 3-27 as N_j, $N_{j-1} \to \infty$. The same result can be obtained for $\gamma < 1$.

To demonstrate the usefulness of the multiplication/averaging procedure consider again the test case for the diffusion process presented in Section 3.3.1. For the simulation shown in Figure 3-3 the constant grid spacing was $\Delta\ell = 0.4$ and the number of elements at each node was $N = 400$. Let us repeat the simulation but this time with grid spacings of $\Delta\ell = 0.04$ in the regions $0 < x < 0.28$ and $0.72 < x < 1.0$, $\Delta\ell = 0.03$ in the regions $0.28 < x < 0.40$ and $0.60 < x < 0.72$ and $\Delta\ell = 0.02$ in the region $0.4 < x < 0.6$. The number of elements at each node is still maintained constant at $N = 400$ and the time step is $\Delta t_d = 0.01$. Figure 3-4 compares the simulated results with the exact solution. As compared to the previous simulation in Figure 3-3 the effect of increasing the resolution in the region near $x = 0.5$ is to increase the accuracy of the solution in that region by reducing the standard error of the numerical estimates.

The modification of Pope's (1981) algorithms for advection and diffusion to handle non-uniform grids and variable element density

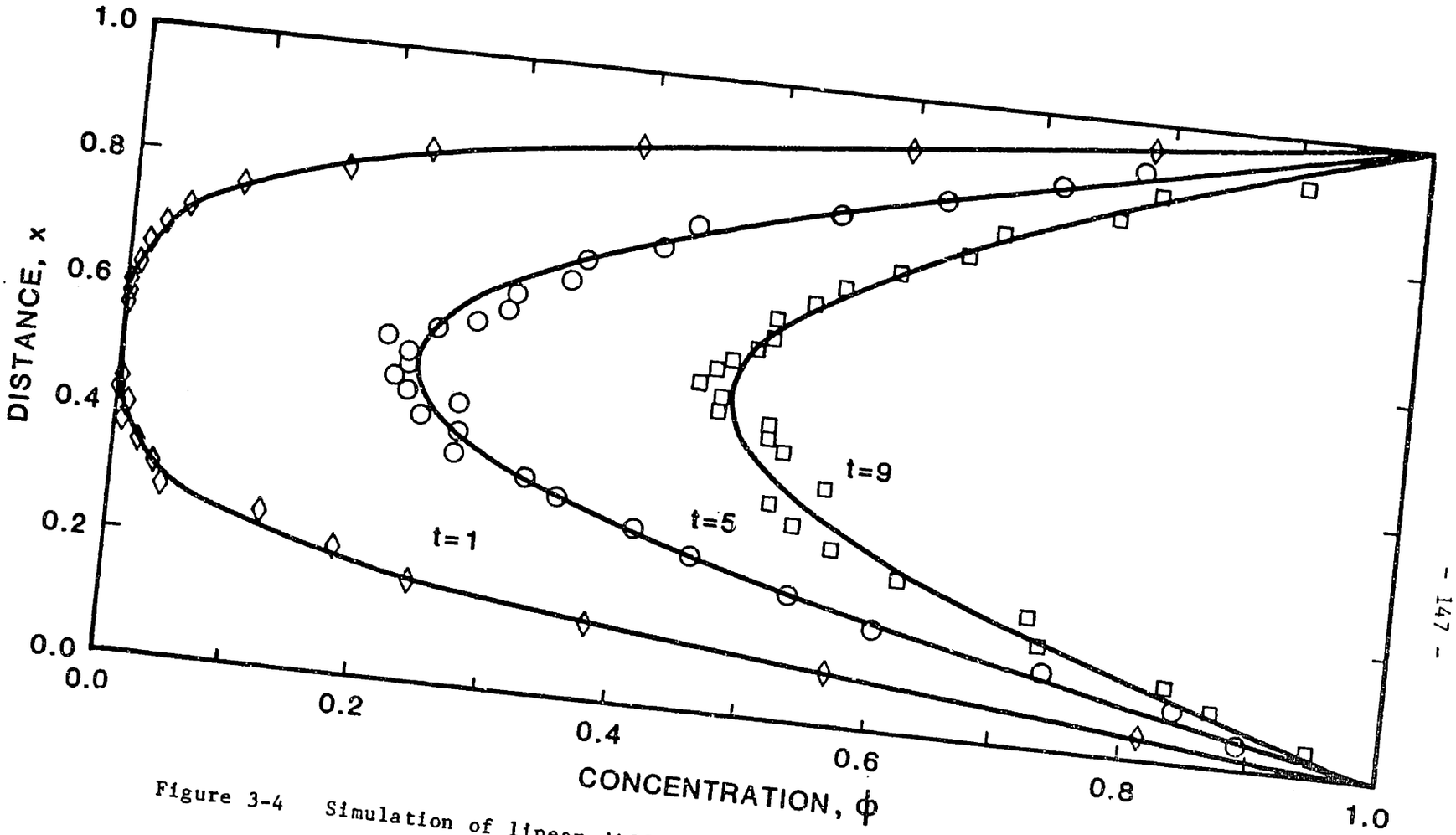

Figure 3-4 Simulation of linear diffusion with a non-uniform grid. Same conditions as in Figure 3-3 except that the grid spacing is $\Delta\ell = 0.04$ for $0 < x < 0.28$ and $0.72 < x < 1$, $\Delta\ell = 0.03$ for $0.28 < x < 0.40$ and $0.60 < x < 0.72$, and $\Delta\ell = 0.02$ for $0.4 < x < 0.6$.

greatly extends the flexibility of the Monte Carlo approach. It is often computationally expedient to vary the spatial resolution of the discretization in order to efficiently resolve the anticipated curvature in the distribution of the modeled variables. The use of variable element densities will allow us to increase or decrease the accuracy of the pdf from one spatial point to the next as is necessary.

3.3.3 An Improved Advection Algorithm

To avoid having to deal with numerical dispersion in highly convective flows an improved advection algorithm has been developed which takes advantage of the Lagrangian nature of the simulated transport of Monte Carlo elements through physical space. Since each node represents a certain volume of space V_i on average each element should remain at a given node for a length of time equal to the residence time V_i/Q_i, where Q_i is the flow rate through V_i. We thus assign each element with an additional attribute that will be called its advective age. In the step that advances time from t to $(t+\Delta t)$ we advance the advective ages of all elements in the system by Δt. Those elements whose advective age becomes greater than the local residence time are chosen to be advected to the downstream node and their residence time is reset to zero. If the element density N_i/V_i is constant for all nodes then irrespective of the grid spacing each node will lose as many elements as it receives during an advection operation. If the element density varies from node to node then the procedure of multiplying or averaging elements described in the previous section must be applied.

With reference to the test case for advection presented in Section 3.3.1, an efficient way of implementing this algorithm is as follows. Initially, the elements at each node x_j are assigned an advective age by numbering the elements from 1 to N_j. During any time step the advective age of each element is advanced by $n_a^{(i)} = \text{int}[|\langle U_i(x_j)\rangle| \Delta t_a^{(i)} N_j/(x_j - x_{j-1})]$. Those elements whose advective age is greater than N_j are singled out to be advected and are renumbered from 1 to $n_a^{(i)}$, the advective age 1 being assigned to the youngest element and $n_a^{(i)}$ to the oldest. If the elements have to be multiplied or averaged the relative age of the elements is still preserved. In this manner the elements move through space at the proper rate.

Figure 3-5 presents the simulated results using the improved advection algorithm for the test case described in Section 3.3.1 and may be compared with Figure 3-2. For the simulation in Figure 3-5, however, we have varied both the grid spacing and the element density in order to demonstrate the validity of the multiplication/averaging procedure. The grid is expanded at the constant rate $\Delta x_j = 1.1 \Delta x_{j-1}$ with distance x, with $\Delta x_1 = 0.01$. Note the elimination of numerical dispersion and the high degree of accuracy possible in representing the square wave. In fact the only error incurred by this algorithm is due to rounding off the quantity $n_a^{(i)}$ to the nearest integer. This error decreases as $n_a^{(i)}$ increases. However, we are obviously still restricted by the limitation $n_a^{(i)}(x_j) < N_j$.

It is admitted that the ability to preserve a square wave in its passage through a control volume is totally inconsistent with the previously stated notion that elements have no relative position within

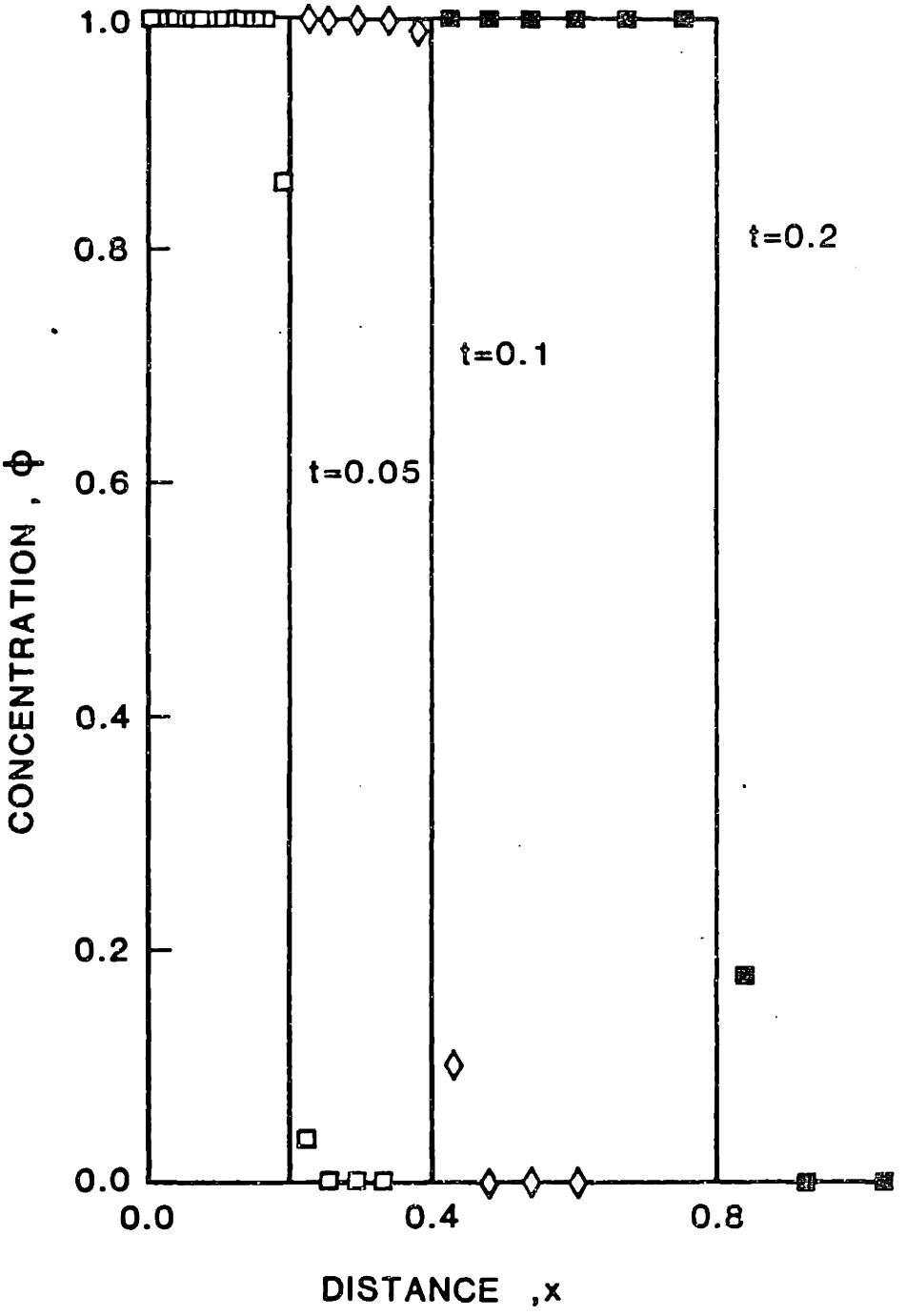

Figure 3-5 Simulation of advection with the improved advection algorithm. Same conditions as in Figure 3-2 except that $\Delta t_a = 6.25 \times 10^{-4}$, $\Delta x_1 = 0.01$, $\Delta x_i = 1.1\Delta x_{i-1}$, and N varies randomly from node to node over the range N = 90 to N = 950.

a control volume. However, since we are usually interested in advection-dominated systems this error seems justified in comparison with the alternative error involving artificial dispersion of elements.

3.3.4 A Differential Settling Algorithm

The term representing differential sedimentation in the pdf transport equation, Eq. 3-16, appears as a correlation with $p'(\underset{\sim}{\psi}; \underset{\sim}{x},t)$, hence we must devise a model for it. Insofar as the settling process resembles an advection process, that is, a vertical transport through space at the speed $w_s^{(\alpha)}$, it is clear that we can pattern the differential settling algorithm after the advection algorithm. Whereas advection transports all constituents at the same rate $\left|\langle U_i(x_j)\rangle\right| \Delta t_a^{(i)}/\Delta \ell_j$ with differential settling each particle size class α changes spatial location at a different rate $w_s^{(\alpha)}\ \Delta t_s^{(\alpha)}/\Delta \ell_j$. Thus each size class has its own settling time scale $\Delta t_s^{(\alpha)}$ and the algorithm is performed for each size class separately.

Since the diffusive transport of large particles is negligible in comparison to the settling transport, to avoid numerical dispersion the differential settling algorithm is patterned after the improved advection algorithm described in the previous section. Each representative solid concentration corresponding to a specific size class α, $\phi_\alpha^{(k)}$, is assigned a separate settling age from 1 to N_j as an attribute. (In the advection process all size classes and constituents of a given element, $\underset{\sim}{\phi}^{(k)}$, are assigned the same advective age.) During any time step the settling age of each representative solid concentration is advanced by $n_w^{(\alpha)} = \text{int}[w_s^{(\alpha)}\ \Delta t_s^{(\alpha)}\ N_j/\Delta \ell_j]$. Those representative concentrations whose settling age is greater than N_j

are singled out to be settled and renumbered from 1 to $n_w^{(\alpha)}$, the settling age 1 being assigned to the youngest representative concentration in each size class α and $n_w^{(\alpha)}$ to the oldest. If the representative concentrations have to be multiplied or averaged the relative age of the values is still preserved. In contrast to the advection algorithm, however, representative concentrations $\phi_\alpha^{(k)}$ chosen at x_j are not replaced with representative concentrations of the same element number k chosen at x_{j-1}, but rather are replaced by values from randomly chosen element numbers from the set of $\phi_\alpha^{(k)}$ chosen to be settled at x_{j-1}.

In addition, special considerations need to be taken at the surface and bottom boundaries. If there is no flux of particles through the surface boundary then representative concentrations that have settled out of the top control volume must be replaced with zero concentration values. At the bottom boundary one can account for the loss of mass from the system by accumulating the concentration flux from the bottom control volume in a separate variable array.

3.3.5 An Efficient Radial Diffusion Algorithm

The formulation of an efficient radial diffusion algorithm requires special consideration. This may be appreciated by examining the central difference operator for radial diffusion over a non-uniform grid for the case where the radial diffusion coefficient Γ_r is constant,

$$D^{(r)}\, p(r_j) = \frac{\Gamma_r}{r_j \Delta r_j}\left[\frac{(r_j + r_{j+1})}{2(r_{j+1} - r_j)}\,(p(r_{j+1}) - p(r_j)) - \frac{(r_j + r_{j-1})}{2(r_j - r_{j-1})}\,(p(r_j) - p(r_{j-1}))\right] \qquad (3\text{-}30)$$

where Δr_j is the radial width of the control volume surrounding node r_j. The corresponding stochastic algorithm is to choose two groups of elements at each node without replacement. The first group of $n_{d+}(r_j) = \text{int}[\Gamma_r(r_{j+1} + r_j)\ \Delta t_d\ N_j/(2r_j\ \Delta r_j(r_{j+1} - r_j))]$ elements chosen at r_j is commuted with the $n_{d-}(r_{j+1}) = \text{int}[\Gamma_r(r_{j+1} + r_j)\ \Delta t_d\ N_{j+1}/(2r_{j+1}\Delta r_{j+1}(r_{j+1} - r_j))]$ elements chosen at r_{j+1}. The second group of $n_{d-}(r_j) = \text{int}[\Gamma_r(r_j + r_{j-1})\Delta t_d N_j/(2r_j\Delta r_j(r_j - r_{j-1}))]$ elements chosen at r_j is commuted with the $n_{d+}(r_{j-1}) = [\Gamma_r(r_j + r_{j-1})\ \Delta t_d\ N_{j-1}/(2r_{j-1}\Delta r_{j-1}(r_j - r_{j-1}))]$ elements chosen at r_{j-1}. If we are not willing to use the multiplication/averaging procedure then to maintain N_j constant we must have the element density $N_j/r_j\Delta r_j$ constant for all nodes. This means that the total number of elements must increase with increasing radial distance r_j. If we want to model the outward radial diffusion of a constituent, however, this is exactly the opposite way that we would wish to assign N_j, that is, for the sake of accuracy we would like to have N_j decrease with increasing r_j. Use of the multiplication/averaging procedure will alleviate the problem somewhat but not entirely since we are still constrained to shift in any direction at least one but no more than $N_j/2$ elements, that is,

$$1 \leq \text{int}\left[\frac{\Gamma_r(r_j + r_{j\pm1})\ \Delta t_d\ N_j}{2r_j\ \Delta r_j\ |r_j - r_{j\pm1}|}\right] \leq \frac{N_j}{2} \tag{3-31}$$

Thus if at the outer-most node r_m we set the time scale Δt_d such that

$$\frac{\Gamma_r\ (r_M + r_{M-1})\ \Delta t_d\ N_M}{2r_M\ \Delta r_M\ (r_M - r_{M-1})} = 1 \tag{3-32}$$

then at the inner-most node r_1 we must satisfy

$$\frac{\Gamma_r\ (r_1 + r_2)\ \Delta t_d\ N_1}{2r_1\ \Delta r_1\ (r_2 - r_1)} < \frac{N_1}{2} \tag{3-33}$$

implying that

$$N_M > \frac{2r_M\ \Delta r_M (r_M - r_{M-1})(r_1 + r_2)}{(r_M + r_{M-1})\ r_1\ \Delta r_1\ (r_2 - r_i)} = O\left[\frac{2(r_M - r_{M-1})\ \Delta r_M}{(r_2 - r_1)\ \Delta r_1}\right] \tag{3-34}$$

Since for an outward diffusion problem we would normally separate the nodes further and further apart with increasing radial distance we see from Eq. 3-34 that N_j will still have to increase with r_j.

The real source of the problem is not in the choice of N_j or the grid spacing Δr_j but rather in the fact that the diffusion rate $\Gamma_r/r_j\Delta r_j$ decreases with increasing r_j. This implies that the diffusion time scale Δt_d should increase with increasing r_j. To see how this can be accomplished let us write the radial diffusion operation over the finite domain $0 < r < R$ as a series of operations over a finite number n of subdomains,

$$\frac{\partial p}{\partial t}(r,t) = \frac{\Gamma_r}{r}\frac{\partial}{\partial r}\left[r\ \frac{\partial p}{\partial r}\right] \sum_{k=1}^{n} (H(r_k) - H(r_{k+1})) \tag{3-35}$$

where $H(r_j)$ denotes the Heavyside function, which equals zero for $r < r_j$ and one for $r \geq r_j$. The summation in Eq. 3-35 thus represents the entire spatial domain $0 < r < R$. Now since Eq. 3-35 is a linear

equation with variable coefficients we can use the method of approximate factorization of operators (Yanenko, 1971) in formulating the finite difference scheme. The conventional explicit scheme

$$p(r_j,\ t+\Delta t) = \left[1 + \Delta t \sum_{k=1}^{n} (H(r_k) - H(r_{k+1}))\ D^{(r)}\right] p(r_j, t) \qquad (3\text{-}36)$$

is approximately factorized as

$$p(r_j,\ t+\Delta t) = \prod_{k=1}^{n} \left[1 + \Delta t(H(r_k) - H(r_{k+1}))\ D^{(r)}\right] p(r_j, t) \qquad (3\text{-}37)$$

with an error of order $(\Delta t)^2$. Note that the subdomains $r_k \leq r < r_{k+1}$ may contain two or more nodes but the end points r_k and r_{k+1} must correspond to nodal points. Eq. 3-37 is equivalent to the following sequence of operations:

$$\begin{aligned} p(r_j,\ t_1) &= L_1(\Delta t)\ p(r_j, t) \\ p(r_j,\ t_2) &= L_2(\Delta t)\ p(r_j, t_1) \\ &\ \ \vdots \qquad\qquad \vdots \\ p(r_j,\ t_n = t+\Delta t) &= L_n(\Delta t)\ p(r_j,\ t_{n-1}) \end{aligned} \qquad (3\text{-}38)$$

where the operator $L_k(\Delta t) = [1 + \Delta t(H(r_k) - H(r_{k+1}))\ D^{(r)}]$. The intermediate times $t_1, t_2, \ldots, t_{n-1}$ are notional rather than particular. They merely indicate the order in which the operations are performed since all operations represent an integration over a full time step Δt. The ordering of the operations L_k is arbitrary. Note also that we have not yet gained anything since for diffusion between each

pair of nodes one and only one step in (3-38) will be performed and each diffusion operation will be performed at the same rate $1/\Delta t$.

If each radial subdomain is characterized by a typical radial distance d_k, where $r_k < d_k < r_{k+1}$, and a typical grid spacing Δd_k, then the nominal diffusion time scale for each subdomain is $d_k \Delta d_k / \Gamma_r$. Suppose the smallest and largest subdomain diffusion time scales are Δt_{ds} and $\Delta t_{d\ell}$, respectively. If the integration time step is set at $\Delta t = b\, \Delta t_{ds}$, where $b < 1/2$, then the error due to the neglected terms in Eq. 3-37 will be approximately proportional to b^2. If the integration time step is set at $\Delta t = b\Delta t_{d\ell}$ then the error will be approximately proportional to $(b\Delta t_{d\ell}/\Delta t_{ds})^2$, although the computational cost will be reduced by $\Delta t_{ds}/\Delta t_{d\ell}$. To reach a compromise between accuracy and efficiency we note that any step in Eq. 3-38 can be represented as a further sequence of operations each corresponding to an integration over a shorter time step Δt_k, that is

$$p(r_j,\ t_k + \Delta t) = p(r_j,\ t_k + m_k \Delta t_k)$$

$$= [L_k(\Delta t_k)]^{m_k}\ p(r_j, t_k) \qquad (3\text{-}39)$$

The final result represents the sequence of operations

$$p(r_j,\ t_k + \Delta t_k) = [L_k(\Delta t_k)]\ p(r_j, t_k)$$

$$p(r_j,\ t_k + 2\Delta t_k) = [L_k(\Delta t_k)]\ p(r_j,\ t_k + \Delta t_k)$$

$$\vdots \qquad\qquad \vdots$$

$$p(r_j, t_k + m_k \Delta t_k = t_k + \Delta t) = [L_k(\Delta t_k)]\ p(r_j,\ t_k + (m_k - 1)\Delta t_k) \qquad (3\text{-}40)$$

For these operations the intermediate times are real times since the

same operation is being performed at every time step Δt_k. The best estimate of $p(r_j, t_k + i\Delta t_k)$ is obtained by updating the pdf as each diffusion operation in a subdomain appears in chronological order. If we set $\Delta t_k = bd_k \Delta d_k/\Gamma_r$ and the master time scale $\Delta t = \Delta t_{d\ell}$ so that $m_k = \Delta t_{d\ell}/\Delta t_k$ then the error in Eq. 3-37 will be approximately proportional to $(b\Delta t_{d\ell}/m_k\Delta t_k)^2 = b^2$. As well, compared to the case where the master time scale is set at $\Delta t = \Delta t_{ds}$, the computational cost will be considerably reduced.

What we have just described in mathematical terms is an efficient time-splitting algorithm for performing the stochastic radial diffusion operation. Summarizing the procedure, the radial domain $0 < r < R$ is subdivided into n subdomains and each subdomain is assigned a diffusion time scale based on a typical radial distance and grid spacing within the subdomain. Diffusion in each subdomain proceeds at a rate determined by the subdomain time scale. After each diffusion operation the subdomain diffusion time is updated by the subdomain diffusion time scale. The choice of which subdomain in which to perform the next diffusion operation is determined by that subdomain that has the smallest diffusion time. In this manner the complete cycle of operations (3-38) will be performed on average once every $\Delta t_{d\ell}$, where $\Delta t_{d\ell}$ is the longest of the subdomain time scales. The advantage of this technique is that it allows one to set the total number of elements N_j in each control volume independently of the choice of the radial grid.

To evaluate the accuracy of this algorithm the following test case was analyzed. We consider a cylindrical domain of radius R = 1 with the tracer concentration maintained at a value of one along the

circumference. The grid spacing is compressed at the rate $\Delta r_j = \Delta r_{j-1}/1.1$ with radial distance, with $\Delta r_1 = 0.1$. The total number of elements at each node is N = 400. The domain is subdivided into seven subdomains each with its own diffusion time scale. The time scales decrease with radial distance, with a time scale of 4×10^{-4} at the inner-most subdomain and 7.5×10^{-5} at the outer-most subdomain. Initially all the nodes are assigned a zero concentration. At time t=0 tracer begins to diffuse from the boundary at the rate $\Gamma_r = 1.0$. The exact solution describing the diffusion of the tracer is (Carslaw and Jaeger, 1959)

$$\phi(r,t) = 1 - 2 \sum_{k=1}^{\infty} \exp[-\Gamma_r \alpha_k^2 t] \frac{J_o(r\alpha_k)}{\alpha_k J_1(\alpha_k)} \qquad (3\text{-}41)$$

where α_k is the k^{th} root of the Bessel function J_o. Figure 3-6 compares the simulated concentration profiles with the exact solution. The simulated results are in good agreement with the exact solution, especially at early times. The degeneration in the accuracy of the solution with time may be due to the accumulation of errors from rounding off real values to integer values in applying the multiplication/averaging procedure.

3.4 Stochastic Modeling of Molecular Mixing

The molecular mixing term in the transport equation for the joint scalar pdf appears as a correlation with the function $p'(\underset{\sim}{\psi}; \underset{\sim}{x}, t)$, hence, it must be modeled. Any model of molecular mixing must reflect the balance between the steepening of local scalar gradients by the turbulent stretching of material surfaces and the smearing out of these

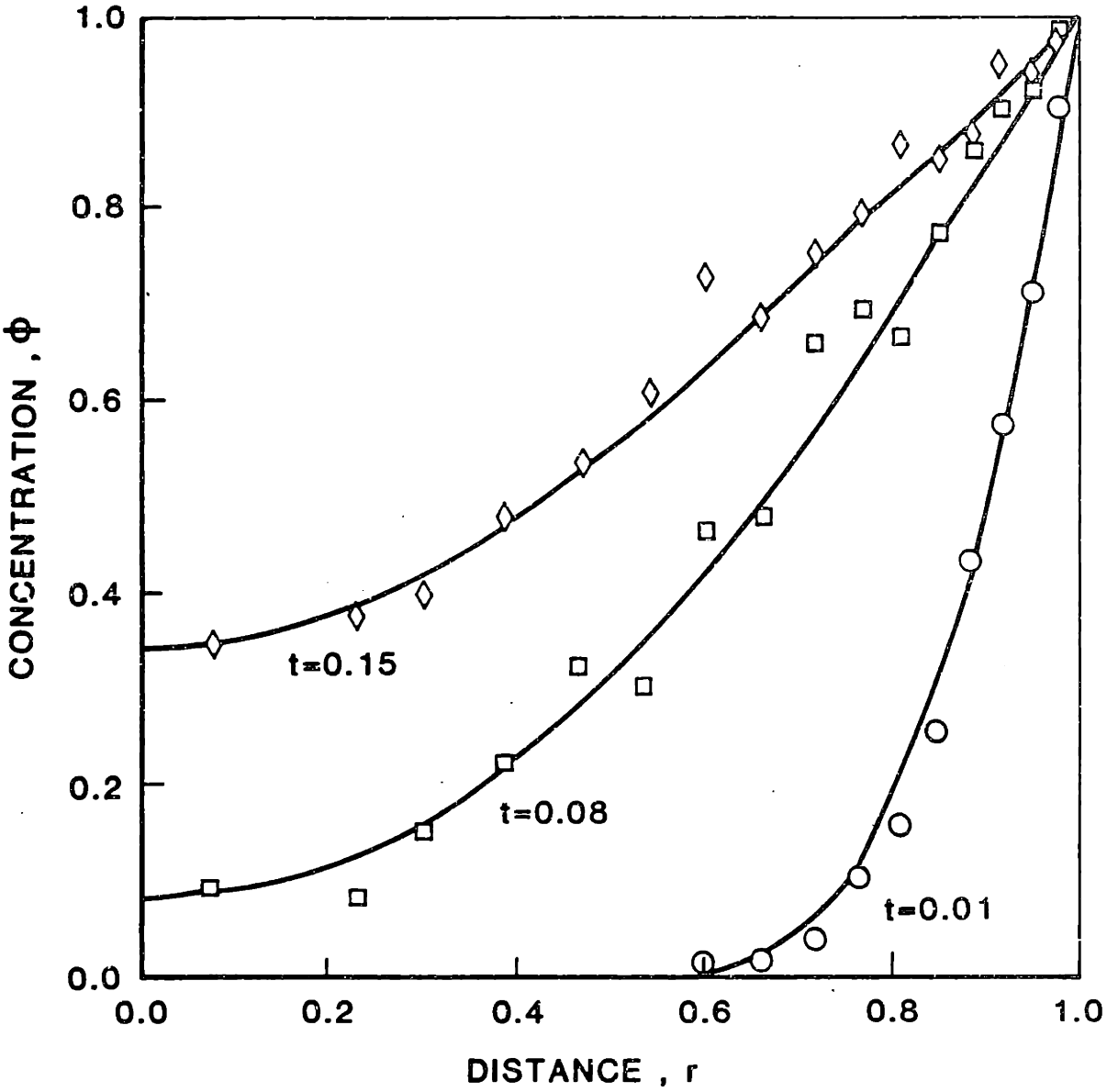

Figure 3-6 Simulation of radial diffusion of a tracer at a rate Γ = 1.0 within an infinite cylindrical domain of radius one. The circumference is maintained at a constant concentration of one ($N = 400$, $\Delta r_j = \Delta r_{j-i}/1.1$, $\Delta r_1 = 0.1$, $7.5 \times 10^{-5} < \Delta t_d < 4 \times 10^{-4}$).

gradients by molecular diffusion. In terms of its effect on the joint scalar pdf the first influence results in the increase of local probability density by the creation of interfaces (and thus correlations) between fluid regions of different concentration. The second influence reduces the local probability density by smoothing out concentration differences and destroying correlations. The rate-limiting step is the creation of local discontinuities in concentration by turbulence. The time scale of this process is the mixing time scale, previously defined in Section 1.1,

$$t_m = 2.7(3 - Sc)^{-2}\, k/\varepsilon \qquad Sc \leq O(1) \qquad (3\text{-}42)$$

$$t_m = 2.0\, k/\varepsilon + 0.5(\nu/\varepsilon)^{1/2} \ell n\, Sc \qquad Sc \gg 1 \qquad (3\text{-}43)$$

where Sc is the Schmidt number. Hence, a semi-empirical model for describing the influence of molecular mixing on the joint scalar pdf may be formulated as (Curl, 1963; Dopazo, 1979)

$$\frac{\partial p(\underset{\sim}{\psi};\, \underset{\sim}{x}, t)}{\partial t} = \frac{b}{t_m}\left[\int_0^{\underset{\sim}{\psi}} p(\underset{\sim}{\psi}_a;\, \underset{\sim}{x},\, t)\, d\underset{\sim}{\psi}_a \int_{\underset{\sim}{\psi}}^{\infty} p(\underset{\sim}{\psi}_b;\, \underset{\sim}{x}, t)\, G(\underset{\sim}{\psi};\underset{\sim}{\psi}_a,\, \underset{\sim}{\psi}_b)\, d\underset{\sim}{\psi}_b - p(\underset{\sim}{\psi};\, \underset{\sim}{x}, t)\right] \qquad (3\text{-}44)$$

where b is a numerical constant. The first and second terms on the right-hand side account for the generation of $p(\underset{\sim}{\psi};\, \underset{\sim}{x}, t)$ by microscale turbulence and its destruction by molecular processes, respectively. The function $G(\underset{\sim}{\psi};\, \underset{\sim}{\psi}_a,\, \underset{\sim}{\psi}_b)$ relates the mixed fluid concentration $\underset{\sim}{\psi}$ to its possible sources, namely, the interaction between two fluid

regions of concentration $\underset{\sim}{\psi}_a \leq \underset{\sim}{\psi}$ and $\underset{\sim}{\psi}_b > \underset{\sim}{\psi}$.

Several models have been put forward for the interaction kernel $G(\underset{\sim}{\psi};\ \underset{\sim}{\psi}_a,\ \underset{\sim}{\psi}_b)$. Pope (1982) has shown that they can all be expressed in the form

$$G(\underset{\sim}{\psi};\ \underset{\sim}{\psi}_a,\ \underset{\sim}{\psi}_b) = \int_0^1 A(\alpha)\delta(\underset{\sim}{\psi} - (1-\alpha)\ \underset{\sim}{\psi}_a - \alpha(\underset{\sim}{\psi}_a + \underset{\sim}{\psi}_b)/2)\ d\alpha \qquad (3\text{-}45)$$

where α is a mixing parameter. For $\alpha = 1$ complete mixing occurs since the Dirac delta function will be zero unless $\underset{\sim}{\psi} = 1/2(\underset{\sim}{\psi}_a + \underset{\sim}{\psi}_b)$. For $\alpha = 0$ no mixing occurs and $\underset{\sim}{\psi} = \underset{\sim}{\psi}_a$. Curl (1963) proposed the model $A(\alpha) = \delta(1-\alpha)$, or

$$G(\underset{\sim}{\psi};\ \underset{\sim}{\psi}_a,\ \underset{\sim}{\psi}_b) = \delta(\underset{\sim}{\psi} - (\underset{\sim}{\psi}_a + \underset{\sim}{\psi}_b)/2) \qquad (3\text{-}46)$$

corresponding to a fixed value of $\alpha = 1$. This model indicates that when two fluid regions of concentration $\underset{\sim}{\psi}_a$ and $\underset{\sim}{\psi}_b$ are brought together any mixing that occurs between the two regions is instantaneously complete; the region of interaction between the two initial fluid regions is characterized by a uniform concentration equal to the average of the concentrations $\underset{\sim}{\psi}_a$ and $\underset{\sim}{\psi}_b$. In reality, of course, the region of interaction between the two initial fluid regions should be characterized by a continuous gradient in concentration with initial concentrations $\underset{\sim}{\psi}_a$ and $\underset{\sim}{\psi}_b$ as extreme values. Curl's model is thus not physical since it does not properly describe the microscale mixing process. Consequently, use of Curl's model in a numerical simulation of the pdf transport equation results in the evolution of discontinuous scalar pdf's.

To remedy this situation we must permit the interaction of fluid regions of concentration $\underset{\sim}{\psi}_a$ and $\underset{\sim}{\psi}_b$ to generate fluid regions of any possible concentration $\underset{\sim}{\psi}$ between $\underset{\sim}{\psi}_a$ and $\underset{\sim}{\psi}_b$. This amounts to specifying a function $A(\alpha)$ that is continuous in the interval $0 \leq \alpha \leq 1$. Dopazo (1979) proposed the model

$$A(\alpha) = 2(\underset{\sim}{\psi}_b - \underset{\sim}{\psi}_a) \frac{d}{d\alpha} \text{erf}^{-1}(\alpha-1) \tag{3-47}$$

so that

$$G(\underset{\sim}{\psi};\ \underset{\sim}{\psi}_a,\ \underset{\sim}{\psi}_b) = \frac{d}{d\underset{\sim}{\psi}} \text{erf}^{-1} \left(\frac{2\underset{\sim}{\psi} - (\underset{\sim}{\psi}_a + \underset{\sim}{\psi}_b)}{\underset{\sim}{\psi}_b - \underset{\sim}{\psi}_a} \right) \tag{3-48}$$

where erf^{-1} is the inverse of the error function. Janicka, Kolbe and Kollmann (1979) put forward the model $A(\alpha) = 1$ so that

$$G(\underset{\sim}{\psi};\ \underset{\sim}{\psi}_a,\ \underset{\sim}{\psi}_b) = 1 \tag{3-49}$$

Janicka et al.'s model indicates that when two fluid regions of concentration $\underset{\sim}{\psi}_a$ and $\underset{\sim}{\psi}_b$ are brought together mixing between the two regions generates lumps of fluid of all intermediate concentrations $\underset{\sim}{\psi}_a \leq \underset{\sim}{\psi} \leq \underset{\sim}{\psi}_b$ with equal probability. Dopazo's model, on the other hand, assigns a relatively higher probability to the generation of fluid lumps of concentration near $\underset{\sim}{\psi}_a$ or $\underset{\sim}{\psi}_b$, and relatively lower probability to the generation of fluid lumps of concentration near $(\underset{\sim}{\psi}_a + \underset{\sim}{\psi}_b)/2$.

The constant b in Eq. 3-44 is different for every choice of $A(\alpha)$ and is determined from the decay rate of the variance of concentration σ_α^2 for any species α,

$$\frac{d\sigma_\alpha^2}{dt} = -\frac{\sigma_\alpha^2}{t_m} \tag{3-50}$$

Multiplying Eq. 3-48 by ϕ_α^2 and integrating over $d\underset{\sim}{\phi}$ results in

$$\frac{d\sigma_\alpha^2}{dt} = \frac{-b(a_1 - a_2/2)\ \sigma_\alpha^2}{2t_m} \tag{3-51}$$

where a_i is the i^{th} moment of $A(\alpha)$. For Curl's model, for example, $a_1 = a_2 = 1$. Hence, for compatibility with Eq. 3-50 we must set $b = 4$.

The stochastic form of the molecular mixing model represented by Eqs. 3-44 and 3-45 is essentially the well-known coalescence-dispersal model (Curl, 1963; Spielman and Levenspiel, 1965). At any node x_j the mixing operation is performed every mixing time step Δt_m, where $\Delta t_m << t_m/b$, by choosing $n_m = (b\Delta t_m/t_m)N_j$ elements at random from the ensemble of N_j elements. The elements $\underset{\sim}{\phi}^{(k)}$ chosen for mixing randomly choose partners and mix according to

$$\begin{aligned}
\underset{\sim}{\phi}_a^{*(k)} &= (1 - \alpha)\underset{\sim}{\phi}_a^{(k)} + \alpha(\underset{\sim}{\phi}_a^{(k)} + \underset{\sim}{\phi}_b^{(k)})/2 \\
\underset{\sim}{\phi}_b^{*(k)} &= (1 - \alpha)\underset{\sim}{\phi}_b^{(k)} + \alpha(\underset{\sim}{\phi}_a^{(k)} + \underset{\sim}{\phi}_b^{(k)})/2
\end{aligned} \tag{3-52}$$

where α is the mixing parameter, $\underset{\sim}{\phi}_a^{(k)}$ and $\underset{\sim}{\phi}_b^{(k)}$ are the concentrations of the pair of elements prior to the mixing operation, and $\underset{\sim}{\phi}_a^{*(k)}$ and $\underset{\sim}{\phi}_b^{*(k)}$ are the respective concentrations after mixing. If Curl's model is used α is fixed at the value one and both elements are reassigned the same

concentration corresponding to the average value of the initial concentrations. With Dopazo's and Janicka et al.'s models the parameter α is chosen at random from the probability density function $A(\alpha)$ for every pair of elements.

Pope (1982) has criticized the models of Dopazo and Janicka et al. on the basis that in homogeneous and isotropic turbulence they do not evolve the joint scalar pdf to a Gaussian form. Whereas all moments of the Gaussian distribution are finite, Pope shows that any choice for the function $A(\alpha)$ will result in asymptotic scalar pdf's whose higher order moments grow in time without bound. To overcome this problem Pope proposed a modification to the basic model form, Eq. 3-44. The derivation of the model equations is quite complicated and the reader is referred to Pope's paper for details. Only the modification to the stochastic algorithm will be presented here.

Pope (1982) showed that scalar pdf's with infinite higher moments result when the choice of elements to be mixed is unbiased, as for the models presented above. Accordingly, he proposed that every element be assigned a random mixing age τ and a random life expectancy τ^*, where $0 \leq \tau, \tau^* \leq 15/(16b)$, as additional attributes. The probability density function of mixing ages is denoted by $r(s)$ and that of life expectancies by $r^*(s)$. These two functions are related by

$$r^*(s) = -\frac{1}{2}\frac{dr(s)}{ds} \tag{3-53}$$

Pope studied the behavior of a number of different choices for the functions $A(\alpha)$ and $r(s)$. Based on the criteria that in homogeneous and isotropic turbulence the mixing process should generate scalar pdf's

that become asymptotically Gaussian with time, he recommended the following probability density functions,

$$A(\alpha) = 10\,\alpha^3\,(1 - 3\alpha/4) \tag{3-54}$$

$$r(s) = 2b\left[1 - \left(\frac{16b}{15}\right)^2 s^2\right]^2 \tag{3-55}$$

Using Eq. 3-53

$$r^*(s) = 4\left(\frac{16b}{15}\right)^2 bs\left[1 - \left(\frac{16b}{15}\right)^2 s^2\right] \tag{3-56}$$

Also, the value of b indicated by Eq. 3-51 with this choice of $A(\alpha)$ is $b = 3.482$.

To implement the modified algorithm initially all elements are assigned a random age $\tau^{(k)}(\underset{\sim}{x},t)$ from the distribution r(s) and a random life expectancy $\tau^{*(k)}(\underset{\sim}{x},t)$ from the conditional distribution

$$r_c^*(s^*|s) = H(s^* - s)\,r^*(s^*)/\int_0^\infty r^*(s')\,ds' \tag{3-57}$$

where H(s) is the Heavyside function. Note that $r^*(s)$ is the pdf of life expectancy for elements of zero mixing age. If an element has already attained the age $\tau = s$ then its life expectancy is described by the conditional pdf $r_c^*(s^*|s)$.

During any time step Δt_m all elements age by $\Delta t_m/t_m$. All elements whose age becomes greater than their life expectancy are singled out for mixing. The chosen elements randomly choose partners and mix according to Eq. 3-52 with the mixing parameter α chosen at random for each element pair from the pdf $A(\alpha)$ specified by Eq. 3-54. After mixing the ages of the mixed elements are set to zero and their

life expectancies are reset by randomly chosen values from the pdf $r^*(s)$.

A useful test case for the stochastic mixing algorithm involves the mixing of a single scalar in steady, homogeneous and isotropic turbulence. We postulate an initial random scalar field with two equally probable states, $\phi = 0$ and $\phi = 1$. The corresponding initial scalar pdf is

$$p(\phi;\ 0) \ = \ 0.5[\delta(\phi) + \delta(1 - \phi)] \tag{3-58}$$

With the onset of mixing there is a transfer of probability density from the extreme values at $\phi = 0$ and $\phi = 1$ to intermediate values $0 < \phi < 1$. As a result the two delta functions decrease in magnitude $P_1(t)$ and a continuous distribution $p_c(\phi;\ t)$ forms in the range $0 < \phi < 1$. At any time $t > 0$ the scalar pdf may be expressed in the form

$$p(\phi;\ t) = p_c(\phi;\ t) + P_1(t)[\delta(\phi) + \delta(1-\phi)] \tag{3-59}$$

After a sufficiently long time $P_1(t) = 0$ and the normalized pdf $p(\phi;\ t)/\sigma(t)$, where $\sigma(t)$ is the standard deviation, tends to a Gaussian form,

$$\frac{p(\phi;\ t)}{\sigma(t)} \ = \ \frac{1}{(2\pi)^{1/2}} \exp\left[\frac{-(\phi - 0.5)^2}{2\sigma^2(t)}\right] ; \quad t \to \infty \tag{3-60}$$

In order to reduce the statistical uncertainty and demonstrate the validity of the algorithm the simulation was performed with N = 12,000 elements. The initial condition, Eq. 3-58, was generated by assigning half the elements the concentration one and the other half the

concentration zero. The mixing time scale was set at $t_m = 1.0$ and the time step was chosen as $\Delta t_m = 0.001$. Figure 3-7 illustrates the simulated reduction with time of the standard deviation according to

$$\sigma(t) = \sigma(0) \exp(-t/t_m) \tag{3-61}$$

with $\sigma(0) = 1.0$. Figure 3-8 shows the simulated evolution of the functions $P_1(t^*)$ and $p_c(\psi;\ t^*)$ as a function of the non-dimensional time $t^* = t/t_m$. After a time equal to the mixing time scale the delta functions have essentially disappeared and $p_c(\psi;\ t^*)$ begins to take on a Gaussian form. Figure 3-9 demonstrates that for times $t^* \geq 1.5$ the normalized pdf is Gaussian. These results confirm the excellent performance of Pope's stochastic mixing algorithm. In all subsequent simulations Pope's molecular mixing model will be employed.

3.5 The Source Term

Pope (1981) showed that the effect of reaction on the ensemble of elements is to modify the concentration of all elements $\phi_\alpha^{(k)}(\underset{\sim}{x},t)$ by $\Delta\phi_\alpha^{(k)}(\underset{\sim}{x},t)$, where

$$\Delta\phi_\alpha^{(k)}(\underset{\sim}{x},t) = \int_t^{t+\Delta t_r} S^{(\alpha)}(\underset{\sim}{\phi}(\underset{\sim}{x},t))\ dt \tag{3-62}$$

The reaction time step Δt_r must satisfy

$$\Delta t_r < \min \left[\left| \phi_\alpha^{(k)} / S^{(\alpha)}(\underset{\sim}{\phi}) \right| \right] \qquad \begin{matrix} \alpha = 1,\ldots,\sigma \\ k = 1,\ldots,N \end{matrix} \tag{3-63}$$

This criteria ensures numerical stability if $S^{(\alpha)}(\underset{\sim}{\phi})$ is a linear

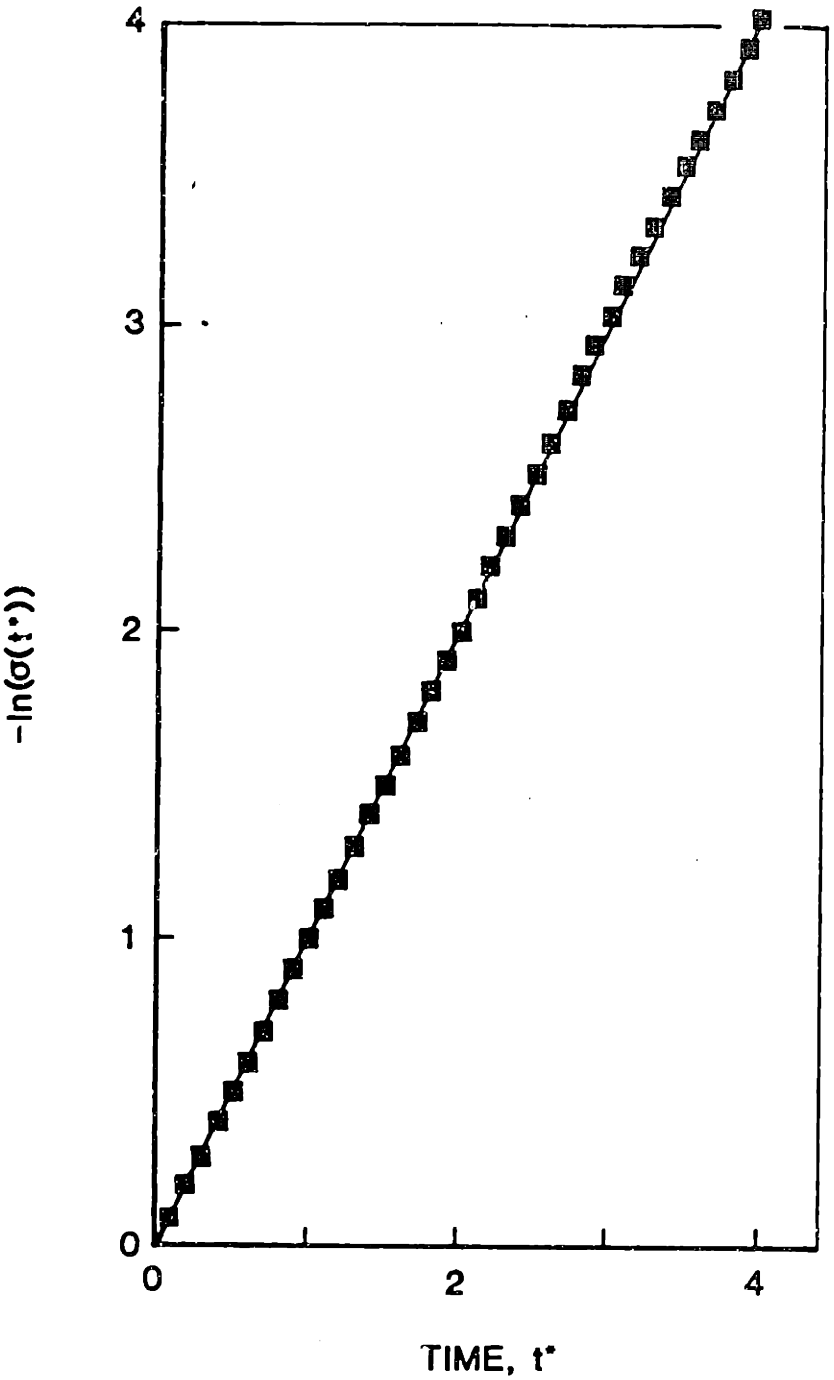

Figure 3-7 Reduction of the variance in tracer concentration due to mixing in homogenous and isotropic turbulence at a rate $1/t_m = 1.0$. Initially the variance is equal to one. The symbols are the simulated results. The solid line is the exact solution.

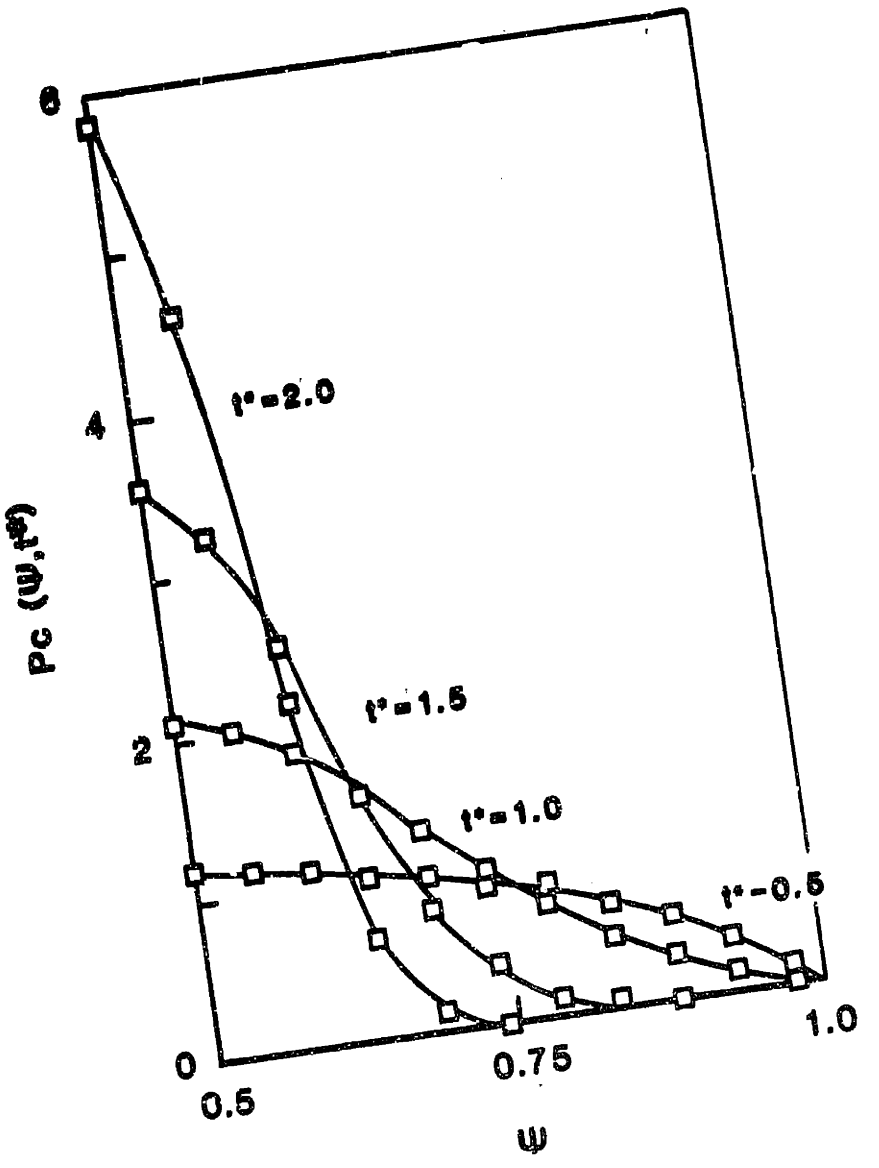

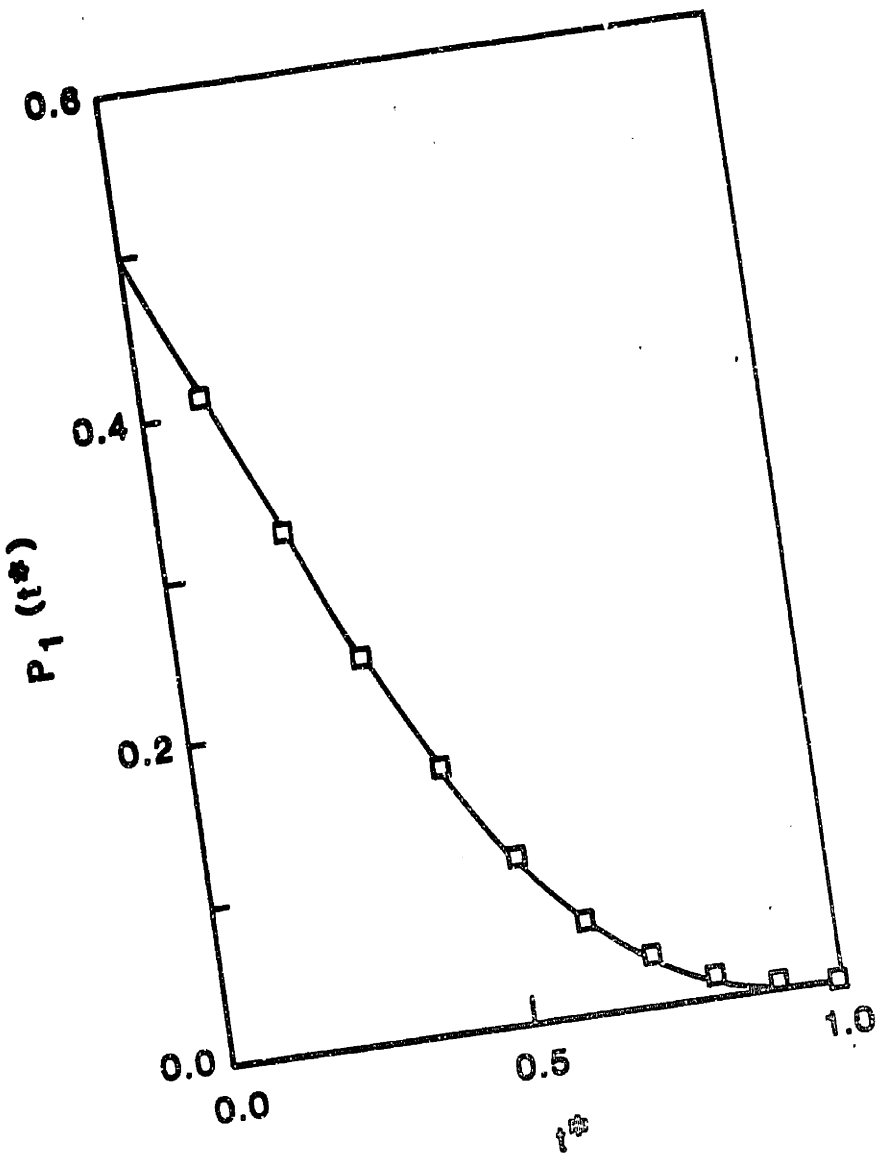

Figure 3-8 Evolution of the pdf of tracer concentration due to mixing for the conditions in Figure 3-7.

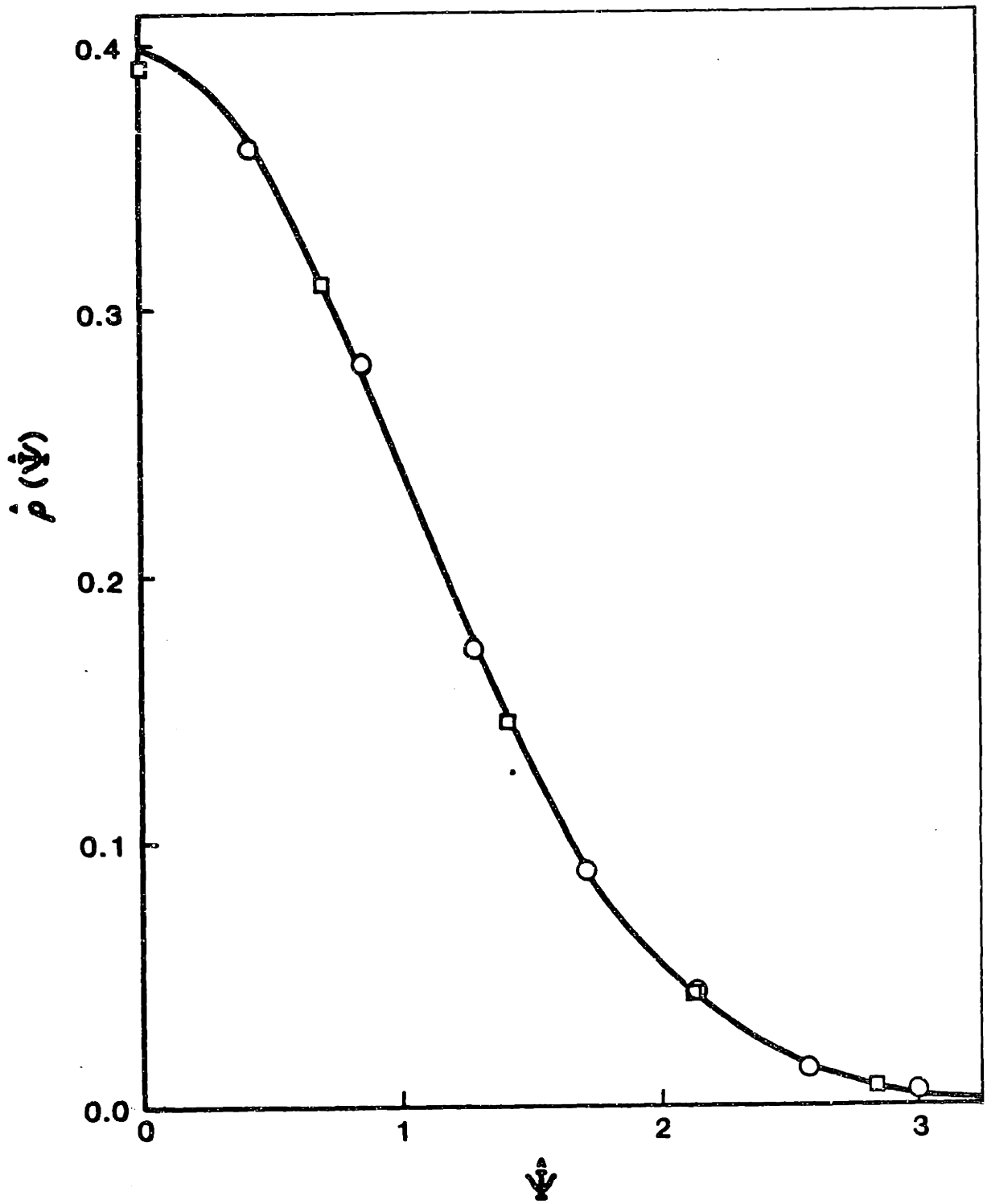

Figure 3-9 Asymptotic form of the normalized pdf of tracer concentration for the conditions in Figure 3-7 (circles, $t^* = 1.5$; squares, $t^* = 2.0$).

function of $\underset{\sim}{\phi}$ and is often sufficient to quarantee stability if $S^{(\alpha)}(\underset{\sim}{\phi})$ is nonlinear.

For fast reactions it is possible that the reaction time scale $\left|\phi_\alpha / S_\alpha^{(\alpha)}(\underset{\sim}{\phi})\right|$ is so short as to be comparable to the Kolmogorov time scale $(\nu/\varepsilon)^{1/2}$. If the source function $S^{(\alpha)}(\underset{\sim}{\phi})$ is dependent on the microscale shear rate $(\varepsilon/\nu)^{1/2}$, as for transport-limited particle growth reactions, for example, then there will be additional nonlinear interactions due to the correlation between the fluctuating dissipation rate and the fluctuating concentrations. To capture these interactions it is necessary to somehow simulate the spatial-temporal variation of the energy dissipation rate field.

In Section 2.2.1 the theory and experimental evidence for the statistics of the fluctuating turbulent energy dissipation rate were reviewed and it was indicated that the pdf of ε is highly skewed and approximately log-normal. By adopting this probability distribution for ε a crude but physically reasonable model for simulating its temporal variation may be devised. An advantage of assuming a log-normal form is that only two parameters are required to completely specify it, namely, the mean $\langle \ell n\ \varepsilon \rangle$ and variance $\sigma^2_{\ell n\ \varepsilon}$ of the logarithm of ε. Alternatively, we need only specify the mean value of ε and kurtosis of the velocity derivative since, employing the local isotropy assumption,

$$\langle \ell n\ \varepsilon \rangle = \ell n \langle \varepsilon \rangle - \ell n\ K_u^{1/2} \tag{3-64}$$

$$\sigma^2_{\ell n\ \varepsilon} = \ell n\ K_u \tag{3-65}$$

where K_u is the kurtosis of the fluctuating isotropic shear. The

kurtosis may be determined from the turbulent Reynolds number using the experimental data presented in Figure 2-1. Since K_u and $\langle\varepsilon\rangle$ will in general vary from node to node we have a crude representation of the spatial variation of the dissipation rate field.

To simulate the temporal variation of ε we adopt the following simple algorithm. Starting from t = 0 a random value of $\varepsilon(\underset{\sim}{x},0)$ is chosen from the pdf of ε, knowing the local values $\langle\varepsilon(\underset{\sim}{x})\rangle$ and $K_u(\underset{\sim}{x})$. This level of ε is assumed to be constant for a time equal to the Kolmogorov time scale $\Delta t_1 = (\nu/\varepsilon(\underset{\sim}{x},0))^{1/2}$. At time $t_1 = \Delta t_1$ a new random value $\varepsilon(\underset{\sim}{x}, t_1)$ is chosen and held constant for a time $\Delta t_2 = (\nu/\varepsilon(\underset{\sim}{x},t_1))^{1/2}$. By building up a times series of ε values in this way both the statistics of the fluctuating dissipation rate and its intermittent behavior (once in a while a very large value of ε from the tail of the log-normal distribution will be chosen and held constant for a very short time) at a point in space will be preserved. A separate ε-time series is simulated for each element $\underset{\sim}{\phi}^{(k)}$ at each node.

Although the formulation of the reaction algorithm is conceptually the simplest the computer time required to integrate the source function $S^{(\alpha)}(\underset{\sim}{\phi})$ over the time step Δt_r for all elements at all nodes is normally the rate-limiting step in the entire simulation. It is thus expedient to make sure that the algorithm that performs the integration in Eq. 3-62 is as computationally efficient as possible.

3.6 Assessment of the Model

In the last three sections we have presented algorithms for simulating the influence of various processes on the evolution of the local joint scalar probability density function. All of the algorithms

are procedures for modifying one or more attributes of the Monte Carlo elements. The attributes that have been identified include representative concentration, location in physical space, advective age, settling age, mixing age and life expectancy. Each physical or chemical process has its own time scale. The time scales are summarized in Table 3-1. In the simulation each process is performed at a separate rate with the process time step being a fraction of the process time scale. With these algorithms in hand it is now quite simple to put them together into a complete model of any level of complexity. All that is required is a main program to keep track of all the process times and control the execution of each process. It is evident that the Monte Carlo technique for solving the pdf transport equation is particularly attractive because it can be implemented easily and adapted for a wide range of applications.

Test simulations have been performed to demonstrate the validity of each stochastic algorithm. These simulations have also illustrated the level of accuracy that may be achieved with the Monte Carlo technique. There are two types of error that are associated with the Monte Carlo procedure. Since the joint scalar pdf is represented at each point by a finite number N of elements there is sampling error that is proportional to $N^{-1/2}$. To reduce the sampling error by a factor of one-half one must either quadruple the number of elements in the simulation or perform the simulation four times and average the results. Pope (1981) has shown that the sampling error is unbiased and is independent of the grid spacing. Based on extensive analysis he determined that the standard error in the mean concentration estimate for constituent α, $(\varepsilon_{st})_\alpha$, may be estimated from

Table 3-1. Process Time Scales

Process	Time Scale	
advection	$t_a^{(i)} = \dfrac{(x_j - x_{j-1})}{\langle U_i(x_j)\rangle}$	$i = 1,2,3$
diffusion	$t_d^{(i)} = \dfrac{(x_j - x_{j-1})\,\Delta x_j}{\Gamma^{(i)}((x_j + x_{j-1})/2)}$	$i = 1,2,3$
settling	$t_s^{(\alpha)} = \dfrac{(x_j - x_{j-1})}{w_s^{(\alpha)}}$	$\alpha = 1,2,\ldots,\sigma$
mixing	$t_m = \begin{cases} 2.7\ (3 - Sc)^{-2}\ k/\varepsilon & Sc \leq O(1) \\ 2.0\ k\ /\varepsilon + 0.5(\nu/\varepsilon)^{1/2}\ \ell n\ Sc & Sc \gg 1 \end{cases}$	
reaction	$t_r = \left\lvert \dfrac{\langle \phi_\alpha \rangle}{S^{(\alpha)}(\underset{\sim}{\phi})} \right\rvert$	$\alpha = 1,2,\ldots,\sigma$

$$(\varepsilon_{st})_{\alpha} = b\,\sigma_{\alpha}\,N^{-1/2} \qquad (3\text{-}66)$$

where σ_{α} is the standard deviation of the pdf for constituent α and b is a constant equal to 1 ± 0.5. The second type of error is due to the use of stochastic algorithms that are equivalent to truncated finite-difference operators. Since the solution procedure is explicit the scheme is first-order accurate in time. If Pope's advection algorithm is used the scheme is also first-order accurate in space. With the use of the improved advection algorithm, however, the spatial accuracy becomes limited by the diffusion operator, which is second-order. Hence, the overall accuracy of the simulation may be controlled through the time step, the grid spacing and the total number of elements per node.

Any increase in the desired accuracy of the simulation will come at the expense of additional computational cost. Consider an integration performed over a total simulation time T. During the simulation each process will be executed a total number of times equal to the simulation time divided by the time step for that process. If only dissolved constituents are included in the simulation then all constituents will be transported through physical space at the same rate. In this case the advection and diffusion algorithms will modify the spatial location of elements only. If solid and dissolved constituents are included, however, each will be transported differentially through physical space and we must keep track of the spatial location of each representative concentration in each element. For the estimates presented below it will be assumed that both solid and dissolved constituents are included

in the simulation. Let the total number of constituents be denoted by σ and the total number of elements in the simulation by N_T. The total amount of computer work involved in performing the advection and diffusion operations will be proportional to the total number of representative concentrations whose spatial location is modified times the total number of operations performed in the simulation. For Pope's advection and diffusion algorithms the computer work will be proportional to $(\sigma N_T \langle U \rangle \Delta t_a / \Delta x)\ (T/\Delta t_a)$ and $(\sigma N_T \Gamma \Delta t_d / (\Delta x)^2)(T/\Delta t_d)$, respectively. Thus we see that the computer work for these algorithms is independent of the time step. For these algorithms no penalty is incurred in decreasing the time step to improve the accuracy. With the extension of Pope's algorithms to variable grid spacing and element density it is not possible to write an exact expression for the computer work, but whatever it may be it will still be independent of the time step. Let us assume that for this case the computer work may be described with a proportionality similar to that for Pope's algorithms but with characteristic values of $N_T \langle U \rangle / \Delta x$ and $N_T \Gamma / (\Delta x)^2$ instead of exact values. As compared to Pope's simple algorithms the extended algorithms will also have a larger proportionality constant because of the larger number of manipulations involved in the execution of each operation. The computer work involved in executing the improved advection algorithm is proportional to $\sigma N_T (T/\Delta t_a)$ since at every time step all the elements must be aged and searched for those elements whose advective age exceeds the residence time. A similar proportionality holds for the differential settling algorithm except that only the solid constituents have their spatial location modified by this process, and the settling of each size class is executed at a different rate. For

Pope's molecular mixing algorithm we must age all elements and search for those elements whose mixing age exceeds their life expectancy. Assuming that all constituents mix at the same rate the computer work is thus proportional to $N_T T/\Delta t_m$.

The proportionality expressions for the computer work due to each process are summarized in Table 3-2. Also included are the unit costs in terms of CPU seconds on a Honeywell/Multics computer. For the advection, diffusion and settling algorithms the unit costs correspond to the cost of modifying the spatial location of a single representative concentration by that algorithm. For the mixing algorithm the unit cost represents that required to mix a single pair of elements. These estimates are necessarily quite gross and are reported only for the purpose of estimating the order of magnitude of the cost of an anticipated simulation. As previously mentioned the rate-limiting step in any simulation is normally due to the reaction process. For the coagulation process, for example, the cost of implementing the reaction algorithm is proportional to $1/2\ \sigma^2 N_T T/\Delta t_r$.

As discussed in Section 3.1 the solution of the pdf transport equation is generally necessary if one wants to compute the transport of constituents undergoing fast, nonlinear reactions. If the reactions considered are very slow with respect to the mixing rate or they are linear, then it is more expedient to solve a finite difference or finite element formulation of the transport equation for the mean concentration, Eq. 1-1. On the other hand, as pointed out by Pope (1981), a finite difference or finite element solution of the pdf transport equation is computationally inefficient because of the high cost associated with evaluating the double integral in the mixing model, Eq.

Table 3-2. Computational Efficiency of the Monte Carlo Model

Algorithm	Computer Work Proportional To	Unit Cost (CPU Seconds)
Pope's advection	$\sigma N_T \langle U \rangle T/\Delta x$	1×10^{-4}
Pope's diffusion	$\sigma N_T \Gamma T/(\Delta x)^2$	2×10^{-4}
variable N_j and Δx_j advection	$\sigma(N_T \langle U \rangle/\Delta x)^* T$	1×10^{-4}
variable N_j and Δx_j diffusion	$\sigma(N_T \Gamma/(\Delta x)^2)^* T$	2×10^{-4}
improved advection	$\sigma N_T T/\Delta t_a$	6×10^{-5}
differential settling (per solid constituent)	$N_T T/\Delta t_s^{(\alpha)}$	6×10^{-5}
Pope's mixing	$\sigma N_T T/\Delta t_m$	1×10^{-4}

* denotes characteristic value

3-44, over all constituent concentrations and for each node. Pope estimates this cost to be proportional to $\exp(6\sigma)$. With the Monte Carlo technique, however, the cost of solving the pdf transport equation generally increases linearly with σ (although with coagulation included it increases with σ^2). Pope indicated that for $\sigma \geq 4$ a finite difference solution of the pdf equation was not feasible.

Thus, if we want to model fast, nonlinear reactions the Monte Carlo technique presented here is the most computationally efficient scheme and it also has the advantage of being extremely flexible and easy to implement. It was indicated in Section 2.4 that the coagulation of particles at concentrations of 100 mg/ℓ or greater is sufficiently fast to interact nonlinearly with the turbulence. The initial formation of frazil ice in rivers is another example of a fast nonlinear reaction involving suspended particles. In the next chapter we will demonstrate the potential usefulness of the Monte Carlo model by performing several hypothetical, but typical, simulations involving the reactive transport of suspended particles.

IV. MODEL APPLICATIONS

In this chapter we wish to present several examples involving the modeling of the reactive transport of suspended particles. Suspended particles participate in such reactions as precipitation/dissolution, coagulation, and sorption. Accordingly, the model applications presented here involve the nucleation and growth of frazil ice in rivers, the coagulation and settling of sludge particles discharged from a coastal outfall, and the desorption of copper from contaminated sediments following a resuspension event. The examples have been chosen so as to demonstrate as much as possible the full range of capabilities afforded by the modeling techniques presented in the previous two chapters.

4.1 Frazil Ice Formation

The initial formation of ice in natural water bodies is governed by the interaction of both physical and climatic factors. If the flow is only weakly turbulent then heat transfer across the water surface will deplete the heat content of the surface waters while the deeper waters remain relatively unaffected. As the surface water temperature drops below the freezing point thin floating ice plates form which grow slowly in lateral extent and attach themselves to each other and to solid boundaries, such as the shore. The accumulation of free-floating ice plates by attached plates results in the formation of a continuous ice sheet that grows outward from solid boundaries and eventually forms a complete ice cover. If the water is sufficiently turbulent, however, mixing of surface waters with deeper waters will create a uniform

temperature distribution with depth. The turbulence will also carry ice nuclei formed at the surface downward into suspension. As they melt the suspended ice nuclei will continually cool the water column until it becomes supercooled by a few hundredths of a degree Centigrade. At this point the ice nuclei will begin to give off heat and grow in size into what is known as frazil ice (Michel, 1971; Ashton, 1979).

Frazil crystals growing in supercooled water are called active frazil because of their fast rate of growth and their strong tendency to attach themselves to boundaries and other solid objects in the flow, including each other. As the crystals grow and flocculate they eventually reach a size where their buoyancy overcomes the turbulent transport and they float to the surface. These spongy masses of ice then agglomerate into so-called pans of order 1 m in diameter and 0.1 to 0.5 m in thickness and finally into floes with diameters of order 1 to 30 m and thickness 0.5 to 5 m. When the frazil ice particles have depleted the supercooling they become non-cohesive and are then called passive frazil (Ashton, 1979; Martin, 1981).

Because frazil ice is only formed in high energy flows it is not often observed in lakes but it occurs regularly in northern rivers and coastal ocean waters. The formation of ice particles in suspension and the subsequent agglomeration process result in the production of tremendous volumes of porous ice. Consequently, frazil ice may be responsible for severe obstruction of flow passages and thus cause such problems as blockage of hydroelectric reservoirs, freezing of submerged hydraulic structures, flooding, interference with navigation, and obstruction of intakes for water supply (Michel, 1971; Osterkamp, 1978). The development of an analytical framework for predicting the

initiation and for computing the production of frazil ice would thus be of great engineering interest.

In the hope of making further progress towards this goal we will present a kinetic model for the nucleation and growth of suspended frazil ice particles. The kinetic model will then be incorporated into a one-dimensional formulation of the scalar pdf transport model and used to examine the formation of frazil ice in rivers. We begin with a brief review of the kinetics of frazil ice growth. Further details on frazil ice dynamics may be obtained from the recent report by Daly (1984).

4.1.1 Initial Nucleation

The nucleation of frazil ice is observed to occur at a level of supercooling of only a few hundredths of a degree Centigrade. This observation rules out homogeneous nucleation of pure water as a possible nucleation mechanism because it is only effective at water temperatures less than -38°C, which are never found in any natural water body. The second possible mechanism, heterogeneous nucleation, requires the presence of foreign particles as nucleation sites and a level of supercooling of -4°C or more. Although suspended particles are abundant, water temperatures of -4°C have never been observed in turbulent natural flows, not even in the thermal boundary layer at the water surface. The only remaining possibility is a mass transfer process whereby seed crystals are introduced from the atmosphere into the water column. Likely sources of seed crystals are snow and ice particles that fall from trees or are carried by the wind and air-borne water droplets created by splashing, wind spray and air-bubble bursting that freeze in the air and drop into the flow as ice particles (Osterkamp, 1978; Daly, 1984).

While the introduction of seed crystals into the flow from the atmosphere may be the initial source of frazil ice nuclei, it does not account for the very high particle number concentrations that are observed. The mechanism which generates frazil nuclei from ice particles already present in the flow is secondary nucleation.

4.1.2 Secondary Nucleation

Secondary nucleation is termed secondary because it requires the presence of seed crystals of the material being crystallized, as opposed to primary (homogeneous and heterogeneous) mechanisms which do not require seed crystals. Denk and Botsaris (1972a) have identified three mechanisms by which secondary nuclei may be generated by the parent crystal: (a) by the growth and detachment of surface irregularities, (b) by the ordering of the solute molecules near the surface of the parent crystal which leads to a high local supersaturation and induces primary nucleation, and (c) by the uptake of impurities by the growing parent crystal which reduces the impurity concentration near the crystal surface sufficiently that primary nucleation becomes possible locally. With respect to frazil ice formation the last two mechanisms are unlikely sources of secondary nuclei because of the high levels of supersaturation (supercooling) required for primary nucleation and because the possible numbers of nuclei produced by these mechanisms would not be sufficient to explain the observations. In any case, at low supersaturation the first mechanism is the main source of secondary nuclei (Ottens, Janse, and DeJong, 1972).

Evans, Margolis, and Sarofim (1974) demonstrated experimentally that the rate of production of secondary nuclei in agitated

crystallizers is removal-limited, that is, depends on the rate of detachment of surface irregularities rather than the rate of growth of the irregularities. They indicated that fluid shear and collisions of crystals with hard surfaces (including other crystals) could cause the detachment of surface irregularities. In the literature the latter mechanism is called contact nucleation or collision breeding. Based on experimental studies, Denk and Botsaris (1972b) and Desai, Rachow, and Timm (1974) have shown that the number of nuclei produced by contact nucleation is a function of the contact energy, the supersaturation, the impurity concentration, and the level of mixing.

To explain the observed dependence on the supersaturation Lal, Mason and Strickland-Constable (1969) put forward the "survival" theory whereby the number of nuclei produced by the collision itself was independent of the supersaturation but only those nuclei that were larger than the critical radius grew in size while those smaller dissolved. The critical radius r_c is that required to overcome the effect of surface tension and is determined from the Gibbs-Thomson equation as (Lal et al., 1969)

$$r_c = \frac{2\gamma}{\rho_i L} \left(\frac{T_e}{T_e - T}\right) \qquad (4\text{-}1)$$

where, for ice crystals, γ is the ice-water interfacial tension, ρ_i is the density of ice, L is the latent heat of fusion, T_e is the equilibrium temperature of the ice-water mixture (i.e., the saturation temperature) and T is the bulk fluid temperature in °K. For ice, γ = 22 ergs/cm^2, L = 3.3 × 10^9 ergs/gm and ρ_i = 0.92 gm/cm^3 (Fletcher, 1970). From Eq. 4-1 we see that as the supersaturation increases the

critical radius decreases so that more nuclei may survive. Garside and Larson (1978) investigated the production of secondary nuclei by direct microscopic observation of low energy contacts between a crystal and a solid rod. Contrary to the survival theory they observed that secondary nuclei were produced over the size range between 1 and 50 μm and that the level of supersaturation determined the number of large nuclei that were chipped off the parent crystal. In saturated and undersaturated solutions large nuclei were not produced by contact of the rod with the crystal.

Summarizing, for frazil ice crystals it appears that the dominant mechanism of secondary nucleation is collision breeding. The rate of production of nuclei depends on the rate of collisions between crystals, on the energy associated with each collision and, to a lesser extent, on the super-saturation and the impurity concentration. Since the supercooling is so small, on the order of 0.01 °C, we can assume that no large nuclei are produced by collisions between crystals and that all the nuclei have a size comparable to the critical radius. Substituting a supercooling of 0.01 °C into Eq. 4-1 indicates that the critical radius for ice is of order 4 μm.

4.1.3 Growth

In general, the growth of frazil ice is controlled by the crystal morphology, the rate of incorporation of water molecules into the crystal surface, and the transfer of latent heat away from the crystal. At low supercoolings characteristic of turbulent waters the dominant shape for ice crystals is a flat disc with diameter-to-thickness ratio ranging from 5 to 100. Frazil ice crystals apparently maintain their

disc shape up to a diameter of 300 μm. Further growth results in the appearance of scalloped edges and dendritic growths along the perimeter of the crystal. This instability seems to limit the maximum disc size to about 300 μm (Daly, 1984).

The disc shape morphology is a result of anisotropy in the growth rates of ice along the two axes. The growth rate along the radial axis is heat transfer controlled while that along the longitudinal axis is much slower and controlled by the intrinsic kinetics at the crystal surface. Daly (1984) has shown that if the size of the frazil disc is defined by its radius r, then the crystal growth rate may be modeled with an expression indicative of transport (heat transfer) limitation, namely,

$$\frac{dr}{dt} = \frac{h}{\rho_i L}(T_e - T) \tag{4-2}$$

where h is the heat transfer coefficient.

Batchelor (1979, 1980) has determined that the heat transfer rate from small particles suspended in turbulent fluid is

$$h = \frac{k}{r}[1 + 0.17\ Pe^{1/2}] \qquad Pe = \frac{r^2 \varepsilon^{1/2}}{\alpha \nu^{1/2}} \ll 1 \tag{4-3}$$

$$h = \frac{k}{r}[1 + 0.55\ Pe^{1/3}] \qquad Pe \gg 1 \tag{4-4}$$

where Pe is the particle Peclet number and α and k are the thermal diffusivity and the thermal conductivity, respectively, of the fluid. These relationships are applicable for spherical particles of radius $r < 10\eta$, where η is the Kolmogorov micro-scale. Since $Pe = Pr(r/\eta)^2$ where

the Prandtl number Pr for heat transfer is 13, then Pe < 1 for r < 0.3 η. For a minimum value of η = 0.3 mm in the aquatic environment we see that the low Peclet number relation will usually be appropriate since the maximum disk size is 150 μm in radius. We also note that at small Peclet numbers the heat transfer is dominated by diffusion and is thus insensitive to the shape of the particle. In modeling the growth of frazil ice in natural waters we need not concern ourselves with the fact that the crystals are discs rather than spheres.

4.1.4 Sintering

The mechanism which causes frazil ice crystals to flocculate is fundamentally different from that which causes coagulation of colloidal particles. The coagulation of colloids in water of sufficient ionic strength is brought about by interactions between electrostatic forces and attractive van der Waals' forces. The flocculation of ice crystals, on the other hand, results from the tendency of crystals to minimize their surface free energy. The most stable shape in terms of surface free energy is a sphere. The point of contact between two frazil discs thus represents a highly unstable system. The chemical potential gradient existing between two crystals brought into contact drives the transfer of material to the point of contact in such a way that a solid neck or bridge forms between them. This process is called sintering. The rate of growth of the neck is proportional to the supercooling (Hobbs, 1974). Extrapolating from experimental measurements of the sintering of the two spheres in air, Martin (1981) has determined that the time required for two spheres of radius 1 μm to form a neck of width equal to one-quarter of the sphere diameter would be of the order of

10^{-2} seconds. This is sufficiently fast to account for the observed flocculation of frazil ice particles in turbulent flow.

4.2 A Zero-Dimensional Model of Frazil Ice Kinetics

To develop a model for the kinetics of frazil ice growth we may make use of the few reported experimental studies of frazil formation in laboratory flumes. The ability of the proposed model to reproduce the experimental data as well as the observed sensitivity to variations in physical parameters is interpreted as a convincing demonstration of its validity.

4.2.1 Model Assumptions

A complete model for the kinetics of frazil ice requires separate submodels for the effects of initial nucleation, secondary nucleation, growth, and flocculation. In addition the model must conserve overall mass and energy. Consider an isotropic and homogeneous water environment initially at temperature $T > T_e$, where T_e is the ice-water equilibrium temperature, and from which heat is continually and uniformly extracted at the constant rate Q (energy per unit volume of water per unit time). To model initial nucleation, as soon as the temperature drops below the equilibrium temperature we introduce seed crystals of radius r_c, where r_c is the critical radius, into the environment at a constant rate I_o (number per unit volume of water per unit time). The parameter I_o must be specified empirically. Since there are no available measurements of initial seeding rates or size distributions, the approximate value of I_o will be deduced by comparison of observations with simulated supercooling curves. The only

observed effect that the initial seeding has on the formation of frazil ice is in the time lag required to reach the point of maximum supercooling. Therefore, there is no point in attempting to specify the size distribution of the initial nuclei since the additional empirical parameters that would be introduced would not contribute any more information.

To model secondary nucleation we adopt the procedure put forward by Evans, Sarofim, and Margolis (1974). The number of nuclei produced per unit volume per unit time $I(v_i,v_j)$ due to collisions between crystals of size v_i and v_j is modeled as

$$I(v_i,v_j) = Z\, c(v_i,v_j) \tag{4-5}$$

where $c(v_i,v_j)$ is the rate of energy transfer to the crystals by the collisions, per unit fluid volume, and Z is the number of nuclei generated per unit of collision energy. In principle Z is a function of the impurity concentration and the level of supercooling. However, since we are dealing with very small variations in the supercooling and impurity concentration, Z will be assumed constant. As with the initial seeding rate the approximate magnitude of Z will be obtained by comparison of observations with simulated results. Also, as discussed above, since the supercooling will be very low there will be effectively no large nuclei produced by collisions so that it can be assumed that all secondary nuclei have a radius comparable to the critical radius r_c. Following Evans et al., to model the function $c(v_i,v_j)$ we assume that collisions between particles are sufficiently inelastic that after colliding two particles have no relative velocity. Conservation

of momentum and energy then yields the result

$$c(v_i,v_j) = \frac{1}{2}\frac{m(v_i)\ m(v_j)}{m(v_i) + m(v_j)}\left[\beta_{sh}(v_i,v_j)\ E_{sh}(v_i,v_j)\right.$$
$$\left.\omega_{sh}^2\ (v_i,v_j) + \beta_{dr}(v_i,v_j)\ E_{dr}(v_i,v_j)\ \omega_{dr}^2(v_i,v_j)\right]$$
$$g(v_i)\ g(v_j) \qquad (4\text{-}6)$$

where $g(v_i)$ is the number density function, $m(v_i)$ is the mass associated with particles of size v_i, $\omega(v_i,v_j)$ is the relative velocity of the particles prior to collision, $\beta(v_i,v_j)$ is the collision frequency function and $E(v_i,v_j)$ is the collision efficiency function. The subscripts sh and dr indicate the turbulent shear and differential rising mechanisms. Since the minimum particle size is of order 4 μm in radius we can neglect Brownian motion as a collision mechanism. Substituting the expressions for β and ω presented in Section 2.2.1 yields

$$c(v_i,v_j) = \frac{1}{2}\rho_i\frac{v_i\ v_j}{v_i + v_j}\left[b(v_i^{1/3} + v_j^{1/3})^5\ (\frac{<\varepsilon>}{\nu})^{3/2}\ E_{sh}(v_i,v_j)\right.$$
$$+ 0.00076\ \left(\frac{g}{\nu}\frac{(\rho - \rho_i)}{\rho}\cdot\left|v_j^{2/3} - v_i^{2/3}\right|\right)^3 (v_j^{1/3} + v_i^{1/3})^2$$
$$\left.E_{dr}(v_i,v_j)\right]\ g(v_i)\ g(v_j) \qquad (4\text{-}7)$$

where ρ_i is the ice density and $b = 0.0033$ with Saffman and Turner's (1956) model for the collision frequency function for turbulent shear while $b = 0.0066/K_u^{3/4}$ for the improved model proposed in Section 2.2.1.

To conserve mass, when nuclei are removed from the parent crystal we must decrease the volume of each parent crystal by $\Delta v_{ij} = I(v_i,v_j)v_c\Delta t/2$, where $v_c = 4\pi r_c^3/3$. Since the continuous size range will be discretized into size classes, this is accomplished by removing all the mass from size class v_i and re-proportioning it between the size classes v_k and v_{k+1}, where $v_k \leq v_i + \Delta v_{ij} \leq v_{k+1}$. The re-proportioning is performed in the same manner as in the solution of the coagulation equations described in Section 2.4.

The actual growth of frazil ice crystals is governed by the thermal energy balance

$$\frac{d M_i}{dt} = \frac{1}{L}\left(\rho c_p \frac{dT}{dt} + Q\right) \tag{4-8}$$

where M_i is the total mass of ice per unit volume of water, ρ is the water density, L is the latent heat of fusion and c_p is the heat capacity of water. The cooling rate Q is specified as input. The rate of increase of total ice mass is given by

$$\frac{dM_i}{dt} = \rho_i \int_{r_c}^{\infty} \frac{4\pi r^3}{3} g(r,t)\, dr \tag{4-9}$$

where $g(r,t)$ is the particle number density distribution. The rate of growth dr/dt is computed from Eqs. 4-2 and 4-3 or 4-4. The growth of ice crystals results in a volume increase Δv_j for each size class. As with the removal of secondary nuclei, the addition of ice mass is accomplished by removing all the mass from size class v_i and re-proportioning it between the size classes v_k and v_{k+1}, where $v_k \leq v_j + \Delta v_j \leq v_{k+1}$. Having computed dM_i/dt the bulk water temperature may be updated using Eq. 4-7.

To model the flocculation of frazil crystals the coagulation equation will be employed with only turbulent shear and differential rising considered as collision mechanisms. It will also be assumed that the collision efficiency functions presented in Section 2.2.2 are applicable. To limit the number of unknown parameters the collision efficiency function for turbulent shear corresponding to a value of $H = 10^{-2}$, defined by Eq. 2-30, will be adopted for all the simulations to be performed. As indicated by Figure 2-3, this is a relatively high level of efficiency. The integration of the coagulation equation will be performed as described in Section 2.4.

4.2.2 Model Verification

To determine typical values of the parameters I_o and Z and to demonstrate the validity of the kinetic model described above comparisons of model simulations with experimental data will be made. All the experiments have produced the same kind of quantitative result, namely, a time history of the bulk water temperature as frazil ice nucleates and grows through its active phase. A typical supercooling curve is shown in Figure 4-1, taken from Michel (1963). The initial linear decrease in temperature is due to a constant cooling rate in the absence of ice growth. Shortly after the temperature drops below the equilibrium temperature frazil ice particles begin to nucleate and grow. The release of latent heat of fusion causes the time rate of decrease of temperature to decrease until a minimum temperature is reached at which the rate of heat extraction from the ice-water mixture is balanced by the rate of latent heat release by the growing crystals. Up to this point the rate of frazil ice production increases steadily,

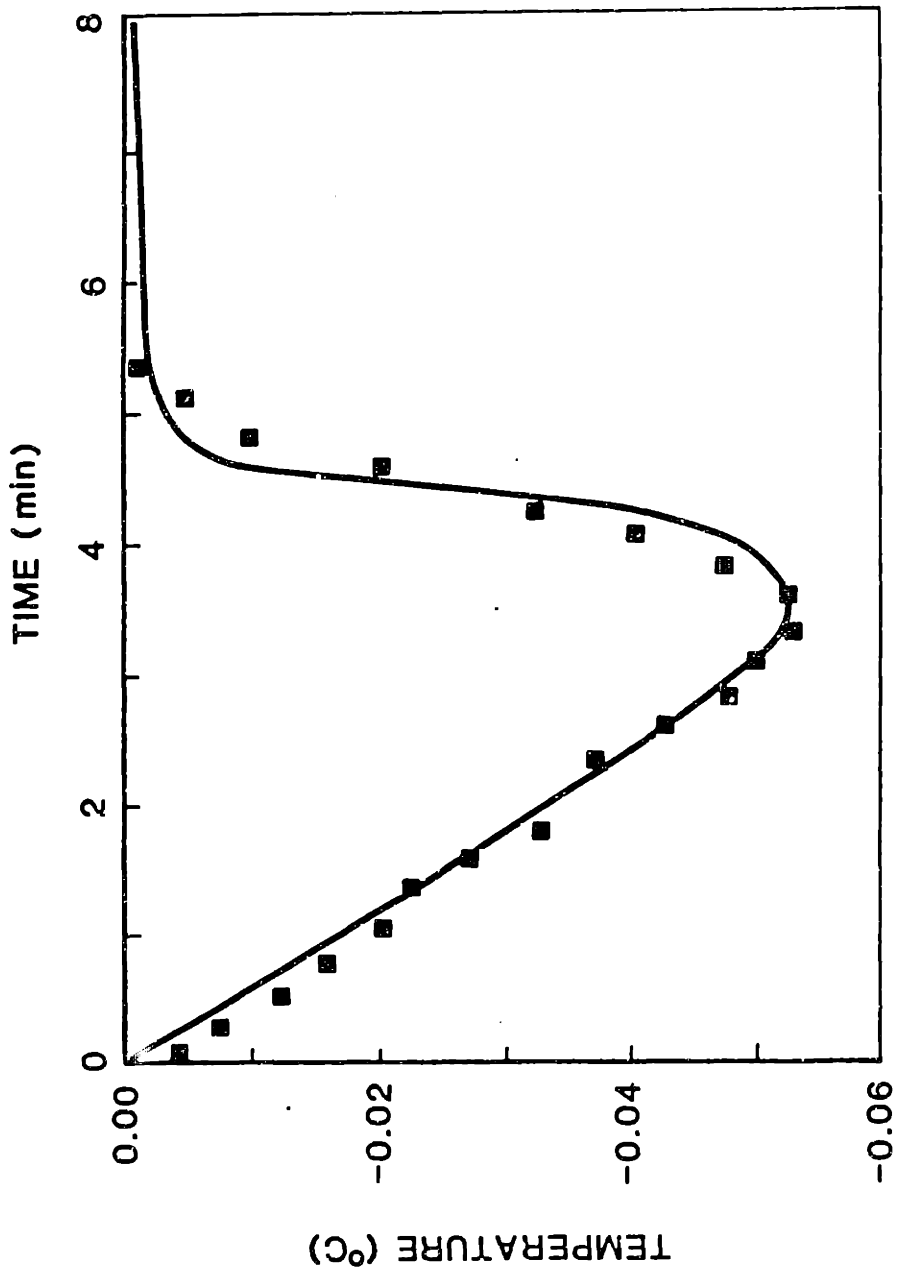

Figure 4-1 Calibration of kinetic model of frazil ice growth (symbols, Michels' (1963) data; solid line, model simulation with $\langle \epsilon \rangle = 50$ cm^2/sec^3, $I_o = 0.05$ nuclei/cm^3-sec, $Z = 4 \times 10^{17}$ nuclei/J, $Q = 0.0012$ J/cm^3-sec).

although the particles are still not large enough for their buoyancy to be significant. Beyond the point of maximum supercooling the release of latent heat exceeds the surface cooling rate and the temperature rises again at a relatively rapid rate. This rapid temperature increase corresponds to the maximum rate of ice production. The frazil particles begin to flocculate and rise to the water surface. As the temperature approaches a constant but very small level of supercooling, termed the residual supercooling, the rate of ice production decreases and levels off at a constant rate that is a function of the cooling rate only. Beyond this point the surface cooling causes the passive growth of the floating ice floes.

The first comparison is with the observations of Michel (1963), Figure 4-1. Michel performed his experiments in an outdoor recirculating flume consisting of a channel of 12 in. by 12 in. cross-section and a return 6-in. diameter pipe. All the conduits were fabricated of plexiglass. The flow was driven by a pump and could be varied from 150 gpm to 600 gpm. Since the turbulence intensity will be relatively high just downstream of the pump and relatively low in the channel section that in the pipe section of the flume may be considered as representing average conditions. For an average flow of 375 gpm, the Reynolds number is 3.6×10^4 and the friction factor $f = 0.0225$. The average energy dissipation rate may be estimated from $\varepsilon = f\bar{U}^3/2d$ as 50 cm^2/sec^3, where $\bar{U}$ is the average velocity and d is the pipe diameter. With this parameter fixed and the heat removal rate Q determined from the initial slope of the supercooling curves as 0.0012 J/cm^3 sec, the parameters I_o and Z were optimized to achieve the best model fit to Michel's experimental data, as shown in Figure 4-1.

The optimized values for the initial seeding rate I_o and the number of nuclei generated per unit of collision energy Z were 0.05 nuclei/cm^3-sec and 4×10^{17} nuclei/J, respectively. While the parameter Z may be regarded as somewhat universal, the initial seeding rate depends on local conditions and may be expected to vary.

There have been some experimental measurements of the parameter Z. Clontz and McCabe (1971) measured the energy of collision of a steel hammer striking a fixed crystal of epsomite immersed in a flowing supersaturated solution and, by viewing the crystal under a microscope, counted the number of nuclei that were produced. They obtained a value of $Z = 5 \times 10^6$ nuclei/J. Denk and Botsaris (1972b) used essentially the same technique and obtained a value of $Z = 1 \times 10^6$ nuclei/J for sodium chlorate. Strickland- Constable (1976) questioned the accuracy of the collision energy measurements since theoretical calculations which he performed to determine the minimum work needed to form a compact nucleus of epsomite yielded a value of $Z = 10^{13}$ nuclei/J. These results were obtained for crystals with smooth surfaces. To explain the somewhat higher value of $Z = 4 \times 10^{17}$ nuclei/J obtained in the numerical simulation we may note that the main contribution to secondary nucleation comes from the largest crystals present in the flow. As previously mentioned, frazil ice crystals develop dendritic growths and scalloped edges as they grow to sizes of order 300 μm in diameter. These surface irregularities will be sheared off quite easily upon contact. Hence we should expect the value of Z indicated by a growing suspension of frazil ice crystals to be much larger than that associated with the contact of a smooth crystal surface.

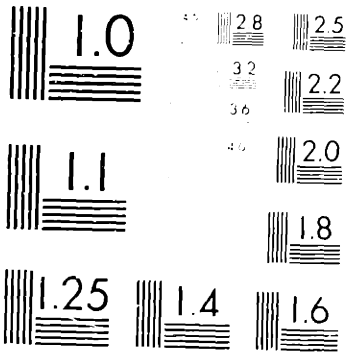

24x

The next two model simulations are to be compared with the observations of Carstens (1966). Carstens performed his experiments in an indoor flume in the shape of a race track with cross-section 20 cm by 20 cm. The flow was driven by a propeller. The first simulation corresponds to the data in Carstens' Figure 6A in which the flow velocity was reported to be 50 cm/sec. The friction velocity for an open channel flow may be estimated from the relationship $u_* = \bar{U}(f/8)^{1/2}$ where, for a smooth boundary, the friction factor f is determined from (Schlichting, 1968)

$$f^{-1/2} = 2 \log(R\, f^{1/2}) - 0.8 \qquad (4\text{-}10)$$

where $R = 4\bar{U}\, h/\nu$ is the Reynolds number. For a depth of flow h = 20 cm the Reynolds number R is 4×10^5, the friction factor is f = 0.14 and the friction velocity is $u_* = 2.4$ cm/sec. The depth variation in the energy dissipation rate for a channel flow is given by

$$\varepsilon(y) = \frac{u_*^3}{\kappa y}\left(1 - \frac{y}{h}\right) \qquad (4\text{-}11)$$

where κ is von Karman's constant. The average dissipation rate may be obtained by integrating this relationship from the top of the viscous boundary layer, $y = \nu/u_*$, to the water surface, y = h. The depth-average dissipation rate $\bar{\varepsilon}$ is

$$\bar{\varepsilon} = \frac{1}{h - \nu/u_*} \int_{\nu/u_*}^{h} \varepsilon(y)dy = \frac{u_*^3}{\kappa h}\left(\ln \frac{u_* h}{\nu} - 1\right) \qquad (4\text{-}12)$$

and is equal to 13 cm^2/sec^3 for this case. The cooling rate

indicated by Carstens' data is 0.0014 J/cm^3-sec. With the parameters I_o and Z fixed at their values determined from the fit to Michel's data, Figure 4-2 compares the model results with Carstens' experimental data presented in Figure 6A of his paper. The agreement is quite remarkable, although the experimental conditions do not vary that much from those reported by Michel, for which the model was calibrated. The final comparison is with the data presented in Carstens' Figure 7. Here the reported flow velocity was 33 cm/sec, corresponding to an average dissipation rate of $\bar{\varepsilon}$ = 4.0 cm^2/sec^3. The cooling rate indicated by the data is 5.5 × 10^{-4} J/cm^3-se . Figure 4-3 compares the model results with the experimental data and further confirms the validity of the kinetic model of frazil ice growth.

4.2.3 Sensitivity Analysis

To further demonstrate the validity of the kinetic model, the sensitivity of the model to variations in the physical input parameters will be compared with experimental observations. The base case for the simulations corresponds to the simulation of Michel's (1963) experimental data. Figure 4-4 shows the effect of varying the energy dissipation rate. In agreement with Carstens' (1966) observations, increasing the energy dissipation rate decreases the maximum supercooling and increases the rate of increase of temperature beyond the maximum supercooling. Figure 4-5 illustrates the differences in the particle size distributions resulting from different levels of ε. Since the particle growth rate is proportional to $\langle\varepsilon\rangle^{1/4}$, the coagulation rate to $\langle\varepsilon\rangle^{1/2}$ and the secondary nucleation rate to $\langle\varepsilon\rangle^{3/2}$, variations in the energy dissipation rate will influence the rate of

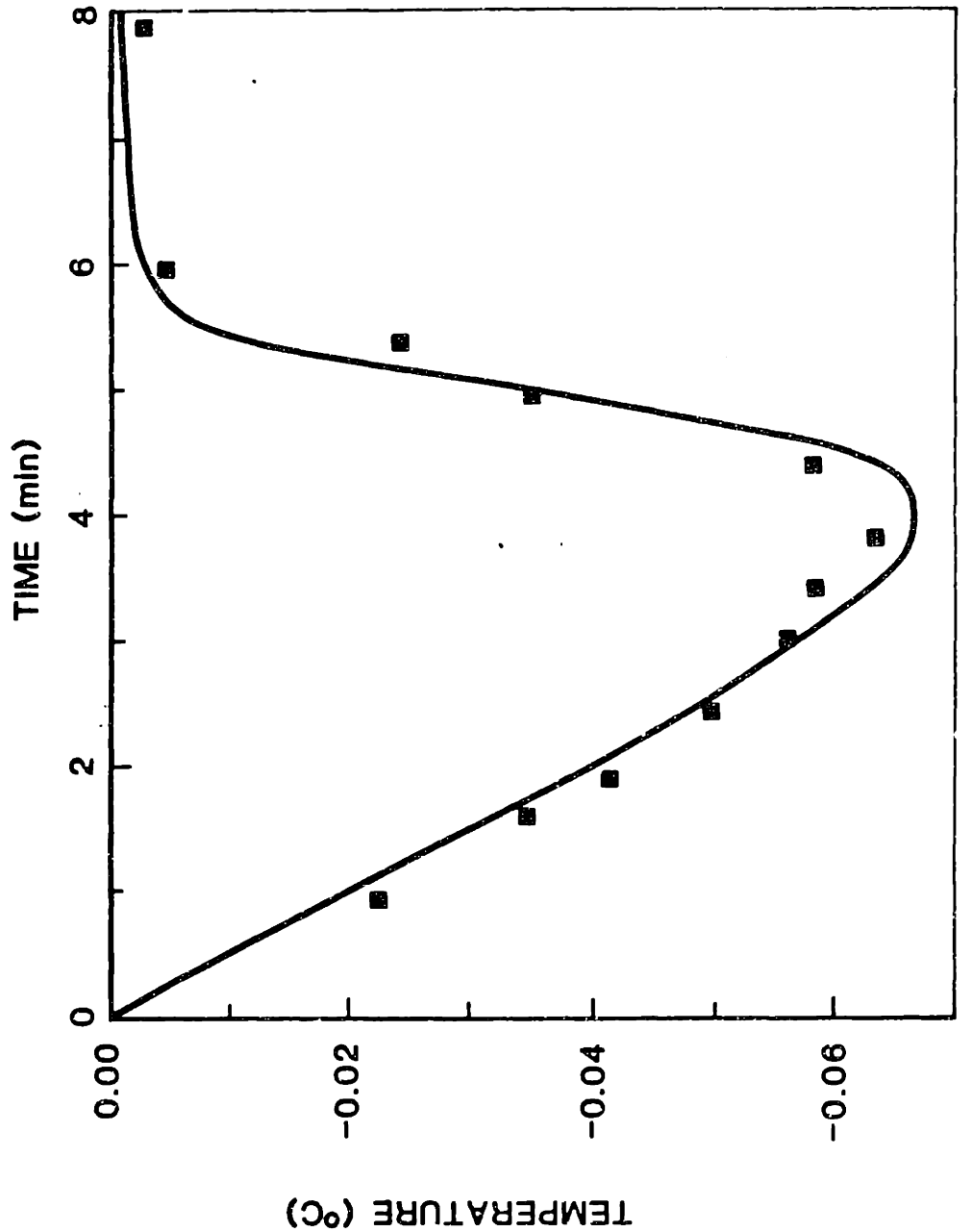

Figure 4-2 Verification of kinetic model of frazil ice growth (symbols, Carstens' (1966) Fig 6A data; solid line, model simulation with $\langle\varepsilon\rangle$ = 13 cm^2/sec^3, I_o = 0.05 nuclei/cm^3-sec, Z = 4 × 10^{17} nuclei/J, Q = 0.0014 J/cm^3-sec).

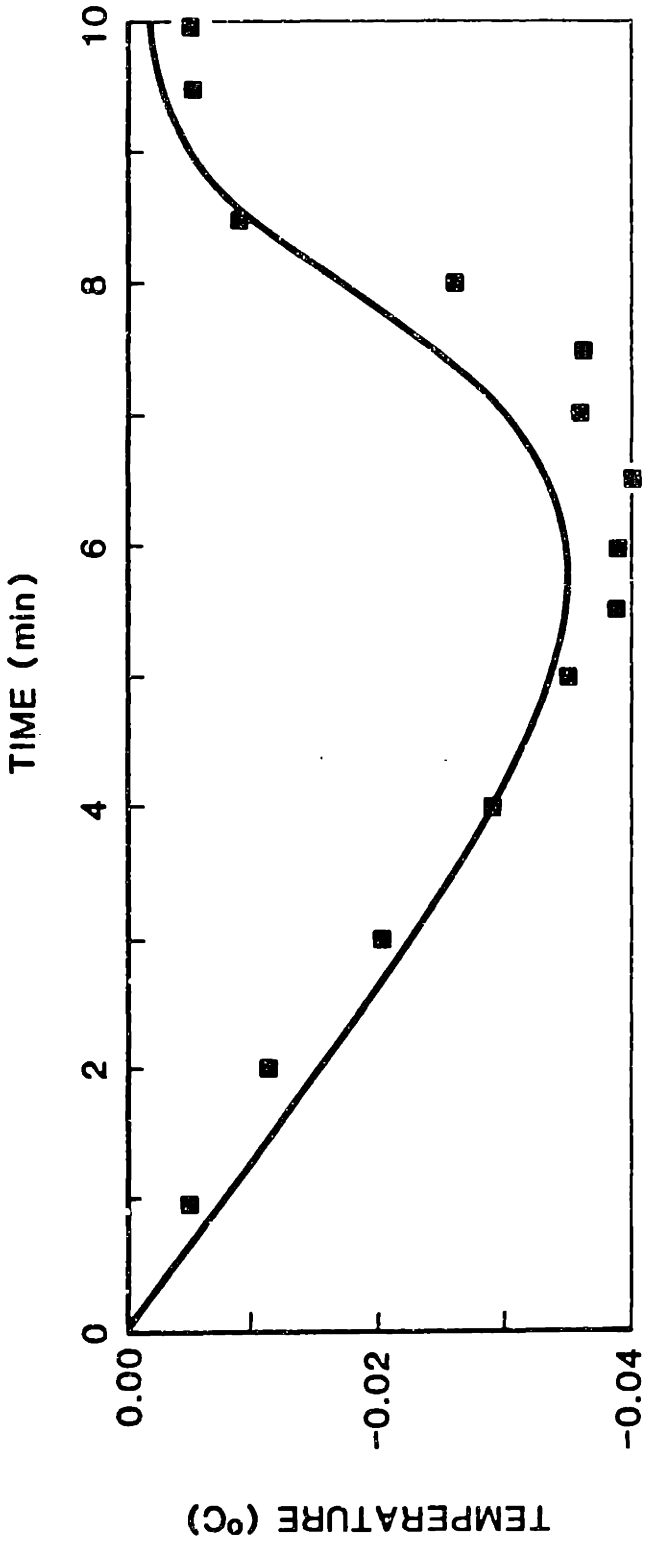

Figure 4-3 Verification of kinetic model of frazil ice growth (symbols, Carstens' (1966) Fig. 7 data; solid line, model simulation with $\langle \epsilon \rangle$ = 4 cm^2/sec^3, I_o = 0.05 nuclei/cm^3-sec, Z = 4 × 10 17 nuclei/J, Q = 0.00055 J/cm^3-sec).

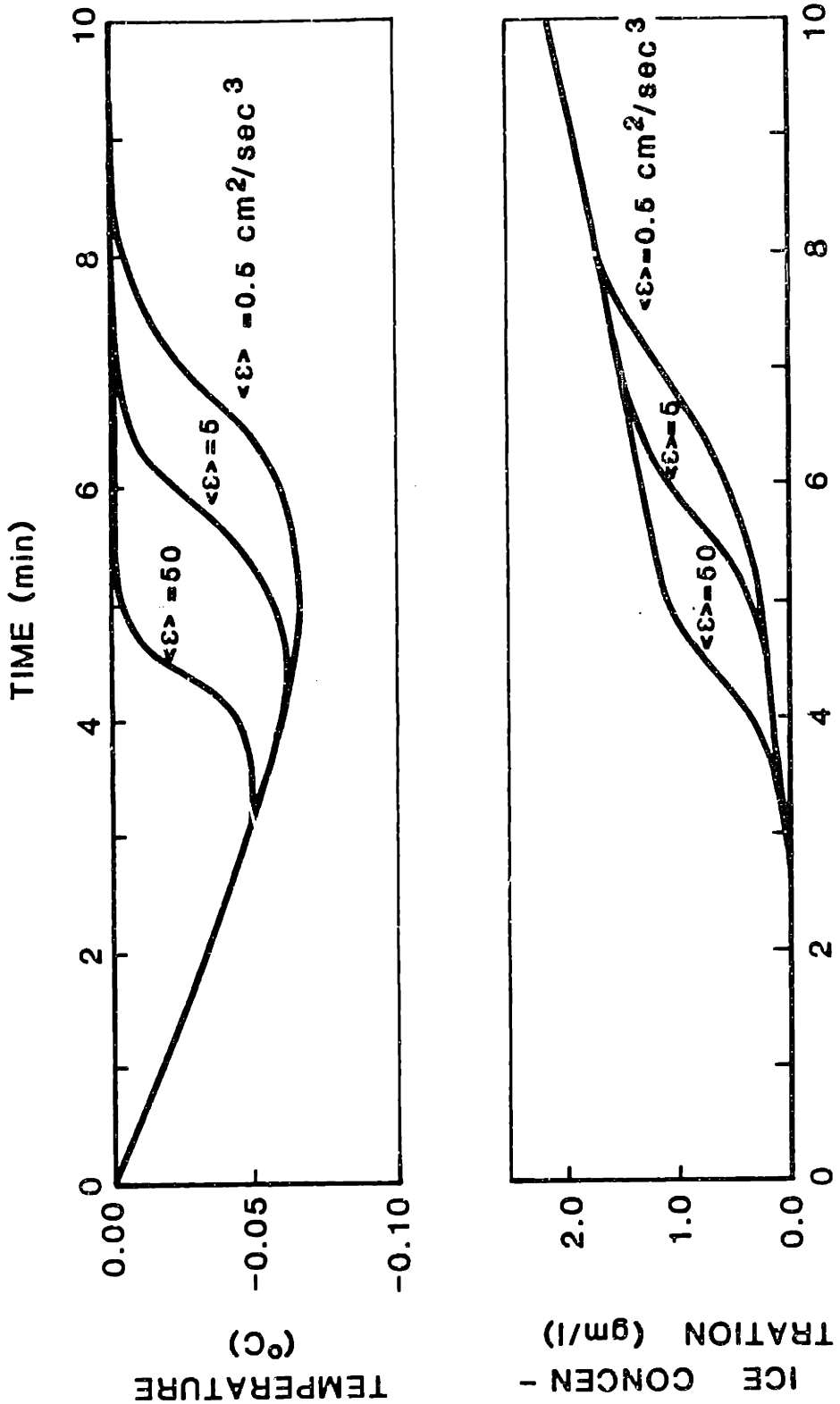

Figure 4-4 Model sensitivity: effect of varying the energy dissipation rate (I_o = 0.05 nuclei/cm^3-sec, Z = 4 × 10^{17} nuclei/J, Q = 0.0012 J/cm^3-sec).

secondary nucleation most noticeably. We should expect that increasing the dissipation rate will shift the particle size distribution towards increasing numbers of small particles and this is indeed what is demonstrated in Figure 4-5. For the same reason the effect of increasing the number of secondary nuclei generated per unit of collision energy is the same as increasing the energy dissipation rate, as illustrated in Figure 4-6. In accordance with the observations of Hanley and Tsang (1984) increasing the initial seeding rate (Figure 4-7) decreases the time lag prior to reaching the point of maximum supercooling so that smaller levels of supercooling result. Increasing the initial seeding rate also increases the rate of increase of temperature beyond the point of maximum supercooling. Finally, as illustrated in Figure 4-8, increasing the rate of heat removal increases the maximum supercooling and the rate of increase of temperature beyond the point of maximum supercooling, in agreement with Carstens' (1966) observations.

To explain the sensitivity of the model to variations in the system parameters we will determine an analytical expression for predicting the time t_s required to reach the point of maximum supercooling. Since initially the contribution of the latent heat release by ice growth to the thermal energy balance, Eq. 4-8, is small we can approximate the temperature history up to the point of maximum supercooling by

$$T(t) = - Qt/\rho c_p \qquad (4\text{-}13)$$

where $t = 0$ corresponds to the point where the temperature is at the

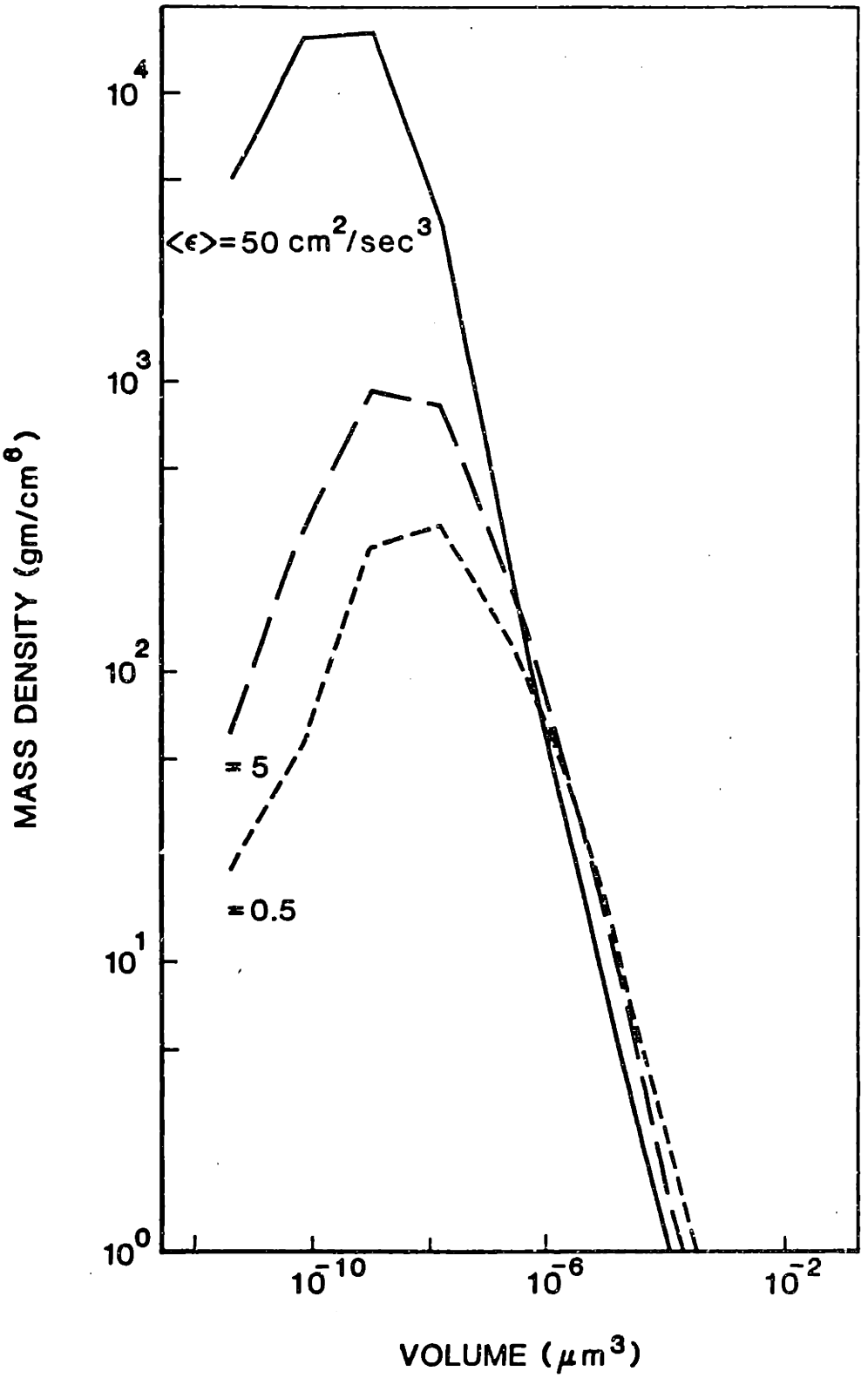

Figure 4-5 Simulated particle size distributions for conditions in Figure 4-4.

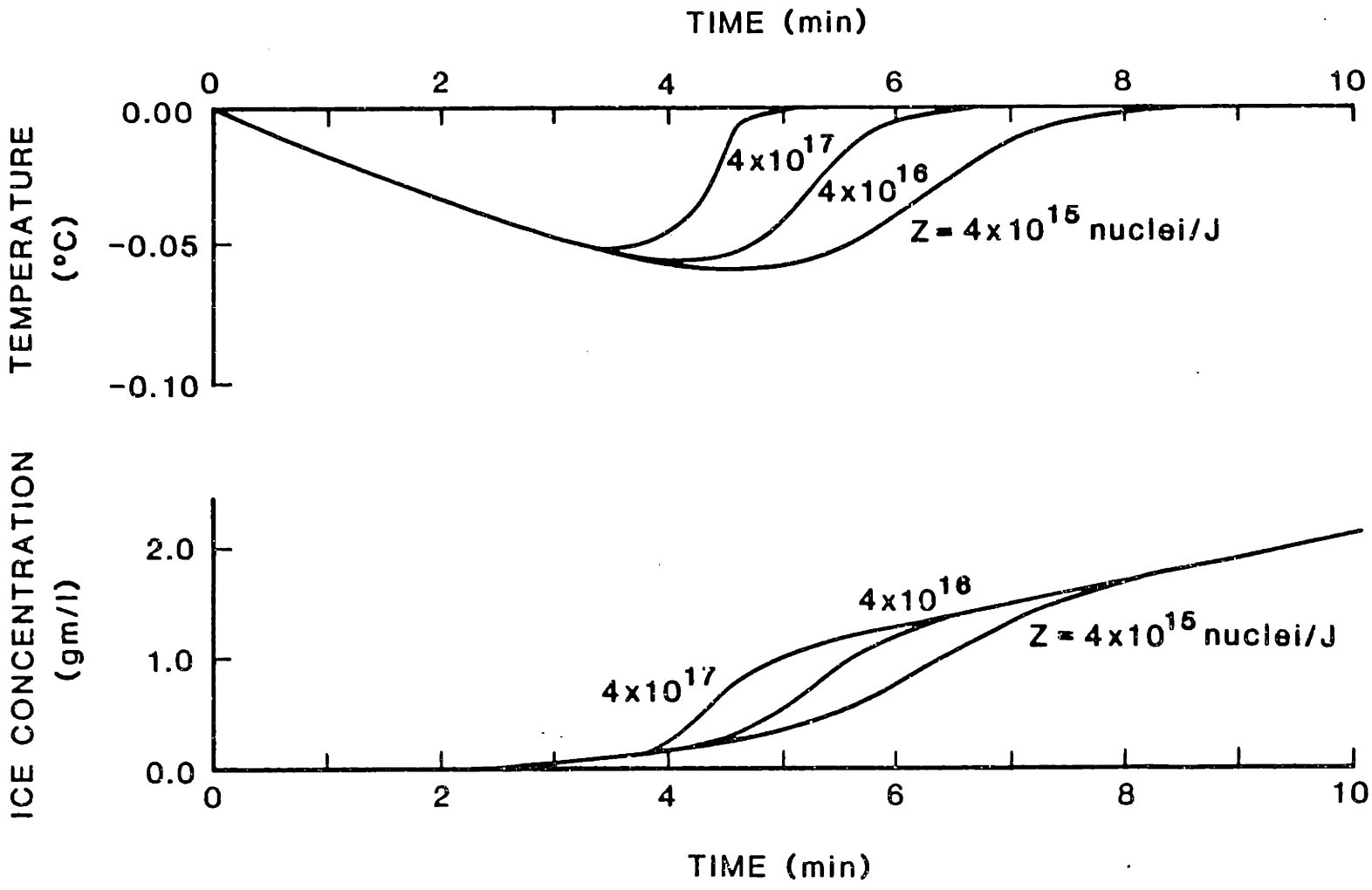

Figure 4-6 Model sensitivity: effect of varying Z ($\langle\varepsilon\rangle$ = 50 cm^2/sec^3, I_o = 0.05 nuclei/cm^3-sec, Q = 0.0012 J/cm^3-sec).

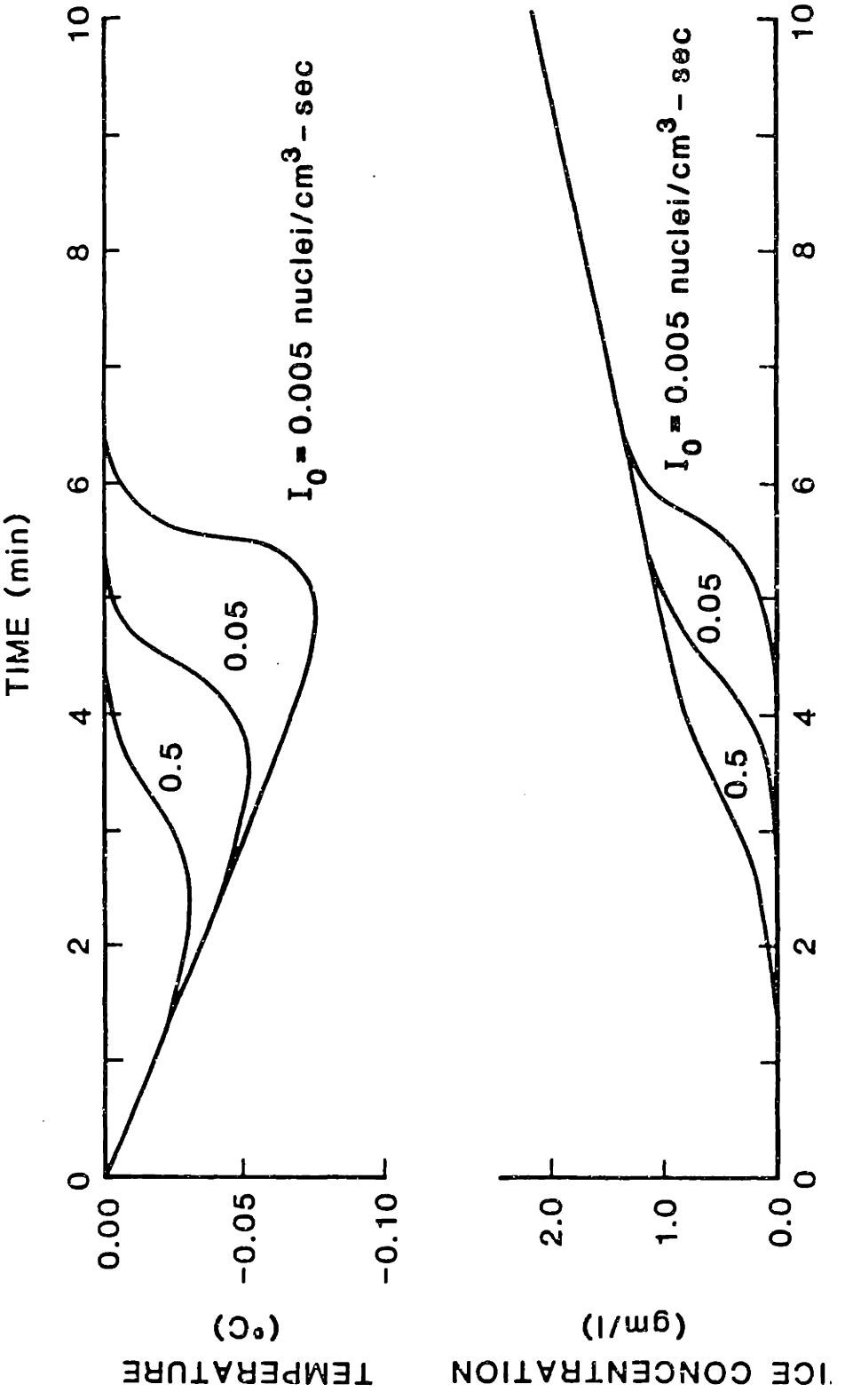

Figure 4-7 Model sensitivity: effect of varying the initial seed concentration ($\langle\varepsilon\rangle$ = 50 cm^2/sec^3, Z = 4 x 10^{17} nuclei/J, Q = 0.0012 J/cm^3-sec).

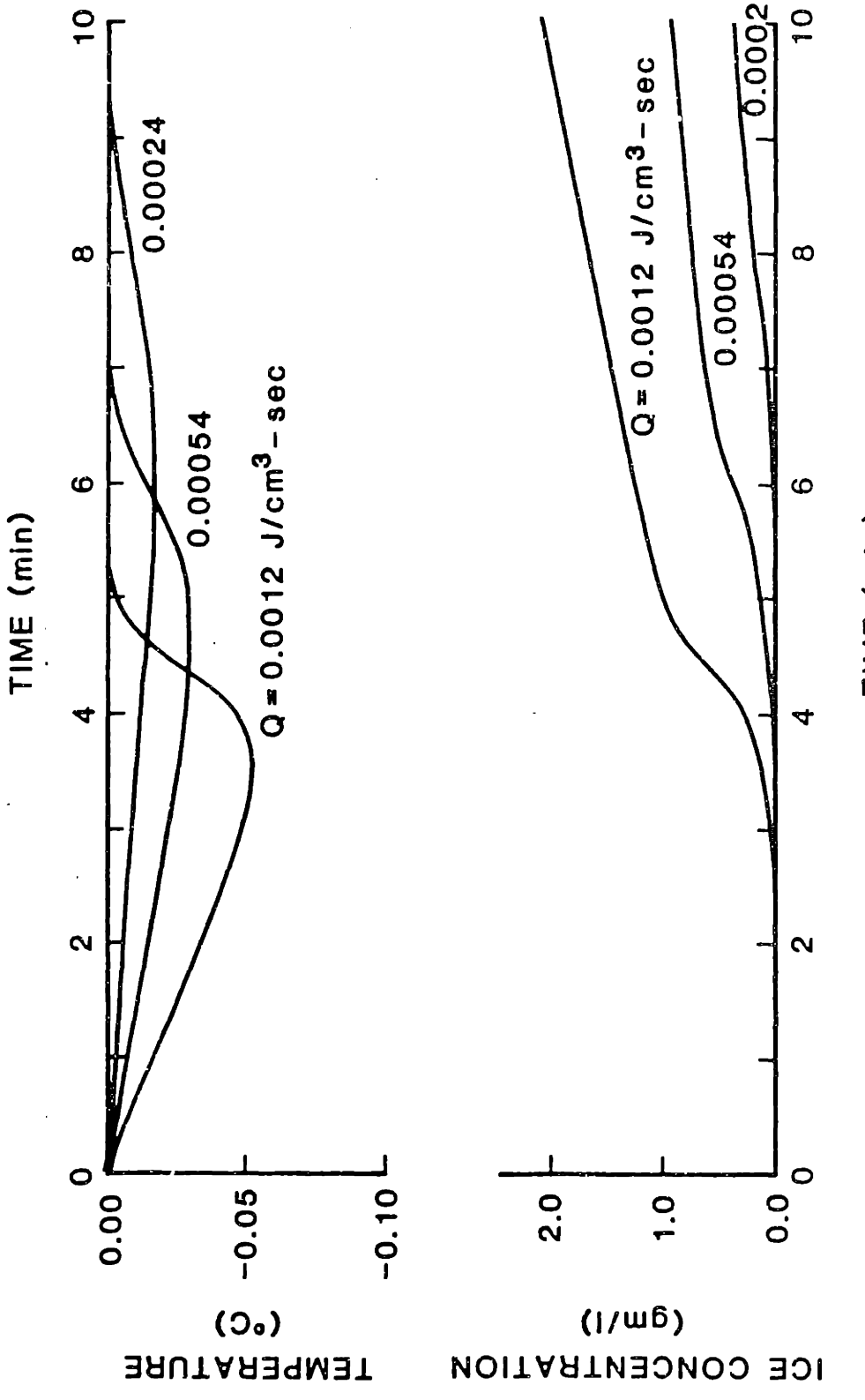

Figure 4-8 Model sensitivity: effect of varying the cooling rate ($\langle\varepsilon\rangle$ = 50 cm^2/sec^3, I_o = 0.05 nuclei/cm^3-sec, Z = 4 x 10^{17} nuclei/J)

equilibrium temperature, assumed equal to 0°C. Note that although dT/dt will not be constant and will change rapidly near the point of maximum supercooling, the value of T(t) given by the relationship will be a good approximation to the temperature at that point. The rate of crystal growth may be approximated by

$$\frac{dr}{dt} = \frac{kT}{r\,\rho_i\,L}\left[1 + 0.17\ Pe^{1/2}\right] \simeq \frac{kT}{r\,\rho_i\,L} \qquad (4\text{-}14)$$

for particles smaller than 100 μm in radius, which is about the maximum size the particles will have attained by the time the point of maximum supercooling is reached. Integrating this relation yields an expression for the crystal size as a function of time t' after nucleation

$$r(t') = \left[\, r_c^2 + \frac{k\,Q\,t'^2}{\rho\rho_i\,L\,c_p}\,\right]^{1/2} \qquad (4\text{-}15)$$

For typical cooling rates of order 10^{-3} J/cm^3-sec the second term within the brackets dominates over the first for times greater than 30 seconds so that the growth rate may be written as

$$r(t') = \left[\,\frac{kQ}{\rho\rho_i\,L\,c_p}\,\right]^{1/2} t' = \lambda t' \qquad (4\text{-}16)$$

If there were no secondary nucleation the particle number density distribution would evolve as a square wave of amplitude $g(r,t) = I_o/\lambda$ for $r_c \leq r \leq \lambda t$. With secondary nucleation, however, the number density at any size r will grow in time approximately according to

$$g(r,t) = \begin{cases} [I_T(t - r/\lambda) + I_o]/\lambda & r_c \leq r \leq \lambda t \\ 0 & r > \lambda t \end{cases} \qquad (4\text{-}17)$$

where I_T is the total number of secondary nuclei produced per unit time per unit fluid volume,

$$I_T(t) = Z \int_{r_c}^{\lambda t} \int_{r_j}^{\lambda t} c(r_i, r_j)\, dr_i\, dr_j \tag{4-18}$$

Eq. 4-17 does not account for the removal of nuclei from the large parent crystals, only for their addition to the size r_c. Assuming that up to the point of maximum supercooling the production of secondary nuclei is dominated by the turbulent shear mechanism,

$$I_T(t) = 0.018\, Z\, \rho_i \left(\frac{\varepsilon}{\nu}\right)^{3/2} \int_{r_c}^{\lambda t} \int_{r_j}^{\lambda t} \frac{(r_i + r_j)^5 (r_i r_j)^3}{(r_i^3 + r_j^3)}\, g(r_i, t)\, g(r_j, t)\, dr_i dr_j \tag{4-19}$$

The major contribution to the double integral will come from collisions of the largest size particles of size $r_m \sim \lambda t$ for which $g(r,t) \sim I_o/\lambda$. Approximating $g(r,t)$ by I_o/λ and replacing the lower limit r_c by zero yields

$$I_T(t) = 0.018\, Z\, \rho_i \left(\frac{\varepsilon}{\nu}\right)^{3/2} (I_o/\lambda)^2\, [1.67 + 0.45\, \ell n(\lambda t)]\, (\lambda t)^{10} \tag{4-20}$$

The total ice mass at any time t after the start of supercooling

and up to the point of maximum supercooling is

$$M_i(t) = \rho_i \int_0^{\lambda t} \frac{4\pi}{3} r^3 g(r,t)\, dr$$

$$= \frac{\pi}{3} \rho_i \lambda^3 I_o t^4 + \left(\frac{4\pi}{3}\right)^2 (0.018)\, Z\, \rho_i \left(\frac{\varepsilon}{\nu}\right)^{3/2} I_o^2 \lambda^{11}$$

$$(4.3 \times 10^{-4})\, t^{14} \qquad (4\text{-}21)$$

At the point of maximum supercooling, $dM_i/dt = Q/L$. The time of maximum supercooling t_s is thus obtained by implicit solution of

$$t_s^3 \left(1 + \zeta t_s^{10}\right) = \frac{0.24\, Q}{\rho_i L \lambda^3 I_o} \qquad (4\text{-}22)$$

$$\zeta = 4.5 \times 10^{-4} \rho_i Z (\varepsilon/\nu)^{3/2} I_o \lambda^8 \qquad (4\text{-}23)$$

Table 4-1 compares the values of t_s obtained with Eq. 4-22 with those obtained in the numerical simulations presented in Figures 4-4, 4-6, 4-7 and 4-8. The values of ζt_s^{10} presented in Table 4-1 are generally of order one. The point of maximum supercooling is thus controlled by both the rate of initial seeding and the rate of secondary nucleation. For $\zeta t_s^{10} \ll 1$, the value of t_s is controlled by the initial seeding rate and is independent of the secondary nucleation rate. The discrepancy between the results is less than 10% confirming the validity of the assumptions made in arriving at Eq. 4-22. The major assumptions are that for $t < t_s$ the contribution of the latent heat release by ice growth to the thermal energy balance is negligible, turbulent shear is the dominant mechanism controlling the production of secondary nuclei, and collisions between the largest crystals produce most of the

Table 4-1 Comparison of Simulated Values of t_s With Those Obtained From Eq. 4-22

Z	I_o	$\langle\varepsilon\rangle$	Q	t_s (minutes)		
(erg^{-1})	$(cm^{-3}\text{-}sec^{-1})$	$(cm^{2}\text{-}sec^{-3})$	$(J\text{-}cm^{-3}\text{-}sec^{-1})$	Simulated	Eq. 4.22	ζt_s^{10}
4×10^{10}	0.05	50.	1.2×10^{-3}	3.5	3.2	5.9
4×10^{10}	0.05	5.	1.2×10^{-3}	4.5	4.1	2.2
4×10^{10}	0.05	0.5	1.2×10^{-3}	5.1	5.0	5.1
4×10^{9}	0.05	50.	1.2×10^{-3}	4.1	3.8	3.3
4×10^{8}	0.05	50.	1.2×10^{-3}	4.5	4.5	1.8
4×10^{10}	0.5	50.	1.2×10^{-3}	2.4	2.2	1.4
4×10^{10}	0.005	50.	1.2×10^{-3}	4.9	4.6	22.3
4×10^{10}	0.05	50.	5.4×10^{-4}	4.7	4.2	3.7
4×10^{10}	0.05	50.	2.4×10^{-4}	5.9	5.5	2.1

secondary nuclei. Knowing t_s the approximate value of the maximum supercooling may then be obtained by substitution into Eq. 4-13.

Having formulated a kinetic model of frazil ice growth we may now incorporate it within the framework of the pdf transport model to examine the additional effect of turbulent transport on the formation of frazil ice in rivers.

4.3 A One-Dimensional Model of Frazil Ice Growth in Rivers

4.3.1 Model Description

The one-dimensional model of frazil ice growth presented here assumes a steady, uniform channel flow over a smooth bottom. The flow is assumed to be well-mixed in the lateral direction and diffusion in the flow direction is neglected. The reactive flow within the bottom and surface boundary layers is not modeled. We are thus following a column of water in its passage downstream at the constant rate $U = (x-x_o)/(t-t_o)$ where x_o is the position of the water column at the initial time t_o.

The vertical structure of the turbulence is included in the model through the following relationships for the turbulent kinetic energy, k, the energy dissipation rate, ε, and the vertical eddy diffusivity, Γ_v,

$$k(y) = \frac{u_*^2}{0.3}\left(1 - \frac{y}{h}\right) \tag{4-24}$$

$$\varepsilon(y) = \frac{u_*^3}{\kappa y}\left(1 - \frac{y}{h}\right) \tag{4-25}$$

$$\Gamma_v(y) = \kappa\, u_* y \left(1 - \frac{y}{h}\right) \tag{4-26}$$

where y is the height above the bottom, h is the depth of flow, κ is von

Karman's constant, $u_* = (gh\theta)^{1/2}$ is the friction velocity, and θ is the channel slope.

The model computes the reactive transport of suspended ice crystals, discretized into a number of size classes, and thermal energy as measured by temperature. The bottom boundary condition is one of zero flux for both particles and heat. Heat fluxes due to ground-water flow and the terrestial heat flux are neglected since these are very small compared with the surface heat flux (Carstens, 1970). The surface boundary condition for the particles is also zero flux, except for the addition of initial seed nuclei at the rate I_o' (number per unit surface area per unit time). The surface boundary condition for heat is a constant removal at the rate Q' (energy per unit surface area per unit time).

Incorporated in the model are stochastic algorithms for simulating the differential rising of ice particles and the vertical diffusion and mixing of ice and heat. All particle sizes are assumed to mix at the same rate, but the difference in the mixing rates for heat and particles is retained. The algorithm for computing secondary nucleation, growth and flocculation of the ice particles is as described in the previous section with the only difference being that the temporal behavior of the energy dissipation rate is simulated according to the algorithm presented in Section 3.5. The time scale for the growth of the smallest particles is

$$t_r^{(\alpha)} = \left(\frac{1}{v_\alpha}\frac{dv_\alpha}{dt}\right)^{-1} = \left[\frac{3kT}{\rho_i L\, r^2}\right]^{-1} \qquad (4\text{-}27)$$

For a supercooling of order T = 0.04°C and particle radii ranging from 4

to 100 μm, the time scale indicated by Eq. 4-27 ranges from 0.07 to 45 sec, fast enough for the growth of the smaller particles to interact nonlinearly with the fluctuating energy dissipation rate.

The growth rate of the particles, as represented by Eqs. 4-2 and 4-3 is linearly dependent on the supercooling but nonlinearly dependent on the energy dissipation rate. The rates of secondary nucleation and flocculation are nonlinearly dependent on the energy dissipation rate and on the number density distribution. In addition to examining the effect of vertical transport, we will also be interested in the extent to which the coupling between the fluctuating particle concentrations and energy dissipation rate influences the formation of frazil ice.

4.3.2 Model Results

To investigate the effects of vertical transport and nonlinear reactions on the formation of frazil ice in rivers, three simulations have been performed. For the first case, the zero-dimensional model presented in Section 4.1 was employed to model frazil ice growth without nonlinear turbulence interactions and assuming complete vertical mixing. For the second and third cases, the Monte Carlo model was employed, thus incorporating vertical transport. However, for the second simulation, the effect of turbulent mixing on reaction was eliminated by assigning an infinite mixing rate. In other words, immediately following each operation the new average concentrations of all constituents at all nodes were computed and all representative concentrations were assigned their corresponding average value. For the third simulation, it was assumed that all particle size classes mix at the same rate. However, the difference between the mixing rates for particles and heat was retained.

In all cases the depth of water is either explicitly or implicitly assumed to be h = 5 m. For the cases with vertical transport, the river slope is set at 0.0002 so that the corresponding average velocity is 1 m/sec. The surface cooling rate is 650 J/m^2-sec and the initial seeding rate is 2500 nuclei/m^2-sec. The corresponding rates for the zero-dimensional model are a heat loss of 130 J/m^3-sec and an initial seeding rate of 500 nuclei/m^3-sec. In all cases the particle size range considered is 4 $\mu m < r < 1435$ μm, divided into 8 logarithmic size classes. The number of elements at each node for the Monte Carlo model is 100.

Figure 4-9 illustrates the simulated time histories of temperature. For the case with complete vertical mixing, the peak supercooling is reached earlier and, therefore, has a smaller magnitude than the cases with vertical transport. By limiting the rate of transport of initial seed nuclei from the surface waters, it is not surprising that the peak supercooling for the cases with vertical transport lags that for the case with complete vertical mixing by a time interval approximately equal to the diffusion time $h^2/\Gamma_v \sim (5m)^2/(0.04\ m^2/sec) = 10$ min.

Except for the late stages of supercooling, the results for the two simulations with vertical transport are indistinguishable. Even beyond t = 50 min, when the result begin to diverge, the differences between the two simulations are very small. This is an indication that the coagulation, growth and secondary nucleation reactions may not be sufficiently fast or nonlinear to interact with the turbulence. Figure 4-10 compares the growth of ice mass for the three cases. As expected from the previous result, the early peaking in temperature for the case

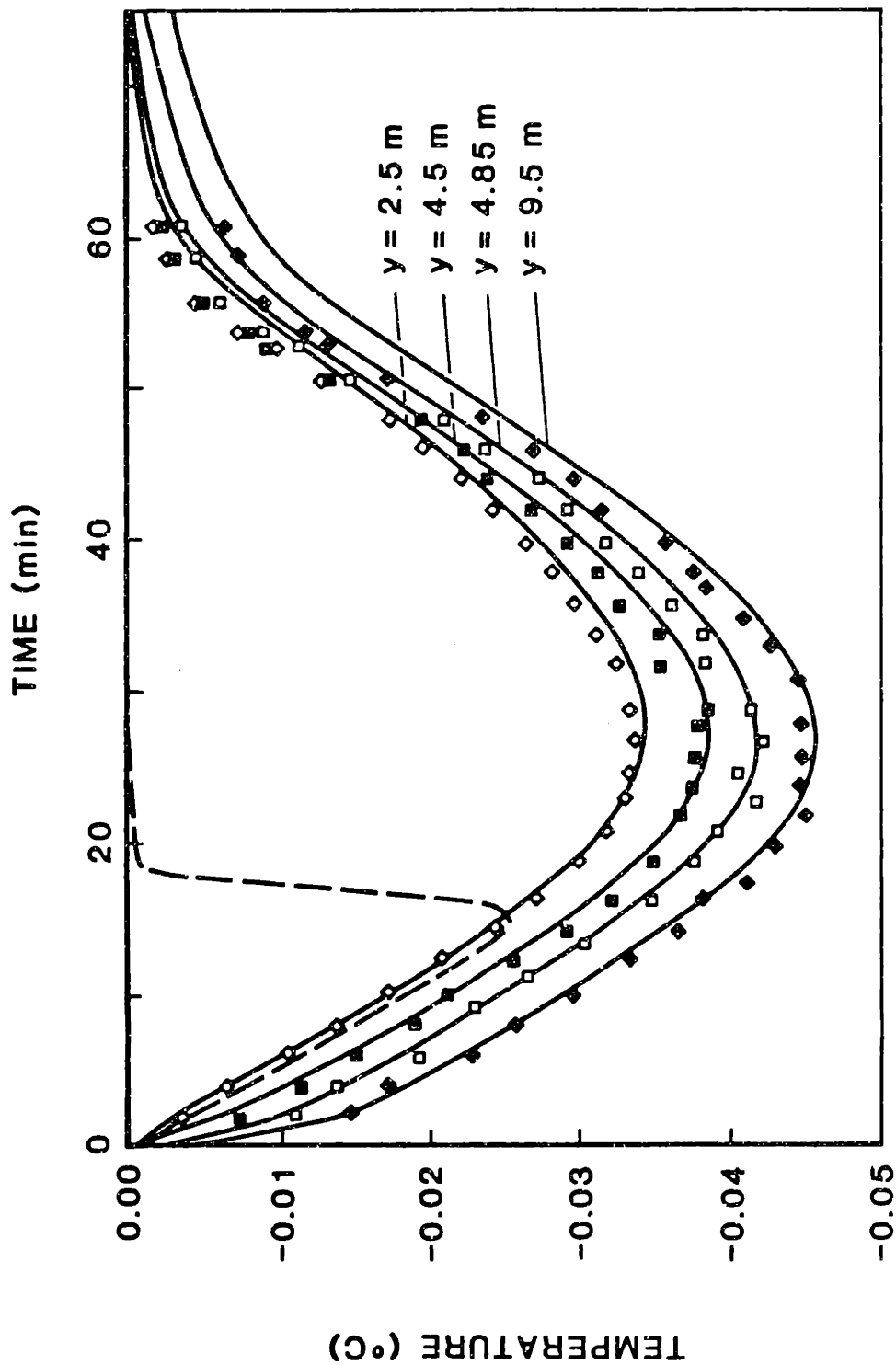

Figure 4-9 Time history of temperature (dashed line, zero dimensional model; solid line, Monte Carlo model with infinite mixing rate; symbols, Monte Carlo model with mixing modeled appropriately).

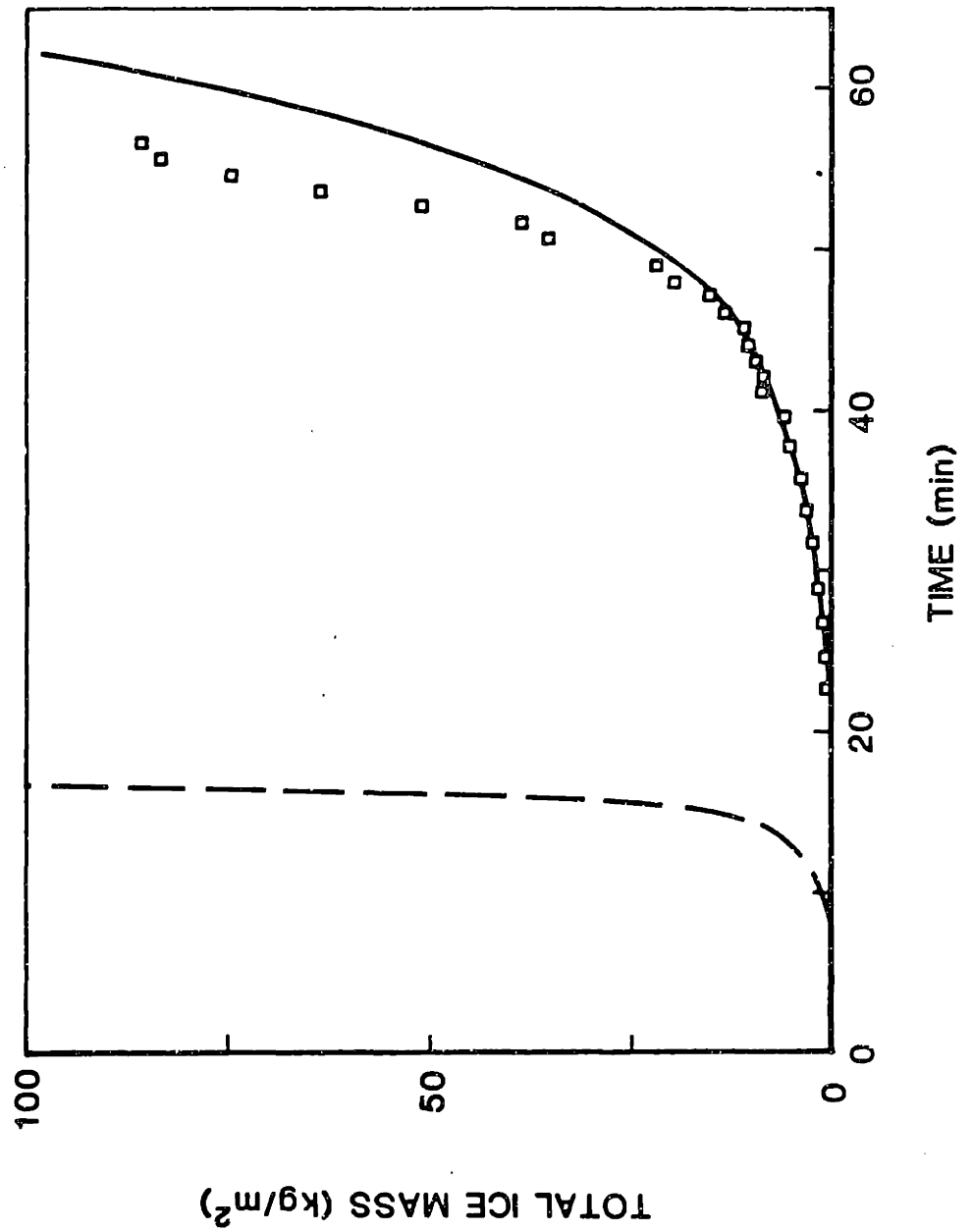

Figure 4-10 Time history of ice formation (dashed line, zero-dimensional model; solid line, Monte Carlo model with infinite mixing rate; symbols, Monte Carlo model with mixing modeled appropriately).

without transport requires a shorter time lag before significant ice growth than the case with vertical transport. The small differences for the two cases with vertical transport confirm that the nonlinear interaction between mixing and reaction is not important for frazil ice growth in rivers. The remainder of this section will be devoted to a discussion of results obtained for the Monte Carlo model simulation with mixing modeled appropriately.

Figure 4-11 presents simulated vertical profiles of mass concentration. At early times the largest crystal sizes are still small enough that their buoyancy is insignificant so that mass is uniformly distributed with depth. At later times, due to crystal growth and flocculation, the frazil particles are much larger, their buoyancy is more significant and, hence, there is a large vertical gradient in mass concentration with most of the ice mass accumulated at the surface. Figure 4-12 illustrates the growth of the larger particles at mid-depth. The larger particles grow in numbers until about the time of peak supercooling. Beyond this time as the supercooling decreases, the rate of formation of larger particles becomes less than the rate of removal by rising. Hence the number concentrations of larger particles at mid-depth decrease again. Figure 4-13 shows the vertical profiles of mass density for the various size classes at t = 35 min. It is evident that the frazil seed nuclei introduced through the water surface actually grow to intermediate sizes before they can be transported to deeper waters. Thus, the introduction of frazil ice nuclei in deeper waters is due primarily to secondary nucleation.

Figure 4-14 presents the time history of standard deviation for the pdf's of number concentration for various size classes and of

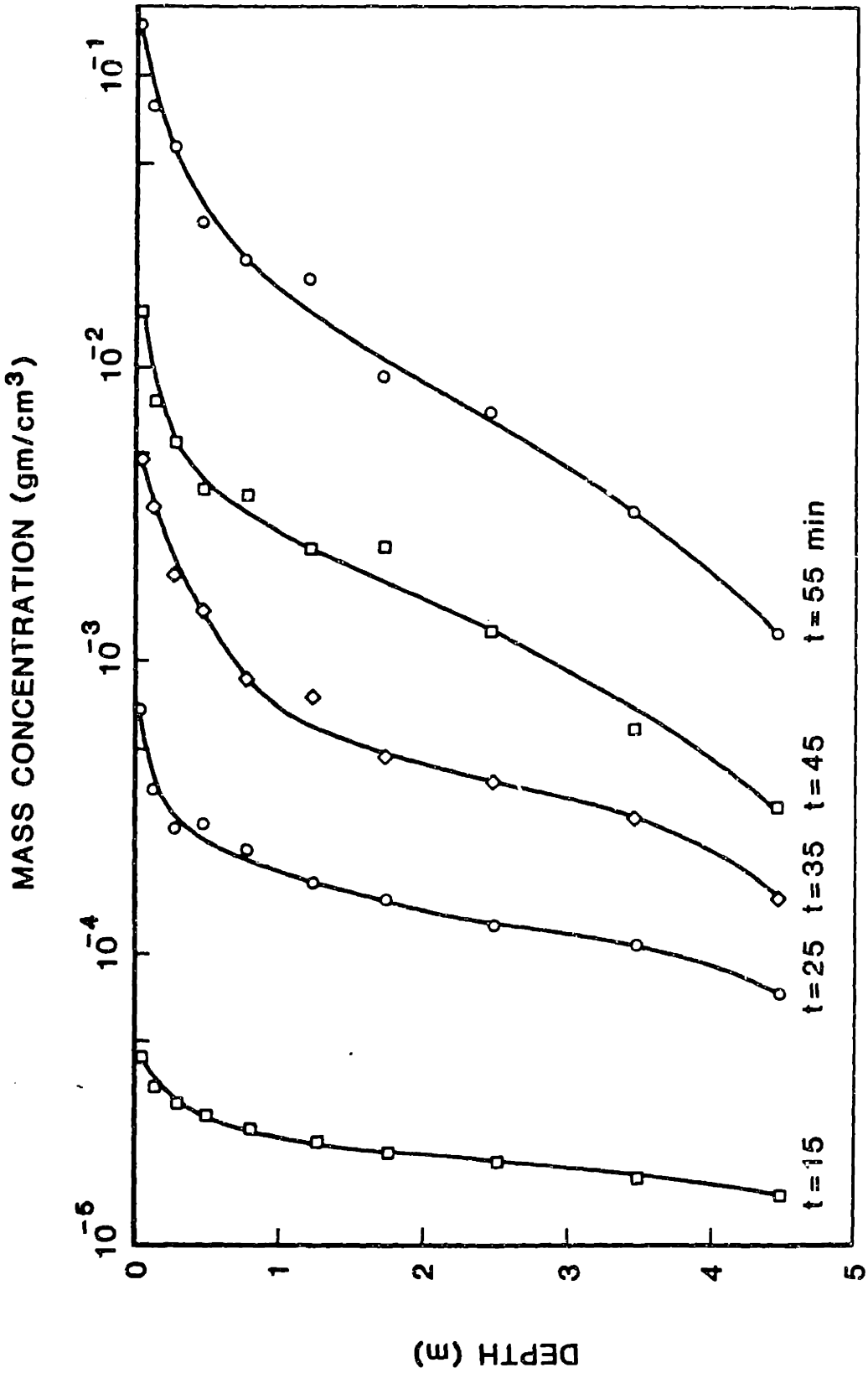

Figure 4-11 Profiles of mass concentration at various times.

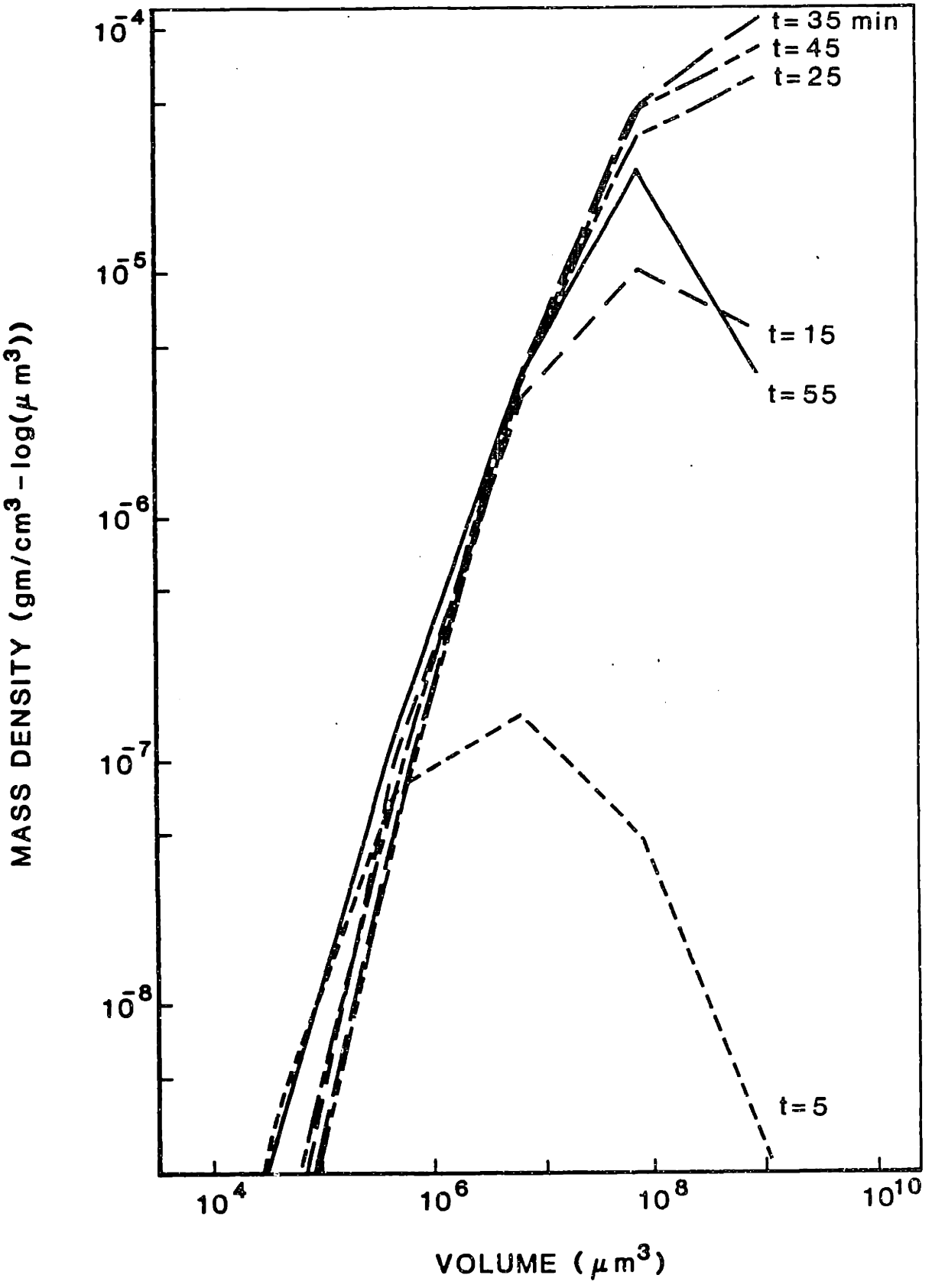

Figure 4-12 Particle size distributions at various times at a depth of 2.5 m.

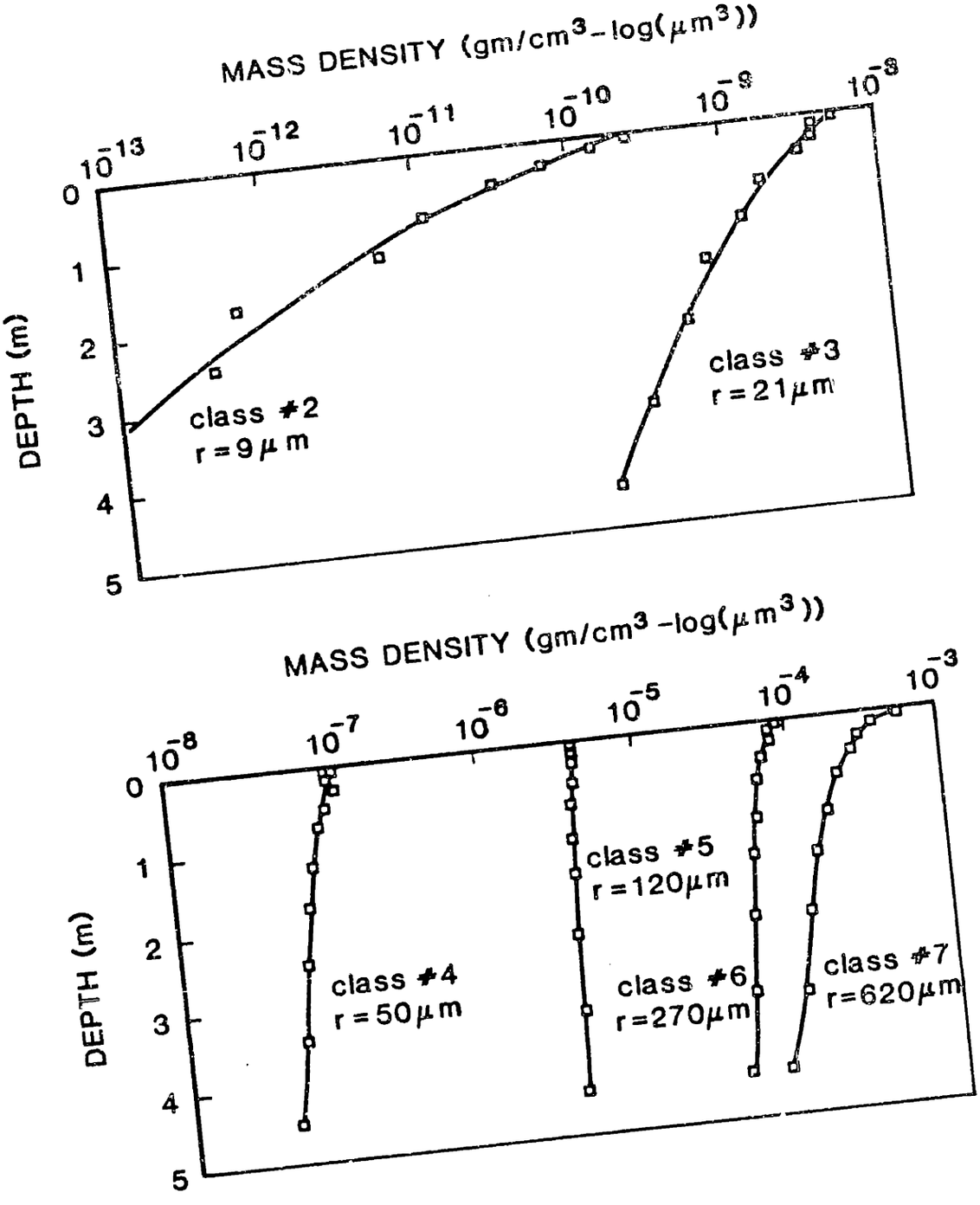

Figure 4-13 Depth profiles of mass density for vario

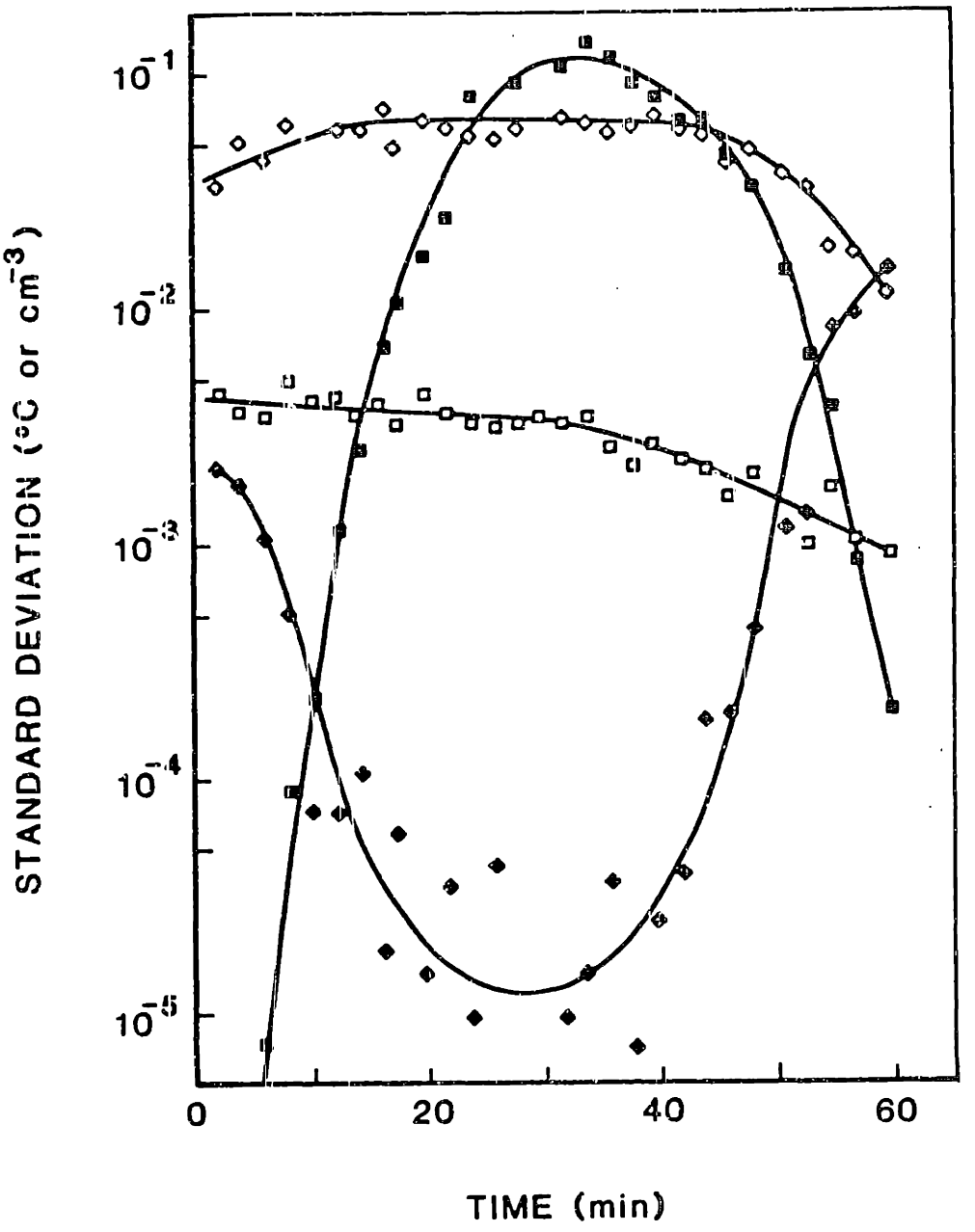

Figure 4-14 Time history of the standard deviation of the pdf's for temperature and particle number concentration (depth = 0.8 m; open squares, temperature; solid diamonds, class #1, r = 4 μm, open diamonds, class #4, r = 50 μm; solid squares, class #7, r = 620 μm).

temperature at a depth of 0.8 m. From the large variation in the standard deviation for size classes 1 and 7 it is evident that there is significant interaction with the turbulence. However, it seems that the overall effect on the total ice mass and water temperature is such that the turbulence interaction is negligible. Perhaps one of the reasons why this is so is that the standard deviations for the intermediate size classes show little change with time, while those for the smallest and largest size classes exhibit opposite trends; while the standard deviation of the pdf of the largest particles is increasing, that for the smallest particles is decreasing. Indeed, if one were to average the standard deviations for size classes 1 and 7 in Figure 4-14, it appears that the result would not vary much in time. Perhaps these opposite trends cancel each other out in their overall interaction with turbulent mixing. In any case, the dynamics are too complicated to be able to say for certain. Finally, Figure 4-15 shows that the normalized pdf's of number concentration for size classes 1, 4 and 7 at t = 31 min and a depth of 0.8 m are slightly positively skewed.

In summary, as compared with the case with complete vertical mixing, the effect of vertical transport on frazil ice growth in rivers is to reduce the rate of introduction of seed nuclei to deeper waters, thus increasing the time to reach the peak supercooling and increasing the magnitude of the maximum supercooling. The growth, secondary nucleation, and coagulation reactions involved in the formation of frazil ice do not seem to be sufficiently fast or nonlinear to necessitate being concerned about possible interactions with turbulent mixing.

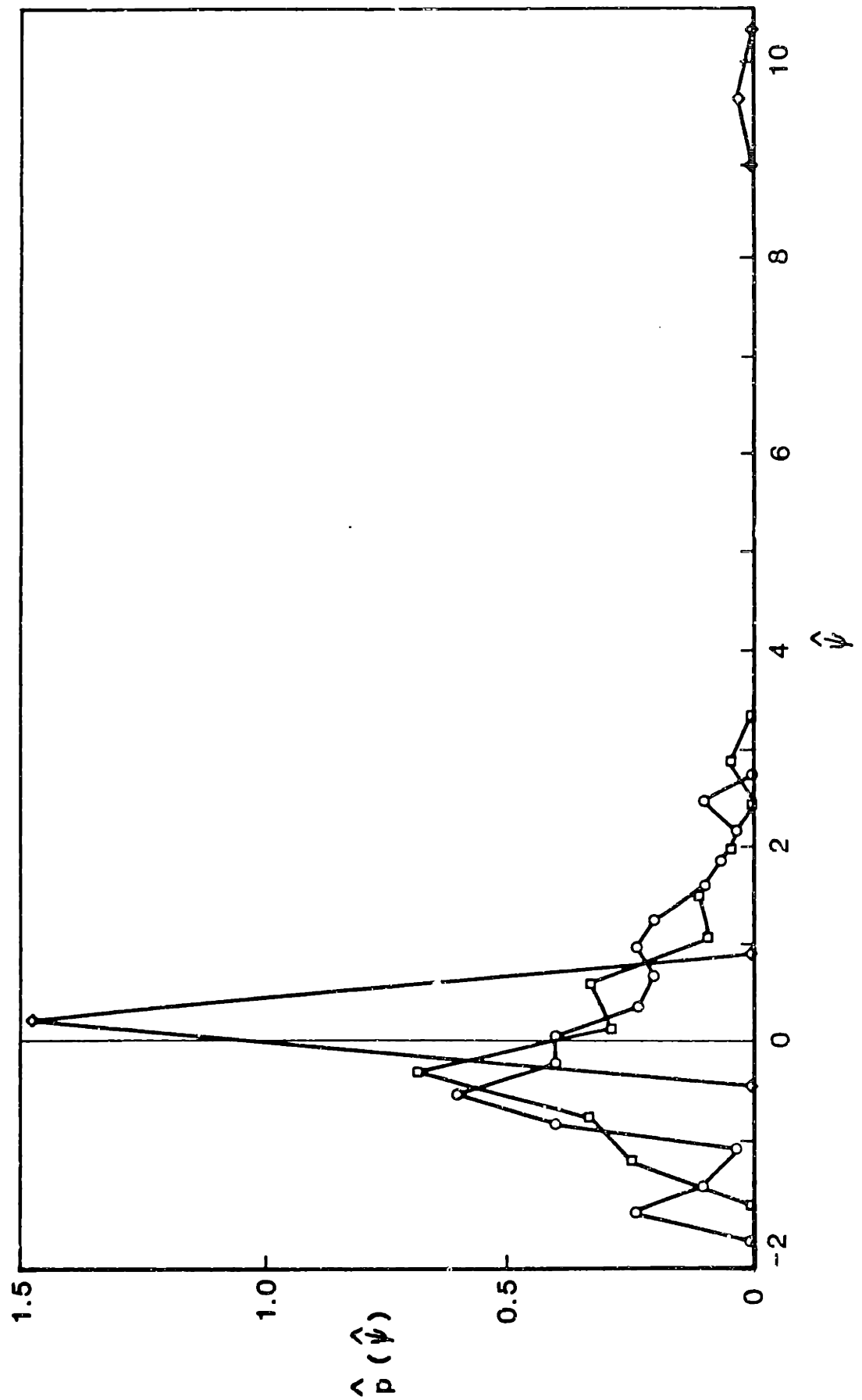

Figure 4-15 Sample pdf's of number concentration for various size classes (depth = 0.8 m, t = 31 min; diamonds, r = 4 μm; circles, r = 50 μm; squares, r = 620 μm).

4.4 A Two-Dimensional Model of the Transport and Deposition of Sewage Sludge from a Coastal Outfall

Concern over the fate of particles that are emitted from municipal ocean outfalls arises from the fact that the largest fractions of most types of waste constituents (organic compounds and trace metals) are associated with the particulate phase. As a result, the particles can affect marine life by acting as the transport vector for toxic species and by accumulating organic debris in bottom sediments adjacent to the outfalls. To understand the fate of particles upon disposal, one needs to be able to estimate deposition rates as a function of location and to relate those to the mass emission rates, the sedimentation characteristics of the particles, and the hydrodynamic regime of the receiving waters.

When sludge issues from the outfall, it undergoes immediate dilution within the resulting turbulent buoyant jet as it rises to some equilibrium height dependent on the ambient stratification, among other factors. After reaching the equilibrium height in a matter of minutes, the neutrally buoyant wastewater cloud is then subject to advection by local currents and dispersion by current shear and oceanic turbulence. As they are being transported by the fluid, the suspended sludge particles coagulate with each other and with natural marine particles and slowly settle out of the water column.

In this section, a two-dimensional far field model for the transport and deposition of waste particles emitted from a coastal outfall will be presented. The model extends current analytical techniques in that coagulation is accounted for in addition to particle transport and settling. Accordingly, the purpose of the model

simulations presented here is to assess the relative importance of coagulation as a mechanism affecting the fate of discharged particles.

4.4.1 Model Description

Consider a municipal outfall terminating in water of depth h and from which issues a wastewater flow Q containing a solids concentration c_o. The plume rises to an equilibrium height z_o above the bottom. Thereafter the plume disperses at the rates Γ_v vertically and Γ_h horizontally, while the suspended particles coagulate and settle. For simplicity the mean current velocity is assumed to be zero. The plume is thus radially symmetric about the source.

The two-dimensional model is a far field model, that is, the dynamics of the initial dilution process are not modeled. Instead, a constant mass flux, Qc_o, of particles at the equilibrium height, z_o, is assumed. The particles at the source are assumed to be distributed as d^{-4} within the limits 1 μm < d < 100 μm, in accordance with the data of Faisst (1980); the mass and number densities of waste particles smaller than 1 μm are neglected. The surface and bottom boundary conditions for vertical diffusion are zero-flux. Particles are removed from the system only by settling to the bottom. Since the problem is radially symmetric, the horizontal concentration gradient at r = 0 is zero. The outer radial boundary is chosen as a distance sufficiently large that only the smallest particles are still suspended in the water column at that distance and approximately steady conditions have been attained by the time the smallest particles have reached the outer boundary. The initial condition is zero concentration everywhere. Very far from the source when the suspended waste particle concentration has

decreased to a level comparable to the natural background concentration, coagulation with natural particles will become significant; however, at this point the total mass of waste particles remaining in suspension will be very small. The background concentration of natural particles may thus be safely neglected. The wastewater flow is "turned on" at t = 0 and the plume development is simulated until approximate steady state conditions are established.

Incorporated in the model are stochastic algorithms for simulating differential settling, radial eddy diffusion, vertical eddy diffusion, and mixing of particles. All particle sizes are assumed to mix at the same rate. Coagulation of particles is computed as described in Section 2.4.

4.4.2 Model Results

As previously stated, the purpose of the model simulations is to assess the relative importance of coagulation as a mechanism affecting the transport and deposition of discharged particles. Accordingly, two simulations have been performed, one with coagulation included and the other with coagulation neglected. In both cases the depth of the water was $h = 80$ m, the equilibrium rise height was $z_o = 40$ m and the mass emission rate was $Qc_o = 1$ kg/sec. The particle size range, $0.5\ \mu m < r < 50\ \mu m$, at the source was divided into 8 logarithmic size classes. Within the water column particles sized up to $r = 170\ \mu m$ were accounted for with two additional size classes. The particle density was assumed to be 1.1 gm/cm^3. Constant values of the Kolmogorov time scale, $(\nu/\langle\varepsilon\rangle)^{1/2} = 10$ sec, the integral time scale, $k/\langle\varepsilon\rangle = 3000$ sec, the radial eddy diffusivity, $\Gamma_r = 30$ m^2/sec, and the vertical eddy

diffusivity, $\Gamma_v = 10^{-4}$ m^2/sec, were employed. The outer boundary was chosen at a radial distance of 15 km. The 80 m by 15 km spatial domain was discretized with an 11 by 9 (respectively) node grid with the grid resolution decreasing with increasing distance from the source. The number of Monte Carlo elements per node was 50.

Figure 4-16 compares the total particle mass deposition rates as a function of time for the two simulated cases. The mass deposition rates are expressed as a percentage of the mass emission rates. The fluctuations in the deposition rates are due to the fact that the rates represent instantaneous values which have been smoothed somewhat by the application of a moving average of width 1.8×10^{-5} sec. Since coagulation contributes to the removal of the smallest particles which would otherwise not settle, it is not surprising that including coagulation results in quasi-steady state conditions being established sooner with the quasi-steady state deposition rate being slightly larger than for the case with coagulation neglected.

Figure 4-17 illustrates the steady state distribution of the sedimentation flux with radial distance. Near the source the sedimentation flux for the case with coagulation included is almost twice as large as that with coagulation neglected. Beyond a distance of 4 km the distributions of sedimentation flux for the two cases differ negligibly. Figure 4-18 is a contour plot showing the distributions of suspended particle mass at steady state. At any point in space the lower suspended mass concentrations for the case with coagulation included are consistent with the enhanced mass removal rates demonstrated above.

Figures 4-19 and 4-20 illustrate the steady state particle size distributions at a depth of 55 m and at various radial distances for the

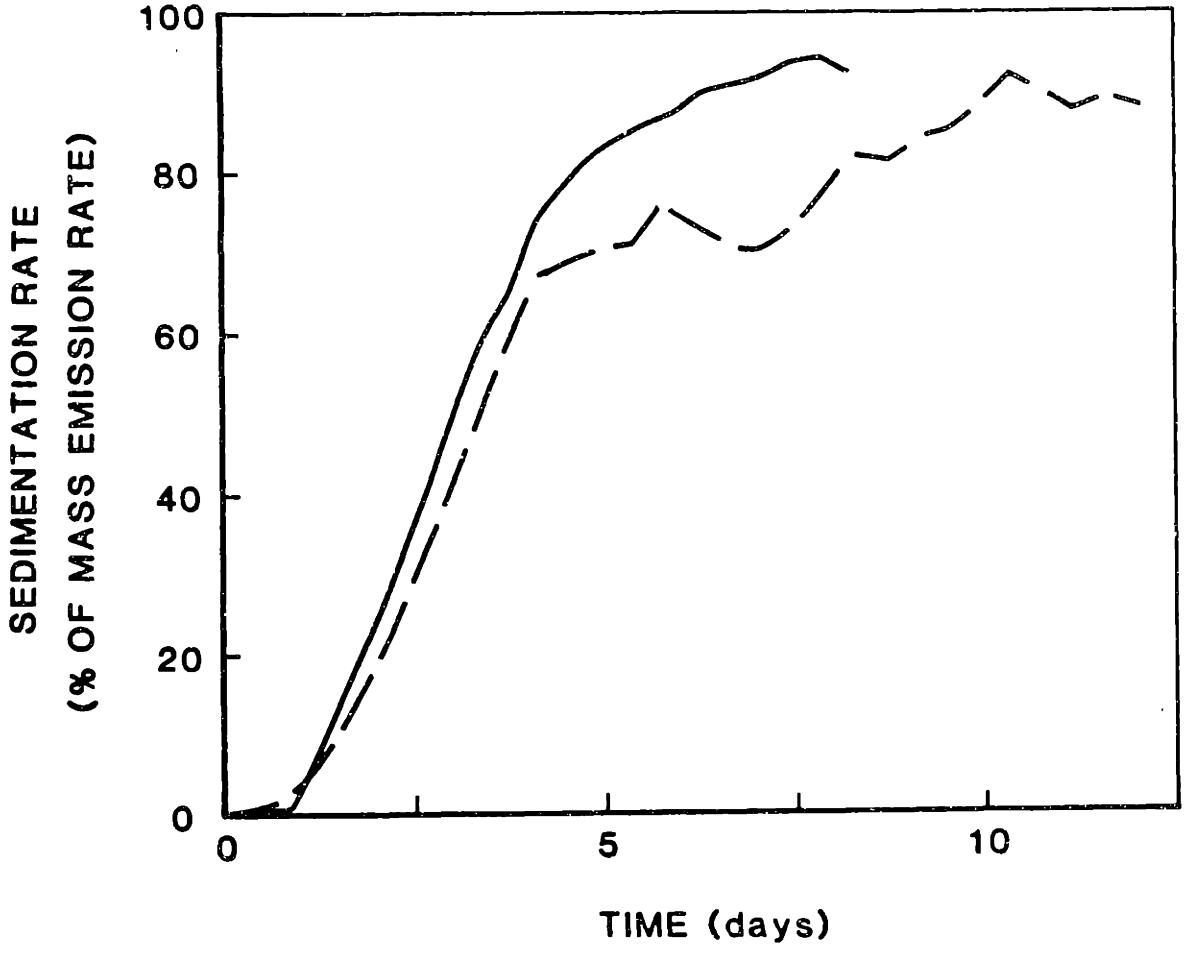

Figure 4-16 Sedimentation rate (expressed as a percentage of the mass emission rate) versus time (solid line, coagulation included; dashed line, coagulation neglected).

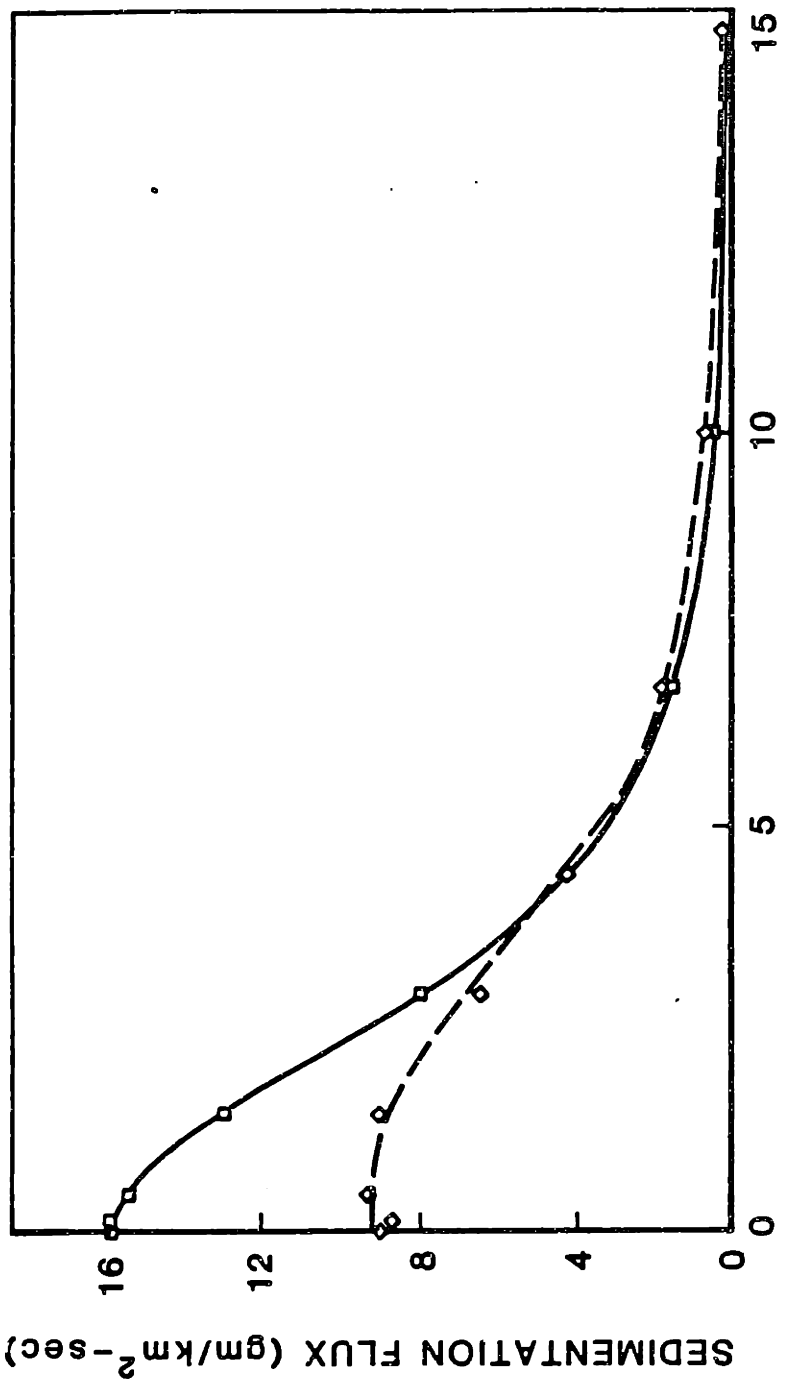

Figure 4-17 Steady state sedimentation flux versus radial distance (solid line, coagulation included; dashed line, coagulation neglected).

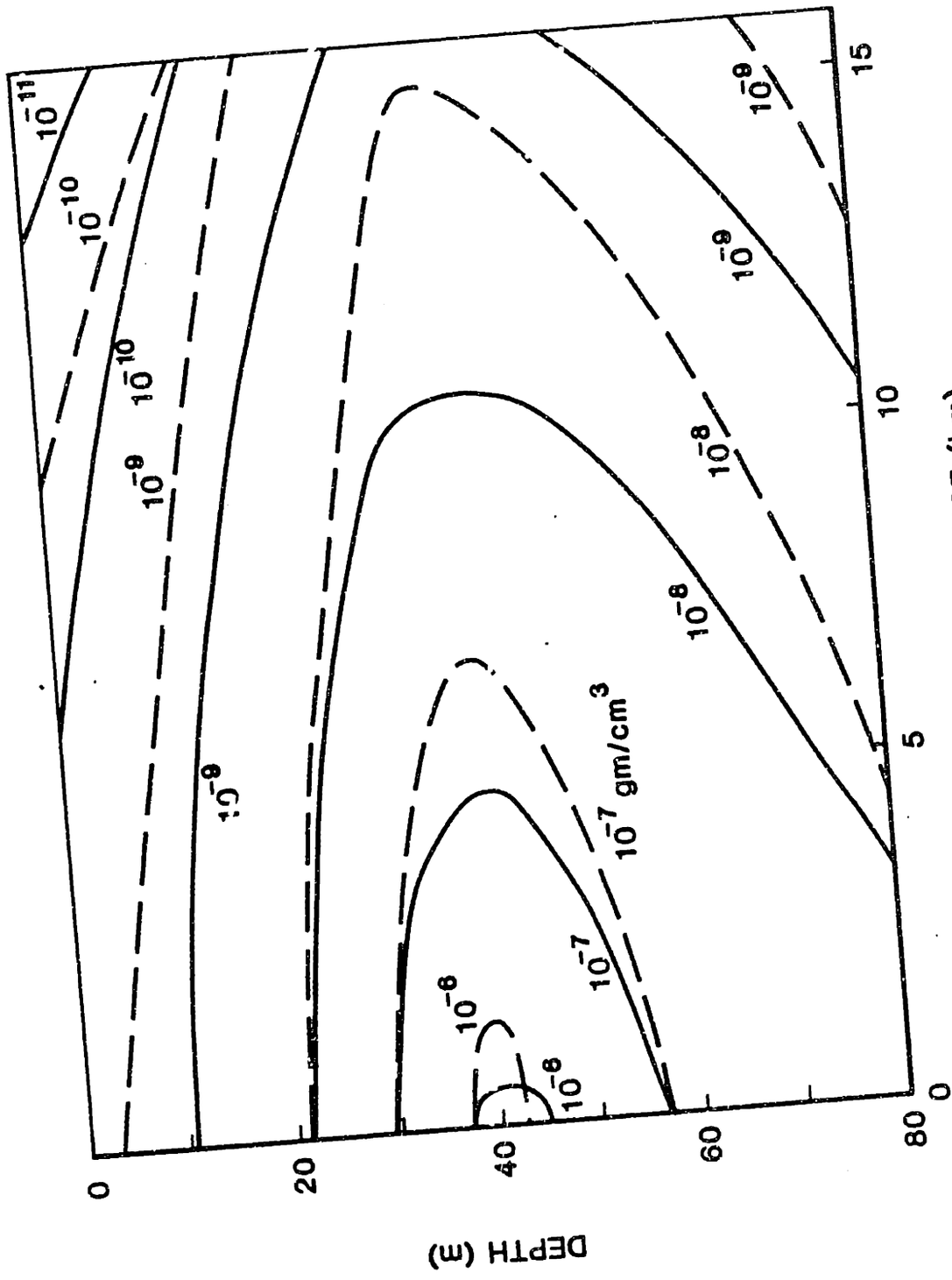

Figure 4-18 Contour plot of steady state mass concentration distribution (solid line, coagulation included; dashed line, coagulation neglected).

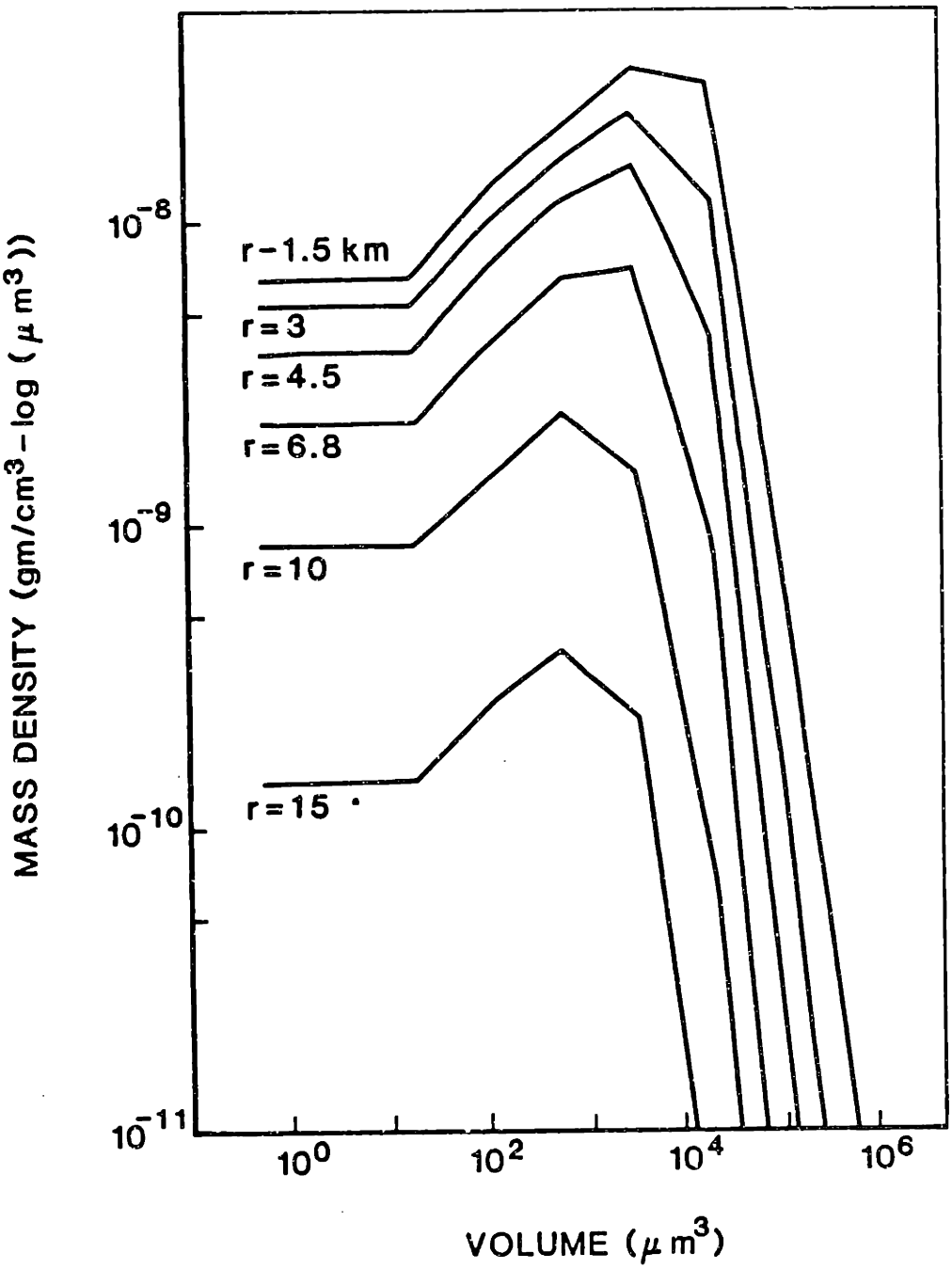

Figure 4-19 Steady state particle size distributions at a depth of 55 m at various radial distances for the simulation with coagulation included.

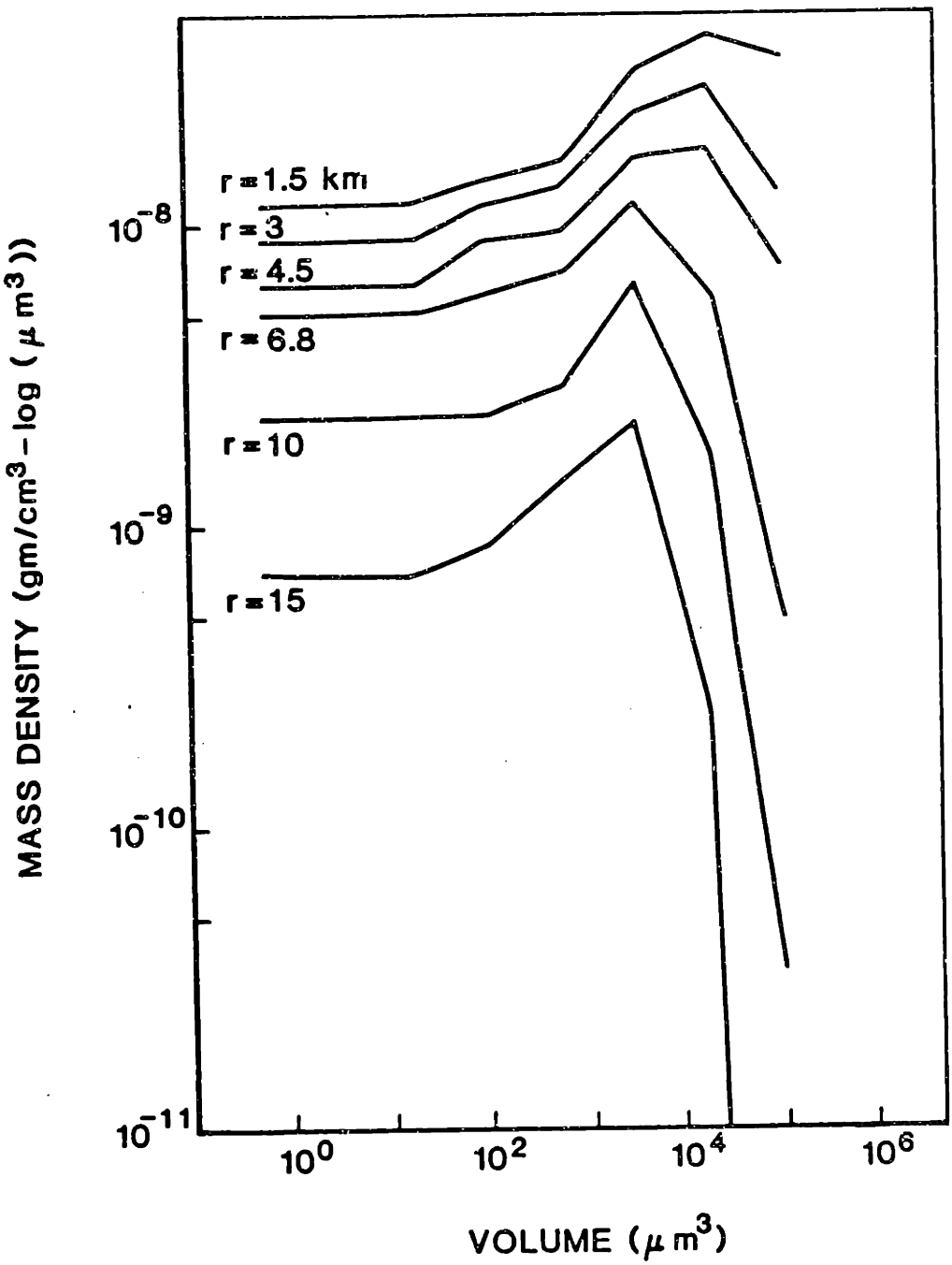

Figure 4-20 Steady state particle size distributions at a depth of 55 m at various radial distances for the simulation with coagulation neglected.

two cases. For the case with coagulation included it is evident that the mass densities are lower, as expected. For both cases there is a peak in the distribution for particle sizes in the neighborhood of r = 10 μm reflecting accumulation of mass which has settled out of the waters above that depth. Particles of size much larger than r = 10 μm settle to the bottom very quickly and experience little radial diffusion. Particles much smaller than 10 μm do not settle significantly but experience a uniform reduction in mass density due to the coagulation process.

In summary, coagulation of waste particles enhances the removal of mass from the water column, especially within a few kilometers from the source. The simulations presented did not consider coagulation of particles during the initial dilution process or coagulation with natural particles already present in the water column. Since the emitted particle concentrations may be as high as 50,000 mg/ℓ for some sludge discharges, the extent of coagulation within the near field plume may be quite significant even though the residence time is only a few minutes. Taking these factors into account, the enhanced mass deposition rate near the source due to coagulation may be significantly greater than the factor of two simulated here.

4.5 A Two-Dimensional Model for the Desorption of Trace Elements from Resuspended, Contaminated Sediments

The intentional or accidental discharge of industrial and municipal wastes often results in the accumulation of trace metals within the sediments adjacent to the disposal site. The trace metal concentrations within the sediments may be reduced by mixing processes in the

sediments, or by desorption from the sediments after they have been resuspended due to a storm event. In shallow coastal waters, unless the bottom current velocity is very large, the last mechanism of concentration reduction is normally the most efficient. Accordingly, as a final demonstration of the capabilities of the Monte Carlo approach, a two-dimensional model for computing the transport of dissolved (free) and adsorbed (bound) trace metal species will be presented. Featured in the model will be the computation of the chemical equilibrium between free and bound states, the differential transport of dissolved and adsorbed species, and particle coagulation.

4.5.1 Model Description

Consider a lens of contaminated sediment of radius R in a coastal waterbody of uniform depth h. The sediments outside the lens and the overlying waters are assumed to be uncontaminated. The occurrence of a storm event will result in the resuspension of sediments. For the initial condition it is assumed that the resuspended sediments have a uniform mass concentration c_o with depth, that they are distributed in particle diameter as d^{-4} over the size range $1\ \mu m < d < 60\ \mu m$, and that the resuspended contaminated sediments are confined to the cylindrical region directly above the initial sediment lens. Outside this cylindrical region the resuspended sediments are assumed to be uncontaminated. Following the resuspension event, the particles begin to coagulate and settle while contaminant desorbs from the particles. Since the mean velocity is assumed to be zero, the only means of transport for the bound and free contaminant, apart from settling, is vertical and radial dispersion.

The modeling of trace metal adsorption/desorption requires special consideration. The adsorption of solute onto a solid surface is a two-step process requiring physical transfer of mass through the fluid phase and chemical reaction at the solid-liquid boundary. Since the reaction at the phase boundary may be as fast as the diffusive transport, either diffusion or reaction may limit the overall reaction rate. However, it is often very difficult to determine which step is controlling. The time scale for equilibrium to be reached for the fluid phase transport and interface reaction is on the order of minutes to hours. In addition to these processes, there is often a slower adsorption process involving diffusion of the adsorbate toward the interior of the solid. The kinetics of this intra-particle diffusion typically occur on a time scale of days to months. The kinetics of surface adsorption are very complicated and not well understood. As a result, there is very little information available on appropriate rate laws and associated kinetic constants. The most successful approaches to date all require invoking chemical equilibrium (Morel, 1983; Karickhoff, 1984).

The traditional modeling of adsorption requires relating, at equilibrium, the number of moles of solute adsorbed per unit mass of solid to solution phase concentration of solute by an empirical curve fit known as an adsorption isotherm. The term isotherm is used to signify that the model is strictly applicable only under conditions of constant temperature, although this restriction is not that critical for aqueous systems. The adsorption isotherm level of modeling is very useful for simple systems at constant pH and ionic strength and where a single adsorbing species is being considered (Morel, 1983).

To incorporate pH and electrostatic effects, the adsorption process may be modeled as a complexation reaction. In addition, the so-called surface complexation model can allow for various kinds of surface sites and more than one adsorbate that will compete for those sites. To apply the surface complexation model it is assumed that a standard free energy of adsorption can be assigned to each reaction. This free energy change is the sum of an intrinsic and a coulombic change, which accounts for the electrostatic effect. The corresponding equilibrium constant is thus given as the product of an intrinsic and a coulombic constant (Morel, 1983). A description and comparison of various models for estimating the coulombic constant may be found in Westall and Hohl (1980). Once a surface complexation model has been chosen, it may be quite simply incorporated into a numerical scheme for computing chemical equilibria (Westall, 1979).

For simplicity, local equilibrium will be invoked and the surface complexation approach will be adopted in the modeling of adsorption, with electrostatic effects neglected. Accordingly, the equilibrium between solid surface sites, XSO^-, and metal cations, M^+, is described by an equilibrium constant that is a function of pH and of the metal species only.

Once local chemical equilibrium has been invoked, the local concentrations of the constituents participating in the reversible reactions are governed by chemical thermodynamics. If a system of n constituents, or species, s_i, $i = 1,2,\ldots,n$ is known to be in chemical equilibrium, then it is possible to choose from the set of n species a subset of $m < n$ components c_j, $j = 1,2,\ldots,m$ whose total concentration is reaction invariant and, thus, chemically conserved (Morel, 1983).

The subset is chosen such that each component is a "building block" for at least one species and such that the total concentration of each component is independent of the total concentration of any other component. Once the components have been chosen, the equilibrium of each species may be expressed in terms of the set of components according to

$$s_i \rightleftharpoons a_{i1}c_1 + a_{i2}c_2 + \ldots + a_{ij}c_j + \ldots + a_{im}c_m \qquad (4\text{-}28)$$

where a_{ij} are stoichiometric coefficients. The equilibrium concentration $[s_i]$ is determined by the mass law equation

$$\frac{[c_1]^{a_{i1}}\,[c_2]^{a_{i2}} \ldots [c_j]^{a_{ij}} \ldots [c_m]^{a_{im}}}{[s_i]} = \frac{1}{K_i} \qquad (4\text{-}29)$$

where K_i is the equilibrium constant. Since the set of m components is contained in the set of n species, the computation of the component concentrations $[c_j]$ is obtained by solving the equations (4-29) by iteration, subject to the constraint that $[c_j]$ be non-negative and

$$\sum_{i=1}^{n} a_{ij}[s_i] = [c_j]_T \qquad (4\text{-}30)$$

that is, that the total concentration $[c_j]_T$ of each component be conserved. To solve the nonlinear algebraic equations, Eq. 4-29 and Eq. 4-30, the MICROQL algorithm developed by Westall (1979) will be employed. This algorithm is essentially the same as the well known computer code MINEQL (Westall et al., 1976) except that the subroutines

for computing equilibrium solid formation (i.e., precipitation) have been removed.

The species that are included in the model are the particles divided into a number of size classes, the dissolved fractions and the adsorbed fractions of each trace metal species. Since the particle size distributions will be horizontally uniform for all times after the resuspension event, it is only necessary to compute the influence of settling and coagulation on the size distributions in the vertical direction (i.e., in one dimension). The transport of the bound and free components of the trace metals, however, will be in both the horizontal and vertical directions, hence a two-dimensional computation is required for the trace metal species.

4.5.2 Model Results

In modeling the reactive transport of resuspended, contaminated sediments we are mainly concerned with computing the horizontal dispersion and the re-deposition of copper to the bottom sediments. The role of coagulation in the re-deposition of copper is particularly interesting. Unfortunately, it is unknown at this time to what extent coagulation reduces the specific surface area available for adsorption, if at all. When two particles coagulate it seems that any solute that is already adsorbed onto the surfaces which come into contact should become trapped within the agglomerate. It also seems that further adsorption onto the surfaces which are now in contact should be impaired. For simplicity and definitiveness, it will be assumed that the adsorbing capacity of any particle is proportional to its instantaneous equivalent spherical surface area. This assumption is

unrealistic since it means that, given two particles whose adsorbing capacity is saturated, should these particles coagulate adsorbate will have to desorb from the new agglomerate since its capacity based on the new equivalent surface area will be exceeded. Since the following simulations are only for demonstration purposes, it must be kept in mind that the conclusions to be drawn from the results are grossly biased by this idealized assumption. Note also that the applicability of the model is not tied to this idealization. Any rule describing how coagulation of two particles affects the adsorbing capacity of the resulting agglomerate may easily be incorporated into the model without loss of generality.

To examine the influence of coagulation two simulations have been performed, one with coagulation included and the other with coagulation neglected. In both cases the depth of the water was set at h = 30 m, the radius of the contaminated lens was r = 1 km, and the initial resuspended sediment concentration was c_o = 100 mg/l. The initial particle size range was 0.5 μm < r < 30 μm, divided into 6 logarithmic size classes. With the onset of coagulation, particle sizes up to r = 100 μm were accounted for with two additional size classes. The particle density was assumed to be 2 gm/cm^3. Constant values of the Kolmogorov time scale, $(\nu/\langle\varepsilon\rangle)^{1/2}$ = 10 sec, the integral time scale, $k/\langle\varepsilon\rangle$ = 3000 sec, the radial eddy diffusivity, Γ_r = 30 m^2/sec, and the vertical eddy diffusivity, $\Gamma_v = 10^{-4}$ m^2/sec, were employed.

For simplicity only one trace metal species was considered in the simulation, namely, copper. Copper forms the following major complexes in seawater: XSOCu, $CuOH^+$, $Cu(OH)_2$, $CuCO_3$, $CuCl^+$, and $CuSO_4$. A complete list of species includes these complexes in addition to the

ionic species Cu^{2+}, XSO^-, H^+, OH^-, HCO_3^-, Cl^-, and SO_4^-. From these 13 species a set of 6 components may be chosen: XSO^-, Cu^{2+}, Cl^-, HCO_3^-, SO_4^{2-}, and H^+. The total concentrations of the seawater ions Cl^-, HCO_3^-, SO_4^{2-}, and H^+ will for all intents and purposes remain unchanged, hence, they were fixed at their natural concentrations. The total concentrations of surface sites and copper will vary in time and space due to differential transport and coagulation. However, since the rate of change of total surface site and copper concentrations at a point in space will be much slower than the rate or re-equilibration, the assumption of local chemical equilibrium is valid.

Table 4-2 is the tableau for the chemical equilibrium computation. The numbers in the central part of the tableau are the stoichiometric coefficients, a_{ij}. Looking horizontally across the tableau one obtains the information to solve the mass action equations, Eq. 4-29. Looking vertically down the tableau yields the information required to solve the mass conservation equations, Eq. 4-30. The total seawater ion concentrations and the equilibrium constants were obtained from Morel (1984) and Mantoura et al. (1978). The surface site density was assumed to be 5×10^{-8} moles/cm^2. Since the total concentrations of the seawater ions are fixed, only two equations need to be solved, the two unknowns being the concentration of adsorbed copper, [XSOCu], and the concentration of dissolved copper, ($[Cu^{2+}] + [CuOH^+] + [Cu(OH)_2] + [CuCO_3] + [CuCl^+] + [CuSO_4]$). Given the total concentration of dissolved copper, the partitioning among the various dissolved copper species is fixed by the stoichiometry, that is, the concentrations of the dissolved copper species will always be in the same fixed relative proportions.

Table 4-2 Tableau for the Computation of the Equilibrium Concentrations

Species	XSO^-	Cu^{2+}	Cl^-	HCO_3^-	SO_4^{2-}	H^+	Log of Stability Constants
XSOCu	1	1	0	0	0	0	8.0
Cu^{2+}	0	1	0	0	0	0	0.
XSO^-	1	0	0	0	0	0	0.
H^+	0	0	0	0	0	1	0.
OH^-	0	0	0	0	0	-1	-13.81
HCO_3^-	0	0	0	1	0	0	0.
Cl^-	0	0	1	0	0	0	0.
$CuOH^+$	0	1	0	0	0	-1	-7.75
$Cu(OH)_2$	0	1	0	0	0	-2	-16.41
$CuCO_3$	0	1	0	1	0	-1	-4.52
$CuCl^+$	0	1	1	0	0	0	-0.14
SO_4^{2-}	0	0	0	0	1	0	0.
$CuSO_4$	0	1	0	0	1	0	0.64
Total Concentrations			$10^{-0.26}$	$10^{-2.62}$	$10^{-1.55}$	$10^{-8.1}$	

Figure 4-21 compares the total particle mass deposition as a function of time for the two simulated cases. As expected, coagulation greatly enhances the deposition of particles on the sea bed. With coagulation neglected, the rate of mass deposition decreases monotonically with time. With coagulation included, the initial rate of deposition is very fast. However, once the largest particles have settled out of the water column carrying with them all the additional particles they have coagulated with (at about t = 0.5 days), the remaining suspended mass concentrations are low enough that the rate of deposition is actually less than the corresponding rate for the case with coagulation neglected. Thereafter the deposition rate increases slightly, exceeding the corresponding rate for the case with coagulation neglected at about t = 4 days, then begins to decrease again very slowly. This observation is supported by the profiles of mass concentration, Figure 4-22. With coagulation neglected, the depth profiles exhibit a decrease in mass concentration near the surface as the larger particles settle out of the water column. With time, only the smallest particles remain which essentially do not settle. As a result, the mass concentration becomes uniform with depth. With coagulation included, the initial mass removal is much more extensive. By t = 0.25 days, half the initially suspended mass has been removed from the water column. The difference between the two profiles, with and without coagulation, is quite significant at this time. Thereafter the difference between the profiles decreases, since the mass deposition rate for the case with coagulation is less than that without coagulation, until t = 5 days. After t = 5 days, the difference between the corresponding profiles increases again. A comparison of Figures

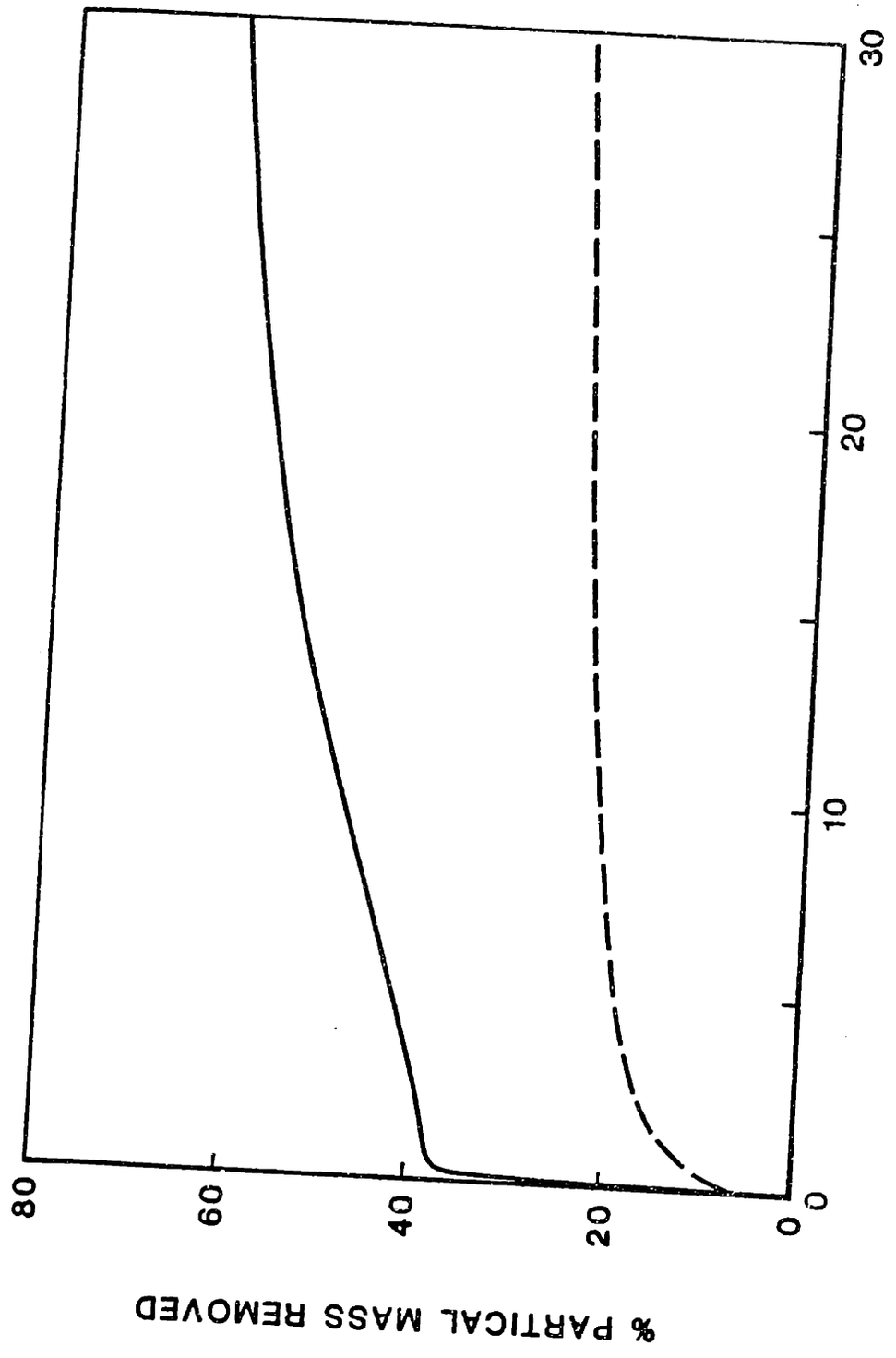

Figure 4-21 Removal of particle mass from the water column as a function of time (solid line, coagulation included; dashed line, coagulation neglected).

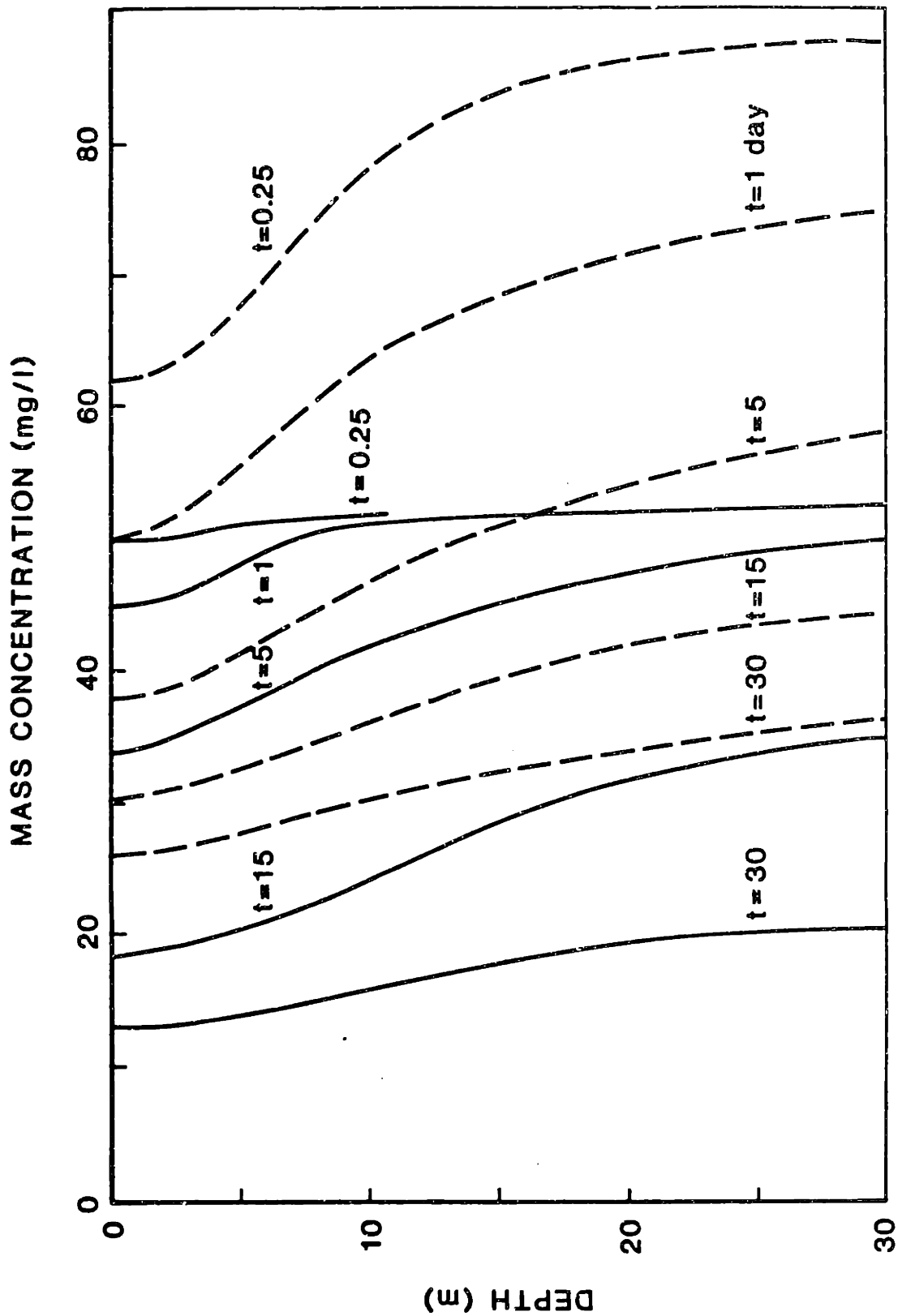

Figure 4-22 Profiles of mass concentration (solid line, coagulation included; dashed line, coagulation neglected).

4-23 and 4-24 shows that with coagulation more large particles are removed than without coagulation. Since we already know that the dominant collisions are with the smallest particles, it is not surprising that the mass concentration of small particles should decrease so fast as well.

Figure 4-25 compares the total redeposited copper as a function of time. Since coagulation reduces the specific surface area of particles, the amount of adsorbed copper that settles out of the water column is initially less for the case with coagulation than without. With less surface area available per unit fluid volume, the equilibrium is shifted towards higher concentrations of dissolved copper. However, the dominant collisions are with the smallest particles. Since most of the copper will be adsorbed to the smallest particles, ultimately the mechanism which removes tha smallest particles most efficiently will also remove the most copper. Hence, after the large particles have settled out of the water column, the rate of removal of copper is greater for the case with coagulation than without. Figures 4-26 and 4-27 support these observations and indicate that with coagulation included less copper is redeposited near the inital sediment lens, but, at later times, more copper is redeposited at greater radial distances than with coagulation neglected. It is evident that coagulation actually contributes indirectly to the dispersion of the contaminant.

Figure 4-28 illustrates the horizontal distribution of adsorbed copper at a depth of 12.5 m at various times. The differences in the distributions for the two cases, with and without coagulation, are so small as to be negligible (though the adsorbed copper concentration is consistently higher for the case without coagulation than with), hence,

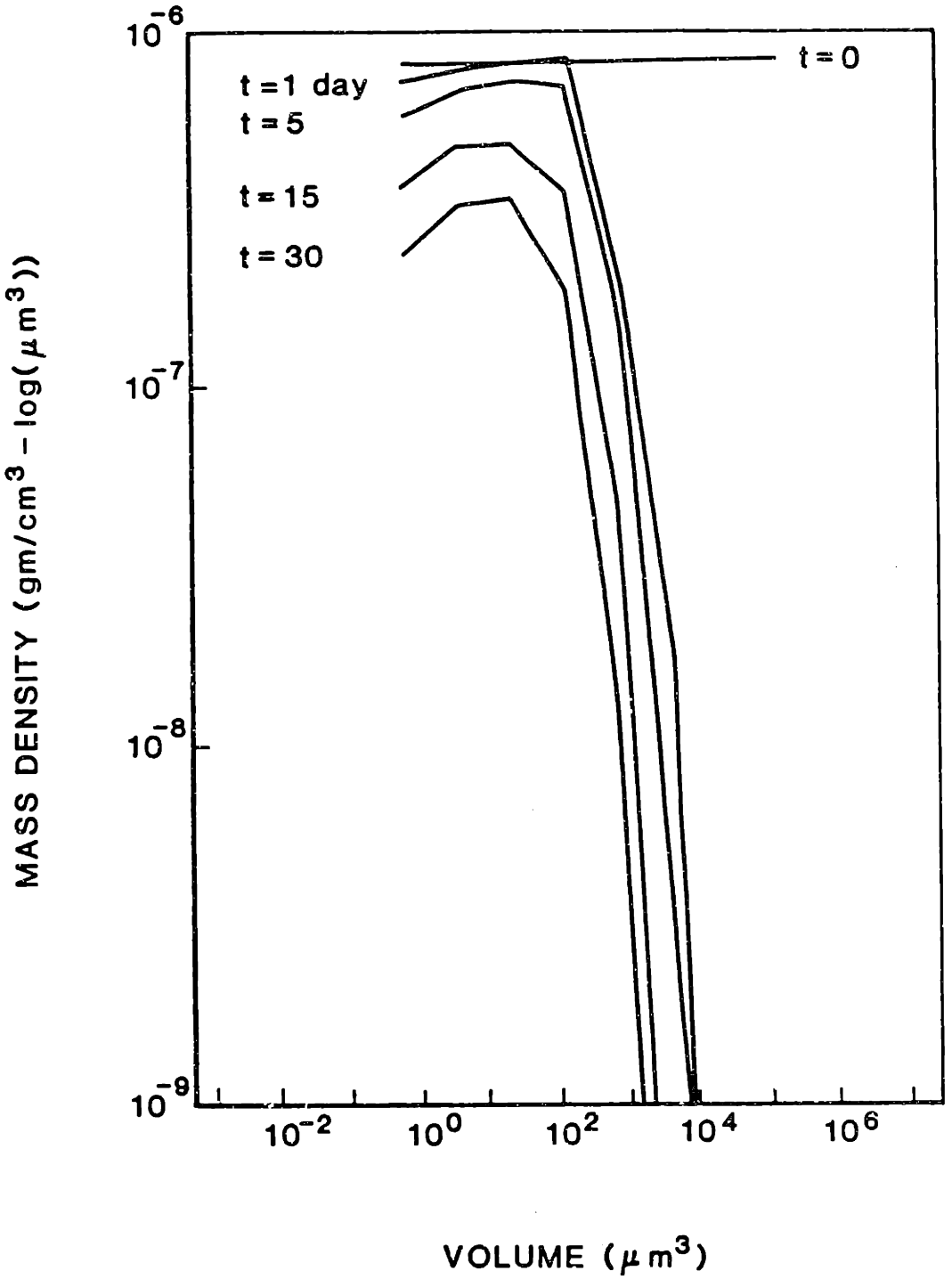

Figure 4-23 Particle size distributions at a depth of 12.5 m at various times for the simulation with coagulation included.

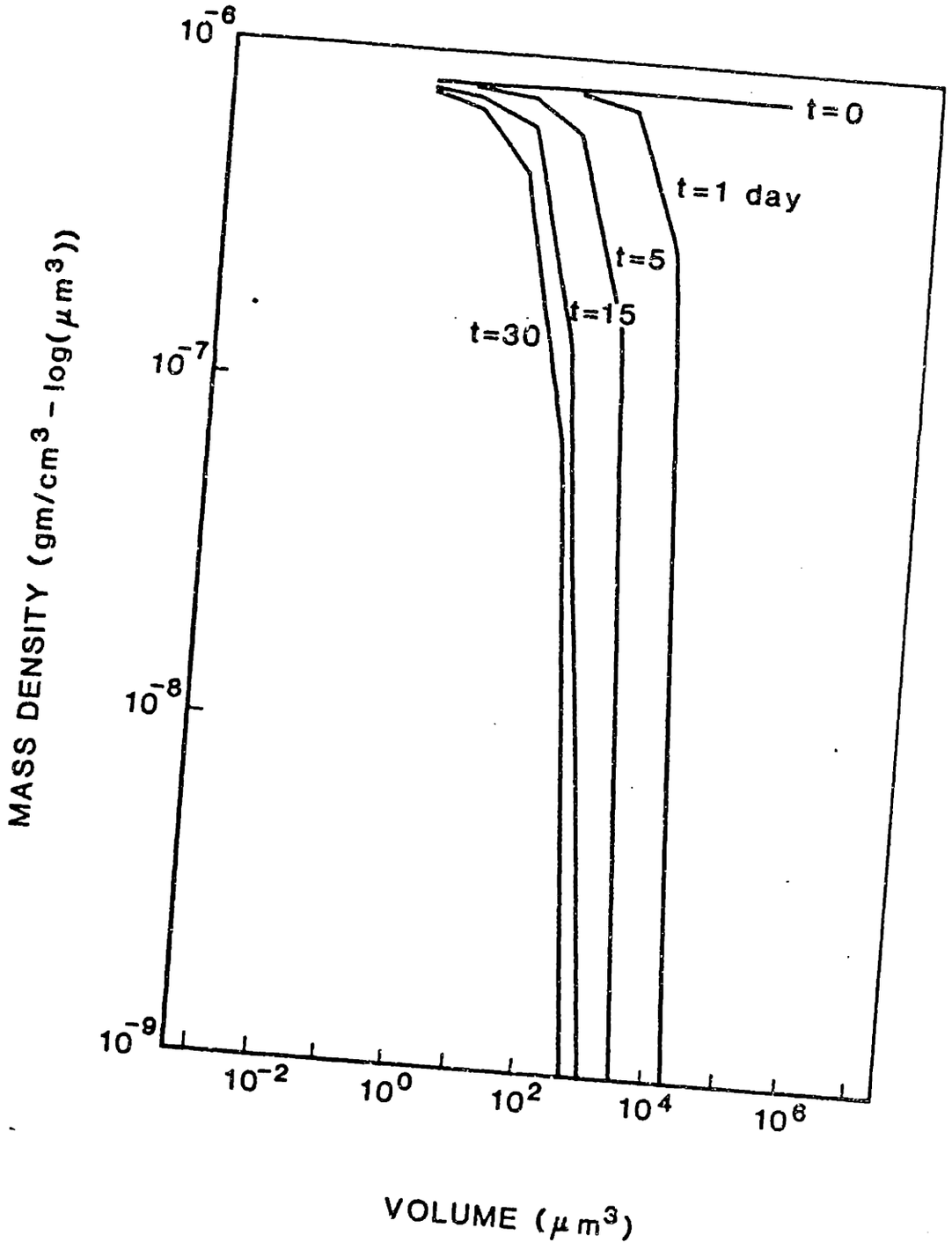

Figure 4-24 Particle size distributions at a depth of 12.5 m at various times for the simulation with coagulation neglected.

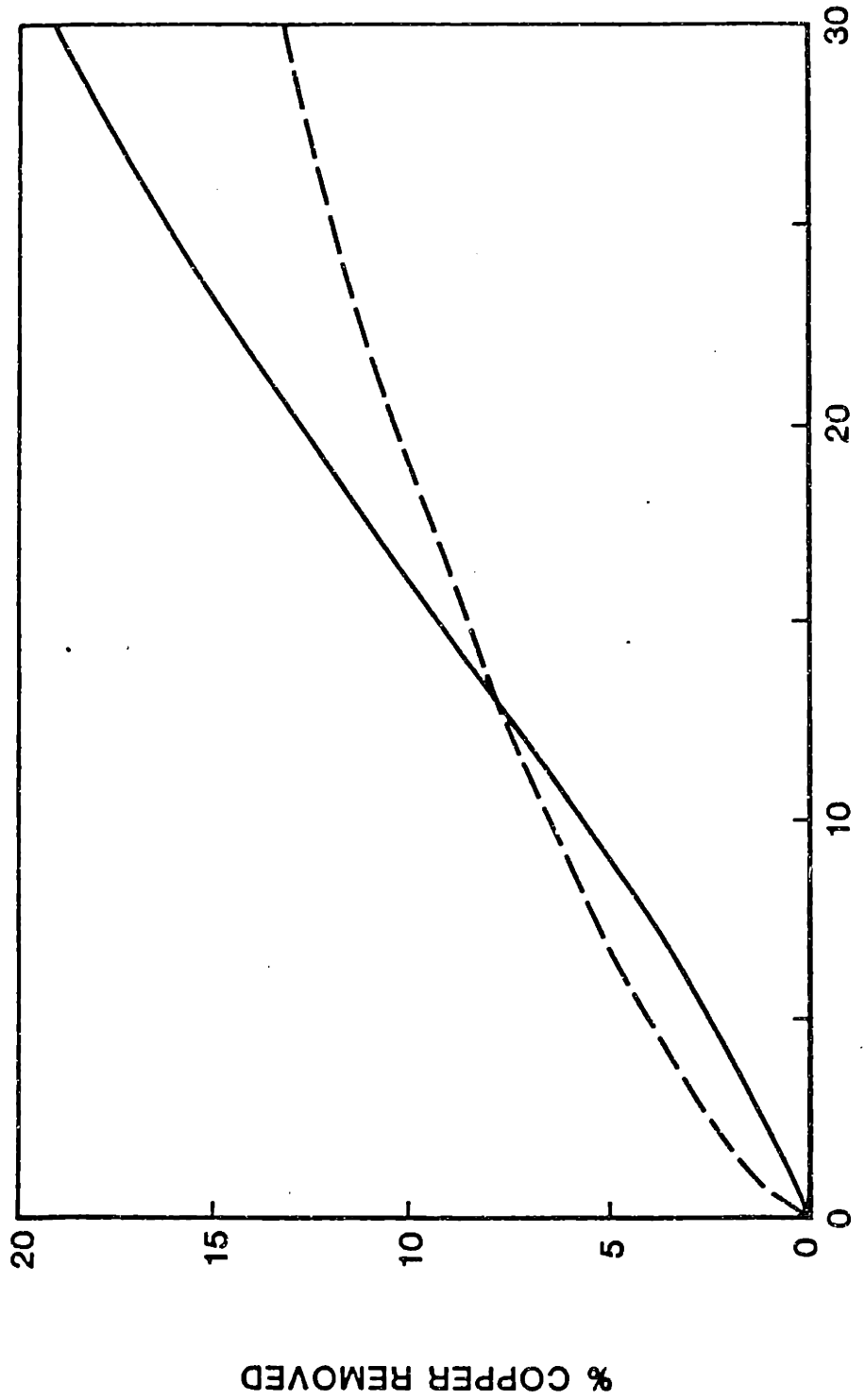

Figure 4-25 Removal of copper from the water column as a function of time (solid line, coagulation included; dashed line, coagulation neglected).

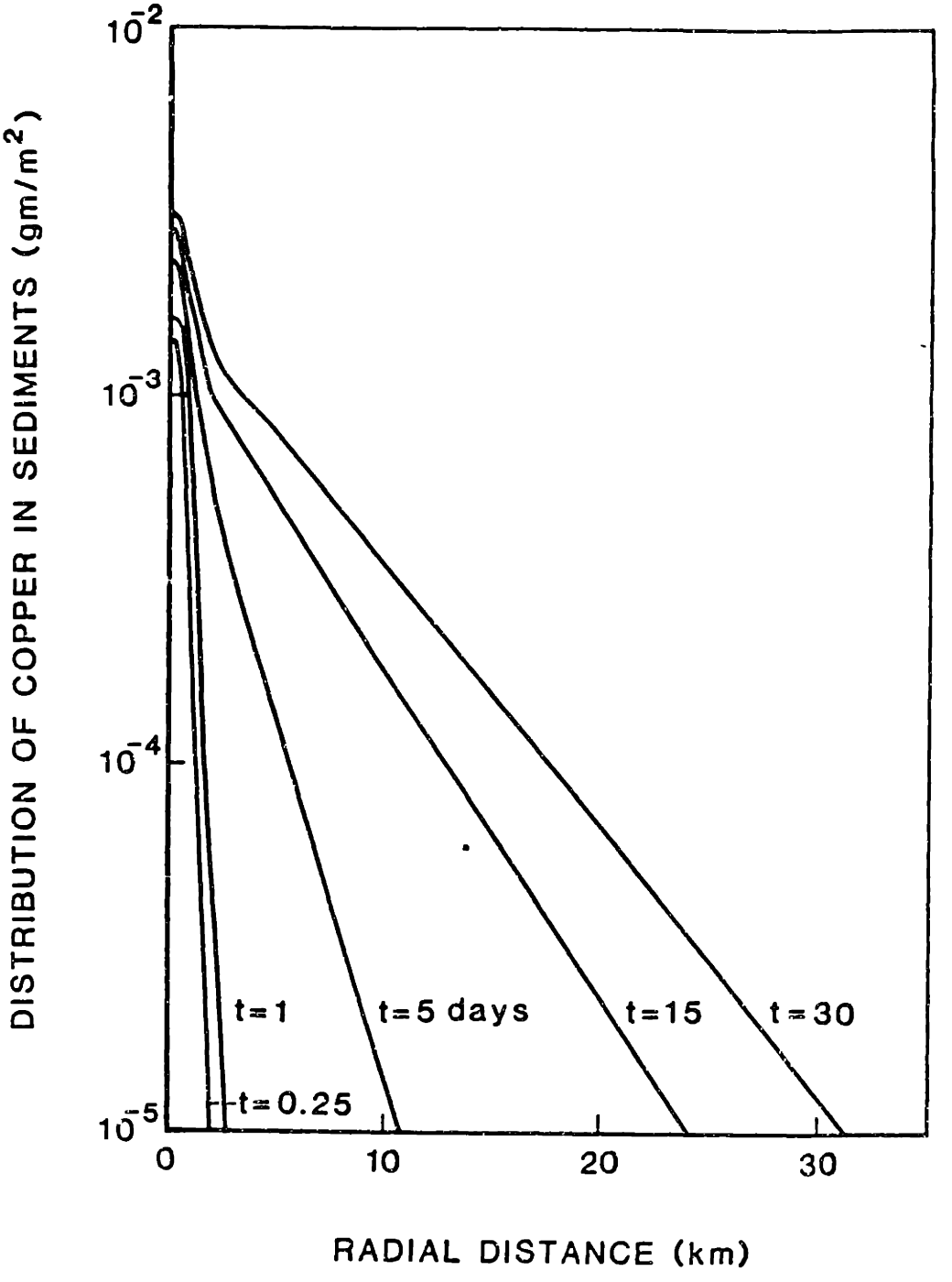

Figure 4-26 Distribution of copper in sediments at various times for the simulation with coagulation included.

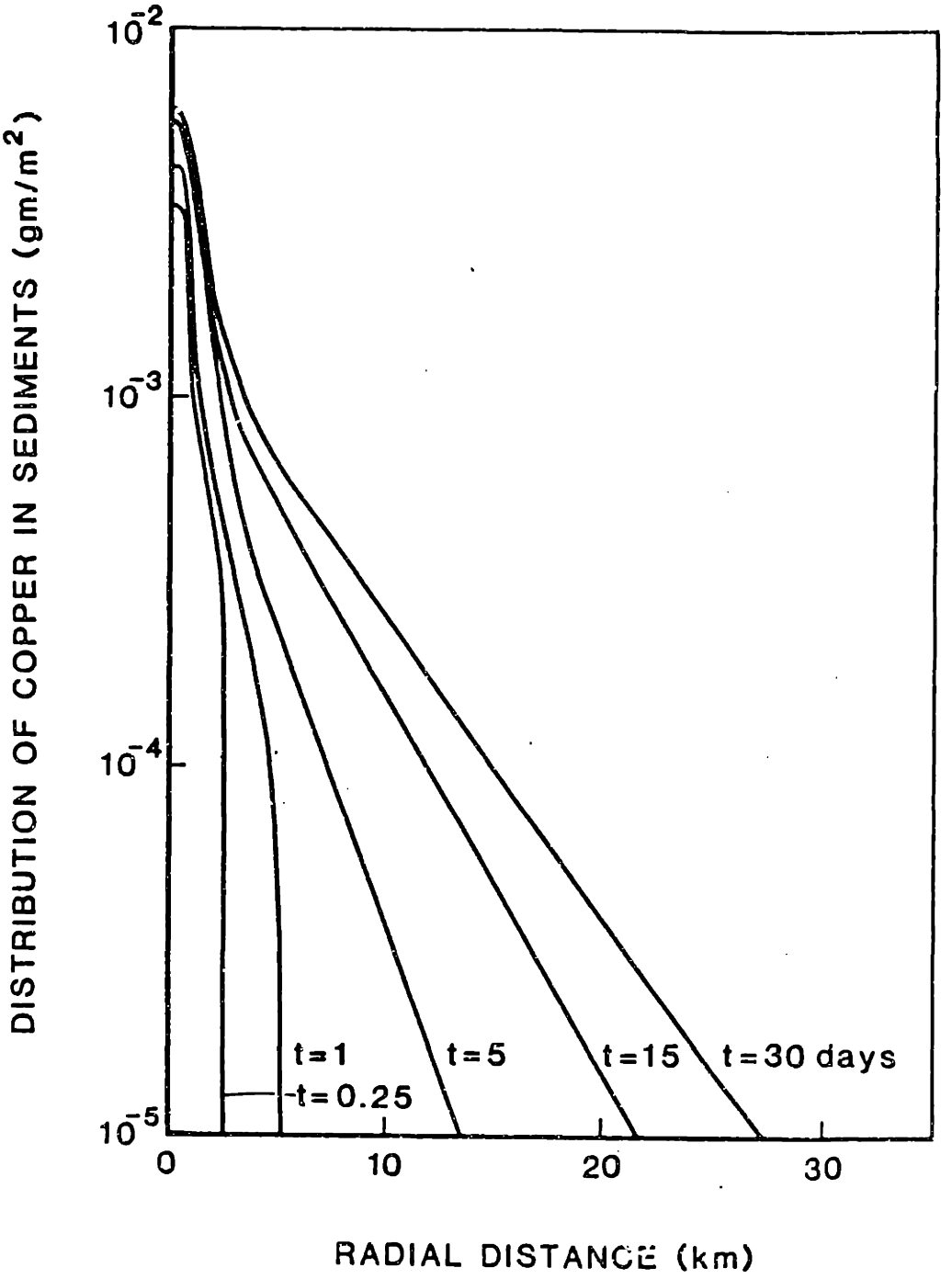

Figure 4-27 Distribution of copper in sediments at various times for the simulation with coagulation neglected.

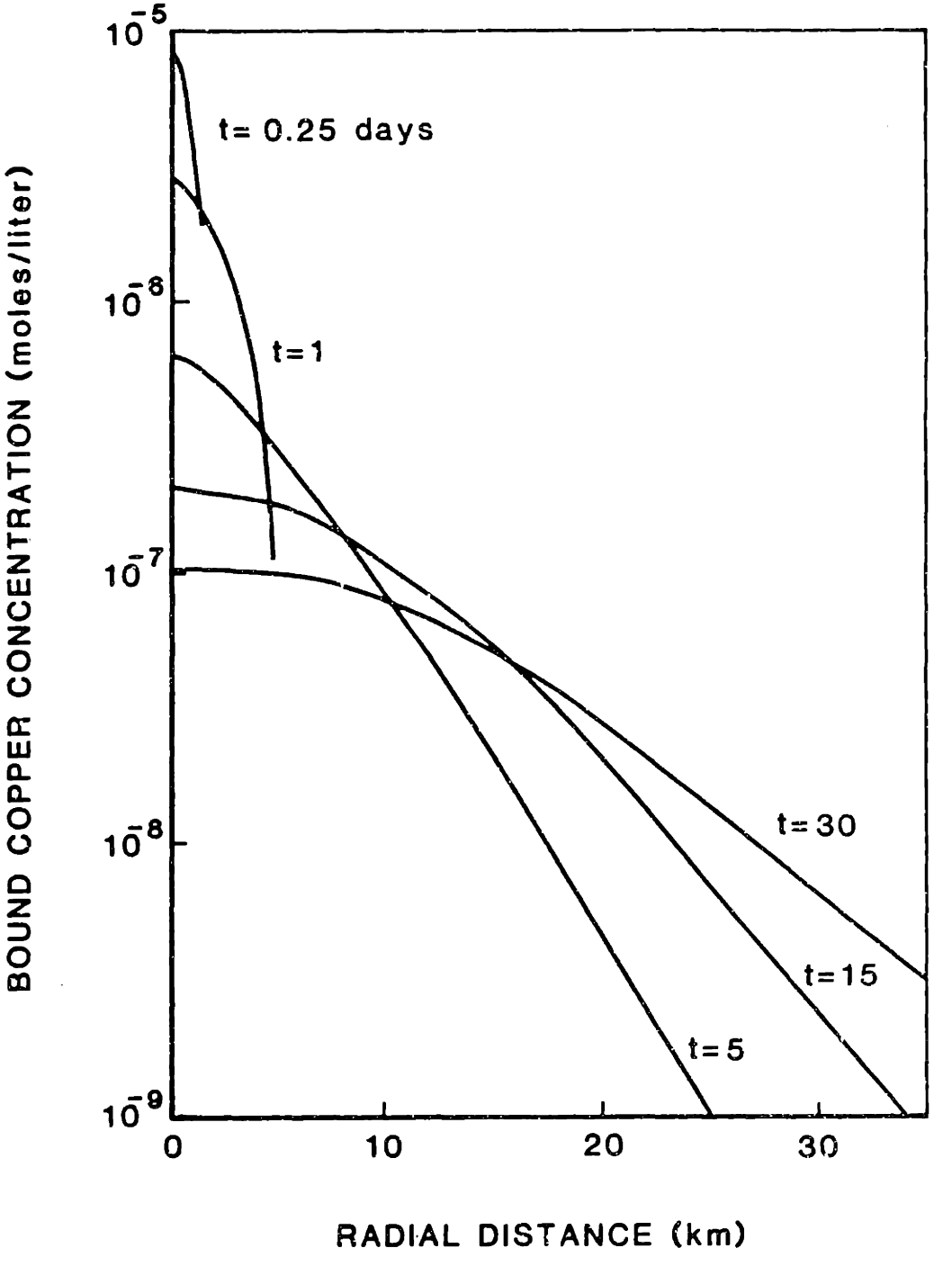

Figure 4-28 Horizontal distribution of adsorbed copper at a depth of 12.5 m at various times.

only one plot is presented. Figure 4-29 compares the horizontal distributions of dissolved copper at a depth of 12.5 m for the two cases. The relative fractions of the various dissolved copper complexes are indicated by the scales on the right. The dissolved copper concentrations for the case without coagulation are lower than for the case with coagulation since in the latter case the total surface area available for adsorption is less. Note again that these conclusions are grossly biased by the idealized assumption regarding the adsorbing capacity of coagulated particles.

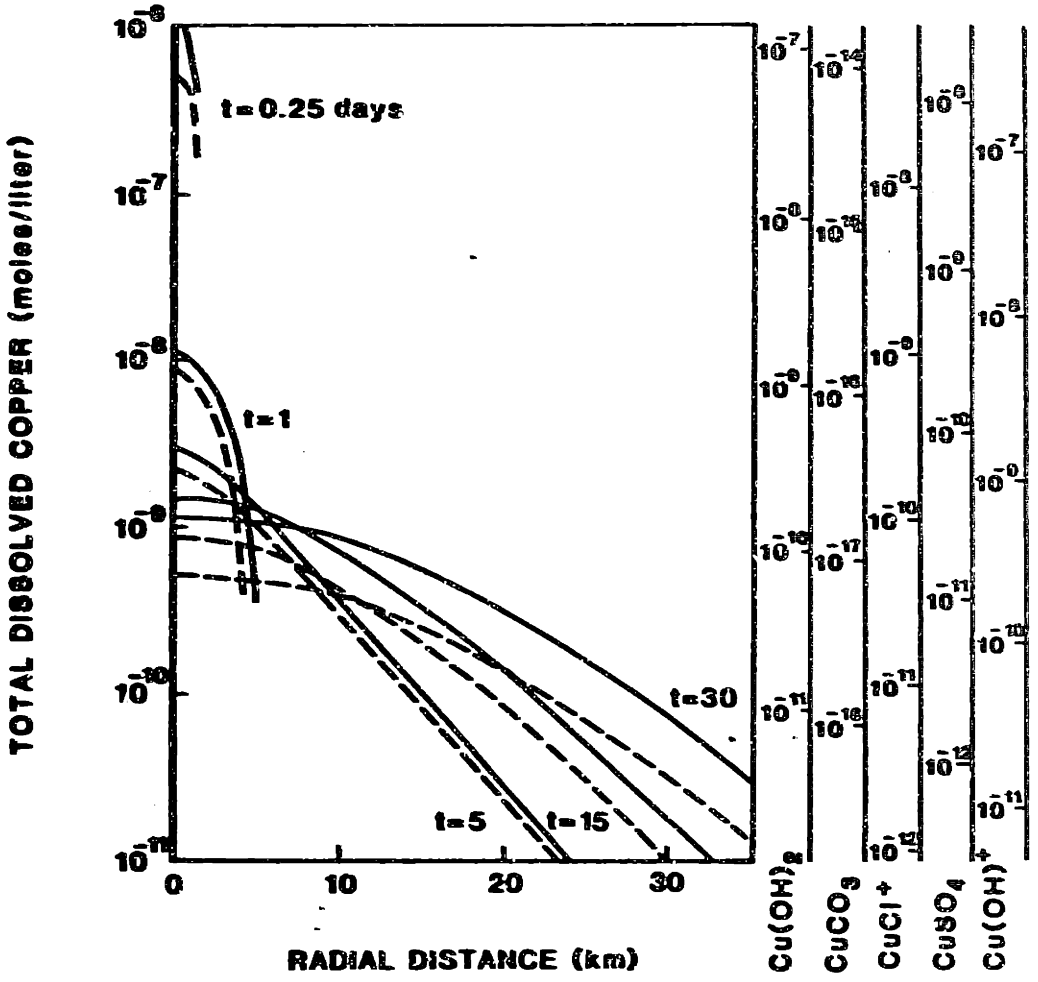

Figure 4-29 Horizontal distribution of dissolved copper at a depth of 12.5 m at various times (scales at right indicate concentrations of various copper complexes; solid line, coagulation included; dashed line, coagulation neglected).

V. SUMMARY AND CONCLUSIONS

The focus of this thesis has been the analytical modeling of transport and reaction involving suspended particles. The modeling of the reactive transport of suspended particles is particularly challenging because particles settle differentially, and they are involved in physicochemical reactions that are often nonlinear and sometimes fast with respect to the fluid turbulence. Due to lack of experimental data, present day understanding of how particle transport and reaction mechanisms interact is limited. The development of a global modeling technique for simulating particle transport and reaction is thus a useful means of synthesizing the available knowledge and increasing our understanding of the dynamics of suspended particles. However, to be a reliable tool, the global model must incorporate submodels for the component processes that have a sound physical basis. Accordingly, a major part of the thesis has been devoted to improving and developing analytical models and computational techniques for the component processes of interest in order to meet this requirement. The following is a summary of the major contributions and conclusions.

An improved model for the collision frequency function for turbulent shear-induced coagulation which takes into account the intermittency in the microscale shear rate has been proposed. The improved model describes the experimental data of Delichatsios and Probstein (1975) better than the well estableished model of Saffman and Turner (1956), although the differences are small.

Based on a discussion of the stochastic nature of coagulation, approximate criteria have been derived for determining whether or not particle correlation effects may be neglected in the modeling of coagulation. The criteria are verified by applying them to the Monte Carlo simulations of Pearson et al. (1984). For typical particle concentrations observed in the aquatic environment, the criteria indicate that particle correlations will always be significant, particularly for the dynamics of the larger particles. Since there is no means of modeling these correlations at present, other than by the Monte Carlo technique of Pearson et al., we must be aware that numerical simulations will tend to under predict the extent of coagulation.

By considering the relative contributions of individual particle interactions to the coagulation process it was shown, contrary to the theory of Hunt (1980, 1982), that steady state coagulation of particles is mainly a result of collisions with the very smallest particles. Klett's (1975) analytical solutions of the coagulation equations were employed to uncover the inconsistency in Hunt's theory. Numerical simulations were used to demonstrate that the generally observed shape of the size distribution for particle mass in coastal waters is a result of particle interactions that may be related to the inclusion of collision efficiency functions in the numerical scheme rather than a local (in particle size space) equilibrium of volume flux, as proposed by Hunt.

To permit the incorporation of fast, nonlinear reaction kinetics in the global modeling framework it was recommended that the model be based on the solution of the transport equation for the one-point, joint scalar probability density function. Pope (1981) devised a very simple

and efficient Monte Carlo technique for solving the pdf transport equation which unfortunately requires a uniform grid. To extend the technique to allow simulation over non-uniform grids, the procedure of duplicating or averaging Monte Carlo elements was put forward and proven to be a valid statistical operation.

An improved advection algorithm was proposed to permit accurate modeling of the differential sedimentation process. While the infinite spatial resolution provided by this algorithm is inconsistent with other alogorithms which limit the spatial resolution to the scale of the grid spacing, the error in applying the improved alogorithm for advection-dominated systems is judged to be less severe than the alternative of suffering numerical dispersion through the use of Pope's (1981) advection algorithm.

Based on the use of operator splitting, an efficient radial diffusion algorithm was developed which allows greater flexibility in the design of the grid and the choice of the element density. Also, for nonlinear reactions that are both sensitive to the microscale shear rate and sufficiently fast (i.e., with a reaction time scale of less than 100 sec) as to be sensitive to fluctuations in the energy dissipation rate, a simple stochastic algorithm was suggested for simulating the temporal variation in the magnitude of the dissipation rate at a point in space.

As an application of some of the concepts discussed in the chapter on coagulation kinetics, and extending the work of Daly (1984), a kinetic model for frazil ice growth was formulated. The model is calibrated and verified against experimental data. A simple analytical expression for estimating the time to reach the point of maximum supercoooling as computed by the zero-dimensional kinetic model is derived.

To examine the effect of vertical transport, the kinetic model of frazil ice growth was incorporated into the Monte Carlo model and a simulation of the formation of frazil ice in rivers was performed. It was determined that, as compared to the case where vertical mixing is infinitely fast, the effect of vertical transport is to delay the time to reach the point of maximum supercooling by an additional increment approximately equal to the diffusion time h^2/Γ_v, where h is the depth of flow. By comparing a simulation in which the interaction between mixing and reaction was suppressed with one in which the interaction was retained, it was demonstrated that the effect of turbulent mixing on the nonlinear growth, coagulation and secondary nucleation reactions is very small. Hence, there really is no need of the capability to model fast (with respect to the mixing rate), nonlinear reactions when modeling the reactive transport of suspended particles. However, note that the improved advection algorithm associated with the Monte Carlo solution procedure is a very accurate and efficient way of modeling differential sedimentation. Given that the capability to model mixing could be removed without significant error, the cost of model computations would be considerably reduced since the reaction would only have to be computed for one element per node (at a given node all elements would be identical and the pdf would be a delta function). Also, considering the simplicity and flexibility of the Monte Carlo approach, it is still recommended for use as the general transport model.

To further demonstrate the capabilities of the Monte Carlo model it was adapted for computations of the transport and deposition of sewage sludge discharged from a coastal outfall and of the desorption of trace

metals from resuspended, contaminated sediments. To be able to easily identify the significance of coagulation as a mechanism affecting the removal of mass and the transport of trace metals in coastal waterbodies the flow regimes in these simulations were grossly oversimplified. In a real simulation of the coastal environment, of course, much more effort would be devoted to characterizing the spatial distributions of mean velocity, eddy diffusivity, and energy dissipation rate.

It is recognized that the kinetic models employed in this thesis need refinement and/or further verification. It is also well known that obtaining experimental data relating to the reactive transport of suspended particles is very difficult. In particular, the problem of measuring particle size distributions is non-trivial and often limits tha accuracy and frequency of experimental measurements. However, a significant amount of research effort is currently being devoted to developing techniques for optically or electronically detecting particle size distributions and these techniques should be perfected within the near future. Let us assume for the moment that such techniques are now available for making particle measurements both in the lab and in the field. What kinds of experiments can be designed to verify the model predictions?

At the zero-dimensionl level it is conventional to perform stirred-beaker experiments to test kinetic models and examine the influence of turbulent mixing. This type of experimental design is not favored here because the very high shear rates near the impeller may cause particle breakup and the non-uniformity of the flow makes it very difficult to characterize the turbulence regime. Instead it is recommended that such experiments be conducted in a container in which

turbulence is generated by uniform buoyant convection. With such a method of mixing the turbulence is quite uniform in all directions over most of the flow field and the turbulence scales may be easily controlled via the heat flux and the plate separation. The problem with this approach is that the level of turbulence required to keep the particles suspended calls for a very large heat flux. Also, to avoid secondary circulations the container must be carefully insulated and the temperature distribution at the top and bottom plates must be maintained horizontally uniform to better than 0.1 degrees Centigrade per meter. Though these problems are quite restrictive, given sufficient resources they may be overcome.

To perform experiments in the container relating to coagulation, micron-sized particles may be mixed in solution of sufficiently low ionic strength that coagulation is suppressed. By slowly increasing the ionic strength of the solution, a well defined point will be reached at which coagulation begins to occur. The time evolution of the particle size distribution may then be measured and compared with the numerical predictions. Any nonlinear behavior due to the interaction of the turbulence with the coagulation process may then be investigated by repeating the experiment at varying levels of the energy dissipation rate. Similarly, to examine nonlinear behavior due to particle correlation effects, the experiment may be repeated at different levels of the initial particle number concentration.

The models of the component processes of frazil ice formation need to be verified with experimental data. To verify the secondary nucleation model it is necessary to suppress the sintering mechanism so that the evolving number concentrations and size distributions may be

uniquely related to the microscale shear rate through the proposed model. This may be accomplished by using other types of crystals that form secondary nuclei but do not sinter. In performing such experiments it will be important to ensure that after the initial seeding no further nuclei are introduced into the chamber other than those formed by the secondary nucleation process. Also, in verifying the model it should be possible to determine for each type of crystal a unique physical constant describing the number of secondary nuclei formed per unit of collision energy. Batchelor (1980) has already shown that his transport-limited growth model describes the available data very well. That frazil ice formation is indeed a transport-limited reaction may need to be further demonstrated. To isolate the growth mechanism, secondary nucleation and sintering must be suppressed. This may be done by introducing only a very small number of initial seed nuclei and effectively increasing the lag period where crystal collisions may be neglected. The rate of growth of the initial seed nuclei should then be described by the growth model. Once the secondary nucleation and growth models have been verified the effect of sintering may then be examined by performing growth experiments at high initial concentrations of seed nuclei. Any behavior not predicted by the secondary nucleation and growth models will then be due to the sintering mechanism. In addition to measuring particle size distributions, high speed photography could be used to provide direct observations of the sintering process. As with coagulation, the influence of turbulence on the reaction rates may be assessed through repeated experiments at varying levels of the energy dissipation rate.

Due to the variability and complexity of sorbent/sorbate composition, chemical character, and sorptive interactions, considerable more laboratory data are required before realistic kinetic models of the adsorption process may be developed. Given that in some instances the microscale turbulent shear rate may determine the reaction rate, the use of a controlled turbulent environment such as the convection chamber in which to perform fundamental adsorption experiments would thus appear to be a necessity.

To examine the effect of transport on reaction at the one-dimensional level, it is recommended that field experiments be conducted in man-made open channels, such as navigation channels, irrigation canals, or drainage ditches. The distributions of the mean velocity and turbulence parameters in these flows may be modeled with reasonable accuracy. In addition, perturbations such as local additions of tracers may be applied and the time response may be monitored by sampling appropriately at downstream locations. Coagulation experiments may be conducted by adding a suitable coagulant in the channel flow and observing the subsequent coagulation of the natural particles. Under suitable atmospheric conditions, frazil ice formation may be induced by increasing the turbulence level in the channel (by increasing the flow rate) to a point where the vertical diffusion rate becomes comparable to the crystal growth rate. Adsorption experiments may be conducted by adding a suitable adsorbate and monitoring its subsequent adsorption onto the natural particles. As demonstrated by the simulation of frazil ice formation in rivers in section 4.3, such experiments may be easily simulated by the Monte Carlo model for comparison purposes.

The use of more complex two- or three-dimensional natural flows to produce experimental results against which model predictions may be verified is not recommended. Since it is very difficult to predict mean circulations and the distributions of the turbulence parameters in such flows, one can only expect to reproduce gross features with numerical computations. Once the model has been verified at the zero- and one-dimensional levels it may be expected to produce results at the two- and three-dimensional levels whose accuracy is limited by the accuracy with which the hydrodynamic inputs may be specified.

In closing, it is emphasized that the primary utility of the reactive transport model is as an engineering tool, that is, to provide understanding as to interactions between various mechanisms of transport and reaction, to examine the consequences of any hypotheses or models made with regards to any reaction process, to aid in the design of lab and field experiments, and to evaluate the gross effects of any artificial perturbation applied to the aquatic environment. Quite simply, the analytical models and computational techniques presented in this thesis provide a framework within which the dynamics of suspended particles may be studied.

REFERENCES

Adler, P.M., 1981. Heterocoagulation in shear flow. J. Colloid Interf. Sci., 83:106-115.

Ariathurai, R. and R.B. Krone, 1976. Finite element model of cohesive sediment transport. ASCE J. Hyd. Div., 102(HY3):323-338.

Ashton, G.D., 1979. River ice. American Scientist, 67(1):38-45.

Batchelor, G.K. and A.A. Townsend, 1949. The nature of turbulent motion at large wave numbers. Proc. Roy. Soc. (London), A199, 1057:238-255.

Batchelor, G.K., 1959. Small-scale variation of convected quantities like temperature in turbulent fluid. Part I. General discussion and the case of small conductivity. J. Fluid Mech., 5:113-133.

Batchelor, G.K., I.D. Howells and A.A. Townsend, 1959. Small-scale variation of convected quantities like temperature in turbulent fluid. Part 2. The case of large conductivity. J. Fluid Mech., 5:134-139.

Batchelor, G.K. and J.J. Green, 1972a. The hydrodynamic interactions of two small freely-moving spheres in a linear flow field. J. Fluid Mech., 56:375-400.

Batchelor, G.K. and J.J. Green, 1972b. The determination of the bulk stress in a suspension of spherical particles to order c^2. J. Fluid Mech., 56:401-427.

Batchelor, G.K., 1979. Mass transfer from a particle suspended in fluid with a steady linear ambient velocity distribution. J. Fluid Mech., 95:369-400.

Batchelor, G.K., 1980. Mass transfer from small particles suspended in turbulent fluid. J. Fluid Mech., 98:609-623.

Bayewitz, M.H., J. Yerushalmi, S. Katz and R. Shinnar, 1974. The extent of correlations in a stochastic coalescence process. J. Atmos. Sci., 31:1604-1614.

Belyaev, V.S., M.M. Lubimtzev and R.V. Ozmidov, 1975. The rate of dissipation of turbulent energy in the upper layer of the ocean. J. Phys. Oceanogr., 5:499-505.

Benjamin, J.R: and C.A. Cornell, 1970. Probability, Statistics and Decision for Civil Engineers, McGraw-Hill, 684 pp.

Berry, E.X., 1967. Cloud droplet growth by collection. J. Atmos. Sci., 24:688-701.

Bowden, K.F., 1962. Measurement of turbulence near the sea bed in a tidal current. J. Geophys. Res., 67:3181-3186.

Brewer, P.G., D.W. Spencer, P.E. Biscaye, A. Hanley, P.L. Sachs, C.L. Smith, S. Kadar, and J. Fredericks, 1976. The distribution of particulate matter in the Atlantic Ocean. Earth and Planetary Science Letters, 32:393-402.

Brodkey, R.S., 1975. Mixing in turbulent fluids. In Turbulence in Mixing Operations (R.S. Brodkey, ed.), Academic Press, pp. 48-119.

Brun-Cottan, J.C., 1971. Etude de la granulometrie des particules marines, measures effectuees avec un compteur Coulter. Cahier Oceanographiques, 23:193-205.

Caldwell, T.R. and T.M. Chriss, 1981. The viscous sublayer at the sea floor. Science, 205:1131-1132.

Carder, K.L., G.F. Beardsley and H. Pak, 1971. Particle size distributions in the eastern equatorial Pacific. J. Geophys. Res., 76:5070-5077.

Carslaw, H.S. and J.C. Jaeger, 1959. Conduction of Heat in Solids (2nd Ed.), Oxford University Press, 510 pp.

Carstens, T., 1966. Experiments with supercooling and ice formation in flowing water. Geofysiske Publikasjoner, 26(9):3-18.

Carstens, T., 1970. Heat exchanges and frazil formation. IAHR Ice Symposium, Reykjavik, Iceland, Paper No. 2.11, 17 pp.

Chapman, B.M., 1982. Numerical simulation of the transport and speciation of nonconservative chemical reactants in rivers. Water Resources Res., 18(1):155-167.

Chase, R.R.P., 1979. Settling behavior of natural aquatic particulates. Limnol. Oceanogr., 24:417-426.

Chen, C.W. and G.T. Orlob, 1975. Ecological simulation for aquatic environments. In Systems Analysis and Simulations in Ecology, Vol. 3 (B. Patten, ed), Academic Press, pp. 475-588.

Chin, E.H.C. and M. Neiburger, 1972. A numerical simulation of the gravitational cc1lection process for cloud droplets. J. Atmos. Sci., 29:718-727.

Clontz, N.A. and W.L. McCabe, 1971. Contact nucleation of magnesium sulfate heptahydrate. Chem. Eng. Progress Symposium Series, No. 110, 67(6).

Cook, G.S., R.W. Morton and A.T. Massey, 1977. A report on environmental studies of dredge spoil disposal sites. In Bottom Turbulence (J.C.J. Nihoul, ed.), Elsevier, pp. 275-299.

Corrsin, S., 1964. The isotropic turbulent mixer: part II. Arbitrary Schmidt number. A.I.Ch.E.J., 10:870-877.

Curl, R.L., 1963. Dispersed phase mixing: I. Theory and effects of simple reactors. A.I.Ch.E.J., 9:175-181.

Daly, S.F., 1984. Frazil ice dynamics. USA Cold Regions Research and Engineering Laboratory, Monograph 84-1.

Delichatsios, M.A. and R.F. Probstein, 1975. Coagulation in turbulent flow: theory and experiment. J. Colloid Interf. Sci., 51:394-405.

Denk, E.G., Jr. and G.D. Botsaris, 1972a. Fundamental studies in secondary nucleation from solution. J. Crystal Growth, 13/14:493-499.

Denk, E.G., Jr. and G.D. Botsaris, 1972b. Mechanism of contact nucleation. J. Crystal Growth, 15:57-60.

Desai, R.M., J.W. Rachow and D.C. Timm, 1974. Collision breeding: a function of crystal moments and degree of mixing. A.I.Ch.E.J., 20(1):43-50.

Dillon, T.M. and T.M. Powell, 1976. Low frequency turbulence spectra in the mixed layer of Lake Tahoe, California-Nevada. J. Geophys. Res., 81(36):6421-6427.

Dillon, T.M. and D.R. Caldwell, 1980. The Batchelor spectrum and dissipation in the upper ocean. J. Geophys. Res., 85:1910-1916.

Dillon, T.M., J.G. Richman, C.G. Hansen and M.D. Pearson, 1981. Near-surface turbulence measurements in a lake. Nature, 290:390-392.

Dillon, W.P., 1964. Flotation technique for separating fecal pellets and small marine organisms from sand. Limnol. Oceanogr., 9:601-602.

Dopazo, C., 1975. Probability density function approach for a turbulent axisymmetric heated jet: Centerline evolution. Phys. Fluids, 18:397-404.

Dopazo, C., 1979. Relaxation of initial probability density functions in the turbulent convection of scalar fields. Phys. Fluids, 22:20-30.

Drake, D.E., 1974. Distribution of suspended particulate matter in submarine canyons off southern California. In Suspended Solids in Water (R.J. Gibbs, ed.), Plenum Press, pp. 133-153.

Drake, D., 1976. Suspended fine sediment transport. In Marine Sediment Transport and Environmental Management (D.J. Stanley and D.J.P. Swift, eds.), Wiley-Interscience, pp. 127.

Drake, R.L. and T.J. Wright, 1972. The scalar transport equation of coalescence theory: new families of exact solution. J. Atmos. Sci., 29:548-556.

El Telbany, M.M.M. and A.J. Reynolds, 1981. Turbulence in plane channel flows. J. Fluid Mech., 111:283-318.

Evans, T.W., G. Margolis and A.F. Sarofim, 1974. Mechanisms of secondary nucleation in agitated crystallizers. A.I.Ch.E.J., 20(5):950-958.

Evans, T.W., A.F. Sarofim and G. Margolis, 1974. Models of secondary nucleation attributable to crystal-crystallizer and crystal-crystal collisions. A.I.Ch.E.J., 20(5):959-966.

Faisst, W.K., 1980. Characterization of particles in digested sewage sludge. In Particulates in Water (M.C. Kavanaugh and J.O. Leckie, eds.), Advances in Chemistry Series #189, American Chemical Society, Washington, D.C., pp. 259-282.

Farley, K.J., 1984. Sorption and sedimentation as mechanisms of trace metal removal. Ph.D. Thesis, Civil Engineering Dept., Massachusetts Institute of Technology, Cambridge, Mass., 125 pp.

Feke, D.L. and W.R. Schowalter, 1983. The effect of Brownian diffusion on shear-induced coagulation of colloidal dispersions. J. Fluid Mech., 133:17-35.

Findheisen, W., 1939. Zur Frage der Regentrop-fenbildung in reinem wasserwolken. Meteor. Z., 56:365-368.

Fischer, H.G., E.J. List, R.C.Y. Koh, J. Imberger and N.H. Brooks, 1979. Mixing in Inland and Coastal Waters, Academic Press, 483 pp.

Flagan, R.C. and J.P. Appleton, 1974. A stochastic model of turbulent mixing with chemical reaction: nitric oxide formation in a plug flow burner. Combustion and Flame, 23:249-267.

Fletcher, N.H., 1970. Chemical Physics of Ice, Cambridge University Press.

Friedlander, S.K., 1960a. On the particle size spectrum of atmospheric aerosols. J. Meteor., 17:373-374.

Friedlander, S.K., 1960b. Similarity considerations for the particle-size spectrum of a coagulating, sedimenting aerosol. J. Meteor., 17:479-483.

Garabedian, H. and R.F. Stickland-Constable, 1974. Collision breeding of ice crystals. J. Crystal Growth, 22:188-192.

Garside, J. and M.A. Larson, 1978. Direct observation of secondary nuclei production. J. Crystal Growth, 43:694-704.

Gelbard, F., Y. Tambour and J.H. Seinfeld, 1980. Sectional representations for simulating aerosol dynamics. J. Colloidal Interf. Sci., 76:541-556.

Gibson, C.H., G.R. Stegen and R.B. Williams, 1970. Statistics of the fine structure of turbulent velocity and temperature fields measured at high Reynolds number. J. Fluid Mech., 41:153-167.

Gibson, C.H., L.A. Vega and R.B. Williams, 1974. Turbulent diffusion of heat and momentum in the ocean. Adv. Geophys., 18A:353-370.

Gillespie, D.T., 1972. The stochastic coalescence model for cloud droplet growth. J. Atmos. Sci., 29:1496-1510.

Gillespie, D.T., 1975. An exact method for numerically simulating the stochastic coalescence process in a cloud. J. Atmos. Sci., 29:1977-1989.

Golovin, A.M., 1963. The solution of the coagulation equation for cloud droplets in a rising air current. Bull. Acad. Sci. USSR, Geophys. Ser., No. 5:48-487.

Grant, H.L., B.A. Hughes, W.M. Vogel and A. Moilliett, 1968. Some observations of turbulence in and above the thermocline. J. Fluid Mech., 34:443-448.

Grant, H.L., R.W. Stewart and A. Moilliett, 1962. Turbulence spectra from a tidal channel. J. Fluid Mech., 12:241-268.

Grove, D.B. and W.W. Wood, 1979. Prediction and field verification of subsurface water quality changes during artificial recharge, Lubbock, Texas. Ground Water, 17:250.

Hahn, H.H., F. Kaser and R. Klute, 1980. Modeling particulate transport in impounded rivers. In Particulates in Water (M.C. Kavanaugh and J.O. Leckie, eds.). Advances in Chemistry Series No. 189, American Chemical Society, Washington, D.C., pp. 213-231.

Handscomb, D.C. and J.M. Hammersley, 1965. Monte Carlo Methods, Methuen, London.

Hanley, T. O'D. and G. Tsang, 1984. Formation and properties of frazil ice in saline water. Cold Regions Science and Technology, 8:209-221.

Heathershaw, A.D., 1976. Measurements of turbulence in the Irish Sea benthic boundary layer. In The Benthic Boundary Layer (I.N. McCave, ed.), Plenum Press, pp. 11-31.

Herring, J.R., 1980. Wastewater particle dispersion in the southern California offshore region. In Particulates in Water (M.C. Kavanaugh and J.O. Leckie, eds.), Advances in Chemistry Series, No. 189, American Chemical Society, Washington, D.C., pp. 283-304.

Hobbs, P.V., 1974. Ice Physics, Oxford University Press, 837 pp.

Hunt, J.R., 1980. Prediction of oceanic particle size distributions from coagulation and sedimentation mechanisms. In Particulates in Water (M.C. Kavanaugh and J.O. Leckie, eds.), Advances in Chemistry Series, No. 189, American Chemical Society, Washington, D.C., pp. 243-257.

Hunt, J.R., 1982. Self-similar particle size distributions during coagulation: theory and experimental verification. J. Fluid Mech., 122:169-185.

Jamicka, J., W. Kolbe and W. Kollmann, 1979. Closure of the transport equation for the pdf of turbulent scalar fields. J. Nonequil. Thermodyn., 4:47-66.

Jeffrey, D.J., 1981. Quasi-stationary approximations for the size distributions of aerosols. J. Atmos. Sci., 38:2440-2443.

Jones, I.S.F. and B.C. Kenney, 1971. Turbulence in Lake Huron. Water Res., 5:765-776.

Junge, C.E., 1969. Comments on "Concentration and size distribution measurements of atmopsheric aerosols and a test of the theory of self-preserving size distributions". J. Atmos. Sci., 26:603-608.

Kallingal, J.P. and A.J. Barduhn, 1977. Growth rate of an ice crystal in subcooled pure water. A.I.Ch.E.J., 23(3):294-303.

Karickhoff, S.W., 1984. Organic pollutant sorption in aquatic systems. ASCE J. Hyd. Div., 110 (HY6):707-735.

Kattan, A. and R.J. Adler, 1967. A stochastic mixing model for homogeneous, turbulent, tubular reactor. A.I.Ch.E.J., 13:580-585.

Kavanaugh, M.C., C.H. Tate, A.R. Trussel, R.R. Trussel and G. Treweek, 1980. Use of particle size distribution measurements for selection and control of solid/liquid separation processes. In Particulates in Water (M.C. Kavanaugh and J.O. Leckie, eds.), Advances in Chemistry Series, No. 189, American Chemical Society, Washington, D.C., pp. 305-328.

Kholmyanskii, M.Z., 1970. Investigation of the fluctuations of the wind velocity derivative in an atmospheric surface layer. Izv. Akad. Nauk. SSSR. Fiz. Atmosf. i. Okeana, 6:423-430.

Klett, J.D., 1975. A class of solutions to the steady-state, source-enhanced, kinetic coagulation equation. J. Atmos. Sci., 32:380-389.

Kolmogorov, A.N., 1962. A refinement of previous hypotheses concerning the local structure of turbulence in a viscous incompressible fluid at high Reynolds number. J. Fluid Mech., 13:82-85.

Krone, R.B., 1972. A field study of flocculation as a factor in estuarial shoaling processes. Tech. Bull. U.S. Corps Engineers, Committee on Tidal Hydraulics, No. 19, 62 pp.

Krone, R.B., 1976. Engineering interest in the benthic boundary layer. In The Benthic Boundary Layer (I.N. McCave, ed.), Plenum Press, pp. 143-156.

Kuo, A. Y-S. and S. Corrsin, 1971. Experiments on internal intermittency and fine structure distribution function in fully turbulent fluid. J. Fluid Mech., 50:285-320.

Lal, D.P., R.E.A. Mason and R.F. Stickland-Constable, 1969. Collision breeding of crystal nuclei. J. Crystal Growth, 5:1-8.

Lapidus, A. and V. Shafrir, 1972. A new Monte Carlo simulation model for the temporal development of cloud droplet spectra. J. Atmos. Sci., 29: 1308-1312.

Lawler, D.F., C.R. O'Melia and J.E. Tobiason, 1980. Integral water treatment plant design: from particle size to plant performance. In Particulates in Water (M.C. Kavanaugh and J.O. Leckie, eds.), Advances in Chemistry Series, No. 189, American Chemical Society, Washington, D.C., pp. 353-388.

Lerman, A., K.L. Carder and P.R. Betzer, 1977. Elimination of fine suspensoids in the oceanic water column. Earth and Planetary Science Letter, 37:61-70.

Lumley, J.L., 1976. Two-phase and non-Newtonian flows. In Turbulence (P. Bradshaw, ed.), Topics in Applied Science, Vol. 12, Springer-Verlag, pp. 289-324.

Lumley, J.L., 1980. Second order modeling of turbulent flows. In Prediction Methods for Turbulent Flows (W. Kollmann, ed.), Hemisphere, pp. 1-31.

Mantoura, R.F.C., A. Dickson and J.P. Riley, 1978. The complexation of metals with humic materials in natural waters. Estuarine and Coastal Marine Science, 6:387-408.

Marcus, A.H., 1968. Stochastic coalescence. Technometrics, 10:133-143.

Marmorino, G.O. and D.R. Caldwell, 1978. Temperature finestructure and microstructure observations in a coastal upwelling region during a period of variable winds (Oregon, summer 1974). Deep Sea Res., 25:1073-1106.

Martin, S., 1981. Frazil ice in rivers and oceans. Ann. Rev. Fluid Mech., 13:379-397.

McCave, I.N., 1983. Particulate size spectra, behavior, and origin of nepheloid layers over the Nova Scotian continental rise. J. Geophys. Res., 88:7647-7666.

McCave, I.N., 1984. Size-spectra and aggregation of suspended particles in the deep ocean. Deep Sea Res, 31:329-352.

Michel, B., 1963. Theory of formation and deposit of frazil ice. Eastern Snow Conference, Proc. 1963 Annual Meeting, Quebec City.

Michel, B., 1971. Winter regime of rivers and lakes. USA Cold Regions Research and Engineering Laboratory, Cold Regions Science and Engineering Monograph III-B1a.

Monin, A.S. and A.M. Yaglom, 1975. Statistical Fluid Mechanics, Vol. 2, MIT Press.

Morel, F.M.M., 1983. Principles of Aquatic Chemistry, Wiley-Interscience, 446 pp.

Nagakawa, H., I. Nexu, H. Ued and H. Ueda, 1975. Turbulence in open channel flow over smooth and rough beds. Proc. Japan Soc. Civ. Eng. 241:155-168.

Neiburger, M., I.Y. Lee, E. Lobl and L. Rodriguez, Jr., 1974. Computed collision efficiencies and experimental collision efficiencies on cloud drops. Conf. Cloud Physics of the Am. Meteor. Soc., Tucson, Arizona, pp. 73-78.

Newburger, P.A. and D.R. Caldwell, 1981. Mixing and the bottom nepheloid layer. Mar. Geol., 41:321-336.

Nihoul, J.C.J. and Y. Adam, 1975. J. Hyd. Res., I.A.H.R., 13(2):171-186.

Oakey, N.S. and J.A. Elliott, 1980. Dissipation in the mixed layer near Emerald Basin. In Marine Turbulence (J.C. Nihoul, ed.), Elsevier, pp. 123-133.

O'Brien, E.E., 1980. The probability density function (pdf) approach to reacting turbulent flows. In Turbulent Reacting Flows (P.A. Libby and F.A. Williams, eds.), Topics in Applied Physics, Vol. 44, pp. 186-218.

Obukhov, A.M., 1962. Some specific features of atmospheric turbulence. J. Fluid Mech., 13:77-81.

Okubo, A., 1971. Horizontal and vertical mixing in the sea. In Impingement of Man on the Oceans, (D. Hoad, ed.), Wiley-Interscience, pp. 89-168.

O'Melia, C.R., 1980. Aquasols: the behavior of small particles in aquatic systems. Environmental Science and Technology, 14 (9):1052-1060.

Oostdam, B.L., 1977. Suspended sediment transport in the Delaware Bay. In Fate of Pollutants in the Air and Water Environment, Part 1. Mechanisms of Interaction Between Environments and Mathematical Modeling and the Physical Fate of Pollutants (I.H. Suffet, ed.), John Wiley and Sons, pp. 425-472.

Orlob, G.T., 1972. Mathematical modeling of estuarial systems. Proc. of the International Symp. on Mathematical Modeling Techniques in Water Resources Systems (A.K. Biswas, ed.), Environment Canada, Ottawa, Canada, pp. 78-128.

Osborn, T.R., 1980. Dissipation measurements of oceanic turbulence. In Marine Turbulence (J.C. Nihoul, ed.), Elsevier, pp. 143-155.

Osterkamp, T.E., 1978. Frazil ice formation: a review. J. Hyd. Div., ASCE, 104(HY9):1239-1255.

Ottens, E.P.K., A.H. Janse and E.J. DeJong, 1972. Secondary nucleation in a stirred vessel cooling crystallizer. J. Crystal Growth, 13/14:500-505.

Palmer, M.D., 1973. Some kinetic energy spectra in a nearshore region of Lake Ontario. J. Geophys. Res., 78:3585-3595.

Pearson, H.J., I.A. Valioulis and E.J. List, 1984. Monte Carlo simulation of coagulation in discrete particle-size distributions. Part I. Brownian motion and fluid shearing. J. Fluid Mech., 143:367-385

Pope, S.B., 1976. The probability approach to the modeling of turbulent reacting flows. Combustion and Flame, 27:299-312.

Pope, S.B., 1979. The relationship between the probability approach and particle models for reaction in homogeneous turbulence. Combustion and Flame, 35:41-45.

Pope, S.B., 1981. A Monte Carlo method for the PDF equations of turbulent reactive flow. Combustion Science and Technology, 25:159-174.

Pope, S.B., 1982. An improved turbulent mixing model. Combustion Science and Technology, 28:131-145.

Riley, G.A., 1970. Particulate organic matter in seawater. Adv. Mar. Biol., 8, 1-118.

Robertson, D., 1974. Monte Carlo simulations of drop growth by accretion. J. Atmos. Sci., 31:1344-1350.

Rodi, W., 1980. Turbulence models and their application in hydraulics - a state of the art review. IAHR Section on Fundamentals of Division III: Experimental and Mathematical Fluid Dynamics, 104 pp.

Saffman, P.G. and J.S. Turner, 1956. On the collision of drops in turbulent clouds. J. Fluid Mech., 1:16-30.

Sayre, W.W., 1969. Dispersion of silt particles in open channel flow. J. Hyd. Div., ASCE, 95(HY3):1009-1038.

Schlichting, H., 1968. Boundary-Layer Theory (4th Edition), McGraw-Hill.

Schubel, J.R., 1974. Effects of tropical storm Agnes on the suspended solids in the northern Chesapeake Bays. In Suspended Solids in Water (R.J. Gibbs, ed.), Plenum Press, pp. 113-132.

Scott, W.T., 1967. Poisson statistics in distributions of coalescing droplets. J. Atmos. Sci., 24:221-225.

Scott, W.T., 1968. Analytic studies of cloud droplet coalescence I. J. Atmos. Sci., 25:54-65.

Sheldon, R.W., A. Prakash and W.H. Sutcliffe, 1972. The size distribution of particles in the ocean. Limn. Oceanogr., 17:327-340.

Smith, T.J. and B.A. O'Connor, 1977. A two-dimensional model for suspended sediment transport. Reprints of the 17th Congress of the IAHR, Baden Baden, Vol. 1, pp. 79-86.

Smoluchowski, M., 1916. Drei Vortrage uber Diffusion, brownsche Bewegung and Koagulation von Kolloidteilchen. Physik Z., 17:557-585.

Somlyody, L., 1978. An effort for modeling the transport of micropollutants in rivers. Proc. International Symp. on Modeling the Water Quality of the Hydrologic Cycle, Baden, IAHS-AISH Publ. No. 125, pp. 39-49.

Spielman, L.A. and O. Levenspiel, 1965. A Monte Carlo treatment for reacting and coalescing dispersed phase systems. Chem. Eng. Sci., 20:247-254.

Stewart, R.W. and H.L. Grant, 1962. Determination of the rate of dissipation of turbulent energy near the sea surface in the presence of waves. J. Geophys. Res., 67(8):3177-3180.

Stewart, R.W., J.R. Wilson and R.W. Burling, 1970. Some statistical properties of small scale turbulence in an atmospheric boundary layer. J. Fluid Mech., 41:141-152.

Strickland-Constable, R.F., 1976. Collision breeding from solution or melt. In Industrial Crystallization (J.W. Mullin, ed.), Plenum Press, pp. 33-40.

Tambo, N. and H. Hozumi, 1979. Physical characteristics of flocs. II. Strength of floc. Water Res., 13:421-427.

Tambo, N. and Y. Watanabe, 1979. Physical characteristics of flocs. I. The floc density function and aluminum floc. Water Res., 13:409-419.

Tennekes, H. and J.L. Lumley, 1972. A First Course in Turbulence. MIT Press, 300 pp.

Valioulis, I.A., E.J. List and H.J. Pearson, 1984. Monte Carlo simulation of coagulation in discrete particle-size distributions. Part 2. Interparticle forces and the quasi-stationary equilibrium hypothesis. J. Fluid Mech., 143:387-411.

Van Atta, C.W. and R.A. Antonia, 1980. Reynolds number dependence of skewness and flatness factors of turbulent velocity derivatives. Phys. Fluids, 23:252-257.

Van Atta, C.W. and W.Y. Chen, 1970. Structure functions of turbulence in the atmospheric boundary layer over the ocean. J. Fluid Mech., 44:145-159.

Van Atta, C. and J. Park, 1972. Statistical self-similarity and inertial subrange turbulence. In Statistical Models and Turbulence (M. Rosenblatt and C. Van Atta, eds.), Lecture Notes in Physics, Vol. 12, pp. 402-426.

Warshaw, M., 1967. Cloud droplet coalescence: statistical foundations and a one-dimensional sedimentation model. J. Atmos. Sci., 24:278-286.

Webster, F., 1969. Turbulence spectra in the ocean. Deep Sea Res., 16 suppl.:357-368.

Westall, J.C., J.L. Zachary and F.M.M. Morel, 1976. MINEQL: A computer program for the calculation of chemical equilibrium composition of aqueous systems. R.M. Parsons Laboratory for Water Resources and Environmental Engineering, Technical Note No. 18.

Westall, J., 1979. MICROQL: II. Computation of adsorption equilibria in BASIC. EAWAG, Swiss Federal Institute of Technology, Duebendorf, Switzerland.

Westall, J. and H. Hohl, 1980. A comparison of electrostatic models for the oxide/solution interface. Adv. Coll. Interface Sci., 12:265-294.

Williams, R.B. and C.H. Gibson, 1974. Direct measurements of turbulence in the Pacific equatorial undercurrent. J. Phys. Oceanogr., 4:104-108.

Williamson, R.E., R.H. Crowell and H.F. Trotter, 1972. Calculus of Vector Functions, Prentice-Hall, 617 pp.

Wiseman, W.J., 1969. On the structure of high-frequency turbulence in a tidal estuary. Chesapeake Bay Institute, Tech. Rept. No. 59, 76 pp.

Woods, J.D., 1968. An investigation of some physical processes associated with the vertical flow of heat through the upper ocean. Meteorol. Mag., 97:65-72.

Yanenko, N.N., 1971. The Method of Fractional Steps (translated from Russian by M. Holt). Springer-Verlag, 160 pp.

Yousef, Y.A. and E.F. Gloyna, 1977. A transport model for long term release of low level radio-nuclide solutions into a stream ecosystem. In Fate of Pollutants in the Air and Water Environments. Part 2. Chemical and Biological Fate of Pollutants in the Environment, (I.H. Suffet, ed.), John Wiley, pp. 239-259.